Kenta Mizuse

Spectroscopic Investigations of Hydrogen Bond Network Structures in Water Clusters

Springer

Springer Theses

Recognizing Outstanding Ph.D. Research

Aims and Scope

The series "Springer Theses" brings together a selection of the very best Ph.D. theses from around the world and across the physical sciences. Nominated and endorsed by two recognized specialists, each published volume has been selected for its scientific excellence and the high impact of its contents for the pertinent field of research. For greater accessibility to non-specialists, the published versions include an extended introduction, as well as a foreword by the student's supervisor explaining the special relevance of the work for the field. As a whole, the series will provide a valuable resource both for newcomers to the research fields described, and for other scientists seeking detailed background information on special questions. Finally, it provides an accredited documentation of the valuable contributions made by today's younger generation of scientists.

Theses are accepted into the series by invited nomination only and must fulfill all of the following criteria

- They must be written in good English.
- The topic should fall within the confines of Chemistry, Physics, Earth Sciences, Engineering and related interdisciplinary fields such as Materials, Nanoscience, Chemical Engineering, Complex Systems and Biophysics.
- The work reported in the thesis must represent a significant scientific advance.
- If the thesis includes previously published material, permission to reproduce this must be gained from the respective copyright holder.
- They must have been examined and passed during the 12 months prior to nomination.
- Each thesis should include a foreword by the supervisor outlining the significance of its content.
- The theses should have a clearly defined structure including an introduction accessible to scientists not expert in that particular field.

Kenta Mizuse

Spectroscopic Investigations of Hydrogen Bond Network Structures in Water Clusters

Springer

Author
Dr. Kenta Mizuse
Institute for Molecular Science
Okazaki
Japan

Supervisor
Prof. Asuka Fujii
Tohoku University
Sendai
Japan

Parts of this thesis have been published in the following journal articles

Mizuse, K. & Fujii, A. Infrared Spectroscopy of Large Protonated Water Clusters $H^+(H_2O)_{20-50}$ Cooled by Inert Gas Attachment. *Chem. Phys.* **in press**, doi:10.1016/j.chemphys.2012.07.012 (2013).

Mizuse, K. & Fujii, A. Characterization of a Solvent-separated Ion-Radical Pair in Cationized Water Networks: Infrared Photodissociation and Ar-attachment Experiments for Water Cluster Radical Cations $(H_2O)_n+$ (n = 3-8) *J. Phys. Chem. A* in press

Mizuse, K. & Fujii, A. Tuning of the Internal Energy and Isomer Distribution in Small Protonated Water Clusters $H^+(H_2O)_{4-8}$: An Application of the Inert Gas Messenger Technique. *J. Phys. Chem. A* **116**, 4868–4877 (2012).

Mizuse, K., Kuo, J.-L. & Fujii, A. Structural trends of ionized water networks: Infrared spectroscopy of water cluster radical cations $(H_2O)_n^+$ (n = 3-11). *Chem. Sci.* **2**, 868–876 (2011).

Mizuse, K. & Fujii, A. Structural Origin of the Antimagic Number in Protonated Water Clusters $H^+(H_2O)_n$: Spectroscopic Observation of the "Missing" Water Molecule in the Outermost Hydration Shell. *J. Phys. Chem. Lett.* **2**, 2130–2134 (2011).

Mizuse, K. & Fujii, A. Infrared photodissociation spectroscopy of $H^+(H_2O)_6 \cdot M_m$ (M = Ne, Ar, Kr, Xe, H_2, N_2, and CH_4): messenger-dependent balance between H_3O^+ and $H_5O_2^+$ core isomers. *Phys. Chem. Chem. Phys.* **13**, 7129–7135 (2011).

Hamashima, T., Mizuse, K. & Fujii, A. Spectral Signatures of Four-Coordinated Sites in Water Clusters: Infrared Spectroscopy of Phenol−$(H_2O)_n$ ($\sim 20 \leq n \leq \sim 50$). *J. Phys. Chem. A* **115**, 620–625 (2011).

Mizuse, K., Mikami, N. & Fujii, A. Infrared Spectra and Hydrogen-Bonded Network Structures of Large Protonated Water Clusters $H^+(H_2O)_n$ (n = 20–200). *Angew. Chem. Int. Ed.* **49**, 10119–10122 (2010).

Mizuse, K., Hamashima, T. & Fujii, A. Infrared Spectroscopy of Phenol−$(H_2O)_{n>10}$: Structural Strains in Hydrogen Bond Networks of Neutral Water Clusters. *J. Phys. Chem. A* **113**, 12134–12141 (2009).

Supervisor's Foreword

It is great pleasure for me to introduce Dr. Kenta Mizuse's outstanding work for publication in the Springer Theses series. Dr. Mizuse received a B.S. from Tohoku University in March 2006 under the supervision of Prof. Naohiko Mikami. In April 2006 he entered the Graduate School of Science of Tohoku University and started his doctoral study with me. He received his M.S. and Ph.D. in 2008 and 2011, respectively, at Tohoku University for the excellent achievements described in this thesis.

Water clusters have been extensively studied as a microscopic model of water hydrogen bond structures. Dr. Mizuse made the best use of size-selective infrared spectroscopy and succeeded in opening a new stage of water cluster research. His work on large-sized water clusters, new applications of inert gas tagging, and cluster approach to radiation chemistry of water was published as nine original papers in top journals of chemistry and physical chemistry. This thesis gathers these scientific achievements by Dr. Mizuse on water clusters and should attract great interest in the diverse communities of chemistry, biochemistry, and geophysics. I hope this excellent work by Dr. Mizuse will stimulate further development of water chemistry and gas phase cluster study.

Sendai, August 2012   Asuka Fujii

Acknowledgments

My family members gave me an opportunity to study chemistry for 9 years at Tohoku University and provided financial and moral support. I thank them for everything.

Contents

Chapter 1
General Introduction

Abstract Water plays essential roles in the various chemical, biological, and geophysical processes. It is clear that hydrogen bonds are responsible for the unique and important properties of water. Then, hydrogen-bonded network structures in water are of fundamental interest. Many studies have been carried out to probe structures of bulk water with various spectroscopic techniques. However, there have been still many difficulties in understanding the structures of bulk water at the molecular-level. Water clusters $(H_2O)_n$ are a microscopic model for bulk water and they provide detailed information on hydrogen-bonded water networks. Because hydrogen bonding environments of water molecules are sensitively reflected to their OH stretching vibrations, infrared (IR) spectroscopy of a cluster of a specific size (n) has been a powerful tool to probe the network structures. Such studies have been revealed structures of $(H_2O)_n$ $(n \leq 10)$ and succeeded in characterizing chain type, ring type, and three-dimensional water networks. For larger clusters $(n \geq \sim 10)$, higher-order structures, which should be more similar to bulk, are expected. However, much less spectroscopic studies have been reported due to the experimental difficulty in the size-selection.

Keywords Water chemistry · Water clusters · Hydrogen bond networks · Models in science · Infrared spectroscopy

1.1 Hydrogen Bonds and the Properties of Water

Water is one of the most ubiquitous materials on the earth and it plays essential roles in a variety of chemical, biological, physical, and geophysical processes. For example, the oceans of the earth contain 1.4×10^{24} g of water and therefore the earth is known and described as a "water planet" [1, 2]. It is also well known that water accounts for ~ 65 % of the human bodyweight, with many biochemical

reactions occurring in the aqueous environment. In this situation, water acts as a biological solvent. Of course, water is essential and important not only for human beings, but also for living things on the earth. From the viewpoint of chemists and physicists, water is a highly polar solvent with quite anomalous properties compared to other compounds. Typical examples are its exceptionally high boiling/melting/critical points, high surface tension, and the volume expansion upon freezing (with higher density as a liquid than as a solid), and density maximum at 277 K. Many other unique properties of water are mentioned in the literature [1, 2]. These anomalies (unique properties) clearly play key roles in nature. This makes water an exceptional and fundamental matter.

A water molecule consists of two positively polarized hydrogen atoms and one negatively polarized oxygen atom with different electronegativity (Fig. 1.1). When more than one water molecule exists in a system, the polarized nature of the water molecule can be a driving force for an intermolecular interaction known as a hydrogen bond. According to the IUPAC definition, a hydrogen bond is an attractive interaction between an X–H group in which X is more electronegative than H, and an acceptor atom or group [3, 4]. As shown in the structural formulae in Fig. 1.1, there are two non-bonding electron pairs on the oxygen atom of H_2O. These lone pairs can provide a good hydrogen bond acceptor site, while, of course, hydrogen atoms are hydrogen bond donor sites. Hydrogen bonding between water molecules is consequently represented by "O–H⋯:O" (Fig. 1.2a). A hydrogen bond generally has enthalpy of the order of a few tens kJ/mol (a few thousands cm^{-1}) [1, 2, 5–7]. Such a value is larger than that of a van der Waals interaction and it can affect whole properties of water. For example, hydrogen bonding accounts for the resistance from the evaporation upon heating. This results in water's higher than expected boiling point based on its molecular weight. Today, there is no doubt that the hydrogen bond governs the characteristic nature of water.

Because H_2O has two hydrogen bond acceptor sites (two lone pairs) and donor sites (two OH groups), generally up to four hydrogen bonds can be formed around a single H_2O molecule (Fig. 1.2b). Such multiple hydrogen bond formation results in network formation. Because of the intrinsic importance of the hydrogen bond in water science, structures and dynamics of hydrogen-bonded water network have been of broad interest.

Fig. 1.1 Some expressions of a water molecule. **a** Lewis structure. **b** Structural formula. **c** Schematic model with electrostatic potential; and **d** schematic model with bond length and angle
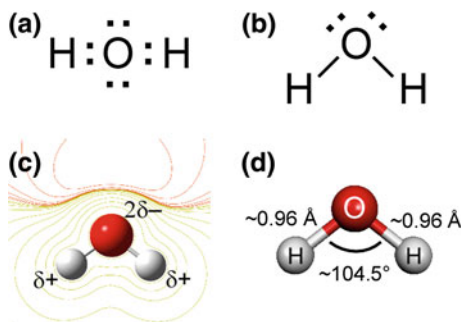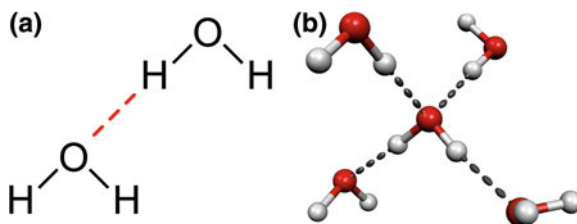
Fig. 1.2 **a** Hydrogen bond between two water molecules (*red dashed line*); and **b** Schematic model of the 4-coordinated water molecule (the *center molecule*)
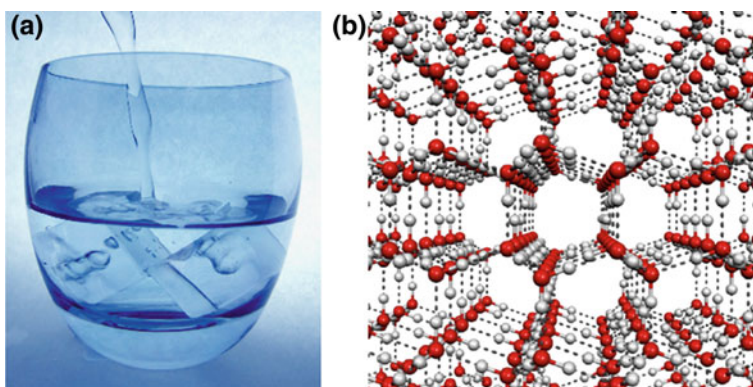
Fig. 1.3 **a** Water with ice. **b** Molecular structure of hexagonal ice (ice Ih)

In the case of ice, X-ray, electron, and neutron scattering experiments have identified the hydrogen-bonded water networks [1]. There are several (at least 12) polymorphs of ice. The most ubiquitous ice Ih (hexagonal ice, Fig. 1.3) has a diamond-like oxygen skeleton, in which all the water molecules are 4-coordinated and the network consists only of the 6-membered ring motif. On the other hand, in the case of liquid water, the great number of molecules and their thermal fluctuation make analysis extremely difficult. For example, there have been many conflicting reports concerning on the average coordination number in liquid water by using X-ray, Raman, infrared, and theoretical methods [8–14].Therefore, it is not a simple task to understand liquid water networks at the molecular level, and analysis has remained a controversial subject. These facts indicate the difficulty and importance of studying hydrogen-bonded water networks.

1.2 Clusters as a Model for Complicated Chemical Systems

When scientists try to understand unknown and complicated phenomena, we often build a model [7, 15, 16]. A model (in science) is a scaled-down version of a target system. A typical example is the ideal gas model for real gases, in which the

molecular volume and intermolecular interaction are neglected. Such simplification enables us to deduce many important properties of gases from the simple expression of the equation of state, "$PV = nRT$". A simplification to deduce essences that govern a system is one of the central instruments of scientific methods.

For studies of hydrogen-bonded water networks (liquid water, ice, aqueous solutions), hydrated clusters (X-$(H_2O)_n$: X = solute, n = 1, 2, 3,…) in the gas phase have been used as microscopic models. In this case, a cluster is an aggregate consisting of a finite number of molecules and the number of molecules n is called cluster size. In contrast to a bulk system, a cluster study enables us to confine the system within the cluster size depending on the purpose of each situation. For example, to study an isolated hydrogen bond between water molecules, the water dimer $(H_2O)_2$ is the smallest system. To cover the first hydration shell, several water molecules only should be taken into account. Furthermore, clusters in the gas phase (more precisely, *in vacuo*) are the ideal target of spectroscopy because they are free from the perturbation of numerous solvents or other molecules. Such a reduction and simplification of a system leads to a detailed and deeper understanding that is not easily accessible by condensed phase (especially liquid phase) studies. We think one of the most important advantages is the fact that we can characterize a variety of water networks at the molecular level, yet we can also probe the flexibility of water networks, and we can study structure-dependent properties (e.g., spectra, dynamics, and reactivity) of hydrogen-bonded water networks.

There have been many cluster studies concerning the microscopic views of hydrogen bond networks. Water clusters $(H_2O)_n$ as a model for pure water networks are the fundamental example of these studies. In following sections, a brief introduction to some studies on water clusters is given. More details (e.g., methods) are also given in the following chapters.

1.3 Previous Studies on Pure Water Clusters $(H_2O)_n$

1.3.1 Pioneering Studies on $(H_2O)_n$ (n = 2–6)

Structures and properties of water clusters in the gas phase have been extensively studied experimentally and theoretically [17]. In this thesis, introductions to previous studies are given from the viewpoint of experimental sides. As for structures, Fig. 1.4 collects the spectroscopically-identified structures of small water clusters $(H_2O)_n$ ($n \leq 10$).

Among all the water clusters and hydrated clusters, water dimer $(H_2O)_2$ is the simplest system that contains a hydrogen bond between water molecules. Moreover, it provides most detailed properties and characteristics of a hydrogen bond of water. Historically, in the 1970s, microwave spectroscopy determined the structure of the water dimer as shown in Fig. 1.4 [18, 19]. In the 1990s, by using vibration–rotation
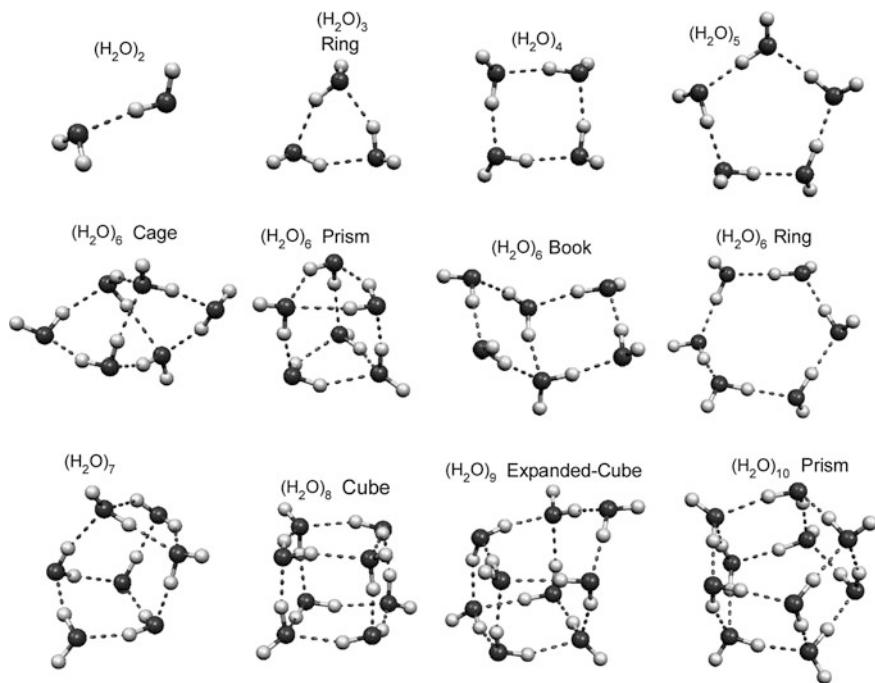
Fig. 1.4 Experimentally-identified structures of small water clusters

tunneling spectroscopy and theory, the water–water pair potential was developed [20, 21]. Recently, hydrogen bond energy (precisely, interaction energy) in a water dimer is determined by infrared photodissociation and the following state-sensitive detection and ion imaging (kinetic energy measurement) technique [22]. The reported energy is 1105 cm^{-1} (13.2 kJ/mol). Here, we note this value is smaller than that of bulk water measured with calorimetry ($\sim$21 kJ/mol, energy value slightly varies depending on a definition) [1]. This difference can be accounted for by the cooperativity of hydrogen bonds.

Details of cooperativity are discussed in Chap. 2. In brief, the cooperativity or cooperative effect refers to the fact that hydrogen bonds mutually enhance their strength [2]. That is, hydrogen bond energy increases with the increasing number of surrounding hydrogen bonds in a system. This is why the reported hydrogen bond in the water dimer, which is regarded as an "isolated" hydrogen bond, is weaker than that in bulk. This also shows that we have to study larger clusters to examine cooperativity. Furthermore, as mentioned above, the water dimer only tells us about "chain" type structures, not higher order structures.

For trimer to hexamer $(H_2O)_n$ ($n = 3$–6) clusters, pioneering vibration–rotation tunneling spectroscopy reported by Saykally's group has characterized the ring type water trimer $(H_2O)_3$, tetramer $(H_2O)_4$, and pentamer $(H_2O)_5$ [23–27]. It has also identified the 3-dimensional cage-type water hexamer $(H_2O)_6$ [28]. This cage

structure is important not only as the smallest 3-dimensional water network but also as the smallest structure that includes a 3-coordinated water molecule. This contrasts with ring-type smaller clusters that have only 2-coordinated water. As clearly shown in these studies, an increase in the number of water molecules provides significant insight into complicated water networks.

Studies on $(H_2O)_6$ have also provided another important side to the nature of water networks: variety or flexibility. Sophisticated cluster production techniques (e.g., helium nanodroplet or tuned molecular beam) have opened the way to observing other isomeric structures such as ring and book types [29–31]. Very recently, Perez et al. have observed the coexistence of the cage, prism, and book isomers by using broadband microwave spectroscopy [32]. Figure 1.4 presents these characterized structures. These studies have observed the variety of hydrogen-bonded water network structures at the molecular level.

Because hydrogen-bonded networks in liquid water have flexibility and they change their forms rapidly (e.g., in the time scale of $\sim$ps), numerous types of networks appear [33]. This means that molecular level identification of multiple network structures in the $(H_2O)_6$ system is very important in the field of water network research. Despite the importance of these studies, only a few network structures have been investigated. Furthermore, all the structures observed consist primarily of 2- or 3-coordinated molecules. This contrasts sharply with bulk water, in which 4-coordinated water is abundant. Based on this, it can be said that there is a clear gap between the small water clusters ($n = 6$ or smaller) and the condensed phase (bulk) water (Fig. 1.5). This indicates that additional studies on larger clusters are necessary for further understanding of water networks.

From an experimental point of view, spectral characterization of these clusters has been done with the measurements that are neither size-selective nor isomer-selective. Spectra do not overlap, mainly because of the simplicity of small cluster systems (i.e., only small number of isomers coexist and spectral difference between other sizes/isomers is relatively large). These spectra are each assigned to a size and structure. For larger clusters, the number of isomers increases and rotational constants become very small (i.e., small rotational band spacing). Furthermore, size- and isomer-dependent spectral features would hardly ever be
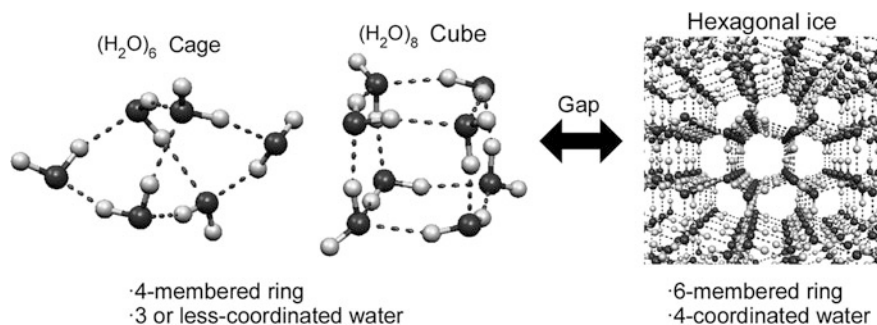
Fig. 1.5 Conceptual diagram of the gap between small water clusters and bulky water networks

seen due to the spectral overlap. It is therefore difficult to analyze spectra and investigate cluster structures without size-selective measurements. These aspects indicate the importance of size-selective spectroscopy for larger clusters. Moreover, high-resolution rotationally-resolved spectroscopy becomes inefficient for larger cluster structural analyses, and in this case other complementary methods would become powerful tools for examining these larger clusters.

1.3.2 Infrared Spectroscopy for Small, Size-Selected (H$_2$O)$_n$ (n ≤ 10)

In general, vibrational spectra sensitively reflect hydrogen bonding environments [1, 2]. For example, OH stretch frequency is shifted to lower frequency upon hydrogen bond formation. Low-frequency shift is larger when stronger hydrogen bonds are formed. This shift is accompanied by band broadening due to the reduced lifetime of the vibrational-excited state. Furthermore, each water molecule in a cluster has different intrinsic frequencies depending on its environment in the hydrogen bond network. OH stretch band is therefore a good marker for hydrogen bonding interactions. Even when a cluster size is considered large and many water molecules are included, local environments of each OH group are reflected in local OH frequencies. This would enable us to assign each band to each water molecule in a specific position in the hydrogen bond network. It is also possible to analyze overlapped bands on the basis of band frequencies. Such powerful use of vibrational spectroscopy for structural investigations will be shown throughout this thesis. It should be noted that vibrational spectroscopy does not lead to an exact cluster structure, which includes exact bond lengths and so on, because vibrational frequency itself does not contain direct structural information (e.g., a harmonic vibrational frequency is just a function of the force constant and reduced mass). This makes a sharp contrast with, for example, microwave spectroscopy in which determined rotational constants are functions of structural parameters. Vibrational spectroscopy is, however, one of the most powerful and popular methods of probing hydrogen bond networks for the above-mentioned reasons.

There have been several infrared spectroscopy (IR) studies of water clusters which are not size-selective [29, 34–39]. The molecular-beam method and matrix (including He droplet) isolation techniques have been utilized. Spectral carriers of reported spectra are the mixture of clusters of different sizes and then detailed analyses were limited to the hexamer or smaller clusters, in which bands can be assigned to each a size.

For detailed information on water clusters, size-selective IR spectroscopy is necessary. In the 1980s, Vernon et al. reported size-selective IR spectra of (H$_2$O)$_n$ ($n \leq 6$) by using a molecular beam apparatus combined with an electron ionization mass spectrometer. Due to the many fragmentation channels upon ionization, rigorous size-selection was not achieved. A more sophisticated approach to

size-selection was presented by the Huisken and Buck groups [17, 40–42]. For the $n = 2$–10 clusters, they have measured size-selective infrared (IR) spectra by using the crossed beam technique [17, 40–42]. In their studies, water clusters are formed in a molecular beam and deflected by a helium beam via a momentum transfer. Size-selective detection is done by tuning a detector angle to the size-specific direction of the deflection. IR spectra were measured by irradiating clusters with IR light prior to the size-selection. IR vibrational excitation-induced fragmentation was monitored as signal depletion of the cluster size of interest. It should be noted that another size-selective spectroscopy, IR–UV double resonance spectroscopy, [43] which is combined with chromophore-labeling to water clusters, has been used to deduce almost the same understanding of clusters of these sizes [44–47]. This method is the focus of the following chapter.

Observed size-selective IR spectra of $(H_2O)_{7-10}$ show extended features from water $(H_2O)_6$. These spectra have been almost fully explained after the effort on quantum chemical calculations [17]. Characterized structures are shown in Fig 1.4. Among these structures, water octamer $(H_2O)_8$ seems quite characteristic because of its highly symmetric cubic structure. Water heptamer $(H_2O)_7$ and nonamer $(H_2O)_9$ can be characterized as defected and extended cubes, respectively. Further step-wise extension of networks (a pentagonal prism type) are seen in structures of water decamer $(H_2O)_{10}$.

Although these studies have succeeded in characterizing three-dimensional water networks at the molecular level, there is also the large gap between these structures and bulky water networks. This is because the observed three-dimensional networks, such as cubic $(H_2O)_8$, are dominated by 4-membered rings (the oxygen skeleton), which consist of distorted hydrogen bonds. Moreover, all molecules locate on the surface of the cluster, and the maximum coordination number of water molecules is 3. These points again make a sharp contrast with bulk water networks such as hexagonal ice (ice Ih), in which the hydrogen bond network is constructed only by 6-membered rings and all water molecules are 4-coordinated (Fig. 1.5). It is therefore considered that a greater number of molecules is required to characterize bulky and/or higher order water networks.

1.3.3 Infrared Spectroscopy for Larger Water Clusters $(H_2O)_n$ $(n > 10)$

All the previous spectroscopic studies on the larger-sized ($n > 10$) water clusters, however, have been carried out without rigorous size-selection. Page et al. measured the IR spectrum of moderately size-selected $(H_2O)_n$ ($n \sim 19$) using electron ionization mass spectrometry [48]. Buck et al. have reported the IR spectrum of an ensemble of clusters in the size range of $n = 10$–20 using the momentum transfer technique [17]. Except for these studies, only IR spectroscopy of the average size ($<n>$)-estimated $(H_2O)_{<n>}$ ($\sim 10 \leq <n> \leq \sim 10^6$) have been performed.

Buck et al. have reported IR photodissociation spectra of $(H_2O)_{<n>}$ $(<n> = 40–2,379)$, in which size distribution is controlled by the supersonic jet expansion conditions [49–51]. Fourier transform (FT)-IR spectra have been also reported in the broad size range $<n> < \sim 10^6$ [50]. These studies have shown that the spectra of the clusters approach that of bulk ice with increasing average cluster size, suggesting development from "amorphous networks" to "crystalline ice nanoparticles with a distorted surface" $(<n> \geq \sim 200–1000)$ [50]. A similar size-dependent crystallization has been shown by electron diffraction studies, in which the cluster size distribution is also broad [52]. These studies have demonstrated that some structural trends can be detected by the average size selection. However, the effect of the broad size distribution on the observed spectra is ambiguous, and it prevents determination of the detailed cluster structures.

1.4 Motivations and Goals

The general purpose of this thesis is to obtain detailed insights into properties (structures, dynamics, reactivity, and so on) of hydrogen-bonded water networks from extended studies on water clusters.

As implied above, size-selective IR spectroscopy on larger (n = tens or more) clusters is the first subject to be examined in this thesis. On the basis that clusters can provide a model for water networks, the increase of constituent water molecules corresponds to the extension and improvement of the scientific modeling. Models in science should be always improvable and extendable. As the introduction of anharmonicity to the harmonic oscillator model allows us to deal with a dissociation process, the increase of water molecules in clusters will provide further information on water networks. It is expected that such an extension of cluster studies will enable us to encounter various hydrogen-bonded water network structures, thereby bridging the gap between the previously characterized small network structures and bulky water networks. We believe these observations add insights into water chemistry (see Figs. 1.6 and 1.7).

It is clear that even though size-selective spectra are measured, analyses of large cluster spectra will face difficulties. Inhomogeneous broadening due to the large number of molecules is their intrinsic nature. In addition, more isomeric structures would coexist with increasing cluster size, resulting in further spectral complication. Moreover, band broadening due to the finite internal (thermal) energy sometimes veils spectral features. Conversely, these facts suggest if the internal energy and isomer distribution are variable, more information on the cluster structure and hydrogen bond network should be available. Therefore, one of the further investigations in this thesis is tuning of the internal energy and isomer distribution in hydrated clusters (Fig. 1.8). In previous cluster studies, these parameters were rarely varied. According to these arguments, this theme is also an extension of clusters as a model of complicated systems.
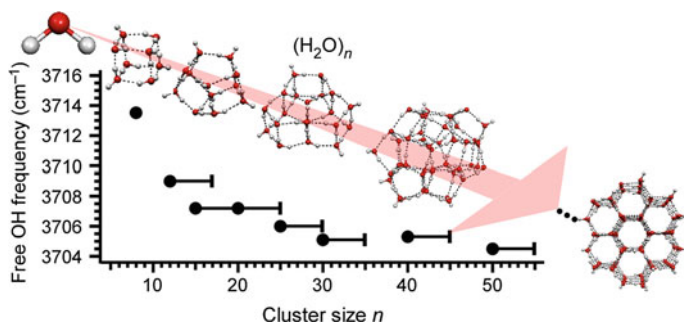
Fig. 1.6 Graphical abstract for IR spectroscopy of large neutral water clusters (Chap. 2). Hydrogen bond distortion is relaxed in larger clusters, bridging the gap between the small clusters and bulky networks [53] (Copyright 2009 American Chemical Society)
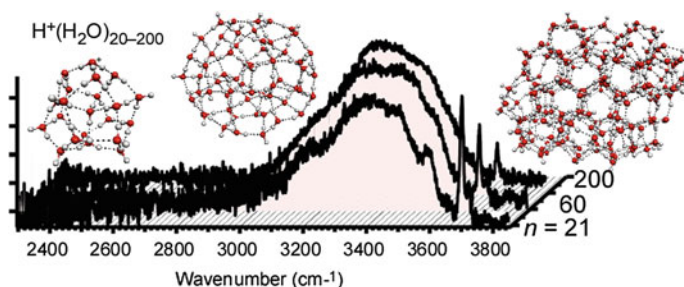
Fig. 1.7 Graphical abstract for IR spectroscopy of large protonated water clusters (Chap. 3). Hydrogen bond networks of more than 200 water molecules are first investigated with size-selective spectroscopy [55] (Copyright 2010 John Wiley and Sons)
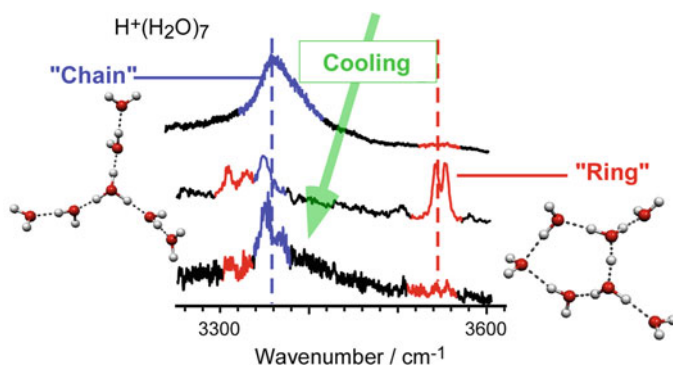
Fig. 1.8 Graphical abstract for the tuning experiments for internal energy and isomer distributions in small to large protonated water clusters (Chap. 4) [59] (Copyright 2009 American Chemical Society)

Fig. 1.9 Graphical abstract for IR spectroscopy of water cluster radical cations (Chap. 5) [60]. The observed structure provides new insights into radiation chemistry of water (Reproduced by Permission of The Royal Society of Chemistry)
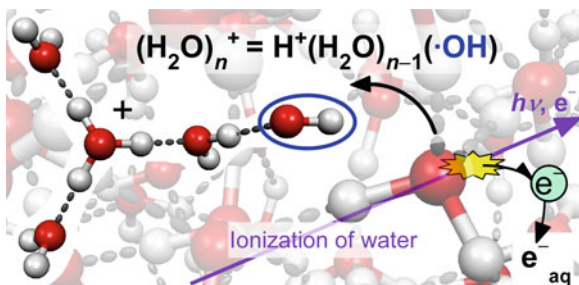
These studies should lead to microscopic insights into hydrogen-bonded water networks. More precisely, the structural aspects of water networks are mainly investigated. In general, chemists study structures of molecules of interest in the first stage of their research because structure is the most important factor in relation to chemical reactivity and other important properties. Once the structure is determined, many properties may be predicted. Therefore, structural studies of water clusters can provide insights into chemical properties. As I believe one of the most important goals of cluster chemistry, or more generally, physical chemistry is to understand chemical reactions, in the last topic in this thesis, I would like to show spectroscopic studies of water clusters succeed in characterizing the trend of a chemical reaction in hydrogen-bonded water networks. I will focus on an elementary step of radiation chemistry of water, as an example of chemical reactions in water networks. In this study, an intracluster reaction in ionized water clusters is modeled and studied systematically (Fig. 1.9). Here, not only a solute but also solvents are taken into account in an obvious manner (by changing the number of water molecules involved).

1.5 Outline

This chapter introduced the general background behind water cluster studies. More detailed and specified backgrounds are given in each chapter. Figures 1.6, 1.7, 1.8 and 1.9 provide a graphical abstract of Chaps. 2, 3, 4 and 5, respectively.

In Chap. 2, to bridge the gap between the well-known small water clusters and bulky water networks and to characterize water networks that consist of more than 10 water molecules, IR spectroscopy of large, neutral water clusters is described [53, 54]. The chromophore-labeling technique was introduced for ionization detection and moderate size-selectivity. The measured spectra are interpreted and hydrogen-bonded network structures are characterized in terms of the hydrogen bond distortion and coordination numbers (Fig. 1.6).

In spectroscopy of neutral clusters, we encounter difficulties on rigorous size-selection. To achieve complete size-selection, ionic water clusters should be the next target. In Chap. 3, for protonated water clusters $H^+(H_2O)_n$ (which have been

extensively studied), size-selective spectroscopy is extended to the hitherto uncovered size region; $n > 200$ [55]. These clusters have been studied as microscopic models for the hydrated proton, however, in our study, we focus on their aspect as "charge-labeled" water clusters. For small-sized clusters, effects of the excess charge (excess proton) on the cluster structure are remarkable, but we would expect these effects to be diluted with increasing cluster size. For ionic clusters, application of mass spectrometric techniques removes the difficulty in the size-selection and opens the way to study larger-scaled water networks. The observed spectra show gradual shift towards bulky water spectra. Here network structures are discussed in terms of coordination number and network ordering (Fig. 1.7).

In spectroscopy of large water clusters, we face a difficulty in analyzing spectra because of their complexity. In Chap. 4, we demonstrate an approach to simplify the spectra of large hydrated clusters [56–59]. By using the so-called messenger technique or inert gas attachment, which is one of the cooling methods for gas phase clusters, internal energy and isomer distribution is at least partly tuned (Fig. 1.8). Such tuning enables us to obtain detailed spectral and structural information. For example, an important cluster structure has been identified which is responsible for hydrogen bond network instability.

Chapter 5, infrared spectroscopy of reactive water networks is presented. Herein, systematic structural studies on water cluster radical cations $(H_2O)_n^+$ are demonstrated and they showed general trends of these networks [60]. The observed trends are used to build new chemical models in radiation chemistry of water (Fig. 1.9).

Chapter 6 provides a summary of important results and an outlook for spectroscopy of gas phase water clusters.

References

1. D. Eisenberg, W. Kausmann, *The Structure and Properties of Water* (Oxford University Press, Oxford, 1969)
2. Y. Maréchal, *The Hydrogen Bond and the Water Molecule* (Elsevier, Amsterdam, 2007)
3. E. Arunan, G.R. Desiraju, R.A. Klein, J. Sadlej, S. Scheiner, I. Alkorta, D.C. Clary, R.H. Crabtree, J.J. Dannenberg, P. Hobza, H.G. Kjaergaard, A.C. Legon, B. Mennucci, D.J. Nesbitt, Pure Appl. Chem. **83**, 1637–1641 (2011)
4. E. Arunan, G.R. Desiraju, R.A. Klein, J. Sadlej, S. Scheiner, I. Alkorta, D.C. Clary, R.H. Crabtree, J.J. Dannenberg, P. Hobza, H.G. Kjaergaard, A.C. Legon, B. Mennucci, D.J. Nesbitt, Pure Appl. Chem. **83**, 1619–1636 (2011)
5. J.N. Israelachvili, *Intermolecular and Surface Forces*, 2nd edn. (Academic Press, London, 1992)
6. L. Pauling, *The Nature of the Chemical Bond*, 3rd edn. (Cornell University Press, New York, 1960)
7. P.W. Atkins, *Physical Chemistry*, 6th edn. (Oxford University Press, Oxford, 1998)

8. P. Wernet, D. Nordlund, U. Bergmann, M. Cavalleri, M. Odelius, H. Ogasawara, L.A. Naslund, T.K. Hirsch, L. Ojamae, P. Glatzel, L.G.M. Pettersson, A. Nilsson, Science **304**, 995–999 (2004)

9. J.D. Smith, C.D. Cappa, K.R. Wilson, B.M. Messer, R.C. Cohen, R.J. Saykally, Science **306**, 851–853 (2004)

10. A. Nilsson, P. Wernet, D. Nordlund, U. Bergmann, M. Cavalleri, M. Odelius, H. Ogasawara, L.A. Naslund, T.K. Hirsch, L. Ojamae, P. Glatzel, L.G.M. Pettersson, Science **308**, 793a (2005)

11. J.D. Smith, C.D. Cappa, B.M. Messer, R.C. Cohen, R.J. Saykally, Science **308**, 793b (2005)

12. A. Lenz, L. Ojamäe, J. Phys. Chem. A **110**, 13388–13393 (2006)

13. D.A. Schmidt, K. Miki, J. Phys. Chem. A **111**, 10119–10122 (2007)

14. R. Ludwig, Chem. Phys. Chem. **8**, 938–943 (2007)

15. D.C. Baird, *Experimentation*, 3rd edn. (Prentice-Hall, Upper Saddle River, 1995)

16. M.B. Hesse, Brit. J. Philos. Sci **4**, 198–214 (1953)

17. U. Buck, F. Huisken, Chem. Rev. **100**, 3863–3890 (2000)

18. T.R. Dyke, J.S. Muenter, J. Chem. Phys. **60**, 2929–2930 (1974)

19. T.R. Dyke, K.M. Mack, J.S. Muenter, J. Chem. Phys. **66**, 498–510 (1977)

20. K.L. Busarow, R.C. Cohen, G.A. Blake, K.B. Laughlin, Y.T. Lee, R.J. Saykally, J. Chem. Phys. **90**, 3937–3943 (1989)

21. R.S. Fellers, C. Leforestier, L.B. Braly, M.G. Brown, R.J. Saykally, Science **284**, 945–948 (1999)

22. B.E. Rocher-Casterline, L.C. Ch'ng, A.K. Mollner, H. Reisler, J. Chem. Phys. **134**, 211101 (2011)

23. N. Pugliano, R.J. Saykally, Science **257**, 1937–1940 (1992)

24. J.D. Cruzan, L.B. Braly, K. Liu, M.G. Brown, J.G. Loeser, R.J. Saykally, Science **271**, 59–62 (1996)

25. K. Liu, M.G. Brown, J.D. Cruzan, R.J. Saykally, Science **271**, 62–64 (1996)

26. K. Liu, J.D. Cruzan, R.J. Saykally, Science **271**, 929–933 (1996)

27. F.N. Keutsch, J.D. Cruzan, R.J. Saykally, Chem. Rev. **103**, 2533–2578 (2003)

28. K. Liu, M.G. Brown, C. Carter, R.J. Saykally, J.K. Gregory, D.C. Clary, Nature **381**, 501–503 (1996)

29. K. Nauta, R.E. Miller, Science **287**, 293–295 (2000)

30. C. Steinbach, P. Andersson, M. Melzer, J.K. Kazimirski, U. Buck, V. Buch, Phys. Chem. Chem. Phys. **6**, 3320–3324 (2004)

31. E.G. Diken, W.H. Robertson, M.A. Johnson, J. Phys. Chem. A **108**, 64–68 (2003)

32. C. Pérez, M.T. Muckle, D.P. Zaleski, N.A. Seifert, B. Temelso, G.C. Shields, Z. Kisiel, B.H. Pate, Science **336**, 897–901 (2012)

33. M. Matsumoto, A. Baba, I. Ohmine, J. Chem. Phys. **127**, 134504 (2007)

34. D.F. Coker, R.E. Miller, R.O. Watts, J. Chem. Phys. **82**, 3554–3562 (1985)

35. L.M. Goss, S.W. Sharpe, T.A. Blake, V. Vaida, J.W. Brault, J. Phys. Chem. A **103**, 8620–8624 (1999)

36. J.B. Paul, C.P. Collier, R.J. Saykally, J.J. Scherer, A. O'Keefe, J. Phys. Chem. A **101**, 5211–5214 (1997)

37. A. Moudens, R. Georges, M. Goubet, J. Makarewicz, S.E. Lokshtanov, A.A. Vigasin, J. Chem. Phys. **131**, 204312 (2009)

38. *Faraday Discuss* **118**, 295–314 (2001)

39. K. Ohno, M. Okimura, N. Akai, Y. Katsumoto, Phys. Chem. Chem. Phys. **7**, 3005–3014 (2005)

40. F. Huisken, M. Kaloudis, A. Kulcke, J. Chem. Phys. **104**, 17–25 (1996)

41. U. Buck, I. Ettischer, M. Melzer, V. Buch, J. Sadlej, Phys. Rev. Lett. **80**, 2578 (1998)

42. J. Brudermann, M. Melzer, U. Buck, J.K. Kazimirski, J. Sadlej, V. Bush, J. Chem. Phys. **110**, 10649 (1999)

43. R.H. Page, Y.R. Shen, Y.T. Lee, J. Chem. Phys. **88**, 5362–5376 (1988)

44. R.N. Pribble, T.S. Zwier, Science **265**, 75–79 (1994)

45. C.J. Gruenloh, J.R. Carney, C.A. Arrington, T.S. Zwier, S.Y. Fredericks, K.D. Jordan, Science **276**, 1678–1681 (1997)
46. S. Tanabe, T. Ebata, M. Fujii, N. Mikami, Chem. Phys. Lett. **215**, 347–352 (1993)
47. T. Watanabe, T. Ebata, S. Tanabe, N. Mikami, J. Chem. Phys. **105**, 408–419 (1996)
48. R.H. Page, M.F. Vernon, Y.R. Shen, Y.T. Lee, Chem. Phys. Lett. **141**, 1–6 (1987)
49. P. Andersson, C. Steinbach, U. Buck, Euro. Phys. J. D **24**, 53–56 (2003)
50. V. Buch, S. Bauerecker, J.P. Devlin, U. Buck, J.K. Kazimirski, Int. Rev. Phys. Chem. **23**, 375–433 (2004)
51. C. Steinbach, P. Andersson, J.K. Kazimirski, U. Buck, V. Buch, T.A. Beu, J. Phys. Chem. A **108**, 6165–6174 (2004)
52. G. Torchet, P. Schwartz, J. Farges, M.F. de Feraudy, B. Raoult, J. Chem. Phys. **79**, 6196–6202 (1983)
53. K. Mizuse, T. Hamashima, A. Fujii, J. Phys. Chem. A **113**, 12134–12141 (2009)
54. T. Hamashima, K. Mizuse, A. Fujii, J. Phys. Chem. A **115**, 620–625 (2011)
55. K. Mizuse, N. Mikami, A. Fujii, Angew. Chem. Int. Ed. **49**, 10119–10122 (2010)
56. K. Mizuse, A. Fujii, *Chem. Phys.* (in press)
57. K. Mizuse, A. Fujii, Phys. Chem. Chem. Phys. **13**, 7129–7135 (2011)
58. K. Mizuse, A. Fujii, J. Phys. Chem. Lett. **2**, 2130–2134 (2011)
59. K. Mizuse, A. Fujii, J. Phys. Chem. A **116**, 4868–4877 (2012)
60. K. Mizuse, J.L. Kuo, A. Fujii, Chem. Sci. **2**, 868–876 (2011)

Chapter 2
Infrared Spectroscopy of Chromophore-Labeled Water Clusters Phenol-$(H_2O)_n$ ($n < \sim 50$)

Abstract To analyze hydrogen bond network structures consisting of tens of water molecules, we measured moderately size-selective IR spectra of large, labeled water clusters phenol-$(H_2O)_n$ in the OH stretch region. The observed spectral features were analyzed in terms of hydrogen bond ring size motifs and coordination numbers of water molecules. The detailed analyses of the free OH band indicated that the observed low-frequency shift originates from the cooperativity of hydrogen bonds and the structural development from the highly strained 4-membered ring motif to the more relaxed 5- and 6-membered ring motifs. The suppression of free OH band intensity with an increase of n represents the increase of the abundance of 4-coordinated waters. We expect that the present characterization method of hydrogen bond networks may be applicable to more complicated, condensed phase water.

Keywords Phenol-water clusters · Supersonic jet expansion · IR–UV spectroscopy · Hydrogen bond network distortion · Coordination number analyses of water

2.1 Introduction

As described in Chap. 1, size-selective IR spectroscopy of large water clusters consisting of ten or more molecules is necessary to study large-scale, bulky hydrogen-bonded water networks. The clear structural differences can be seen between small clusters ($n < \sim 10$) and bulk water. The most obvious differences are coordination numbers of molecules and ring size of hydrogen bond networks; small clusters mainly consist of 3-coordinated molecules and 4-membered rings, while ice Ih consists of 4-coordinated molecules and 6-membered rings (see Fig. 1.5). The main purpose of this chapter is to bridge the gap by extending spectroscopic method to larger water clusters $(H_2O)_n$ ($n > \sim 10$).

Previously, several approaches have been made towards size-selective spectroscopy of large water clusters as introduced in Sect. 1.3.3. Figure 2.1 shows IR spectra reported in these studies [1–6]. Unfortunately, these studies lack size-selectivity and/or size variety. As a result, the structures of large clusters have not necessarily been discussed on the basis of experimental spectra.

On the other hand, there is essentially no difficulty in the size-selection in theoretical calculations, although exponential increase of possible isomer structures is another serious problem for large-sized clusters. Recent development of theories, algorithms, and computer resources make it possible to treat relatively large water networks with reasonable accuracy. Extensive theoretical studies on the $(H_2O)_n$ ($n < \sim 50$) clusters, from empirical methods to sophisticated density functional theory and high-level *ab initio* combined with minimum search algorisms, have predicted that the 4-membered ring motif will become less important with increasing cluster size while the 5- and 6-membered ring motifs will become superior [5, 7–22]. For example, Kazimirski and Buch [7] have carried out a low energy isomer search for $(H_2O)_{48}$ with the empirical TIP4P potential. In the reported structure of $(H_2O)_{48}$ (Fig. 2.2), only 18 % of rings are 4-membered and 5- and 6-membered rings become superior, although $(H_2O)_8$ consists only of 4-membered rings. Another structural transition, the appearance and increase of 4-coordinated water molecules and also the interior formation have been also suggested in this size region [5, 7–22]. For example, Lagutschenkov et al. [10] have suggested the "interior" water molecules arise at around $n = 17$ on the basis of their empirical and high-level *ab initio* calculations (Fig. 2.2). On the other hand, smaller clusters are categorized as "all surface" types, in which all the water molecules are located at the surface of the network. If molecules are completely inside a network, they should be
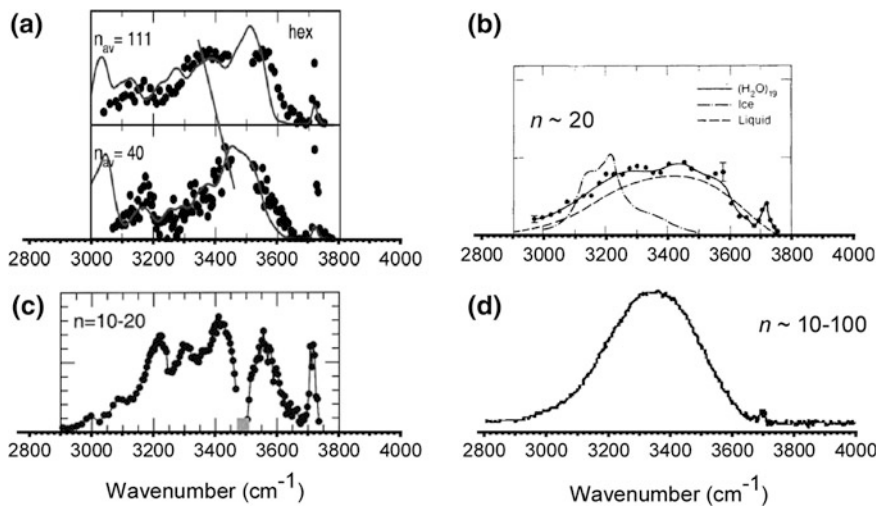
Fig. 2.1 Previously reported IR spectra of roughly size-selected or size-estimated large water clusters. **a** From Ref. [4], **b** from Ref. [2], **c** from Ref. [1], and **d** from Ref. [3]
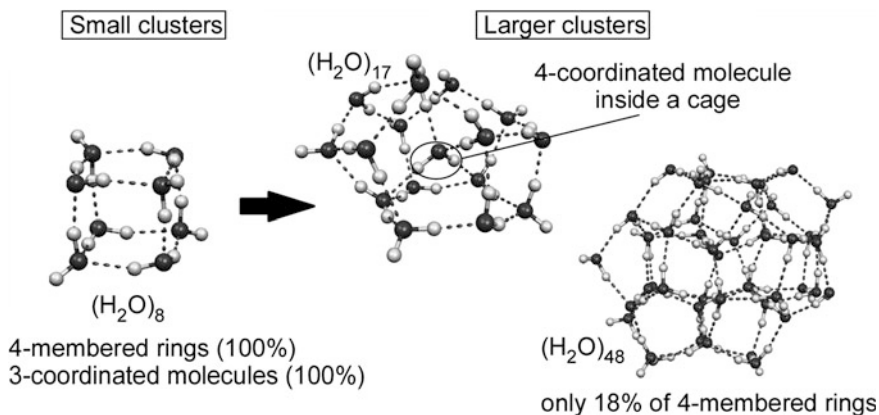
Fig. 2.2 Theoretically predicted cluster structures and structural developments of $(H_2O)_n$ ($n > \sim 10$). Appearance of 4-coordinated molecules and decrease of 4-membered rings is displayed

4-coordinated. This implies that the signature of 4-coordinated molecules would be observed in the size range ($n \sim$ a few tens). To study high order structures of hydrogen-bonded water networks, observation of such interior molecules should be an important step. Figure 2.2 indicates some characteristic cluster structures of $(H_2O)_n$ highlighting the predicted structural changes in the $n > 10$ region. As mentioned here, recent developments in computational chemistry have stimulated size-selective spectroscopy of water clusters consisting tens of molecules. However, correlations between detailed cluster structures and IR spectral features have not been extensively examined. This fact also indicates the importance of size-selective IR spectra of large water clusters.

An experimental bottleneck relates to the detection technique. Clusters of interest are formed by the supersonic jet expansion technique [23], which is the most popular method for cluster production. In this method, a gaseous mixture of sample molecules is expanded into a vacuum chamber. Only low concentration is achieved in the molecular/cluster beam and as a result, direct photo absorption detection, which detects decrease of light intensity, is generally impossible. We therefore have to utilize highly sensitive detection techniques, the fluorescence or ionization detection of gas phase molecular and cluster samples. Water clusters are, of course, not fluorescent. For spectroscopic purposes, ionization by photons is preferable [24], however the ionization energy of water molecules (12.62 eV) is very high and we need a short wavelength vacuum-ultraviolet light ($< \sim 100$ nm, depending on the cluster size [25–27]) or a very intense light source such as a femtosecond laser for photoionization of water clusters [28, 29]. Unfortunately, both of these were not available for our procedures. This problem has made it difficult to select the cluster size with photoionization mass spectrometry and to measure IR spectra with photoionization-based spectroscopic technique, as shown below.

To overcome these problems, we introduced a label to the water clusters. Phenol as an ultraviolet (UV) chromophore was used as a spectroscopic label (Fig. 2.3). The chromophore-labeled water clusters have the advantage of possessing an UV chromophore (the phenyl ring), which enables us to apply various spectroscopic techniques such as resonant two-photon ionization (R2PI) based on UV electronic transition. Since the earlier stages of spectroscopic studies on gas-phase hydrated clusters, phenol-$(H_2O)_n$ have been studied extensively by, for example, fluorescence excitation, R2PI, and various double resonance spectroscopies [30–50].

As shown in Sect. 1.3, IR spectroscopy is a powerful tool to probe hydrogen bond networks. IR–UV double resonance spectroscopy is a technique to measure a size- and isomer-specific IR spectra of gas phase molecules and clusters with a chromophore [44, 51, 52]. This technique was developed by Lee's group in the 1980s [51]. It has been applied to many molecules/clusters including phenol-$(H_2O)_n$ and was successful in characterizing structures and many other properties [44, 52]. Here, an overview of this method is given. The energy scheme is shown in Fig. 2.4. First, UV light is tuned to the wavelength of vibronic transition of the species of interest. Resonant multiphoton ionization signals or fluorescent signals from the electronic excited state are monitored as a measure of population of the ground vibrational state. While monitoring this signal, the IR light pulse is irradiated prior to the UV light pulse. When IR light is absorbed, vibrational transition occurs and the ground vibrational level population is decreased, leading a depletion of the monitored signal. A depletion signal as a function of IR wavelength can be regarded as an IR spectrum. In this method, if the UV wavelength is tuned to size- and isomer-specific transition, the measured IR spectrum is size- and isomer-selective.

Previous studies, especially those on vibrational spectroscopy (IR–UV double resonance spectroscopy) in the OH stretch region, showed that phenol-$(H_2O)_n$ are structural analogues of neat $(H_2O)_{n+1}$ because the hydroxy group of the phenol plays a compatible role to that of a water in the hydrogen bond network [43, 49, 50] (Fig. 2.5). Of course, because phenol is a weak acid molecule, it may act as a stronger hydrogen bond donor, and the hydrogen bond network of phenol-$(H_2O)_n$ is more or less perturbed from the neat $(H_2O)_n$. The reported results, that both labeled and neat clusters have essentially the same network, indicate that perturbation from UV-chromophore is too small to affect hydrogen-bonded water networks in these systems. For phenol-$(H_2O)_n$ [42, 43, 49] and a similar system, benzene-$(H_2O)_{n+1}$ [52–57], size-selected IR spectra have been measured up to $n \leq 8$ using their size-

Fig. 2.3 Introduction of UV-chromophore (label) to water clusters
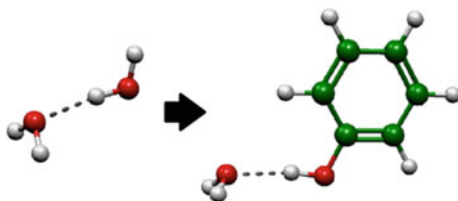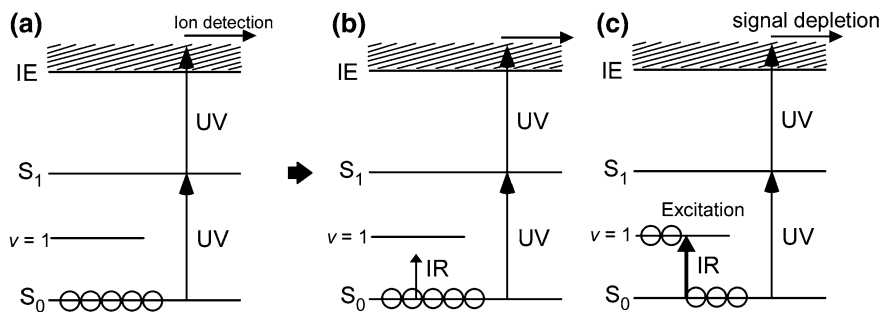
Fig. 2.4 Energy scheme in IR–UV double resonance spectroscopy. *Open circles* denote a molecule/cluster in various states. **a** First, ground vibrational state population was probed with R2PI. **b**, **c** IR light is irradiated and its wavelength is scanned. **c** When IR light is absorbed, vibrational excitation results in the ion signal depletion
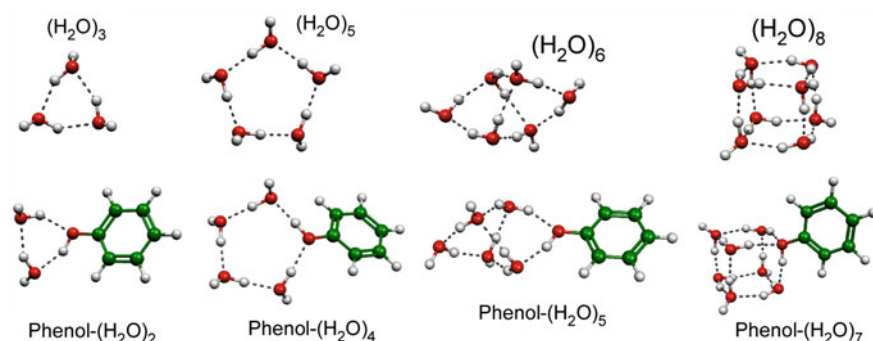
Fig. 2.5 Experimentally characterized structures of phenol-$(H_2O)_n$ and $(H_2O)_{n+1}$. Both hydrogen bond network structures are essentially the same

specific UV transitions. These IR spectroscopic studies on chromophore-labeled water clusters have pioneered structural studies on small-sized water networks, as those of neat $(H_2O)_n$ clusters [2, 58–63] have done.

Here, we comment on the choice of the label. There have been other labels used for water clusters. Benzene-$(H_2O)_n$ and Na-$(H_2O)_n$ clusters have been also studied with photoionization-based methods [52–57, 64–68]. In the case of benzene-$(H_2O)_n$, hydrogen-bonded networks are pure water networks, while phenol-$(H_2O)_n$ contains a phenol molecule in a network. Despite this advantage of benzene, in such a cluster, a benzene ring is bound to an OH moiety of H_2O via an OH…π interaction [53, 54, 69]. Such an interaction is absent from pure water networks and therefore, spectral interpretation would become complicated [53, 69]. Furthermore, an OH…π interaction is generally weaker than hydrogen bonding, therefore yields of benzene-$(H_2O)_n$ are smaller than those of phenol-$(H_2O)_n$. For Na-$(H_2O)_n$, single UV photon ionization can be applied, however, interaction

between a water network and an unpaired electron on Na seems ignorable [67, 68]. According to these considerations, we employed a phenol molecule as a label.

For larger-sized clusters ($n > \sim 10$) with a chromophore, UV absorption bands are generally broadened and IR–UV double resonance spectroscopy has been considered useless for size selection. In this study, however, we use the scheme of the IR–UV double resonance but utilize only photoionization mass spectrometry to select the cluster size. Though we sacrifice rigorous size-selection because of fragmentation upon ionization, we still achieve moderate size-selectivity in the IR spectral measurement of phenol-$(H_2O)_n$ by monitoring the [phenol-$(H_2O)_n$]$^+$ ion signal. In this study, we measured IR spectra of roughly size-estimated clusters to probe hydrogen bond networks of 10 or more water molecules.

2.2 Experimental

2.2.1 Overview of Infrared Spectroscopy

Here, a brief overview of experimental methods is given and details are shown in the following sections. The gas phase phenol-$(H_2O)_n$ clusters were produced in a pulsed supersonic jet expansion of the gaseous phenol/water mixture diluted with helium. IR spectra of moderately size-selected phenol-$(H_2O)_n$ ($n = 11$–49) in the free OH stretch region (2,800–3,800 cm^{-1}) were measured by the IR–UV double resonance technique combined with mass spectrometry. Figure 2.6 shows an energetic scheme of the present "modified" IR–UV double resonance spectroscopy. The [phenol-$(H_2O)_n$]$^+$ ions produced by one-color resonant two-photon ionization (R2PI) of neutral clusters were mass-selected by a time-of-flight (TOF) mass spectrometer. Due to fragmentation upon ionization, [phenol-$(H_2O)_n$]$^+$ ions can be produced by R2PI of phenol-$(H_2O)_{n+\Delta n}$ (Δn is the number of evaporated water molecules upon ionization). As we will discuss later, the maximum Δn upon one-color R2PI is estimated to be 6 or less with the aid of a conservation law of energy (for details, see Sect. 2.2.3.2). The [phenol-$(H_2O)_n$]$^+$ ion intensity can be a measure of the ground state population of phenol-$(H_2O)_{n+\Delta n}$ ($0 \leq \Delta n \leq 6$). Then an IR pulse was introduced prior to the UV pulse and its frequency was scanned. When an IR transition occurs in phenol-$(H_2O)_{n+\Delta n}$, the monitored [phenol-$(H_2O)_n$]$^+$ signal decreases because of the vibrational predissociation of the clusters. IR spectra were thus measured by monitoring the ion intensity while scanning IR wavelength. In typical IR–UV double resonance spectroscopy, just a vibrational population transfer (excitation) is required to observe the dip signal [51], however, when a broadened UV transition is used, species in a vibrational excited state might also absorb UV light and then, vibrational dissociation would be needed for depletion spectroscopy. Of course, if the UV transition probability between the vibrational ground and excited states is different, IR-induced signal arises. However, the exact evaluation of such transition probability is beyond the scope of this work.
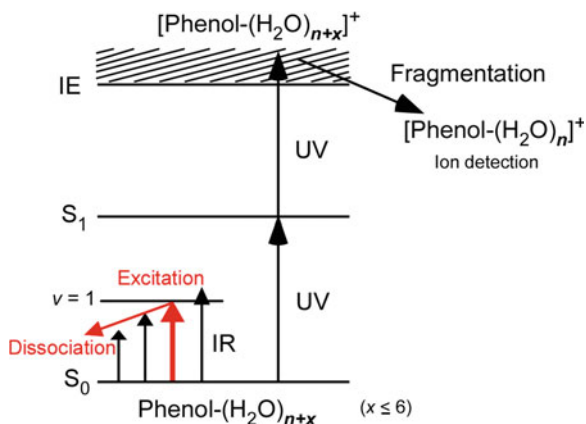
Fig. 2.6 Energy scheme in "modified" IR–UV double resonance spectroscopy used in the present study

2.2.2 Setup

2.2.2.1 Vacuum Chamber

Figure 2.7 shows the scheme of the vacuum chamber used in this study. This chamber consists of a supersonic jet expansion cluster source and a time-of-flight (TOF) mass spectrometer. This chamber was evacuated by two turbomolecular pumps, backed by rotary pumps.

In the cluster source region, the gaseous mixture of phenol (trace), water (trace), and helium (0.3 MPa) was expanded into a chamber through a pulsed valve (General valve Series 9, 0.5 mm nozzle diameter, Parker). The gas pulse was skimmed by a skimmer (2 mm hole diameter) and introduced to the interaction region, between the repeller and extractor electrodes of time-of-flight mass spectrometer.
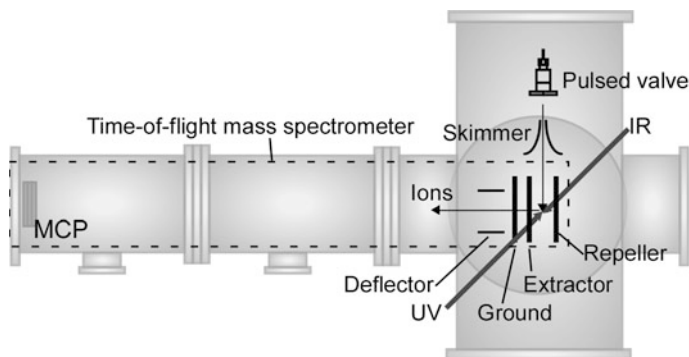
Fig. 2.7 Scheme of the vacuum chamber used in the present study

The time-of-flight mass spectrometer moiety was equipped with a 2-step acceleration region to improve mass resolution (Wiley-McLaren type [70]). The deflector was also equipped to compensate for the initial velocity, which is perpendicular to the TOF axis. Clusters are ionized by UV pulse between the repeller (typically +2500 V) and extractor ($\sim$+1500 V) electrodes. Ions were extracted toward TOF tube (grounded), in which ions were mass-separated and then detected with a stack of microchannel plates (MCP).

2.2.2.2 Laser Systems

Figure 2.8 shows a diagram of the experimental setup. UV light was the second harmonic (SHG) of a dye laser output (Laser Analytical System LDL20505 with Coumarin 540A dye) pumped by a third harmonics (355 nm) of a Nd:YAG laser (1064 nm, Surelite III, Continuum). UV light was introduced to the middle of the repeller and extractor electrodes of time-of-flight mass spectrometer. A plano-convex quartz lens ($f = 500$ mm) was used for focusing the UV light. IR light was obtained by the difference frequency generation (DFG) with a $LiNbO_3$ crystal between the second harmonic (532 nm) of a Nd:YAG laser (1064 nm, Surelite III, Continuum) and an output of a dye laser (ND6000, Continuum, with DCM and LDS698 dyes). The optical path of the IR light was aligned to the same axis as the UV light from the opposite side. The IR light was focused by a plano-convex CaF_2 lens ($f = 250$ mm). In both systems, autotrackers (Inrad) were used to keep the phase matching angle while scanning wavelength. IR power was monitored by installing a CaF_2 beam sampler plate and an IR power meter (Molectron). The wavelength of the IR light was calibrated (in vacuum wavenumbers) by recording an ambient water vapor spectrum. Figure 2.9 shows a typical power curve of IR light obtained with DFG. The gap of around 3,500 cm^{-1} is due to the IR absorption by water impurities in the $LiNbO_3$ crystal. The wavelength of the UV light was calibrated in vacuum wavenumbers by recording a reported R2PI spectrum of phenol-$(H_2O)_{0-2}$.

2.2.2.3 Measurement System

Two YAG lasers and a pulsed valve were triggered by TTL outputs (10 Hz) from digital delay generators (DG 535, SRS). Ion signals from MCP were amplified (wide band preamplifier BX-31A, NF Electronic Instruments) and transferred to an oscilloscope (TDS 640A, 500 MHz, Tektronix) and a boxcar integrator (SR250, SRS). Both of which were triggered by a photodiode, which monitored emissions from Surelite. The oscilloscope was used for monitoring ion signals, gate signals of the boxcars, and IR power. It was also used for the measurement of TOF mass spectra.

For IR measurements, the ion signal of interest and IR power signal were averaged with SR250, and their data were sent to a digitizer (analog-to-digital converter) (SR245, SRS). Thus obtained data points were transferred to a computer
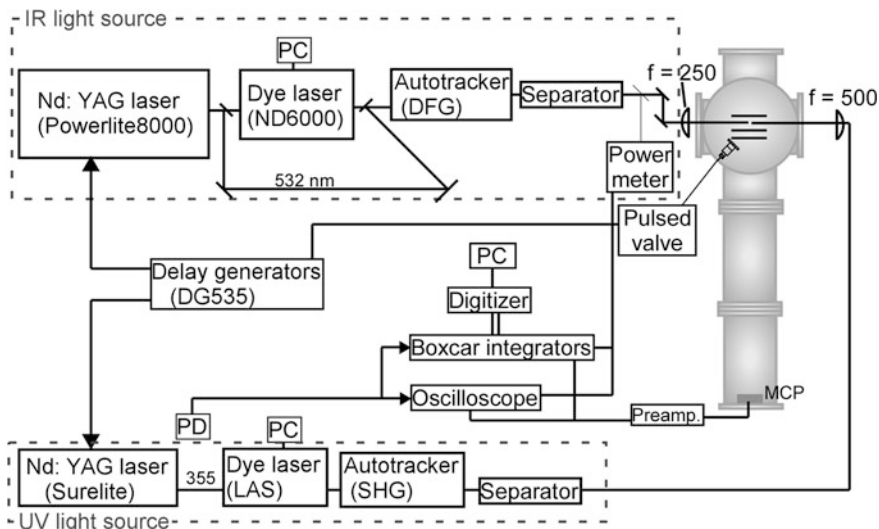
Fig. 2.8 Schematic diagram of the experimental setup

Fig. 2.9 Typical power curve of IR light source obtained with DFG
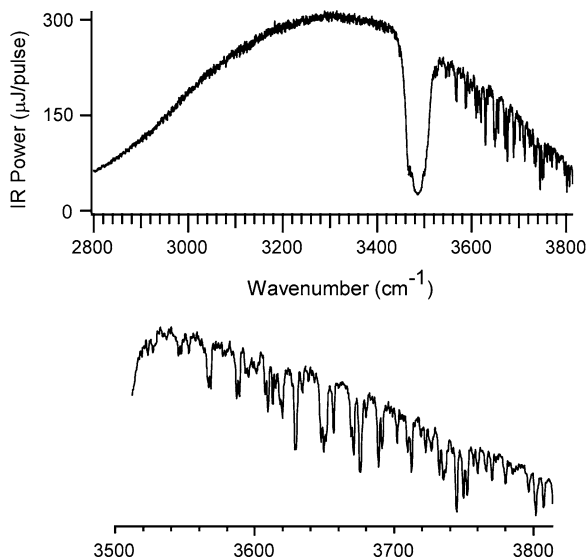
and plotted as a function of IR wavelength. Here, IR wavelength was scanned by operating a ND6000 with a constant speed scan mode. The observed raw IR spectra were normalized by IR power.

In the long-range scan (e.g. for the whole OH stretch region 2,800–3,800 cm^{-1}), the signal intensity sometimes changed in time due to the valve conditions and for other reasons. To improve the quality of observed spectra, the active baseline subtraction technique was applied to reduce artifacts by fluctuation

of the signal baseline. For this technique, the pulsed valve and the pulsed UV light were operated at 10 Hz while the pulsed IR light was at 5 Hz. The (raw) IR spectral data points were obtained from the differences in the ion intensity with and without the IR irradiation.

2.2.3 Measurements

2.2.3.1 Resonant 2-Photon Ionization of Phenol-$(H_2O)_n$

Figure 2.10 shows the one-color R2PI spectra obtained by monitoring [phenol-$(H_2O)_n]^+$ while scanning the UV wavelength. The spectra of the phenol$^+$ and phenol-$(H_2O)_1^+$ channels show essentially the same features as those reported previously [32, 35, 40, 43, 44]. In Fig. 2.10, only a structureless absorption band is seen for $n \geq 9$. The maximum size of the cluster, which shows sharp vibronic bands, has been reported to be $n = 12$ (by two-color R2PI spectroscopy, which minimizes the fragmentation) [48]. Contribution of larger clusters due to fragmentation and inherent broadening in large-sized clusters would wash out sharp spectral features in the present spectra. The UV frequency was tuned to 36,254 cm^{-1}, which is at near the maximum of the broad absorption of large-sized

Fig. 2.10 One-color resonant two-photon ionization spectra of phenol-$(H_2O)_n$ obtained by monitoring [phenol-$(H_2O)_n]^+$ ions. Assignments were taken from previous studies. The *dashed line* indicates the UV photon energy, 36,254 cm^{-1}, used for the photoionization in the IR spectral measurements
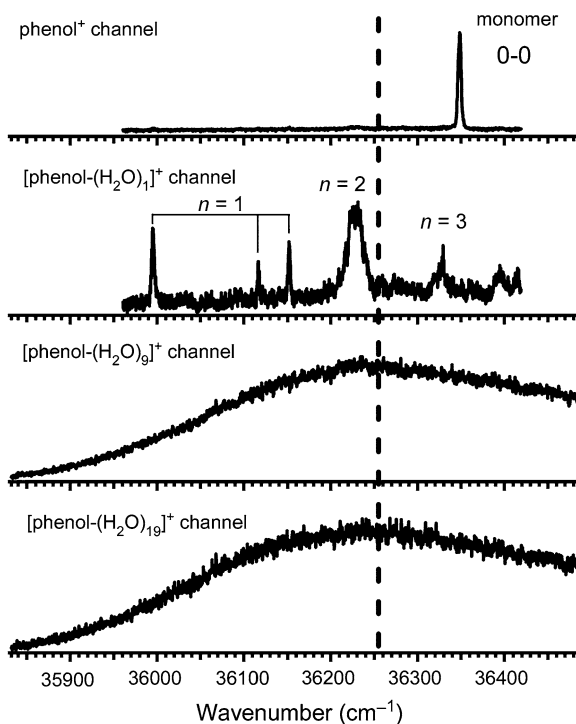
Fig. 2.11 Time-of-flight mass spectrum of [phenol-$(H_2O)_n$]$^+$ obtained with 36,254 cm^{-1} resonant 2-photon ionization
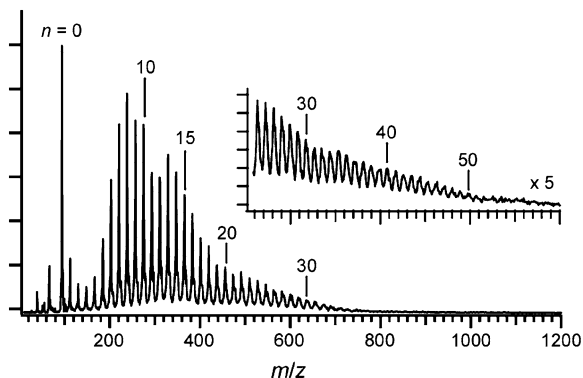
clusters, and the [phenol-$(H_2O)_n$]$^+$ ion intensity was monitored. Figure 2.11 shows a R2PI mass spectrum recorded by irradiating the 36,254 cm^{-1} UV light. Efficient cluster detection of up to $n < \sim 50$ was achieved.

We note that an application of two-color R2PI spectroscopy with an ionization UV pulse at a suitable frequency should reduce the excess energy and suppress fragmentation upon ionization [48]. Though we actually applied the two-color R2PI scheme for the present large-sized clusters, the two-color ionization signal was hardly detectable. This is because the production yields of the large-sized clusters are so low that we needed to use a relatively intense UV pulse for the first electronic excitation, and it significantly reduced the ionization by the second UV pulse.

2.2.3.2 Evaluation of Size-Selectivity

Because hydrogen-bonded clusters usually suffer from fragmentations in an ionization process, it is difficult to precisely measure the size distribution of the neutral clusters only from mass spectrometry. However, for phenol-$(H_2O)_n$, the number of evaporated water molecules (Δn) upon one-color R2PI can be estimated to be 6 or less by the energetics calculations. Figure 2.12 shows the schematic energy diagram on the photoionization and dissociation of phenol-$(H_2O)_n$. Because the one water loss channel ([M-$(H_2O)_n$]$^+ \rightarrow$ [M-$(H_2O)_{n-1}$]$^+$ + H_2O) is the major dissociation path in cationic hydrated clusters with excess energies [71], we assume the sequential evaporation of water molecules one by one upon ionization. Then, the maximum Δn is evaluated by

$$\text{maximum } \Delta n = E_{\text{excess}}/D(D_0) \tag{2.1}$$

where E_{excess} is the maximum excess energy upon ionization and $D(D_0)$ is the dissociation energy of the one water-loss channel in the cationic state. Because [phenol-$(H_2O)_n$]$^+$ ($n \geq 3$ or 4) forms an intracluster proton-transferred [PhO·-H$^+$($H_2O)_n$] type structure [72–74], the dissociation energies of H$^+$($H_2O)_n$, which have been measured by the mass spectrometric technique [75], can be used as $D(D_0)$ here. E_{excess} is given by:

Fig. 2.12 Schematic energy diagram on the photoionization and dissociation of phenol-$(H_2O)_n$

where $E(S_0)$ and $E(D_0)$ are the absolute energies of phenol-$(H_2O)_n$ and [PhO·-H$^+$$(H_2O)_n$] at the zero-point level, respectively, then $[E(D_0) - E(S_0)]$ is the adiabatic ionization energy of the phenol-$(H_2O)_n$; $E(UV)$ is the UV photon energy (36,254 cm^{-1}), and $D(S_0)$ is the dissociation energy in the S_0 state. In Eq. (2.2), $D(S_0)$ accounts for the maximum internal energy of the phenol-$(H_2O)_n$. Though we employ the supersonic jet cooling technique, the clusters have finite internal energies (temperatures). In addition, broadened electronic spectra of the large-sized clusters prevent us from evaluating the internal energy. The maximum internal energy of the cluster should be lower than $D(S_0)$, because clusters with internal energy higher than $D(S_0)$ spontaneously dissociate into smaller-sized clusters prior to arrival at the interaction region with the lasers.

Considering these relationships, we examined the energetics of dissociation of phenol-$(H_2O)_{11,19}$ following the photoionization, as typical examples. $E(S_0)$ and $E(D_0)$ were evaluated using density functional theory (DFT) calculations at the B3LYP/6-31+G(d) level (see Sect. 2.2.4). The structures of [PhO·-H$^+$$(H_2O)_{11,19}$] were constructed by putting a PhO·-radical on a free OH group of the global minimum structures of H$^+$$(H_2O)_{11,19}$, which have been extensively studied experimentally and theoretically [76–78]. Cluster structures calculated for energy evaluation, shown in Fig. 2.13, have a separated radical-charge pair form. Although Kleinermanns et al. [74] reported that the PhO radical directly solvates the H$_3$O$^+$ moiety in the [phenol-$(H_2O)_4$]$^+$, cluster structures with [PhO·H$_3$O$^+$] core did not

$$E_{excess} = 2E(UV) - [E(D_0) - E(S_0)] + D(S_0) \qquad (2.2)$$

Fig. 2.13 Cluster structures of [phenol-$(H_2O)_{11,19}]^+$ ([PhO·-$H^+(H_2O)_{11,19}]$) calculated for energy evaluation
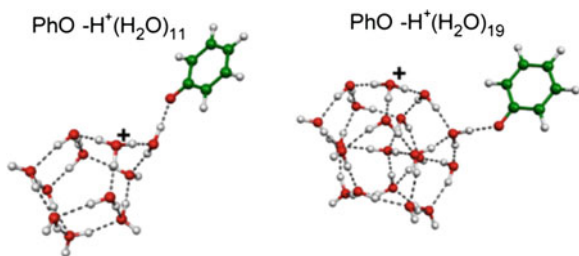
survive during the geometry-optimization steps in our calculations of [phenol-$(H_2O)_{11}]^+$ and [phenol-$(H_2O)_{19}]^+$ because of the intracluster proton transfer. A similar situation was also seen in the $(H_2O)_n^+$ case (Chap. 5). Calculated adiabatic ionization energies, $[E(D_0) - E(S_0)]$, are 56,090 cm^{-1} for phenol-$(H_2O)_{11}$, and 54,935 cm^{-1} for phenol-$(H_2O)_{19}$. For $H^+(H_2O)_{11,19}$, experimental dissociation energy values are larger than 3,000 cm^{-1} [75]. According to the structural and chemical similarity, we assume $D(D_0)$ of [phenol-$(H_2O)_n]^+$ is the same as the reported dissociation energy of $H^+(H_2O)_n$. $D(S_0)$ is generally smaller than $D(D_0)$ because of the enhanced electrostatic interactions in the ionic state. Therefore, from Eqs. (2.1) and (2.2), the maximum Δn is evaluated to be 6 in both the cases..

It should be noted that the estimated value of Δn is based on hypothetical ionic cluster structures and calculated energies. This means an "exact" evaluation of Δn is hardly possible. Furthermore, Δn would be size-dependent because the ionization energy of clusters is size-dependent. This uncertainty is a limitation of the present moderately size-selective spectroscopy. Despite such uncertainty, observed spectra show clear size-dependence indicating good size-selectivity as shown in Sect. 2.3.

2.2.3.3 IR Spectral Measurements

For IR spectral measurement, the timing of the IR pulse was tuned to ~ 50 ns prior to the UV pulse. Optical paths were then optimized by using reported IR transition of the phenol monomer. Re-adjustment of optical paths was not necessary for cluster spectroscopy.

Figure 2.14 shows the mass distribution of [phenol-$(H_2O)_n]^+$ produced by R2PI in the IR spectral measurement condition for phenol-$(H_2O)_{49}$. The red curve in Fig. 2.14 shows the mass distribution with IR irradiation, while the black curve shows it without IR irradiation. Figure 2.14 demonstrates that IR absorption causes predissociation of neutral clusters. The IR spectrum of the moderately size-selected cluster was measured as an ion-dip spectrum by monitoring the [phenol-$(H_2O)_n]^+$ ion intensity. Because IR predissociation of larger-sized clusters results in the fragmentation of the monitored ion channel [phenol-$(H_2O)_n]^+$, it causes an offset to the IR ion-dip spectrum of the cluster size of interest. To reduce such interference from larger-sized clusters, in every IR spectral measurement,
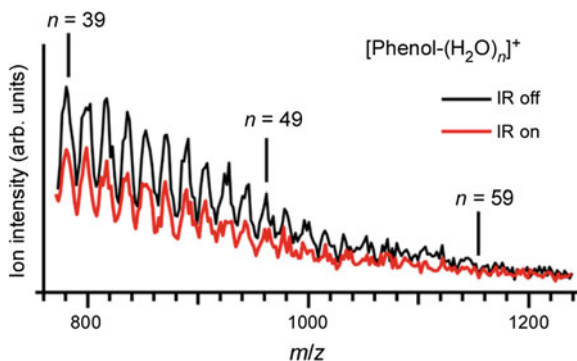
Fig. 2.14 Mass distribution of [phenol-(H$_2$O)$_n$]$^+$ produced by R2PI. The condition of the cluster production was optimized for IR spectral measurement of phenol-(H$_2$O)$_{49}$. The *red curve* shows the mass distribution with IR irradiation, while the *black* one shows the distribution without IR irradiation

we adjusted the cluster size distribution to reduce the clusters larger than those of interest by changing the jet expansion conditions. For example, the size distribution shown as the black curve in Fig. 2.14 is optimized for the IR measurement of $n = 49$.

2.2.4 Quantum Chemical Calculations

2.2.4.1 Calculation Procedures

For the detailed analyses of the cluster structures and their correlations with experimental spectra as well as their energies, DFT calculations were carried out using the B3LYP functional [79, 80] with the 6-31+G(d) basis set. The initial geometries of (H$_2$O)$_n$ were obtained from the reported low-lying minima or characteristic structures [7, 13, 16, 21, 81, 82], or otherwise they were manually constructed. Those of phenol-(H$_2$O)$_{n-1}$ were constructed by substituting one of the free hydrogen atoms in (H$_2$O)$_n$ to the phenyl group. All the cluster structures considered were fully geometry-optimized. In the geometry-optimizations, we typically used the redundant internal coordinates while the use of the distance matrix coordinates sometimes results in a better convergence.

At the stationary points, harmonic frequencies and IR intensities were calculated. All the calculated frequencies were scaled by a single factor of 0.9736, which was determined to reproduce the free OH stretching frequency of the cubic water octamer. There have been three experimental reports on the free OH frequency of cubic water octamer, i.e. (H$_2$O)$_8$, benzene-(H$_2$O)$_8$, and phenol-(H$_2$O)$_7$ [49, 54, 56, 63]. Here we employed the value of benzene-(H$_2$O)$_8$ [54], 3713.5 cm^{-1} as a reference experimental value to determine the scaling factor for

the following reasons: The previously reported spectrum of neat $(H_2O)_8$ suffers from low spectral resolution for precise determination of the free OH frequency. On the other hand, the resolution in the spectra of benzene-$(H_2O)_8$ is high enough. In addition, perturbation of the benzene ring on the free OH frequency is estimated to be negligible because free OH bands in both benzene-$(H_2O)_8$ and (benzene)$_2$-$(H_2O)_8$ show essentially the same frequency [56]. Though Kleinermanns and co-workers reported the free OH frequencies of 3711.5 cm^{-1} (D_{2d}-type) and 3710.5 cm^{-1} (S_4-type) for cubic phenol-$(H_2O)_7$, they employed atmospheric wavenumbers for their calibration [49, 50]. We confirm that their experimental values for phenol-$(H_2O)_7$ are in agreement with our calculated values, 3712.7 cm^{-1} (D_{2d}-type) and 3712.1 cm^{-1} (S_4-type) at the B3LYP/6-31+G(d) level of theory with the scaling factor of 0.9736 when the vacuum correction (addition ca. 0.8–1 cm^{-1} to atmospheric wavenumbers) is included.

The calculated stick spectrum was transformed into the continuous spectrum by using Lorentzian functions of 10 and 50 cm^{-1} full widths at half-maximum for the free and hydrogen-bonded OH stretches, respectively. Here, two bandwidths were used to take into account the lifetime-broadening induced by hydrogen bonding [83]. We note that this convolution was used only for convenience in the comparison with the simulated spectra and the values of the bandwidth have no rigorous physical meanings. The calculated free OH frequency reported in this study is the maximum of the single Lorentzian fitting of these overlapped multiple Lorentzian curves of the free OH bands. Therefore, we should note that we discuss the averaged behavior of the free OH bands. All the energy values include zero-point corrections. All the calculations in this study were carried out using the Gaussian 03 [84] and Gaussian 09 [85] programs. The cluster structures were drawn with the MOLEKEL program [86].

2.2.4.2   Detailed Analyses of Calculated Results

In spectroscopic studies of relatively small clusters, spectral analyses are sometimes carried out just by comparing calculated and experimental IR spectra. If the number of plausible isomers is small and their simulated spectra show isomer-dependent features, such an analysis works well to deduce cluster structures from the spectra. On the other hand, for large systems as in the present case, numerous stationary points should be possible [87, 88]. Furthermore, isomer-specific spectral features would be washed out. In these situations, isomer-based understanding is not possible. In this study, we tried to deduce structural trends of hydrogen bond networks, not exactly molecular-level structures. Calculated cluster structures and spectra were, then, analyzed in terms of the ring size distribution in networks and the coordination numbers of water molecules, both of which are introduced in Sect. 2.1 as the key factor to bridging the gap between the small clusters and bulky networks.

For the purpose of ring-size analyses, calculated structures are denoted by ring-size configuration, For example, the cubic water octamer (see Fig. 2.2) is represented by 4^6 (six 4-membered rings). For the coordination number analyses,

we determined coordination number distributions and spectral contributions of each coordination number according to the following procedures. First, using optimized geometry, atoms were grouped as the units of H_2O molecules. Second, the number of hydrogen bonds around each H_2O moiety (the coordination number) was counted. Here, the hydrogen bond was defined when O… H distance was longer than 1.3 and shorter than 2.3 Å. The definition of hydrogen bonding is thereby not sensitive to results. To estimate the distortion of networks, hydrogen bond angles were also calculated with the cosine formula. Thus determined coordination numbers were used for evaluating spectral contribution of each coordination number. For each normal mode, the magnitude of displacement of each atom was calculated and separately summed up according to each coordination number, to which each atom belonged. The calculated IR intensity of this mode was distributed to each coordination number according to the ratio of the resultant total values, i.e., relative weights of each coordination number. This band decomposition agreed with those reported so far for various sizes of $(H_2O)_n$ [5, 19, 89]. Figure 2.15a shows an example of such spectral decomposition for $(H_2O)_{48}$. The blue and red traces show the decomposition of the simulated spectrum (in black) to the 3- and 4-coordinated water components, respectively. We also tested simplified analyses, in which full IR intensity was assigned to the molecule with the largest displacement (Fig. 2.15b). This procedure resulted in similar trends to those of the detailed method, while vibrational mode was delocalized to several water molecules. For reasonability, we employed the former, detailed method in this study. All the above-mentioned procedures were automated by writing a Perl program.
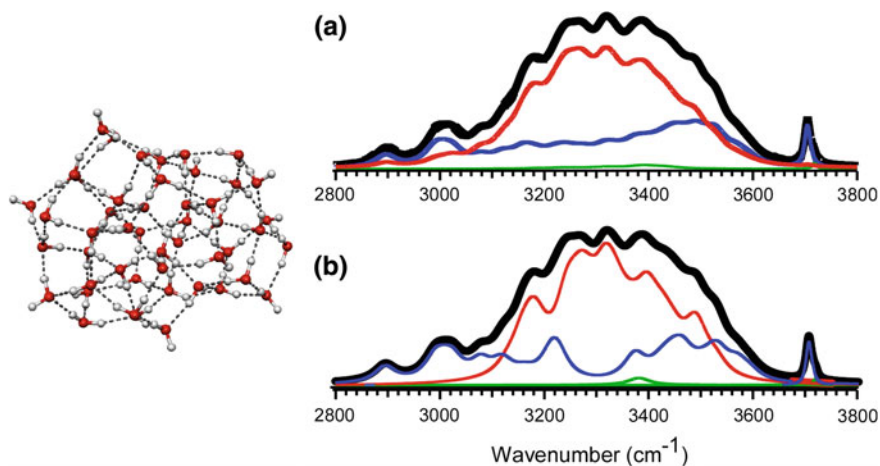
Fig. 2.15 Spectral decompositions for $(H_2O)_{48}$. **a** IR intensity is divided into each coordination number according to its contribution. **b** IR intensity is attributed to one water molecule showing largest displacement

2.2.4.3 Choice of the Calculation Method

As a result of recent progress in theory and also in computer technology, many theoretical methods are available today. Among them, *ab initio* and DFT calculations are powerful and therefore have become standard techniques to examine cluster structures and vibrational spectra. Of course, choice of the methods is important because calculated results often strongly depend on the chemical models employed. It should be noted that if someone strongly relies on calculated results (e.g., when someone compares calculated spectra of only a few isomers and concludes that the cluster structure is the one which shows the largest similarity in the spectral comparison), misinterpretations may occur [90, 91]. Benchmark studies, comparison of several methods and experimental results are required. For small hydrated clusters, Chang's group have carried out systematic calculations for hydrated clusters and compared the results of B3LYP functional, which is one of the most frequently-used methods in many chemical communities and *ab initio* MP2 [92–93]. They have shown both results are consistent with experimental results. Since their studies were conducted, lower-cost B3LYP calculations with the use of a scaling factor for harmonic frequencies have been applied to many hydrogen-bonded clusters of the broad size range ($\sim 6 \leq n \leq \sim 30$) and have successfully reproduced experimental IR spectra with acceptable computational costs [76, 92–95]. Furthermore, for large water clusters, high-level *ab initio*, such as MP2 and CCSD methods are not acceptable due to the computational limitations. Especially a frequency calculation based on these methods is highly time- and resource-consuming and only available with supercomputers. One of the largest systems ever to have been studied is $(H_2O)_{20}$ calculated at the MP2/CBS level [8, 9]. In this study, because we have to examine larger clusters and many structural isomers, the computational cost is an important factor to be considered. According to these considerations, we employed B3LYP here with a standard 6-31+G(d) basis set, which has also been tested previously [76, 92–94, 96].

It has been pointed out that the B3LYP functional is unable to treat systems in which the dispersion interaction plays vital roles. To evaluate the magnitude of the cooperative effect in interaction energy, the B3LYP functional may underestimate such interactions. Many new functionals (ωB97X-D [97], M06-2X [98, 99], etc.) [100] and empirical potentials (e.g., TTM2-F [101, 102]) have recently been proposed and they would be more accurate for energy evaluation due to better inclusion of the dispersion interactions and the long-range corrections. Evaluations of accuracy on vibrational frequencies with these methods are underway [8, 100]. As for frequency calculations of large-sized water clusters, the B3LYP functional with the use of a scale factor still seems to be a well-balanced method [103] between computational cost and accuracy (reliability).

2.2.4.4 Computational Resources

As mentioned above, the cost of the present method (B3LYP/6-31+G(d)) is relatively low. Even for the harmonic frequency calculation of a large system such as $(H_2O)_{48}$, only about 5 GB of memory is required. We then typically use home-built or commercially purchased low-cost computers. Typical specifications are as follows; Intel Core i7-2600 3.40 GHz (4 cores, 8 threads) CPU/DDR3-1333 $4 \times 4 = 16$ GB memory/2 TB SATA HDD/PGI or Intel compilers/Fedora 10 (64-bit) operating system. Of course, we had to calculate many cluster structures to characterize water networks and to find correlations between hydrogen bond network structures and spectral features. For this purpose, parts of the calculations were performed using supercomputing resources at Cyberscience Center, Tohoku University (TX7/i9610, up to 16 CPUs and 128 GB memory) and at the Research Center for Computational Science, Okazaki National Institutes of Natural Sciences (Altix4700, up to 8 CPUs and 64 GB memory).

2.3 Results

Figure 2.16 presents the observed IR spectra of size-selected phenol-$(H_2O)_n$ ($n = 19$–49) in the OH stretching region. Each spectrum includes the contribution of larger-sized clusters of phenol-$(H2O)_{n+\Delta n}$ ($0 \leq \Delta n \leq \sim 6$), but gradual changes of the spectral features prove the size-selectivity in the present spectroscopic scheme. The broadened absorption below 3,600 cm^{-1} is attributed to the hydrogen-bonded OH stretching vibrations, and the sharp band near 3,700 cm^{-1} is the free (dangling) OH stretching vibrations. Insets of Fig. 2.16 represent free and hydrogen-bonded OH stretching motions. The most prominent size-dependence is the decrease of relative intensity of the free band with increasing cluster size.

In previous studies on hydrated clusters, it has been shown that the behavior of free OH is sensitive to the surrounding hydrogen bonding environment. Figure 2.17 shows the expanded IR spectra of phenol-$(H_2O)_n$ ($n = 11$–49) in the free OH stretch region. All the spectra show a single band feature in this region. Since previous studies have revealed that $(H_2O)_n \geq {}_6$ clusters form 3-D structures consisting mainly of three-coordinated water molecules [60, 63], the band is assigned to the free OH stretching modes of such water molecules. Figure 2.17 shows a low-frequency shift of the band with increasing cluster size. Though this shift is somewhat slight, this is clear and reproducible. Observation of this shift also demonstrates that the moderate size selection of the spectral carrier is achieved by using photoionization mass spectrometry. The observed free OH frequencies are summarized in Table 2.1 and plotted in Fig. 2.18 (filled circles). Compared to cubic $(H_2O)_8$ [54], the magnitude of the shift amounts to 9 cm^{-1} in phenol-$(H_2O)_{49}$. We should note that the frequency shift observed in this study would lead to a similar one reported for the water nanoparticles in a much larger

Fig. 2.16 Infrared (IR) spectra of moderately size-selected phenol-$(H_2O)_{n+\Delta n}$ in the OH stretching vibrational region. Each spectrum is obtained by monitoring the [phenol-$(H_2O)_n$]$^+$ cluster ion intensity. The size uncertainty (Δn) is estimated to be $0 \leq \Delta n \leq \sim 6$. The depletion depth of the ion intensity has been plotted. The gap in the spectra around 3,500 cm^{-1} is due to the depletion of the output of the IR light source (see Sect. 2.2)
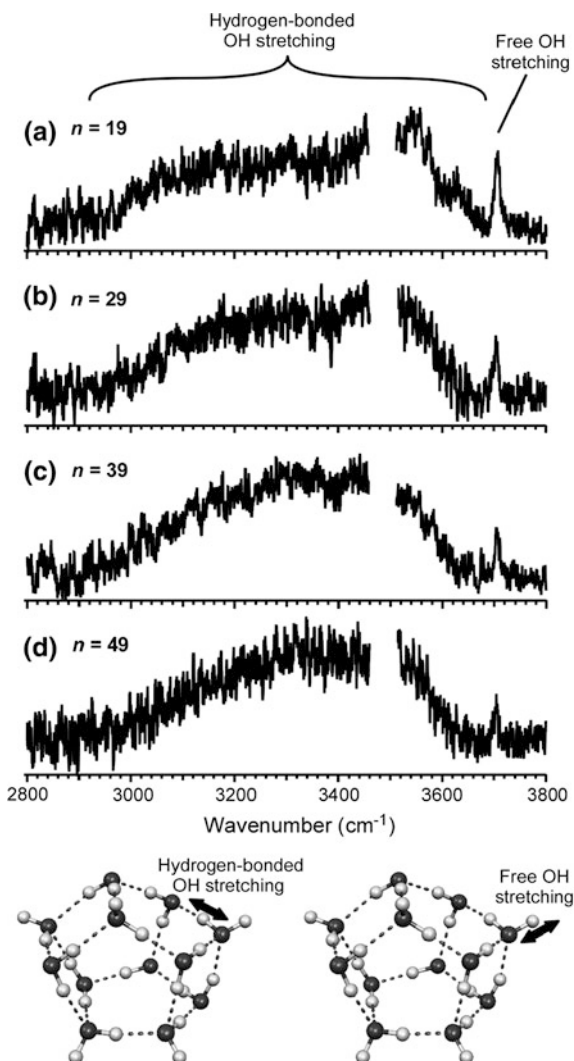
size range ($n = \sim 200$–10^6) [5], though the relation between the shift and hydrogen bond network structures has not been clarified so far.

We should note that structural isomer selectivity is not achieved by the present IR spectroscopy. In a supersonic jet expansion, a number of energetically low-lying isomers would be formed especially for large-sized clusters, and we would observe an ensemble of such various structural isomers in the cluster size of interest. Moreover, there are many OH oscillators in each cluster. The free OH frequency in this experiment was determined by the maximum of the single Lorentzian fitting of overlapped free OH bands. Therefore, the observed spectra should reflect the averaged behavior of the water network structures in the ensemble of the clusters.

Fig. 2.17 Expanded IR spectra of phenol-$(H_2O)_n$ ($n = 11$–49) in the free OH stretch region. The *dashed line* is a visual guide
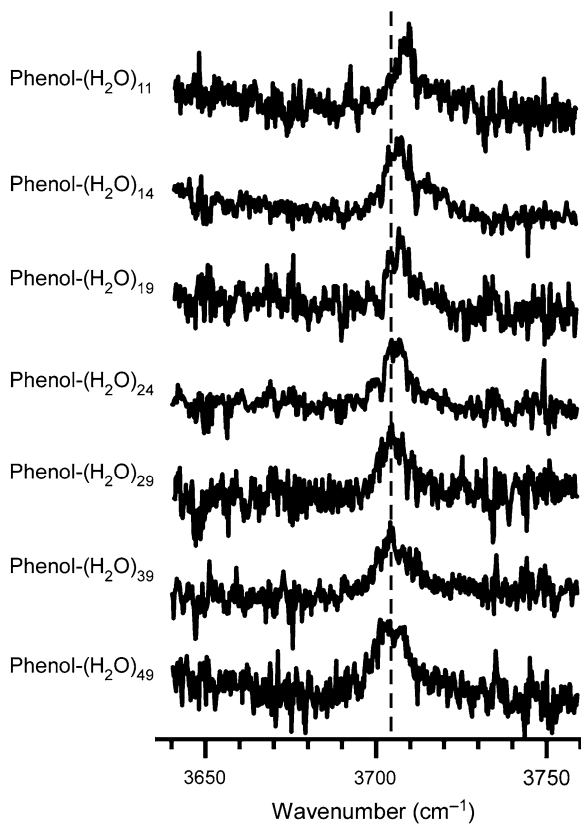
Table 2.1 Observed frequencies of free OH stretching bands in phenol-$(H_2O)_{n+\Delta n}$ ($n = 11$–49)

Cluster	Frequency (cm^{-1})
Benzene-$(H_2O)_8$[a]	3713.5
Phenol-$(H_2O)_{11}$	3709.0
Phenol-$(H_2O)_{14}$	3707.2
Phenol-$(H_2O)_{19}$	3706.8
Phenol-$(H_2O)_{24}$	3706.0
Phenol-$(H_2O)_{29}$	3705.1
Phenol-$(H_2O)_{39}$	3705.3
Phenol-$(H_2O)_{49}$	3704.5

These values are determined by single Lorentzian fitting of free OH bands. Each cluster size has an uncertainty of $0 \leq \Delta n \leq 6$. Errors in frequencies are within ± 1 cm^{-1}. The value of benzene - $(H_2O)_8$ is taken from previous work [54]

[a] From the Ref. [54]
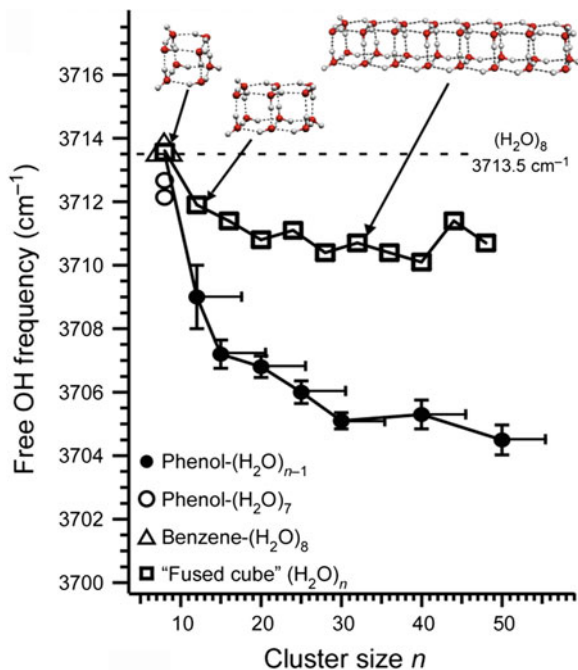
Fig. 2.18 Size-dependent free OH frequencies of phenol-$(H_2O)_{n-1}$ observed by IR spectroscopy (*filled circles*) and those of "fused cube" $(H_2O)_n$ obtained by calculations (*open squares*). Calculated values were obtained at the B3LYP/6-31+G(d) level, in which the harmonic frequencies were scaled by a factor of 0.9736. The *insets* show the "fused cube" structures. The *open circles* and *triangle* show the calculated free OH frequencies for phenol-$(H_2O)_7$ and benzene-$(H_2O)_8$, respectively, which agree with the corresponding experimental values

In the following sections, these spectral features are analyzed in terms of structural information of hydrogen bond networks.

2.4 Discussion

2.4.1 Analyses of Free OH Stretch Bands

2.4.1.1 Overview

To study the structures of hydrogen-bonded water networks, analyses of the free OH band would be a useful tool as OH band frequency is also very sensitive to hydrogen bonding environments [92, 94]. The free OH band is considered in this section. A lower free OH frequency is generally expected when the surrounding hydrogen bonds are stronger [94]. This is because the electron density on the free OH bond is slightly withdrawn by the neighboring proton donor molecules.

The observed low-frequency shift of ~ 9 cm^{-1} from $(H_2O)_8$ (Figs. 2.17 and 2.18) show that the hydrogen bonds increase their mean strengths as the network grows. In the following section, we discuss the origins of the enhancement of the hydrogen bond strengths.

2.4.1.2 Cooperative Effects in Water Clusters

One possible factor that may explain the enhancement of the hydrogen bond strength is cooperativity [83, 104]. The cooperative effect essentially originates from the non-additivity of the induction and dispersion terms. This effect means mutual enhancement among hydrogen bonds, and the magnitude of the effect increases with the number of surrounding hydrogen bonds. Figure 2.19 and its caption show an example schematic explanation of cooperativity in the case of the water trimer.

To evaluate the magnitude of the free OH frequency shifts caused by cooperativity, we performed DFT calculations at the B3LYP/6-31+G(d) level. We calculated the free OH vibrational frequencies of the "fused-cube" type structures (see insets in Fig. 2.18) [8, 9, 15], which are designed to indicate only the cooperative effects. These structures are extensions of cubic $(H_2O)_8$, increasing the number of hydrogen bonds while keeping the network motif, which consists only of 4-membered rings. In Fig. 2.18, filled circles show the observed free OH frequencies plotted versus the cluster sizes. The open circles and the triangle in Fig. 2.18 represent the calculated free OH frequencies for phenol-$(H_2O)_7$ and benzene-$(H_2O)_8$, respectively. These frequencies agree with the previously reported experimental values (see also Sect. 2.2) [49, 54]. Open squares in
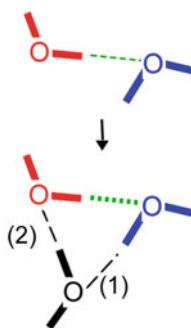
Fig. 2.19 Schematic explanation of cooperativity of hydrogen bonds. Upon trimer formation, two hydrogen bonds (*1* and *2*) are formed. This enhances the strength of the hydrogen bond (*green*) for the following reason. Due to the hydrogen bond (*1*) formation, electron density around the O atom in the H_2O (*blue*) increases (hydrogen bonding can be interpreted as the charge transfer from the lone pair to the anti-bonding orbital). On the other hand, hydrogen bonding (*2*) decreases electron density around the O atom in the H_2O (*red*). As a result, polarization of the original water pair (*blue–red pair*) is enhanced. This leads to the enhancement of the intermolecular interaction (the *green hydrogen bond*)

Fig. 2.18 show the calculated free OH frequencies of "fused-cube" clusters. Calculated frequencies of cubic $(H_2O)_n$ show the low-frequency shift similar to the experimental observations. However, the magnitude of the shifts in the "fused-cube" series is estimated to be much smaller than that in the experimentally observed series. These results suggest that cooperativity accounts for only a part of the observed low-frequency shifts.

It has been pointed out that the B3LYP functional is unable to treat systems in which the dispersion interaction plays vital roles [105]. However, in frequency calculations (at least for scaled harmonic frequencies), the B3LYP functional with a suitable basis set seems to be the best-balanced method between the computational cost and accuracy for large-sized clusters, as mentioned in Sect. 2.2. Furthermore, *ab initio* calculations for cubic $(H_2O)_8$ and $(H_2O)_{20}$ at the MP2/aug-cc-pVDZ level were reported by Xantheas and co-workers [9, 106]. These high level calculations, however, predict the low-frequency shift of $\sim 1 \text{ cm}^{-1}$ from $(H_2O)_8$ to $(H_2O)_{20}$. This small shift suggests that the present DFT calculations do not significantly underestimate the frequency shift due to the cooperative effect.

2.4.1.3 Structural Strains in Water Clusters

Another possible factor for the low-frequency shifts of the free OH bands is the change of the hydrogen bond network structural motif, which also affects hydrogen bond strength. To clarify this point, we calculated structures of small ring-type $(H_2O)_n$ ($n = 3$–8). Figure 2.20 shows their structures with the averaged hydrogen

Averaged hydrogen bond length (Å)	1.88	1.76	1.74	1.74
Averaged hydrogen bond angle (degree)	149.1	167.1	176.1	176.5

Averaged hydrogen bond length (Å)	1.73	1.73
Averaged hydrogen bond angle (degree)	176.2	173.4
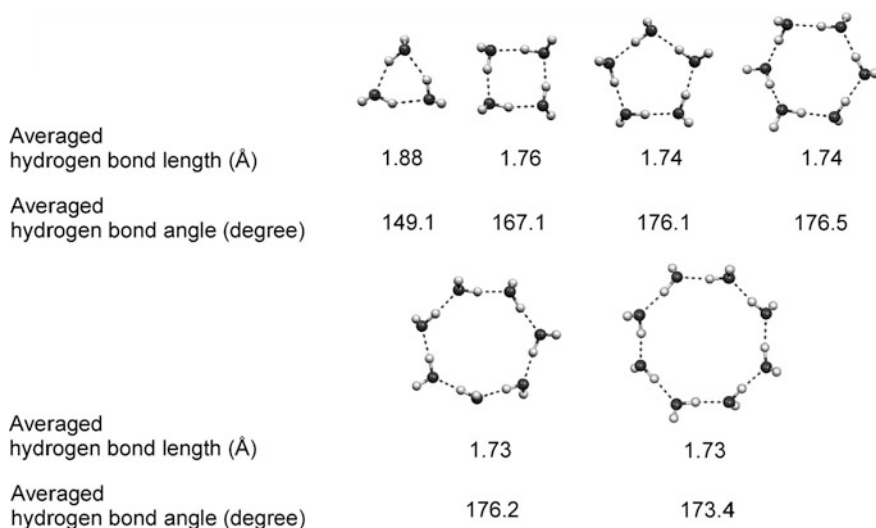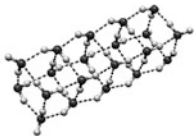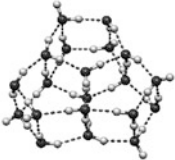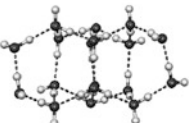
Fig. 2.20 Calculated hydrogen bond parameters of various ring type $(H_2O)_n$. These structures are optimized at the B3LYP/6-31+G(d) level. Hydrogen bonds are clearly weaker in the 3- and 4-membered rings as indicated distorted angles and longer intermolecular distances

bond angles and hydrogen bond lengths. It is clear that hydrogen bonds are weaker in the 3- and 4-membered rings as indicated by distorted hydrogen bond angles and longer hydrogen bond lengths. On the basis of the DFT calculations for the small-sized $(H_2O)_n$ ($n \leq 10$), Jiang et al. [94] have shown the hydrogen bond distortion affects the free OH frequency. To evaluate such a structural effect on the free OH frequency in larger systems, we calculated model structures of larger clusters. Figure 2.21 shows some of the characteristic model structures of $(H_2O)_{18-20}$ and those of corresponding phenol-$(H_2O)_{17-19}$ with their frequencies of the free OH bands simulated using DFT. The frequencies of phenol-$(H_2O)_{17-19}$ of the same hydrogen bond network are presented in parentheses, and they show the perturbation caused by the phenyl group is less than 1.5 cm^{-1} for the free OH frequency. To clarify the correlation between the hydrogen bonding environment and the OH frequency, Fig. 2.22 contains a summary of calculated results on hydrogen bond networks of these four different types. Among these structures (in Figs. 2.21 and 2.22), the "fused-cube" consists only of 4-membered rings and has highly distorted hydrogen bonds, the same as cubic $(H_2O)_8$. The "prism" structure, which consists of 4- and 5-membered rings, has been predicted to be the energy global minimum in $(H_2O)_{20}$ by the various theoretical studies including high level *ab initio* calculations. The "dodecahedral cage" consists of twelve 5-membered rings and can be regarded as a partial structure of clathrate hydrates. "Hexagonal
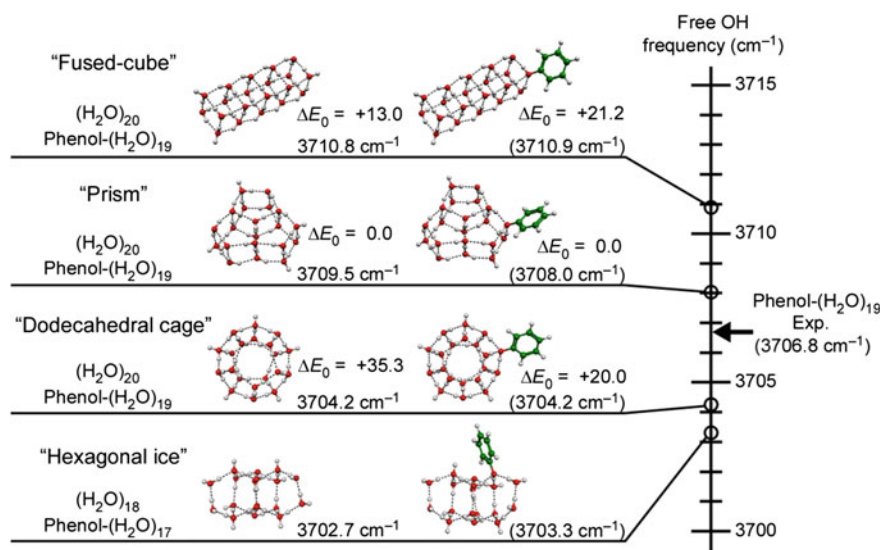
Fig. 2.21 Free OH stretching frequencies of the characteristic cluster structures of $(H_2O)_{18-20}$ and corresponding phenol-$(H_2O)_{17-19}$. For $(H_2O)_{20}$ and phenol-$(H_2O)_{19}$, relative energies at the vibrational zero-point level (ΔE_0) were also shown in kJ/mol. All cluster structures, their harmonic frequencies, and relative energies were calculated at the B3LYP/6-31+G(d) level. Harmonic frequencies were scaled by a factor of 0.9736. In "hexagonal ice", free OH stretching modes of the two-coordinated water molecules and the π-hydrogen bonded OH bond were excluded from the evaluation of the free OH frequency

	Averaged hydrogen bond length (Å)	Averaged hydrogen bond angle (degree)	The number of hydrogen bonds
	1.86	159.0	36
	1.82	163.8	34
	1.78	176.7	30
	1.78	176.2	(24)

Fig. 2.22 Summary of calculated results of the four $(H_2O)_{18-20}$ structures shown in Fig. 2.21. Note that the bottom ("hexagonal ice") is smaller system than the others and therefore, the number of hydrogen bonds should also be small

ice" has a very similar network structure to the crystalline hexagonal ice, consisting only of 6-membered rings. The distortions of hydrogen bonds in the "dodecahedral cage" and "hexagonal ice" structures are much fewer: the hydrogen bond angles are straighter (O–H…O angle is 170–180°) in the 5- and 6-membered rings than those in the 4-membered rings (O–H…O angle is 140–170°) as indicated in Fig. 2.22. Figures 2.21 and 2.22 show the clear correlation between the magnitude of the hydrogen bond distortions and the free OH frequencies. The free OH frequency of the most strained "fused-cube" is predicted to be the highest value, 3710.8 (3710.9 cm^{-1} in corresponding phenol-$(H_2O)_n$), and those of the less strained "dodecahedral cage" and "hexagonal ice" are 3704.2 (3704.2) and 3702.7 (3703.3 cm^{-1}), respectively. The free OH frequency of "prism" is located in between those of the "fused-cube" and "dodecahedral cage" (or "hexagonal ice"), reflecting the coexistence of the 4- and 5-membered ring motifs. It should be noted that the frequency calculations at the MP2/aug-cc-pVDZ level also show a similar correlation.

The experimental frequency of phenol-$(H_2O)_{19}$ is located between "prism" and "dodecahedral". This location suggests the observed water networks of $n \sim 20$ consist not only of 4-membered rings but also of 5- and/or 6-membered rings.

At this time, the 4-membered ring motif is no longer exclusive and the networks are being replaced by more relaxed structural motifs.

Because the observed experimental spectrum measured by monitoring [phenol-$(H_2O)_{19}]^+$ includes the contribution of phenol-$(H_2O)_{20,21...}$, we also carried out similar analyses for these sizes. Figure 2.23 shows optimized structures of $(H_2O)_{20-22}$. These structures have been reported as low-lying minima in previous theoretical studies [13, 21]. In Fig. 2.23, some structures with higher frequencies ($> \sim 3,710$ cm^{-1}, for example) clearly include more 4-membered rings than others. The above-mentioned correlation is therefore confirmed.

For further confirmation, similar analyses were carried out for the larger clusters. Figure 2.24 shows characteristic structures of $(H_2O)_{48}$ with their free OH frequencies and hydrogen bond parameters. The frequencies of corresponding phenol-$(H_2O)_{47}$ are also shown in parentheses. These calculations show the same trend as $(H_2O)_{20}$. The free OH frequency of the most strained "fused-cube" structure is evaluated to be the highest while those of more relaxed "hexagonal prism" and "filled cage" are evaluated to be lower. As is in $(H_2O)_{18-20}$, the frequency of "fused-cube" is much higher than the experimental value, meaning that the 4-membered ring (cubic) motif is not exclusive in the hydrogen bond network. In
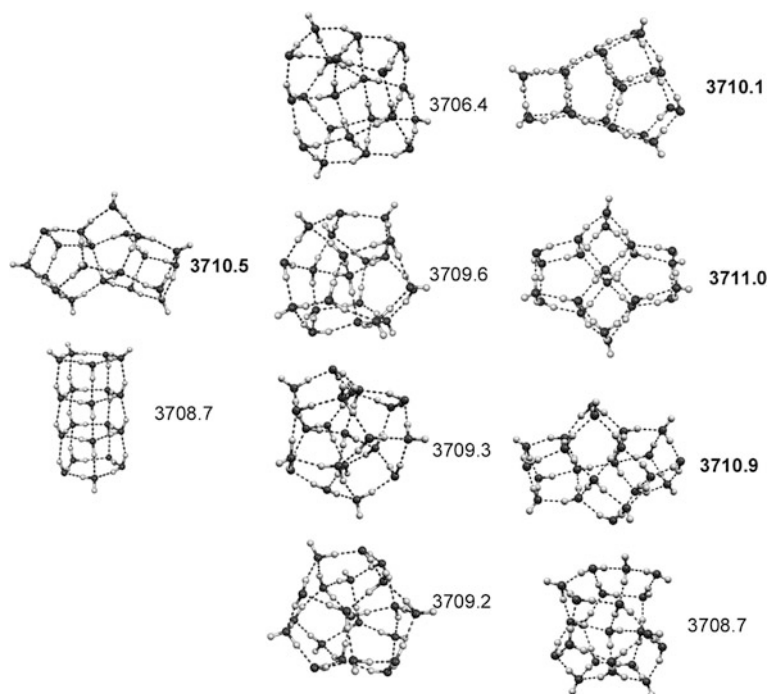
Fig. 2.23 Optimized cluster structures of $(H_2O)_{20-22}$ with the calculated free OH frequency. We can see a clear trend that the structures with 3,710 cm^{-1} or higher frequency contain many 4-membered rings than the others
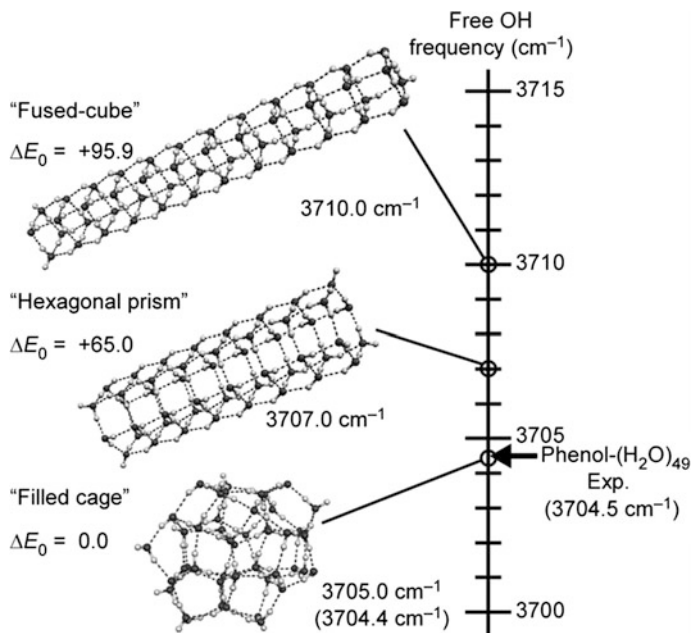
Fig. 2.24 Free OH stretching frequencies and relative energies (ΔE_0) in kJ/mol of the characteristic cluster structures of $(H_2O)_{48}$. Parameters of the hydrogen bond environment are also indicated. Frequencies of corresponding phenol-$(H_2O)_{47}$ are also shown in *parentheses*. Each cluster structure and its energy and harmonic frequencies were calculated at the B3LYP/6-31+G(d) level and all the harmonic frequencies were scaled by a factor of 0.9736

the case of $(H_2O)_{20}$ in Fig. 2.21, the frequency of the "prism" structure is nearest to the experimental value. On the other hand, the free OH frequency of the "hexagonal prism" in $(H_2O)_{48}$ no longer agrees with the experimental value, while the more relaxed "filled cage", which is the reported global minimum on the TIP4P potential energy surface [7], is in good agreement with the observation. The contribution of the 4-membered rings in this "filled cage" was reported to be only 18 %, and the 5- and 6-membered rings are clearly dominant [7].

These results indicate that the hydrogen bond network structure develops from the highly strained 4-membered ring motif to the more relaxed motifs of 5- and 6-membered rings with the growth of the network, and the low-frequency shift of the free OH stretching band originates from the gradual transition of the structural motifs as well as the hydrogen bond cooperativity. This interpretation is consistent with the structural trends of hydrogen bond network development, which have been predicted by theoretical calculations. At $n = 8$, the 4-membered rings are exclusive (100 %). With increasing size, at $n \sim 20$, the contributions of the 5- or 6-membered rings become necessary to reproduce the experimental frequency (in the plausible "prism" structure, the 4-membered rings still take over 67 % of the network). Then, at $n \sim 50$, the contribution of the 4-membered rings is estimated to be ~ 20 %.

Because the experimental and the calculated free OH frequency shifts are somewhat slight (within 10 cm^{-1}), accuracy of the calculated frequencies is critical. Actually, the absolute accuracy of the scaled harmonic frequencies based on the B3LYP/6-31+G(d) level have been estimated to be only $\sim 20 \text{ cm}^{-1}$. However, we optimized the scaling factor for free OH stretching frequencies and essentially focused on the relative frequencies. In this case, the reliability of the present calculations will be higher. Furthermore, the MP2/aug-cc-pVDZ level calculations of $(H_2O)_{20}$ also show a similar correlation between the hydrogen bond distortions and free OH frequencies. The consistency of these higher-level calculations and our DFT calculations suggests that such correlation is a general trend and that the experimental frequency shift, more or less, is accounted for by the relaxation of the hydrogen bond distortions. Of course, further discussion will be done by fine anharmonic frequency calculations, which will be available in the near future.

2.4.1.4 Further Discussion of Free OH Bands

In addition to the effects of the hydrogen bond distortion, Jiang et al. [94] have reported another factor in the free OH frequency shift. On the basis of the DFT calculations for model clusters, they showed that neighboring 4-coordinated waters lower the free OH frequency relative to neighboring 3-coordinated waters. The present calculations are helpful to estimate the magnitude of such a coordination environment effect in the larger-sized region. In Fig. 2.21, the free OH bond in the "dodecahedral cage" is surrounded by three 3-coordinated waters and the "fused-cube" is surrounded by two 3-coordinated and one 4-coordinated waters. However, the free OH frequency in the "fused-cube" is calculated to be higher than that in "dodecahedral cage". These calculations suggest that the network distortion is more effective than the neighboring water coordination effect in the size region of $n \sim 20$.

In the present DFT analyses, we selected some characteristic cluster structures to examine the correlation between the structural strain and the free OH frequency. However, it should be noted that there exist large numbers of structural isomers in the observed sizes, and only their averaged trend associated with size is reflected in the observed frequency. No specific isomer structures can be identified in the present study, but only the general trend in the network development is inferred. Though the present calculations show a clear correlation between the observed frequency shift and the structural strain in the water network, extensive sampling of isomer structures or global search of potential energy surfaces [88] is requested for unequivocal proof of the origin of the shift. Such calculations for clusters of $n > \sim 10$ are very time-consuming, and are beyond the scope of the present study.

Finally, we comment on the effect of the cluster temperature. Finite (and undefined) temperature or internal energy of clusters affects their preferential structures. In conventional IR–UV double resonance spectroscopy of a jet-cooled neutral cluster, only a few energetically low-lying isomers are ordinarily

considered, because the low temperature (or specific internal energy) of the cluster can be ensured by sharp vibronic bands in its electronic spectrum. In the present experiment, broadened electronic spectra of the large-sized clusters prevent us from evaluating the cluster temperature. In addition, the optimization of the size distribution in each IR measurement might cause the size dependence of the temperature of the observed clusters. Though the temperature of the clusters is an ambiguous factor in the present experiment, we infer that the size dependence of the cluster temperature is not a major origin of the observed OH frequency shift for the following reasons: (i) The observed shift is reproducible irrespective of arbitrary optimization of the jet condition and size distribution. (ii) For both $(H_2O)_{20}$ and $(H_2O)_{48}$, the calculated free OH frequencies based on the reported energetically global minimum structures are in agreement with the experimental values. These agreements imply the observed IR spectra of both $n \sim 20$ and ~ 50 reflect low-lying cluster structures. (iii) A similar low-frequency shift has been found for ice nanoparticles of a much larger size range ($n = 200$–10^6) prepared by a collisional cooling cell [5]. The shift reported here would lead to this ice nanoparticle behavior.

2.4.2 Analyses of Hydrogen-Bonded OH Stretch Bands

2.4.2.1 Intensity Ratio

Coordination numbers of water molecules are also important factors in characterizing hydrogen-bonded water networks. The IR spectra of phenol-$(H_2O)_n$ in Fig. 2.16 show that the intensity of the free OH band relative to that of the hydrogen-bonded OH band gradually decreases with increasing n. Because 4-coordinated waters have no free OH, the observed free OH band is mainly attributed to 3-coordinated waters. The decrease of the free OH band intensity is therefore a signature of the increase of 4-coordinated waters.

2.4.2.2 Contribution from Each Coordination Number

Corresponding to this indication of 4-coordinated waters, spectral contributions of the 4-coordinated waters are expected to appear in the hydrogen-bonded OH stretch region. In the spectrum of $n = 19$, the hydrogen-bonded OH band is very broad and it shows the almost flat intensity distribution in the range of 3,000–3,600 cm^{-1}. With increasing cluster size, the absorption at around 3,200–3,500 cm^{-1} gradually rises, while the intensities in both the edge regions of the hydrogen-bonded OH band are relatively suppressed. In the spectrum of $n = 49$, the band finally forms a broad peak at around 3,350 cm^{-1}. Because this spectral change in the hydrogen bonded OH band correlates with the suppression of the free OH band, it is reasonable to attribute the rise of the absorption centered at

$\sim$3,350 cm^{-1} to the increase of 4-coordinated waters. Similar trends have been also reported for average size-estimated water clusters [5].

To provide further confirmation of the contribution of 4-coordinated waters, a similar comparison was carried out among the observed IR spectrum of phenol-$(H_2O)_{49}$ and simulated ones of $(H_2O)_{48}$, as shown in Fig. 2.25a, c. The global minimum structure of $(H_2O)_{48}$ under the TIP4P potential has been reported by Kazimirski et al. [7]. We re-optimized this structure at B3LYP, and the resulting spectral simulation is shown in Fig. 2.25c (the same structure as in Fig. 2.24). To highlight the feature of 3-coordinated waters, we also constructed a model structure consisting only of 3-coordinated waters. This structure became a "hollow-cage type", shown with its simulated spectrum in Fig. 2.25b. The calculated spectrum (b) shows broad absorption in 3,000–3,600 cm^{-1} without a single prominent maximum. This reveals that the peak at $\sim$3,350 cm^{-1} in the observed spectrum (a) cannot be rationalized only with 3-coordinated waters. The free OH band in spectrum (b) is also too intense relative to the hydrogen-bonded OH band, in comparison with spectrum (a). On the other hand, the spectrum in Fig. 2.25c
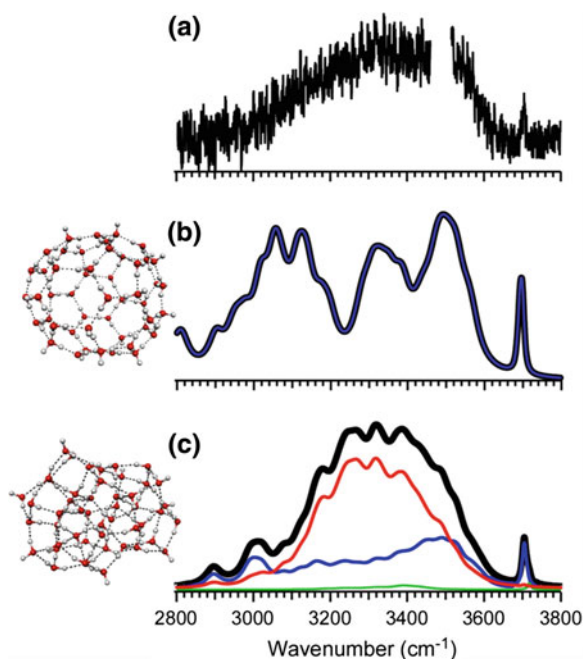
Fig. 2.25 Comparison between (**a**) observed IR spectrum of phenol-$(H_2O)_{49}$ and (**b, c**) simulated spectra of $(H_2O)_{48}$. Simulated spectrum (**b**) is based on all 3-coordinated water structures shown in the *inset*. Spectrum (**c**) is given by the global minimum structure at the TIP4P potential, which is taken from the previous work [7]. Both the structures are (re-)optimized at the B3LYP/6-31+G(d) level. In the simulations, the *black line* represents the IR spectrum, and the *green, blue*, and *red traces* are a decomposition of the spectrum to the 2-, 3-, and 4-coordinated water components, respectively

shows qualitative agreement with spectrum (a): a peak appears at around 3,300 cm^{-1}, and the relative intensity of the free OH stretch band is similar to the observed one. The global minimum structure of $(H_2O)_{48}$ is constructed of 27, 20, and 1 water molecules in the 4-, 3-, and 2-coordinated sites, respectively. The contribution of the 4-coordinated waters is dominant in the simulated spectrum, and it causes the apparent maximum in the hydrogen-bonded OH region. These results show that the absorption maximum centered at $\sim 3,350$ cm^{-1} is reasonably interpreted as a spectral signature of 4-coordinated water sites in the neutral water clusters of $n \leq \sim 50$.

For further confirmation of the 4-coordinated water band, we also simulated spectra of isomers of other sizes, which are used in discussion of free OH behavior or previously reported minima. The band decompositions (Fig. 2.26) show similar trends as that of $(H_2O)_{48}$, showing the generality of coordination number dependent frequencies. This result also supports the formation of 4-coordinated water molecules in the present size range.

Fig. 2.26 a – e Comparison between experimental spectra and simulated spectra for many cluster structures of $(H_2O)_n$ (n = 30-34)
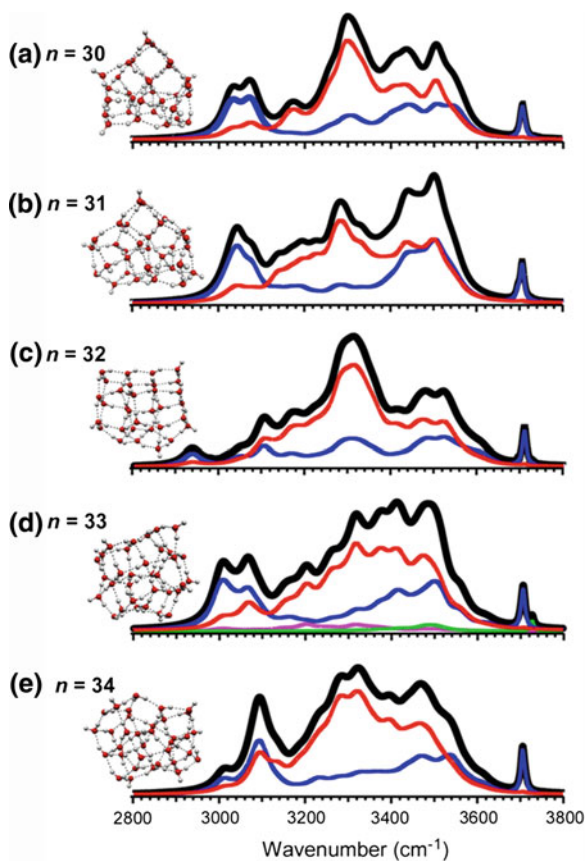
2.4.2.3 Further Discussion of Hydrogen-Bonded OH Bands

Formation of 4-coordinated sites is closely related to formation of the interior moiety in water clusters. This is an important step in the development of hydrogen bond networks from water clusters to bulk water, and the network evolution in this size range ($n < \sim 50$) corresponds to its very early stage. The hydrogen-bonded OH stretch frequency of ice (Ih) is 3,200 cm^{-1} [83, 107, 108], much lower than in the present observations. This means that the OH frequency of 4-coordinated sites in the clusters will show further lowering with the expansion of the network among 4-coordinated waters. Such a shift has been observed in much larger-sized clusters/ ice nano particles [5, 109].

2.5 Conclusion

To analyze hydrogen bond network structures consisting of tens of water molecules, we measured moderately size-selective IR spectra of large, labeled water clusters phenol-$(H_2O)_n$ in the OH stretch region. The observed spectral features were analyzed in terms of hydrogen bond ring size motifs and coordination numbers of water molecules. The detailed analyses of the free OH band indicated that the observed low-frequency shift originates from the cooperativity of hydrogen bonds and the structural development from the highly strained 4-membered ring motif to the more relaxed 5- and 6-membered ring motifs. The suppression of free OH band intensity with an increase of n represents the increase of the abundance of 4-coordinated waters. The rise of the absorption maximum of the hydrogen-bonded OH stretch band at $\sim 3,350$ cm^{-1} can also be attributed to 4-coordinated water sites. The characterized structural trends are bridging the gap between the small clusters and bulky networks. We note that we did not determine the exact or specific structures. As numerous structures should coexist in such a large system and many of them are not distinguishable with spectroscopy, the present approach toward averaged behavior seems helpful in characterizing and understanding hydrogen bond networks. In this study, we discussed the correlation between spectral features and structures by calculating only a few characteristic structures. If many more structures were systematically used, more detailed information could be obtained. Owing to recent progress in computational chemistry, such calculations will become possible in the near future. In such a procedure, we hope that our approach, which checks the coordination number and ring size distribution, will also be useful for evaluating the calculated results. We also expect that the present characterization method of hydrogen bond networks may be applicable to more complicated, condensed phase water.

References

1. R.H. Page, M.F. Vernon, Y.R. Shen, Y.T. Lee, Chem. Phys. Lett. **141**, 1–6 (1987)
2. U. Buck, F. Huisken, Chem. Rev. **100**, 3863–3890 (2000)
3. L.M. Goss, S.W. Sharpe, T.A. Blake, V. Vaida, J.W. Brault, J. Phys. Chem. A **103**, 8620–8624 (1999)
4. C. Steinbach, P. Andersson, J.K. Kazimirski, U. Buck, V. Buch, T.A. Beu, J. Phys. Chem. A **108**, 6165–6174 (2004)
5. V. Buch, S. Bauerecker, J.P. Devlin, U. Buck, J.K. Kazimirski, Int. Rev. Phys. Chem. **23**, 375–433 (2004)
6. P. Andersson, C. Steinbach, U. Buck, Euro. Phys. J. D. **24**, 53–56 (2003)
7. J.K. Kazimirski, V. Buch, J. Phys. Chem. A **107**, 9762–9775 (2003)
8. G.S. Fanourgakis, E. Apra, S.S. Xantheas, J. Chem. Phys. **121**, 2655–2663 (2004)
9. G.S. Fanourgakis, E. Apra, W.A. de Jong, S.S. Xantheas, J. Chem. Phys. **122**, 134304 (2005)
10. A. Lagutschenkov, G.S. Fanourgakis, G. Niedner-Schatteburg, S.S. Xantheas, J. Chem. Phys. **122**, 194310 (2005)
11. S. Bulusu, S. Yoo, E. Apra, S. Xantheas, X.C. Zeng, J. Phys. Chem. A **110**, 11781–11784 (2006)
12. B. Hartke, Angew. Chem. Int. Ed. **41**, 1468–1487 (2002)
13. B. Bandow, B. Hartke, J. Phys. Chem. A **110**, 5809–5822 (2006)
14. L.S. Sremaniak, L. Perera, M.L. Berkowitz, J. Chem. Phys. **105**, 3715–3721 (1996)
15. C.J. Tsai, K.D. Jordan, J. Phys. Chem. **97**, 5208–5210 (1993)
16. D.J. Wales, M.P. Hodges, Chem. Phys. Lett. **286**, 65–72 (1998)
17. H. Kabrede, R. Hentschke, J. Phys. Chem. B **107**, 3914–3920 (2003)
18. A. Lenz, L. Ojamae, Phys. Chem. Chem. Phys. **7**, 1905–1911 (2005)
19. A. Lenz, L. Ojamäe, J. Phys. Chem. A **110**, 13388–13393 (2006)
20. A. Lenz, L. Ojamäe, Chem. Phys. Lett. **418**, 361–367 (2006)
21. H. Takeuchi, J. Chem. Inf. Model. **48**, 2226–2233 (2008)
22. S. Kazachenko, A.J. Thakkar, Chem. Phys. Lett. **476**, 120–124 (2009)
23. G. Scoles (ed.), *Atomic and Molecular Beam Methods* (Oxford University Press, New York, 1988)
24. Electron ionization is an universal detection method, however, overlap of electron beam and IR light, which is for spectroscopy, is not easily achieved. This is because the focusing of electron beam has many difficulties such as repulsion due to the charge. Generally, when the ionization is achieved by photons, an overlapping of the ionization light and the IR light is relatively easy
25. H. Shinohara, N. Nishi, N. Washida, J. Chem. Phys. **84**, 5561–5567 (1986)
26. I.B. Muller, L.S. Cederbaum, J. Chem. Phys. **125**, 204305 (2006)
27. L. Belau, K.R. Wilson, S.R. Leone, M. Ahmed, J. Phys. Chem. A **111**, 10075–10083 (2007)
28. E.S. Wisniewski, J.R. Stairs, A.W. Castleman Jr, Int. J. Mass Spectrom. **212**, 273–286 (2001)
29. P.P. Radi, P. Beaud, D. Franzke, H.M. Frey, T. Gerber, B. Mischler, A.P. Tzannis, J. Chem. Phys. **111**, 512–518 (1999)
30. H. Abe, N. Mikami, M. Ito, J. Phys. Chem. **86**, 1768–1771 (1982)
31. A. Oikawa, H. Abe, N. Mikami, M. Ito, J. Phys. Chem. **87**, 5083–5090 (1983)
32. K. Fuke, K. Kaya, Chem. Phys. Lett. **94**, 97–101 (1983)
33. R.J. Lipert, S.D. Colson, J. Chem. Phys. **89**, 4579–4585 (1988)
34. R.J. Lipert, S.D. Colson, J. Phys. Chem. **93**, 135–139 (1989)
35. R.J. Lipert, S.D. Colson, Chem. Phys. Lett. **161**, 303–307 (1989)
36. R.J. Lipert, S.D. Colson, J. Chem. Phys. **92**, 3240–3241 (1990)
37. R.J. Lipert, S.D. Colson, J. Phys. Chem. **94**, 2358–2361 (1990)

38. G. Reiser, O. Dopfer, R. Lindner, G. Henri, K. Mullerdethlefs, E.W. Schlag, S.D. Colson, Chem. Phys. Lett. **181**, 1–4 (1991)
39. O. Dopfer, G. Reiser, K. Mullerdethlefs, E.W. Schlag, S.D. Colson, J. Chem. Phys. **101**, 974–989 (1994)
40. R.J. Stanley, A.W. Castleman, J. Chem. Phys. **94**, 7744–7756 (1991)
41. G.V. Hartland, B.F. Henson, V.A. Venturo, P.M. Felker, J. Phys. Chem. **96**, 1164–1173 (1992)
42. S. Tanabe, T. Ebata, M. Fujii, N. Mikami, Chem. Phys. Lett. **215**, 347–352 (1993)
43. T. Watanabe, T. Ebata, S. Tanabe, N. Mikami, J. Chem. Phys. **105**, 408–419 (1996)
44. T. Ebata, A. Fujii, N. Mikami, Int. Rev. Phys. Chem. **17**, 331–361 (1998)
45. M. Gerhards, K. Kleinermanns, J. Chem. Phys. **103**, 7392–7400 (1995)
46. G. Berden, W.L. Meerts, M. Schmitt, K. Kleinermanns, J. Chem. Phys. **104**, 972–982 (1996)
47. M. Gerhards, M. Schmitt, K. Kleinermanns, W. Stahl, J. Chem. Phys. **104**, 967–971 (1996)
48. W. Roth, M. Schmitt, C. Jacoby, D. Spangenberg, C. Janzen, K. Kleinermanns, Chem. Phys. **239**, 1–9 (1998)
49. C. Janzen, D. Spangenberg, W. Roth, K. Kleinermanns, J. Chem. Phys. **110**, 9898–9907 (1999)
50. A. Lüchow, D. Spangenberg, C. Janzen, A. Jansen, M. Gerhards, K. Kleinermanns, Phys. Chem. Chem. Phys. **3**, 2771–2780 (2001)
51. R.H. Page, Y.R. Shen, Y.T. Lee, J. Chem. Phys. **88**, 5362–5376 (1988)
52. T.S. Zwier, Annu. Rev. Phys. Chem. **47**, 205–241 (1996)
53. R.N. Pribble, T.S. Zwier, Science **265**, 75–79 (1994)
54. C.J. Gruenloh, J.R. Carney, C.A. Arrington, T.S. Zwier, S.Y. Fredericks, K.D. Jordan, Science **276**, 1678–1681 (1997)
55. R.N. Pribble, F.C. Hagemeister, T.S. Zwier, J. Chem. Phys. **106**, 2145–2157 (1997)
56. C.J. Gruenloh, J.R. Carney, F.C. Hagemeister, C.A. Arrington, T.S. Zwier, S.Y. Fredericks, J.T. Wood III, K.D. Jordan, J. Chem. Phys. **109**, 6601–6614 (1998)
57. C.J. Gruenloh, J.R. Carney, F.C. Hagemeister, T.S. Zwier, J.T. Wood III, K.D. Jordan, J. Chem. Phys. **113**, 2290–2303 (2000)
58. N. Pugliano, R.J. Saykally, Science **257**, 1937–1940 (1992)
59. J.D. Cruzan, L.B. Braly, K. Liu, M.G. Brown, J.G. Loeser, R.J. Saykally, Science **271**, 59–62 (1996)
60. K. Liu, M.G. Brown, C. Carter, R.J. Saykally, J.K. Gregory, D.C. Clary, Nature **381**, 501–503 (1996)
61. K. Liu, M.G. Brown, J.D. Cruzan, R.J. Saykally, Science **271**, 62–64 (1996)
62. K. Liu, J.D. Cruzan, R.J. Saykally, Science **271**, 929–933 (1996)
63. U. Buck, I. Ettischer, M. Melzer, V. Buch, J. Sadlej, Phys. Rev. Lett. **80**, 2578 (1998)
64. I.V. Hertel, C. Hüglin, C. Nitsch, C.P. Schulz, Phys. Rev. Lett. **67**, 1767–1770 (1991)
65. R.M. Forck, I. Dauster, Y. Schieweck, T. Zeuch, U. Buck, M. Oncak, P. Slavicek, J. Chem. Phys. **132**, 221102 (2010)
66. C. Steinbach, U. Buck, J. Phys. Chem. A **110**, 3128–3131 (2005)
67. H.T. Liu, J.P. Müller, N. Zhavoronkov, C.P. Schulz, I.V. Hertel, J. Phys. Chem. A **114**, 1508–1513 (2010)
68. K. Hashimoto, K. Morokuma, J. Am. Chem. Soc. **116**, 11436–11443 (1994)
69. S. Suzuki, P.G. Green, R.E. Bumgarner, S. Dasgupta, W.A. Goddard, G.A. Blake, Science **257**, 942–944 (1992)
70. W.C. Wiley, I.H. McLaren, Rev. Sci. Instrum. **26**, 1150 (1955)
71. T. Schindler, C. Berg, G. Niedner-Schatteburg, V.E. Bondybey, Chem. Phys. Lett. **250**, 301–308 (1996)
72. S. Sato, N. Mikami, J. Phys. Chem. **100**, 4765–4769 (1996)
73. T. Sawamura, A. Fujii, S. Sato, T. Ebata, N. Mikami, J. Phys. Chem. **100**, 8131–8138 (1996)
74. K. Kleinermanns, C. Janzen, D. Spangenberg, M. Gerhards, J. Phys. Chem. A **103**, 5232–5239 (1999)
75. Z. Shi, J.V. Ford, S. Wei, J.A.W. Castleman, J. Chem. Phys. **99**, 8009–8015 (1993)

76. H.C. Chang, C.C. Wu, J.L. Kuo, Int. Rev. Phys. Chem. **24**, 553–578 (2005)
77. J.-L. Kuo, M.L. Klein, J. Chem. Phys. **122**, 024516 (2005)
78. M.P. Hodges, D.J. Wales, Chem. Phys. Lett. **324**, 279–288 (2000)
79. A.D. Becke, J. Chem. Phys. **98**, 5648–5652 (1993)
80. C. Lee, W. Yang, R.G. Parr, Phys. Rev. B **37**, 785 (1988)
81. V. Buch, Data bank on ice and icy particles, http://www.fh.huji.ac.il/~viki/databank/IceParticles.html
82. D.J. Wales, J.P.K. Doye, A. Dullweber, M.P. Hodges, F.Y. Naumkin, F. Calvo, J. Hernández-Rojas, T.F. Middleton, http://www-wales.ch.cam.ac.uk/CCD.html
83. Y. Maréchal, *The Hydrogen Bond and the Water Molecule* (Elsevier, Amsterdam, 2007)
84. M.J. Frisch, G.W. Trucks, H.B. Schlegel, G.E. Scuseria, M.A. Robb, J.R. Cheeseman, J.A. Montgomery Jr, T. Vreven, K.N. Kudin, J.C. Burant, J.M. Millam, S.S. Iyengar, J. Tomasi, V. Barone, B. Mennucci, M. Cossi, G. Scalmani, N. Rega, G.A. Petersson, H. Nakatsuji, M. Hada, M. Ehara, K. Toyota, R. Fukuda, J. Hasegawa, M. Ishida, T. Nakajima, Y. Honda, O. Kitao, H. Nakai, M. Klene, X. Li, J.E. Knox, H.P. Hratchian, J.B. Cross, V. Bakken, C. Adamo, J. Jaramillo, R. Gomperts, R.E. Stratmann, O. Yazyev, A.J. Austin, R. Cammi, C. Pomelli, J.W. Ochterski, P.Y. Ayala, K. Morokuma, G.A. Voth, P. Salvador, J.J. Dannenberg, V.G. Zakrzewski, S. Dapprich, A.D. Daniels, M.C. Strain, O. Farkas, D.K. Malick, A.D. Rabuck, K. Raghavachari, J.B. Foresman, J.V. Ortiz, Q. Cui, A.G. Baboul, S. Clifford, J. Cioslowski, B.B. Stefanov, G. Liu, A. Liashenko, P. Piskorz, I. Komaromi, R.L. Martin, D.J. Fox, T. Keith, M.A. Al-Laham, C.Y. Peng, A. Nanayakkara, M. Challacombe, P.M.W. Gill, B. Johnson, W. Chen, M.W. Wong, C. Gonzalez, J.A. Pople, Gaussian 03, Revision E.01 (Gaussian, Inc., Wallingford CT, 2004)
85. M.J. Frisch, G.W. Trucks, H.B. Schlegel, G.E. Scuseria, M.A. Robb, J.R. Cheeseman, G. Scalmani, V. Barone, B. Mennucci, G.A. Petersson, H. Nakatsuji, M. Caricato, X. Li, H.P. Hratchian, A.F. Izmaylov, J. Bloino, G. Zheng, J.L. Sonnenberg, M. Hada, M. Ehara, K. Toyota, R. Fukuda, J. Hasegawa, M. Ishida, T. Nakajima, Y. Honda, O. Kitao, H. Nakai, T. Vreven, J.A. Montgomery Jr., J. E. Peralta, F. Ogliaro, M. Bearpark, J.J. Heyd, E. Brothers, K.N. Kudin, V.N. Staroverov, R. Kobayashi, J. Normand, K. Raghavachari, A. Rendell, J.C. Burant, S.S. Iyengar, J. Tomasi, M. Cossi, N. Rega, N.J. Millam, M. Klene, J.E. Knox, J.B. Cross, V. Bakken, C. Adamo, J. Jaramillo, R. Gomperts, R.E. Stratmann, O. Yazyev, A.J. Austin, R. Cammi, C. Pomelli, J.W. Ochterski, R.L. Martin, K. Morokuma, V.G. Zakrzewski, G.A. Voth, P. Salvador, J.J. Dannenberg, S. Dapprich, A.D. Daniels, O. Farkas, J.B. Foresman, J.V. Ortiz, J. Cioslowski, D.J. Fox, Gaussian 09, Revision B.01 (Gaussian, Inc., Wallingford CT, 2009)
86. P. Flukiger, H.P. Luthi, S. Portmann, J. Weber, MOLEKEL 4.3, Swiss Center for Scientific Computing, Manno, Switzerland, 2000–2002
87. T. Miyake, M. Aida, Chem. Phys. Lett. **363**, 106–110 (2002)
88. S. Maeda, K. Ohno, J. Phys. Chem. A **111**, 4527–4534 (2007)
89. K. Mizuse, N. Mikami, A. Fujii, Angew. Chem. Int. Ed. **49**, 10119–10122 (2010)
90. Y. Matsuda, M. Mori, M. Hachiya, A. Fujii, N. Mikami, J. Chem. Phys. **125**, 164320 (2006)
91. S. Enomoto, M. Miyazaki, A. Fujii, N. Mikami, J. Phys. Chem. A **109**, 9471–9480 (2005)
92. Y.S. Wang, J.C. Jiang, C.L. Cheng, S.H. Lin, Y.T. Lee, H.C. Chang, J. Chem. Phys. **107**, 9695–9698 (1997)
93. J.C. Jiang, Y.S. Wang, H.C. Chang, S.H. Lin, Y.T. Lee, G. Niedner-Schatteburg, J. Am. Chem. Soc. **122**, 1398–1410 (2000)
94. J.C. Jiang, J.C. Chang, B.C. Wang, S.H. Lin, Y.T. Lee, H.C. Chang, Chem. Phys. Lett. **289**, 373–382 (1998)
95. K. Suhara, A. Fujii, K. Mizuse, N. Mikami, J.L. Kuo, J. Chem. Phys. **126**, 194306 (2007)
96. C.K. Lin, C.C. Wu, Y.S. Wang, Y.T. Lee, H.C. Chang, J.L. Kuo, M.L. Klein, Phys. Chem. Chem. Phys. **7**, 938–944 (2005)
97. J.-D. Chai, M. Head-Gordon, Phys. Chem. Chem. Phys. **10**, 6615–6620 (2008)
98. Y. Zhao, D. Truhlar, Theor. Chem. Acc. **120**, 215–241 (2008)
99. Y. Zhao, D.G. Truhlar, Acc. Chem. Res. **41**, 157–167 (2008)

100. K.E. Riley, M. Pitonak, P. Jurecka, P. Hobza, Chem. Rev. **110**, 5023–5063 (2010)
101. C.J. Burnham, S.S. Xantheas, J. Chem. Phys. **116**, 5115 (2002)
102. G.S. Fanourgakis, S.S. Xantheas, J. Phys. Chem. A **110**, 4100–4106 (2006)
103. A.A. El-Azhary, H.U. Suter, J. Phys. Chem. **100**, 15056–15063 (1996)
104. K. Ohno, M. Okimura, N. Akai, Y. Katsumoto, Phys. Chem. Chem. Phys. **7**, 3005–3014 (2005)
105. P. Hobza, J. Sponer, T. Reschel, J. Comput. Chem. **16**, 1315–1325 (1995)
106. S.S. Xantheas, E. Apra, J. Chem. Phys. **120**, 823–828 (2004)
107. A.Y. Zasetsky, A.F. Khalizov, M.E. Earle, J.J. Sloan, J. Phys. Chem. A **109**, 2760–2764 (2005)
108. M.S. Bergren, D. Schuh, M.G. Sceats, S.A. Rice, J. Chem. Phys. **69**, 3477 (1978)
109. J.P. Devlin, C. Joyce, V. Buch, J. Phys. Chem. A **104**, 1974–1977 (2000)

Chapter 3
Infrared Spectroscopy of Large Protonated Water Clusters $H^+(H_2O)_n$ ($n \leq 221$)

Abstract In studying large-scale hydrogen-bonded water network structures, we have succeeded in measuring the IR spectra of the precisely size-selected protonated water clusters $H^+(H_2O)_n$ up to the hitherto uncovered size of $n = 221$. In IR spectra, we identified the 4-coordinated and 3-coordinated water bands. We also showed that the abundance of 4-coordinated waters gradually increases with increasing cluster size. In the interior of the clusters, as has been seen in the size-averaged $(H_2O)_{<n>}$ studies, the implication of network ordering (crystallization) was observed. The free OH frequency suggests that the surface structures of the large-sized clusters are similar to those of liquid water and ice. The observed spectra, in addition to recently reported spectra for large water clusters, are expected to be a benchmark for studies concerning large-scale hydrogen-bonded networks involving hundreds of water molecules.

Keywords IR photodissociation spectroscopy · Protonated water clusters · Tandem mass spectrometer · Large-sized clusters · Hydrogen bond network order

3.1 Introduction

3.1.1 Toward Larger Clusters

In Chap. 2, we succeeded in measuring moderately size (n)-selective IR spectra of phenol-$(H_2O)_n$ clusters of up to $n \sim 50$. We characterized these cluster structures in terms of coordination number and network ring sizes (hydrogen bond distortion), bridging the gap between the small ($n < \sim 10$) water networks and bulky networks. Because the observed band maximum of the hydrogen-bonded OH stretch band ($\sim 3,300$–$3,400$ cm^{-1}) is far from that of larger nanoparticle and ice

spectra ($\sim 3{,}200$ cm^{-1}) [1, 2], further structural developments are expected in much larger size ranges. However, we are unable to extend our size-selective spectroscopic approach to larger clusters ($n > 50$). One of the main reasons for this is that evaluation of size uncertainty (Δn) due to the fragmentation upon photo-ionization cannot be achieved at the present stage for larger clusters. Because adiabatic ionization energy is size-dependent, Δn should be also size-dependent. For Δn evaluation, we need energetic information of both ionic and neutral states of large clusters, but no such findings have been reported so far. In neutral phenol-$(H_2O)_n$ cluster studies, the inherent difficulties in precise size-selection are difficult for researchers to overcome. Ideally, Δn should be zero for simplicity in spectroscopic analyses; however, it seems to be impossible to achieve this in the case of large neutral clusters.

On the other hand, if we focus on ionic clusters, precise ($\Delta n = 0$) size-selection can be achieved with the aid of mass spectrometric techniques. In the 1980s, Lee's group developed a size-selective spectroscopic method for gas phase cluster ions, IR photodissociation spectroscopy [3–6]. The essential elements for IR photodissociation techniques are a multi- (typically 2-) step mass spectrometer and a tunable IR light source [7]. Cluster ions of interest are mass-selected by the first mass spectrometer and then IR light is irradiated to them. Tunable IR light is available from a YAG laser-based wavelength conversion such as DFG (differential frequency generation, see Chap. 2) and OPA (optical parametric amplification, the same optical process as DFG), or FEL (free electron laser) facility. When the IR photon energy is resonant with the vibrational transition of a size-selected cluster ion, a vibrational predissociation following the transition results in a fragmentation. The second mass spectrometer was used to detect the fragmentation (by observing the enhancement of fragment ions or depletion of precursor ions). Thus, an action spectrum of the size-selected cluster ion was recorded by scanning the light wavelength while monitoring the intensity of the ion current due to the fragment cluster ions.

Some other variations of this method have been also reported [4, 6, 7]. For strongly-bound clusters or molecular ions, single IR photon energy is an inefficient method of photodissociation. In such situations, an assisting light following IR irradiation can be used to enhance IR-induced fragmentation [6]. As it is based on the use of multiple photons, this scheme is called IR multiphoton dissociation spectroscopy. Strong emissions from FEL also induce IR multiphoton dissociation [8–10]. A photodissociation scheme can be also used in visible and UV regions to measure an electronic spectrum [11–13]. For anion, IR-induced electron detachment can also be used for action spectroscopy [14, 15]. The inert gas tagging technique, in which an inert gas atom/molecule is attached to a cluster of interest and IR-induced detachment of this inert gas is probed, has been also applied [4, 16]. In Chap. 4, we will employ this tagging technique and further details will be provided there. It is an important principle that, because there is no upper limit in molecular weight in mass spectrometry, IR photodissociation spectroscopy has also no upper limit in the applicable cluster size. We therefore expect that we can apply size-selective spectroscopy to much larger water clusters.

Pioneering size-selective spectroscopy of cluster ions has been reported on $H^+(H_2)_n$ [3, 17], $H^+(H_2O)_n$ [4, 6, 16], and $NH_4^+(NH_3)_n$ [5, 18]. Since these studies, numerous cluster ions have been studied with IR photodissociation and related techniques. Such spectroscopy has been a powerful tool to investigate, for example, charge-ligand interactions, solvation structures of ion/electrons, and ion-molecular reactions. Parts of these studies have been reviewed by many authors [7, 9, 15, 19–25]. As for previous studies of hydrated clusters, examples include $H^+(H_2O)_n$ [4, 6, 16, 26–38], $NH_4^+(H_2O)_n$ [39–41], $(H_2O)_n^-$ [42–52], $M^{m+}(H_2O)_n$ (M: metal) [7, 20, 53–59]. Among these hydrated clusters, protonated water clusters $H^+(H_2O)_n$ are one of the most frequently studied because of the fundamental importance of hydrated protons [60–66] in various fields such as aqueous chemistry and biochemistry. This system is the first system in which large-sized clusters ($n \leq 28$) were studied with size-selective IR photodissociation spectroscopy [30, 35, 38]. For the purpose of investigating hydrated clusters that are as large as possible, we chose $H^+(H_2O)_n$ as a target system.

In this thesis, to investigate larger hydrogen-bonded water networks, we have tried to extend size-selective IR spectroscopy to a hitherto uncovered size region (up to more than 100) [67]. In the following part in this section, an overview of previous studies on $H^+(H_2O)_n$ and detailed motivations will be provided.

3.1.2 Previous Studies on $H^+(H_2O)_n$

For $H^+(H_2O)_n$, Before the pioneering advent of size-selective IR spectroscopy, many studies simply relied on mass spectrometric techniques [68–85]. Size-dependent abundance, which reflects relative stability, has been investigated by measuring mass spectra. Lin reported on the broad range mass spectrum of $H^+(H_2O)_n$ produced with the supersonic jet expansion followed by electron ionization [68]. The reported spectrum showed an intensity anomaly of between $n = 21$ and 22, with the yields of $n \geq 22$ clusters much smaller than those of $n \leq 21$ clusters. According to this observation, $n = 21$ and 22 are called the 'magic number' and the 'antimagic number', respectively. Similar observations around $n = 21, 22$ were reported by many groups using various cluster sources [68–85]. Magic/antimagic number behaviors have been also reported for $n = 28/29$ and $n = 55/56$, although the latter ($n = 55/56$) magic/antimagic behavior is sensitive to a cluster source, and only a few groups have reported it [68–80]. In addition to size-dependent abundance measurements, size-dependent dissociation energy has also been reported [78]. The observed energy also shows magic/antimagic number behaviors at the same size as the abundance measurements (simple mass spectra). In cluster chemistry, such magic number behaviors have been reported in various systems, e.g., Xe_n, C_n, Na_n, and $(H_2O)_n^-$ [81, 86–89]. The origin of these magic numbers is sometimes attributed to completion of a shell structure and/or a highly symmetric structure, as in C_{60} [86–88]. For $H^+(H_2O)_{21}$, similarly, a dodecahedral cage structure enclosing one H_2O or H_3O^+ has been proposed [90], and several mass spectrometric studies and theoretical

calculations support such a structure [76, 91]. For $H^+(H_2O)_{28 \text{ and } 55}$, water cage structures have been proposed, which encapsulate two and five H_2O molecules, respectively [37, 73]. However, explicit, direct evidence of such cage structures has not been obtained in mass spectrometry. Size-dependent reactivity of $H^+(H_2O)_n$ can be also measured by using tandem mass spectrometry [77, 82, 84, 92], however, structural insights from these mass spectrometric studies are limited.

For rigorous structural investigation based on IR spectroscopy, Fig. 3.1 contains collected previously experimentally characterized cluster structures of $H^+(H_2O)_n$ ($n \leq 9$) [6, 27, 32, 93]. First, IR spectra of $H^+(H_2O)_n$ were measured for $n \leq 4$ by Schwarz but they were not size-selective, and they show only broadened spectral features, which were difficult to analyze [94]. Lee's group reported size-selective IR spectra of the same size range by using IR photo- (multiphoton-) dissociation spectroscopy [4, 6, 16]. The observed spectra were well interpreted and cluster structures were characterized at the molecular level. For $n = 5$–11 clusters, Chang's group reported systematic IR spectroscopic studies combined with theoretical calculations [26, 27, 93]. As shown in Fig. 3.1, all the observed structures of $n \leq 6$ clusters were a simple or branched chain type, in which no rings were found. For $n \geq 6$, the coexistence of multiple isomers is evidenced. For $n \geq 7$, cluster structures that contain a ring (branched ring type) have been observed. In addition to the network structures, ion core motifs have been also of interest. For a hydrated proton in condensed phase, two limiting motifs, "Eigen" (H_3O^+ or $H_3O^+(H_2O)_3$) and "Zundel" ($H_5O_2^+$ or $H_2O \cdots H^+ \cdots OH_2$), have been proposed [60–62]. In gas phase $H^+(H_2O)_n$, these proton hydration motifs can be identified at the molecular level [26, 27, 32, 93]. Because these motifs correlate with proton transfer mechanism in aqueous environments [60–66, 95], identification in cluster chemistry is of interest. This aspect of $H^+(H_2O)_n$ study will be addressed in Chap. 4, while in this chapter we will focus on network structures of large $H^+(H_2O)_n$.

With regard to structural trends in $H^+(H_2O)_n$ in broader size ranges, Miyazaki et al. [35], Shin et al. [30], and Wu et al. [38] have independently reported IR spectra of $H^+(H_2O)_n$ ($n < \sim 30$) revealing structural development from the chain type to the net type and then the closed cage type [30, 35, 38]. Figure 3.2 shows the structural development of $H^+(H_2O)_n$ in this size region and corresponding IR spectral features. As in Fig. 3.2 (lower), at $n = \sim 10$, the formation of closed net (multiple-ring) type networks, which consist only of 2- and 3-coordinated molecules, has been observed. Such a structural transition can be clearly seen in IR spectra. Figure 3.2 (upper) shows IR spectra in the free OH stretching region of $H^+(H_2O)_{5 \text{ and } 12}$ as examples of the chain and multiple ring type, respectively. In IR spectra of $H^+(H_2O)_5$, three bands can be observed and attributed to symmetric (v_1) and antisymmetric (v_3) stretching motions of the 1-coordinated (terminal) water molecules, and free OH stretching of 2-coordinated molecules. With increasing cluster size, 1-coordinated water bands become as small as the other bands, and 3-coordinated water bands appear. At around $n = 10$, the 1-coordinated water band completely disappears, indicating the completion of closed net (multiple-ring) formation. In these structures, no terminal (dangling) water molecules
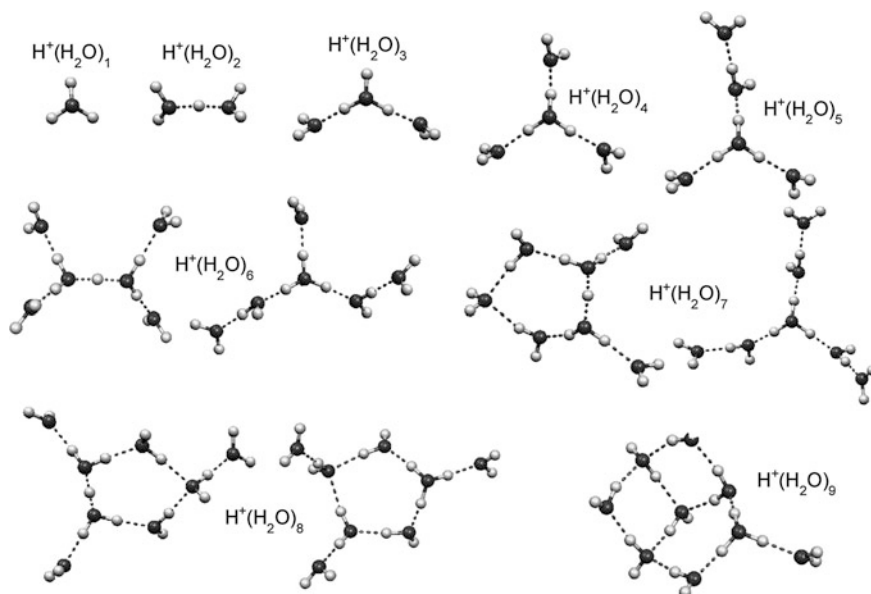
Fig. 3.1 Experimentally characterized structures of $H^+(H_2O)_n$
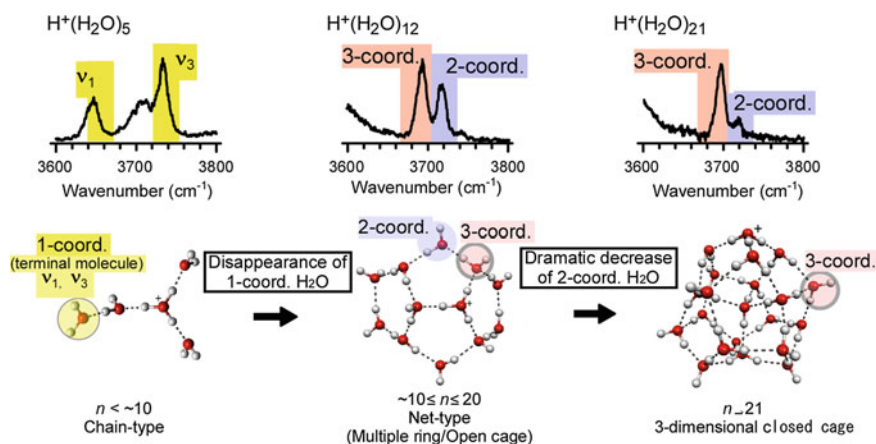
Fig. 3.2 Structural development of $H^+(H_2O)_n$ ($n \leq \sim 30$) revealed by IR spectroscopy

exist. They consist of 2- and 3-coordinated molecules. Such a configuration is reflected in the doublet feature of IR spectra in the free OH region. In the $n > 10$ region, the 2-coordinated water band loses its relative intensity with increasing cluster size. At $n = 21$, a drastic drop of the 2-coordinated water band has been observed (Fig. 3.2 upper). This means cluster structures include only a few 2- (and 1-) coordinated molecules. Such a configuration is found in the 3-dimensional closed cage

type structures (Fig. 3.2 lower). As in cubic $(H_2O)_8$, closed 3-dimensional structures do not have many 2- or less coordinated sites. According to these observations, the cage structure proposed in mass spectrometry and theory has been characterized experimentally.

3.1.3 Purposes of this Study

The structural trends in Fig. 3.2 have been characterized on the basis of relative abundance of 1- to 3-coordinated water molecules. As indicated in Chap. 1, spectral identification of 4-coordinated water molecules is an important step in understanding large water networks. As with the neutral cluster study in Chap. 2, the weight of 4-coordinated molecules should increase with increasing cluster size. Therefore, spectroscopy of larger ($n \geq 30$) clusters should lead to a better understanding of the behavior of these molecules. Furthermore, beyond the neutral cluster study in Chap. 2, which covers $n \leq \sim 50$ size region, approaches to examining much bulky water networks can be expected when we examine much larger clusters such as $H^+(H_2O)_{100}$.

We note that previously demonstrated structures of $H^+(H_2O)_n$ (Figs. 3.1 and 3.2) are quite different from those of neutral water clusters (Chap. 2). This is clearly due to the effect of an excess proton. Such an effect, however, should be diluted with increasing cluster size and hydrogen bond network structures in $H^+(H_2O)_n$, finally converging into those of neutral water. In the case of other hydrated clusters, Williams et al. have reported IR spectra of $Ca^{2+}(H_2O)_{n \leq 69}$ and $SO_4^{2-}(H_2O)_{n \leq 80}$. These systems were the largest cationic and anionic clusters investigated by size-selected IR spectroscopy. In their studies, the hydrogen-bonded OH band center was found to approach to that of the bulk water spectrum with increasing cluster size; however, the band-width of the hydrogen-bonded OH stretch band accounts only for a part of the bulk spectrum. This is potentially because the doubly charged Ca^{2+} and/ or negatively charged SO_4^{2-} ions strongly affect water networks. It is expected that in much larger clusters with a singly-charged ion, the ion effect would be further diluted and the cluster structure would be much closer to that of neat water networks.

To identify the 4-coordinated water, and to discuss the less-perturbed hydrogen-bonded network structures of hundreds of water molecules, we report here on IR spectra of precisely size-selected, large $H^+(H_2O)_n$ in the OH stretching region (2,200–4,000 cm^{-1}) up to a size of $n = 221$, which is expected to be large enough to form a bulklike hydrogen-bonded network in which 4-coordinated water is dominant. For example, the lowest-energy structures of $(H_2O)_n$ ($n \leq \sim 1,000$) on the empirical potential energy surface have been reported, and these studies suggested that crystal cores are formed in the size region of a few hundred water molecules or more. We show clear spectroscopic signatures for the abundance of the interior (4-coord) water. Furthermore, the fact that IR spectral patterns approach those of supercooled water and ice with increasing cluster size suggests formation of more ordered hydrogen-bonded network structures.

3.2 Experimental

3.2.1 Overview of Infrared Photodissociation Spectroscopy

IR photodissociation spectroscopy, as introduced above, can be directly applied to large clusters when we have a suitable cluster source and 2-step mass spectrometric apparatus. To achieve size-selective spectroscopy for large hydrated clusters, we built up a new chamber equipped with a tandem quadrupole mass spectrometer and an efficient ion source, both of which can be optimized for large cluster systems [96]. Here, only brief overviews of experimental apparatus and methods are given and details are shown in the following sections. $H^+(H_2O)_n$ was generated with a supersonic jet expansion. The gaseous mixture of H_2O and He was expanded into a vacuum chamber through a pulsed valve. The gas pulse was perpendicularly crossed by an electron beam of 200 eV generated by an electron gun in the collisional region of the supersonic jet. Cluster ions grew larger in the following collisions and were simultaneously cooled. Ions of interest were selected by a mass spectrometer and irradiated by coherent IR light. Vibrational predissociation causes the depletion of the precursor (target) ion intensity and the increase of fragment ion intensity. In typical IR photodissociation studies, the fragment ion intensity is monitored by the second mass spectrometer because zero or small background measurements are expected. We found, however, that precisely size-selective IR spectra of large clusters are measurable only by monitoring the parent ion intensity as a function of the IR wavelength. This aspect will be discussed in Sect. 3.2.3.

3.2.2 Setup

3.2.2.1 Vacuum Chamber

A scheme of the vacuum chamber equipped with a tandem quadrupole mass spectrometer used in this study is shown in Fig. 3.3. This consisted of an ion source chamber (the left side of Fig. 3.3) and a differentially-pumped ion analyzing chamber (the right side of Fig. 3.3), and they were connected by a skimmer (2.0 mm hole diameter, ~ 50 mm length, model 50.8, BeamDynamics, Inc.). This skimmer was electrically isolated and can be used as an ion-optics component. Typically, the voltage within ± 2 V was applied to optimize the transmittance of produced cluster ions. The source chamber was pumped by a turbomolecular pump (1,600 l/s, TPH1601P, Pfeiffer), which was backed by a rotary pump (500 l/m, T2033SD, Alcatel). The ion analyzing chamber was pumped by two turbomolecular pumps (500 l/s, TMU521P, Pfeiffer; and 60 l/s, TMU071P, Pfeiffer), both of which were backed by a smaller rotary pump (345 l/m, M2021SD, Alcatel). Three vacuum gauges (PKR251, Pfeiffer) were used to monitor vacuum pressure.
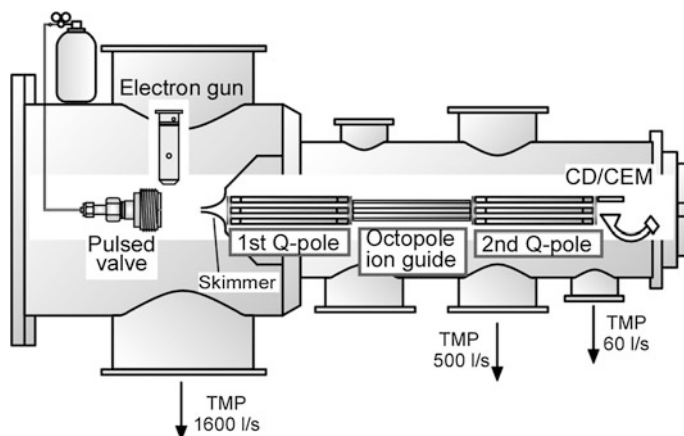
Fig. 3.3 Scheme of the vacuum chamber equipped with tandem quadrupole mass spectrometer used in this study. Quadrupole mass spectrometer *Q-pole*, conversion dynode *CD*, channeltron electron multiplier *CEM*, turbomolecular pump *TMP*. Reproduced from Ref. [96] by permission of the PCCP owner societies

Typical pressure of the source and analyzing chambers without gas loading was 8×10^{-8} and 9×10^{-8} Torr, respectively. In typical experimental conditions (see the next section for our cluster source), corresponding pressures were 3×10^{-6} and 3×10^{-7} Torr, respectively.
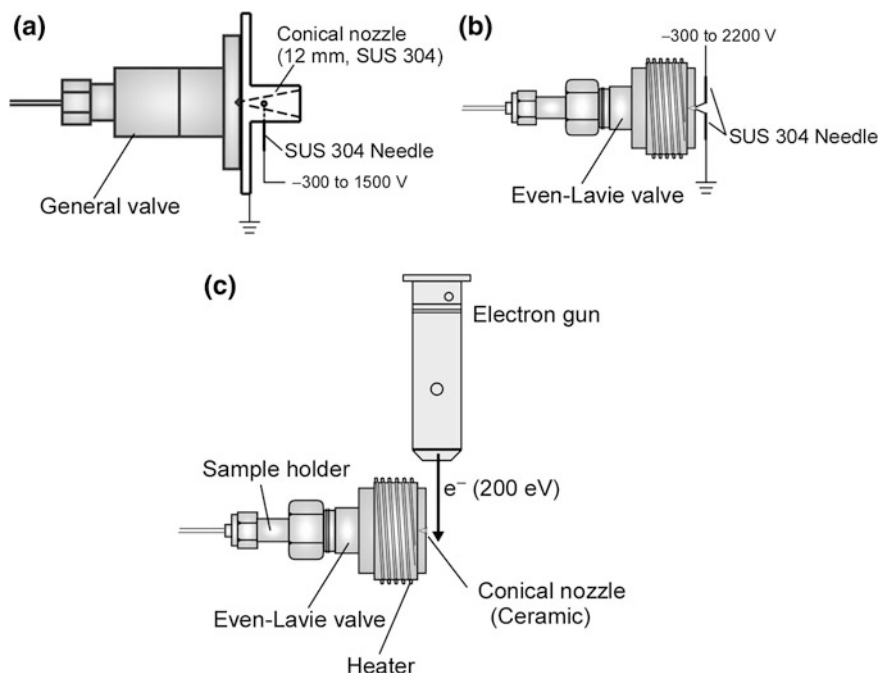
3.2.2.2 Cluster Ion Source

To produce stable large clusters efficiently, a cooling technique will be necessary because large clusters sometimes suffer from short fragmentation lifetimes [83]. The large number of degrees of freedom can act as a heat bath accommodating large internal energy. The larger number of dissociation paths also accounts for shorter dissociation lifetime of larger clusters. A reduction of internal energy would lead to a longer lifetime and therefore efficient production of large clusters. Furthermore, for ionic clusters, there are numerous ionization techniques (and many of them have been used to produce $H^+(H_2O)_n$). Generally, however, excess energy upon ionization is difficult to remove. Therefore further cooling method should be required for spectroscopic purposes—especially for large clusters.

In previous studies, $H^+(H_2O)_n$ were produced with various techniques such as discharge, electron ionization, electrospray ionization, and ion emissions from laser-irradiated liquid [68–85]. As described in Chap. 2, a supersonic jet expansion has been a powerful tool for producing gas phase clusters with low internal energy. In this method, excess energy may be transferred to the carrier gas via the collisions. This method can be coupled with various ionization techniques. Therefore the combination of a supersonic jet and a suitable ionization technique has been a widely-used approach, successfully producing a stable $H^+(H_2O)_n$ that can be used

in gas phase spectroscopic samples [30, 35, 96, 97]. For the cooling of cluster ions, an ion trap technique, in which ions are cooled via collision with cold buffer gas, has been developed [28, 98]. This technique is a powerful method not only to produce cold cluster ions but also to investigate temperature effects on cluster structures and dynamics. However, in the collisional cooling process of this technique, fragmentation of clusters often occurs. Furthermore, this technique generally needs a relatively complicated apparatus, which has an ion trap and a stable refrigerator in addition to tandem mass spectrometer and a cluster ion source. Based on these discussions, we employed the former, simpler approach (a combination of a supersonic jet and ionization), focusing on the efficient production of large clusters in this chapter. We also note approaches to further cooling and investigation of the internal energy (temperature) effects; these will be addressed in Chap. 4.

Among many ionization techniques, some techniques such as electrospray ionization cannot be simply combined with a supersonic jet technique. Discharge, electron beam irradiation, and laser photoionization are typical ionization techniques used with a supersonic jet. As discussed in Chap. 2, for H_2O molecule, photoionization requires short wavelength light or femtosecond light. Therefore, it seems not to be suitable for efficient $H^+(H_2O)_n$ production. Laser vaporization/ desorption and related techniques are also frequently used for gas phase cluster ion source, however, impurities from the metal/matrix substrate are often seen [97].

In this study, we first tried a discharge cluster ion source because similar techniques have been used in previous studies of $H^+(H_2O)_{n \leq \sim 30}$ [35]. Figure 3.4a shows a schematic of this ion source. The gaseous mixture of water (trace), and helium (0.3–0.8 MPa) was expanded into a chamber through a pulsed valve (General valve Series 9, 0.5 mm nozzle diameter, Parker) and a conical nozzle (SUS304, 12 mm long). A small pin electrode (SUS304, typically -500 V) was inserted into a nozzle via an insulator. Pulsed gas loading in a conical nozzle triggered a pulsed discharge. In this method, clusters of $n \leq \sim 100$ were produced [99]. For larger cluster production, we postulated that further efficient cooling and collisions by a supersonic jet would be needed. Recently, Even et al. [100] have designed a new pulsed valve (Even-Lavie valve) which can be operated at up to 10 MPa with shorter duration of ~ 20 μs. At such a high pressure, many more collisions, which would cause efficient cooling and clustering, should occur. They have reported the use of that valve and suitable source chamber conditions lead to the cooling of the large molecular system to below 1 K [100, 101]. The short duration time of gas pulse leads to an intense (concentrated) beam, which can be efficiently detected. For large cluster studies, Mitsui et al. [102, 103] have used an Even-Lavie valve and succeeded in producing large aromatic hydrocarbon clusters such as $(benzene)_{n^-}$ ($n \leq \sim 100$). We then tried to combine an Even-Lavie valve with our discharge source (Fig. 3.4b). This method produced up to $n < \sim 200$ clusters, which is near the upper limit of our mass spectrometer. However, shot-to-shot deviation of cluster yield is too large to measure IR spectra with a good signal-to-noise ratio. Furthermore, we found that discharge causes damage (scorching) to the pin electrode and therefore we needed frequent maintenance of

Fig. 3.4 Three versions of the cluster ion source. **a** General valve with a discharge electrode. **b** Even-Lavie valve with discharge electrodes. **c** Even-Lavie valve with an electron gun. Version (**c**) worked the best for our purpose and it was used in spectral measurement. See text for details

the cluster source components. As a result of these problems, we tried the other method.

To improve shot-to-shot deviation, we next tried a combination with a continuous electron beam (Fig. 3.4c). The yield of thermally emitted electrons from a filament is almost constant in time and therefore, the efficiency change of cluster ion formation in time is expected to be small. In this approach, timing or position of the interaction between the electron beam and the gas pulse is an important factor. When an electron beam crosses a gas pulse in the collision region of a jet (just after the pulsed valve), the main process is ionization of carrier gas (He and Ar, for example) followed by chemical ionization of water molecules. Clusters are gradually formed in the following collisions and simultaneously cooled by evaporative and collisional cooling. On the other hand, when an electron beam interacts with a gas pulse in the collision free region (a few cm downstream of a jet expansion), neutral water clusters are formed and then ionized. In this case, only evaporative cooling can be expected and it seems to be difficult to remove excess energy upon ionization. We tried both approaches by installing an electron gun just after the nozzle or 7 cm after the nozzle. We found the former position leads to a higher yield of large clusters such as $H^+(H_2O)_{100}$. Based on this discussion and preliminary tests, we introduced an electron beam just after the nozzle of the valve

(Fig. 3.4c). By using this approach, we succeeded in producing $H^+(H_2O)_n$ at least up to the size of $n = 221$, which is at the upper limit of our apparatus (see Sect. 3.2.3.1). Furthermore cluster ion intensity was almost constant (within 5 %) for at least 30 h, which is the typical time needed to measure the IR spectrum of a large cluster. We note that even if we used the same method with a general valve, we could not achieve such stability (in that case, ion intensity decreases with time). In the following section, we describe the present cluster ion source.

The gaseous mixture of H_2O (trace; [17, 18] O-depleted $H_2{}^{16}O$, 99.99 % ^{16}O, ISOTEC) and carrier gas (9.5 MPa, He) was expanded into an ion source chamber through a high-pressure pulsed valve (Even-Lavie valve [100], high-temperature, low-repetition rate model, Serial No.98, Tel Aviv University), equipped with a ceramic conical nozzle (0.25 mm nozzle hole diameter, 5 mm length, 40° full angle). We also tried the other nozzle (SUS, 0.20 mm nozzle hole diameter, 5 mm length, 40° full angle). However, no remarkable change in cluster production was observed. Although we also used Ar and Ne as a carrier gas, effects on the IR spectra were negligible for at least $H^+(H_2O)_{20-22}$. H_2O sample was loaded to the sample holder (Fig. 3.4) (a piece of a wet filter paper was put in the holder.) An isotope-separated sample was used to minimize the contamination of $H_2{}^{18}O$ in mass spectrometry. Operating temperature of the valve was 353 K, which was optimized for $H^+(H_2O)_{21}$ intensity. Typical duration times of the valve driver were 25.0 μs and 28.5 μs for $H^+(H_2O)_{21}$ and $H^+(H_2O)_{200}$ production, respectively. The gas pulse was perpendicularly crossed by the electron beam of 200 eV from an electron gun (Omegatron Co.). Cluster ions were produced and simultaneously cooled in the supersonic jet expansion. They were introduced into the differentially-pumped ion analyzing chamber through a skimmer. Distance between the nozzle and the skimmer tip is suggested to be an important parameter for optimizing the intensity of the cluster beam [97, 104]. It was set to about 10 cm, which is the mechanical upper limit. Here we used a relatively slim skimmer (2.0 mm hole diameter, ∼50 mm length, ∼25° total interior included angle at orifice, model 50.8, BeamDynamics, Inc.) as Even et al. [101] recommended for optimal generation of a molecular/cluster beam.

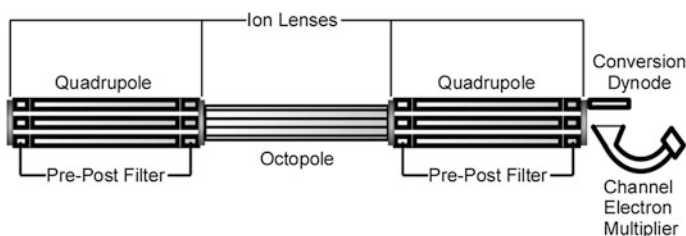### 3.2.2.3 Tandem Quadrupole Mass Spectrometer

In this study we employed quadrupole mass spectrometers for two-step mass spectrometry. In cluster spectroscopy, a two-stage time-of-flight mass spectrometer (equipped with a Refletron) and FT-ICR type are frequently used for photodissociation spectroscopy of cluster ions [7, 8, 12]. However, with the time-of-flight type, spontaneous dissociation in the flight tube (field-free drift region) results in an error and the disturbance of size-selective dissociation spectroscopy. Furthermore, second mass spectrometry bases Refletron, IR-induced dissociation needs to occur in a few μs to be detected. The time scale may be short and therefore, detection efficiency might be low. FT-ICR requires large-scale apparatus and physical space. Furthermore, for ions in a cyclotron motion, irradiation

efficiency of IR light may be low. In FT-ICR mass spectrometry, lifetime should be longer than a few ms, however, large clusters often have a short lifetime and therefore sufficient mass resolution might not be achieved [83]. In a quadrupole mass spectrometer (mass filter), clusters dissociated in the quadrupole are ejected and therefore precise mass selection is achieved even for species of shorter lifetime. Furthermore, the quadrupole type has the advantage of its compactness. Our quadrupole is only ~ 20 cm long. A general shortcoming of the quadrupole is its low upper limit (typically $m/z < 2,000$). We employed a tandem quadrupole mass spectrometer that covers the $m/z \leq 4,000$ region (see below). This region covers large clusters of up to $H^+(H_2O)_n$ ($n \leq 221$), which seems large enough to observe a structural development beyond that of phenol-$(H_2O)_{n<50}$.

Figure 3.5 shows the scheme of the tandem quadrupole mass spectrometer equipped with ion optics. Two quadrupoles (9.5 mmϕ rods, Extrel) were connected by an octopole ion guide (3 mmϕ rods, Extrel). Pre/post filters were installed before and after the quadrupoles to improve transmission efficiency by shielding electric field disturbance from the edges of the quadrupoles. Including the ion optics and detector, components were mounted in line in the following order (here, typical bias voltages applied to each component were also shown): (entrance lens, 0 V)-(pre-filter, -15 V)-(1st quadrupole mass filter, -13 V)-(post-filter, -15 V)-(exit lens, -80 V)-(octopole ion guide, -5 V)-(entrance lens, -15 V)-(pre-filter, -20 V)-(2nd quadrupole mass filter, -30 V)-(post-filter, -20 V)-(exit lens, -30 V)-(conversion dynode, $-4,000$ V/Channeltron electron multiplier, $+1,800$ V).

All the voltage of ion optics, pole bias of each multipoles, fine-tuning of mass resolutions, and detector voltages were controlled by a Merlin controller interface (Model 5221, Extrel) and Merlin Automation Data System program ver. 3 (Merlin software, Extrel). Power supply for the quadrupoles was 150-QC, 300 W, Extrel. The RF frequency was 1.2 MHz for $m/z \leq 2,000$, and 880 kHz for $m/z \leq 4,000$, respectively. Power supply for the octopole was 150QC, 300 W, 2.1 MHz, Extrel.

Mass spectra were also measured with these interfaces and programs. Ion signals from the channeltron electron multiplier (CEM) detector were amplified by preamplifier (Model F-100T, Advanced research instruments corporation) and then sent to the interface. These signals were processed by Merlin software and then a mass spectrum was obtained. Here, mass range of interest was scanned in ~ 14 s and 1,000 scans were averaged for each mass spectrometric measurement.


**Fig. 3.5** Scheme of the tandem quadrupole mass spectrometer with ion optics and a detector

3.2.2.4 IR Light Source

IR light source for gas phase study widely employed differential frequency generation or optical parametric amplification with a $LiNbO_3$ crystal, as in the case of Chap. 2. However, low output efficiency in the 3,500 cm^{-1} region and below 2,700 cm^{-1} region is unwanted because most hydrogen-bonded clusters have absorption in these regions. Recently, a potassium titanyl arsenate ($KTiOAsO_4$, KTA)- based wavelength conversion system has become available. This system produces IR light in a broad wavelength region. We employed a custom-made IR light source (IR-OPO/OPA, LaserVision), which uses KTP/KTA-based OPO/OPA processes, to cover the broad IR region. Figure 3.6 shows a schematic of IR-OPO/ OPA. A pump beam is the fundamental output of a Nd: YAG laser (1,064 nm, ~ 550 mJ/pulse, Quanta-ray, GCR-230). A beam-splitter was used to split the pump beam into two. One of the beams was frequency-doubled with a KTP crystal. Thus, the obtained 532 nm light was used to pump the first OPO stage, which contained two KTP crystals. The output red light (710–880 nm) and the residual light from the pump beam (1,064 nm) were combined and introduced to the OPA stage (four KTA crystals). The idler output of the OPA ($\sim 2,100$– 4,600 cm^{-1}) was used for IR spectroscopy. The wavelength was tuned by adjusting the crystal angles, which were controlled via a computer. A part of the IR light was reflected by a CaF_2 beam sampler plate and introduced to an IR power meter (model J3-05, Molectron). The wavelength of the IR light was calibrated in vacuum wavenumbers (± 2 cm^{-1}) by recording an ambient H_2O/CO_2 vapor spectrum. Figure 3.7 shows a typical power curve of IR light obtained with the IR-OPO/OPA. Maximum power was ~ 10 mJ/pulse in the 3 μm region. We note saturation of the transition can occur with such high power IR light. (We observed 100 % fragmentation of $H^+(H_2O)_{200}$ with a 6 mJ, 3,300 cm^{-1} IR light irradiation). Therefore, IR power was limited to avoid these saturation effects. Typically, we used just 150 μJ/pulse IR power. Our IR light source was mounted on an optical table (Newport).

The IR light was introduced to the ion guide according to the following procedures. First, two iris diaphragms were aligned along the invisible IR light.
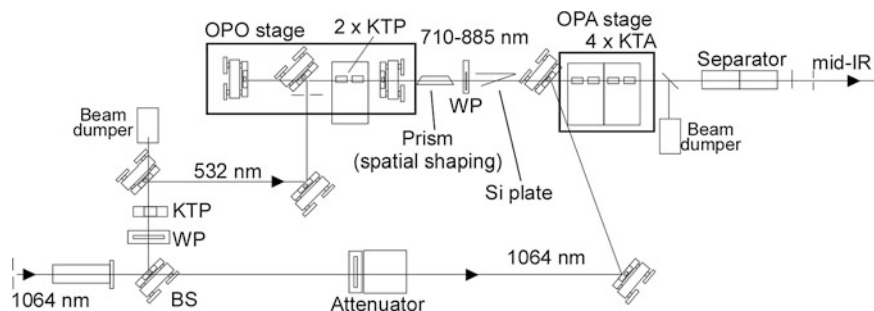
**Fig. 3.6** Scheme of our IR light source (IR-OPO/OPA). Beam splitter *BS*, half-wave plate *WP*
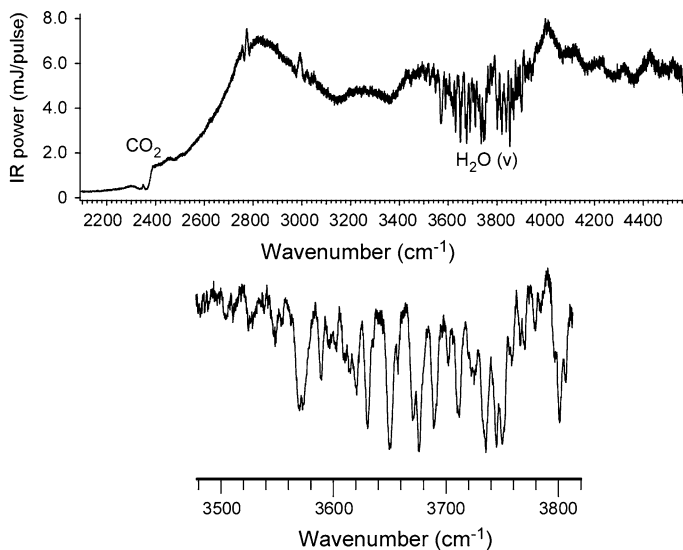
Fig. 3.7 Typical power curve of IR light source obtained with IR-OPO/OPA. Note that we reduced the output power to below 1 mJ/pulse in spectral measurements to avoid the saturation effect (see text for details)

A visible laser for alignment procedures was installed and its path was adjusted to pass through the reference iris pair. For this purpose, I used a compact and low-cost DPSS (diode pumped solid state) green laser module (Kyoritsu), in which an 808 nm LD is driven by the electric current and used to excite Nd:YVO$_4$. The 1,064 nm emission was frequency-doubled in a KTP crystal. The output of the 532 nm ($\sim$5 mW, CW) beam was used for the alignment procedure. After passing through the iris pair, the green light was introduced to a chamber through a CaF$_2$ window by using two Al steering mirrors. The two mirrors were iteratively adjusted to make the green light pass both the centers of the CaF$_2$ window and the skimmer. Then, the green laser was removed and a CaF$_2$ lens ($f = 1,000$ mm) was installed. After this prealignment, an IR optical path was optimized by using a known IR photodissociation process (typically we used the 3,400 cm^{-1} IR light-induced fragmentation of H$^+$(H$_2$O)$_{21}$ by monitoring H$^+$(H$_2$O)$_{20}$ fragment).

3.2.2.5 Measurement System

Figure 3.8 shows the final measurement setup. Ion signals from the detector (CEM) were amplified by a wide dynamic range current amplifier (Model 428, Keithley). A home-built band-pass filter was used to improve signal quality. These signals were monitored by an oscilloscope (TDS 410A, 200 MHz, Tektronix) and sent to boxcar integrators (2 channels for raw IR-induced signal and baseline measurements, respectively) (SR250, SRS). IR power signals were also processed
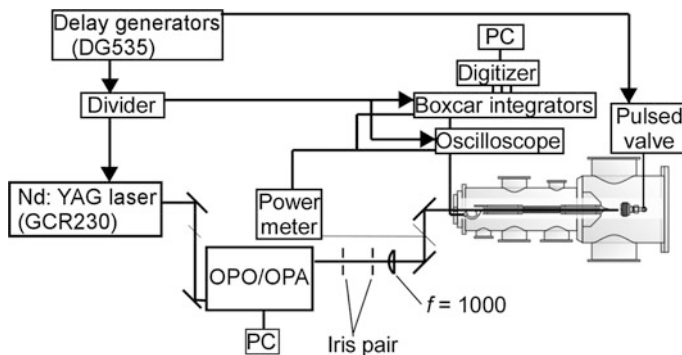
Fig. 3.8 Schematic diagram of the experimental setup

by SR250. These three averaged outputs were transferred to an analog-to-digit converter (SR245, SRS) and recorded by a measurement program (SR270, SRS) on a Windows PC.

As shown in Chap. 2, background fluctuations due to the time-fluctuation of ion yields and spontaneous dissociation should be corrected in IR spectroscopy. We divided the signal by IR power and background ion intensity, which was measured without IR irradiation. The master clock of the system was a delay generator (DG535, SRS) operated at 20 Hz. One of the TTL (transistor–transistor logic) outputs of DG535 triggered the pulsed valve (20 Hz). From another 20 Hz TTL output of DG535, two alternate 10 Hz TTL signals were produced with a home-built frequency divider (Fig. 3.9). One of the 10 Hz TTL was used to trigger the IR light (YAG laser, GCR 230), an oscilloscope, and two boxcar channels for IR-induced ion signal (raw signal) and IR power, respectively. The other 10 Hz TTL was used to trigger the boxcar channel for the ion intensity without IR irradiation (background signal). The IR spectrum obtained was

$$(\frac{Raw\,signal}{Background\,signal} - 1)/(IR\,power) \tag{3.1}$$

This correction is more accurate than the active baseline subtraction technique, in which base signal is simply subtracted. This is because signal intensity should be proportional to the background ion intensity. IR spectra reported in this study are a summation of 3–50 individual measurements to improve the signal to noise ratio.

3.2.3 Measurements and Analyses

3.2.3.1 Size Distribution of the Ion Source

Figure 3.10 shows typical mass spectra of our cluster ion source. In the small size range, mass resolution $\Delta m/z < 1$ was achieved and we found $H^+(H_2O)_n$ series was

Fig. 3.9 *Top*—diagrams of a home-built TTL frequency divider. *Bottom*—TTL signals used in this study
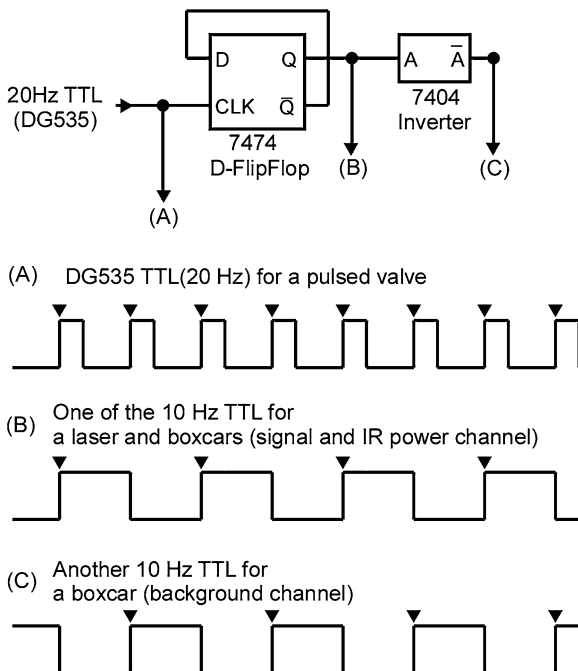
essentially a unique species in mass spectra. Only a small part of $(H_2O)_n^+$ was seen when we used Ar carrier (See Chap. 5 for $(H_2O)_n^+$). $H^+(H_2O)_n$. He was not seen. The observed size distribution was similar to those reported previously [68–85]. Due to the *m/z*-dependent transmittance of mass filter and ion optics, some undulation of intensity distribution can be seen. Magic number behavior can be clearly seen at $n = 21$ and 28. The $n = 55$ has been reported to be a third magic number [79, 84]. However, we could not see a distinct magic feature around $n = 55$. This is probably because the appearance of the third magic number was sensitive to source conditions. Some groups also reported mass spectra without a magic number feature at $n = 55$ [68, 74]. Magic and antimagic number behavior will be addressed in Chap. 4. The lowest mass resolution (at $m/z > \sim 2{,}500$) was $\Delta m/z \sim 14$, which was high enough for precise size-selection of $H^+(H_2O)_n$. Up to $n = 221$, well size-resolved mass spectra were measured implying the possibility of precisely size-selective spectroscopy.

3.2.3.2   IR Spectral Measurements

As mentioned in Sect. 3.2.1, typical IR photodissociation spectra are measured by monitoring IR-induced fragment ion intensity because zero or small background measurements are expected. For clusters up to $n < \sim 30$, this technique leads to
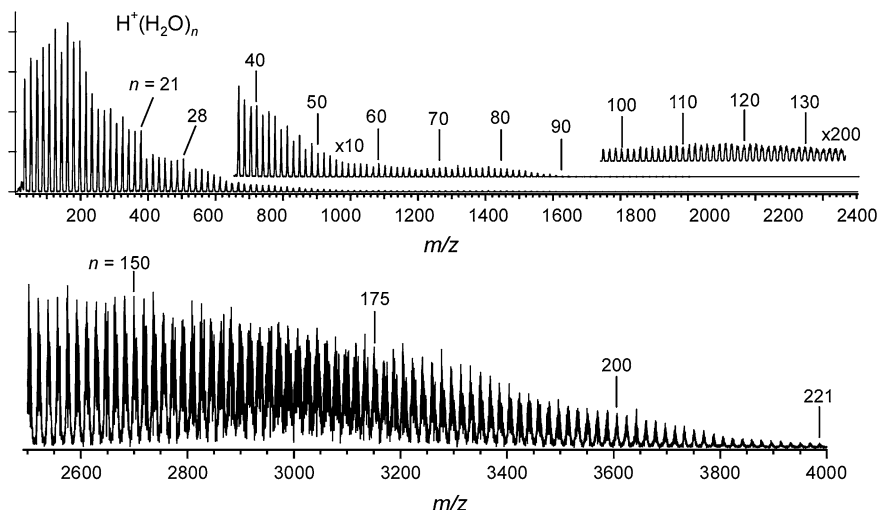
Fig. 3.10 Mass spectra of $H^+(H_2O)_n$ produced with our cluster ion source. Due to the m/z-dependent transmittance of mass filter and ion optics, some undulation of intensity distribution can be seen. Magic number behavior can be clearly seen at $n = 21$ and 28

measurements with good signal to noise ratio. For larger clusters, in contrast, metastable (spontaneous) dissociation of parent $H^+(H_2O)_n$ after the first mass selection produces a considerable amount of fragments, $H^+(H_2O)_{n-1, n-2 \dots}$, even without IR irradiation. In such cases, enhancement of the $H^+(H_2O)_{n-1}$ fragment due to the IR absorption to the parent ion competes with the depletion of $H^+(H_2O)_{n-1}$ by its IR absorption. Smaller $H^+(H_2O)_{n-2, n-3 \dots}$ fragment signals also include contributions from $H^+(H_2O)_{n-1}$. Under such conditions, depletion spectroscopy monitoring only the parent ion is a unique way to precisely measure size-selective spectra.

We discuss this aspect taking the case of $H^+(H_2O)_{200}$ as an example. Figure 3.11 shows a spontaneous dissociation mass spectrum of $H^+(H_2O)_{200}$, obtained by tuning the first mass filter to pass only $H^+(H_2O)_{200}$ and scanning the second mass filter. This mass spectrum shows the greater part of the selected ions fragmented in the ion guide even without IR irradiation. In such a situation, if we monitored $H^+(H_2O)_{199}$, the enhancement of $H^+(H_2O)_{199}$ due to IR photodissociation of $H^+(H_2O)_{200}$ is less than the decrease of $H^+(H_2O)_{199}$ due to the photodissociation of $H^+(H_2O)_{199}$ itself. IR action spectrum obtained by monitoring $H^+(H_2O)_{199}$ is neither spectrum of $H^+(H_2O)_{200}$ nor $H^+(H_2O)_{199}$ (it should be a mixture of them). When we monitored $H^+(H_2O)_{198}$, IR radiation also induced a small depletion. In the case of the $H^+(H_2O)_{197}$ channel, we first observed an IR-induced fragment enhancement signal. However, this spectrum should include the contribution of $H^+(H_2O)_{199 \text{ and } 198}$, which was produced in the ion guide due to spontaneous dissociation after mass selection. For precise size-selection, therefore,
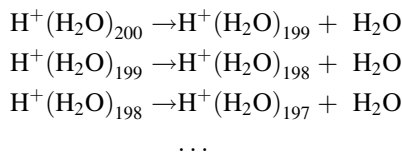
Fig. 3.11 Spontaneous dissociation mass spectrum of $H^+(H_2O)_{200}$. This spectrum was measured by scanning the second mass spectrometer while tuning the first mass spectrometer to $H^+(H_2O)_{200}$
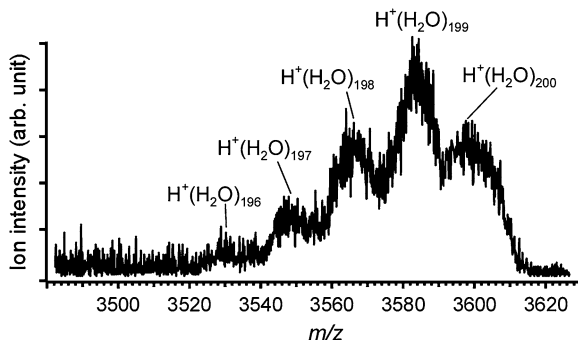
we tuned both mass filters to pass only $H^+(H_2O)_{200}$. By doing so, dissociating components of selected $H^+(H_2O)_{200}$ were ejected from the mass filter and therefore do not contribute to the spectrum.

3.2.3.3 Analyses of Spontaneous Dissociations

For a more detailed understanding of the present method, we analyzed the dissociation pattern shown in Fig. 3.11. We found it can be understood by assuming a step-wise 1st order dissociation model as follows:

$$H^+(H_2O)_{200} \rightarrow H^+(H_2O)_{199} + H_2O$$
$$H^+(H_2O)_{199} \rightarrow H^+(H_2O)_{198} + H_2O$$
$$H^+(H_2O)_{198} \rightarrow H^+(H_2O)_{197} + H_2O$$
$$\cdots$$

The rate constant of each dissociation path (i.e., inverse of dissociation lifetime) is k_{200}, k_{199}, and k_{198}, respectively. Rate equations are as follows:

$$\frac{d[200](t)}{dt} = -k_{200}[200](t)$$

$$\frac{d[199](t)}{dt} = +k_{200}[200](t) - k_{199}[199](t)$$

$$\frac{d[198](t)}{dt} = +k_{199}[199](t) - k_{198}[198](t)$$

Here abundance of $H^+(H_2O)_n$ at the time t is denoted as $[n](t)$. t is the time after the mass selection ($t = 0$ corresponds to the time when ions just passed the first quadrupole). By using initial conditions of $[200](t = 0) = 1$, $[199](t = 0) = 0$, $[198](t = 0) = 0$, the above simultaneous differential equation can be solved.

$$[200](t) = -k_{200} \times e^{-k_{200}t}$$

$$[199](t) = \frac{k_{200}}{k_{199} - k_{200}} \times (e^{-k_{200}t} - e^{-k_{199}t})$$

$$[198](t) = \frac{k_{199} \times k_{200}}{(k_{199} - k_{200}) \times (k_{198} - k_{200})} \times e^{-k_{200}t}$$

$$+ \frac{k_{199} \times k_{200}}{(k_{199} - k_{200}) \times (k_{199} - k_{198})} \times e^{-k_{199}t}$$

$$+ \frac{k_{199} \times k_{200}}{(k_{198} - k_{199}) \times (k_{198} - k_{200})} \times e^{-k_{198}t}$$

Here $[n \leq 197]$ (t) was neglected for simplicity, that is, $[200]$ (t) + $[199]$ (t) + $[198]$ (t) = 1. Although the exact measurement of time t was not practical in our apparatus, the estimated travel time in the ion guide was 180 μs. This has been estimated according to the total time of flight. Of course, the travel time depends on ion optics tunings, carrier gas used, and mass to charge ratio. This estimation means the mass spectrum in Fig. 3.11 reflects relative abundance at $t = 180$ μs. To reproduce this observation, the lifetime of each cluster size τ_n was evaluated as follows: $\tau_{200} = 125$ μs, $\tau_{199} = 200$ μs, $\tau_{198} \sim 500$ μs. (corresponding rate constants are $k_{200} \sim 8{,}000$ s^{-1}, $k_{199} \sim 5{,}000$ s^{-1}, and $k_{198} = 2{,}000$ s^{-1}). We note $H^+(H_2O)_{199}$ considered here is produced by the dissociation of $H^+(H_2O)_{200}$, and therefore, some of the internal energy has been removed in the dissociation. This is reflected by the longer lifetime, and the same goes for $H^+(H_2O)_{198}$. Thus simulated time-dependent ion abundance is shown in Fig. 3.12. We note these analyses did not rely on the experimental time-dependence, which can be measured by using ion trap technique; therefore, only qualitative understanding on dissociation processes has been enhanced.

These analyses also suggest that the timing of IR irradiation affects the efficiency of spectral measurements. After the IR irradiation at $t = t_{IR}$, rate constant becomes $k_{200} + k_{200,IR}$, the latter corresponds with IR-induced fragmentation. Observed IR spectral intensity was $[200](t) - [200]_{IR}(t)$, where $[200]_{IR}(t)$ was obtained by the rate constants of $k_{200} + k_{200,IR}$ after $t = t_{IR}$. In the case of $H^+(H_2O)_{200}$ monitoring, faster IR irradiation leads to the largest intensity in the IR spectrum. This means $t_{IR} = 0$ leads to the largest IR photodissiciation signal. On the other hand, $H^+(H_2O)_{199}$ channel faster IR irradiation leads to the largest

Fig. 3.12 Simulated time-dependent abundance of $H^+(H_2O)_{198-200}$ after the mass-selection of $H^+(H_2O)_{200}$ at $t = 0$. *Dotted line* shows the estimated travel time in the ion guide. See text for details
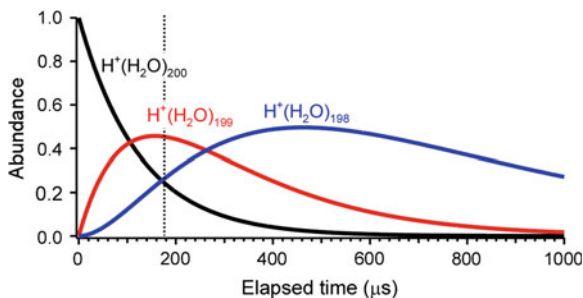
magnitude of $H^+(H_2O)_{200}$ to $H^+(H_2O)_{199}$, however, further fragmentation might be also be enhanced. $t_{IR} = 0$ is not an optimal timing in that case. Optimal IR timing for $H^+(H_2O)_n$ fragment monitoring would be ~ 50 μs, later relative to that for depletion of the $H^+(H_2O)_n$ channel (Typically, IR is irradiated ~ 200 μs faster than ion detection for $H^+(H_2O)_n$ channel monitoring).

3.2.3.4 Quantum Chemical Calculations

For detailed analyses of spectra, we carried out quantum chemical calculations. The methodologies were essentially the same as described in Sect. 2.2.4. Only the differences and additional comments are given here. In contrast to neutral $(H_2O)_n$ clusters, theoretical studies on $H^+(H_2O)_n$ structures have been rare, therefore, we needed to construct initial model structures manually. For coordination number analyses, we just added an exception handling to my Perl program (Chap. 2). This is for classification of the H_3O^+ or $H_5O_2^+$ moieties, both of which are absent in typical neutral $(H_2O)_n$. For the calculation level, B3LYP/6-31+G(d), used in Chap. 2, was used with the same scaling factor of 0.9736 for the harmonic frequencies. This level has been tested also for the $H^+(H_2O)_n$. In the case of larger clusters such as $H^+(H_2O)_{200}$, even relatively low-cost DFT calculations could not be performed with the current computer resources. We therefore used semi-empirical method PM6 for just the preliminary interpretations and to provide support for our discussion.

3.3 Results

3.3.1 IR Spectra of $H^+(H_2O)_n$ (n = 3–32)

Before the spectroscopy of large clusters, we measured the IR spectra of $H^+(H_2O)_n$ ($n \leq 32$). Most of the clusters have been already examined in previous studies. Here, we evaluate the performance of our setup by comparing with the reported spectra. Figures 3.13 and 3.14 show IR spectra of $H^+(H_2O)_n$ ($n \leq 32$) in the OH stretching region. These spectra were measured by monitoring $H^+(H_2O)_{n-1}$ fragment intensity. The spectra presented here are in agreement with those reported previously [30, 33, 35, 38], indicating the validity of our measurements. These figures are first ones in which all the IR spectra of the broad IR region have been compiled. In IR spectra, remarkable size-dependence can be seen in $n < \sim 10$, while $n > \sim 10$ spectra show relatively similar features. Structural aspects of these clusters are well understood from the free OH stretching region, in which clearer, well-resolved spectral structures can be seen. Figure 3.15 presents expanded IR spectra of $H^+(H_2O)_n$ ($n \leq 32$) in the free OH stretching region. Visual guides in orange, blue, and red indicate bands of 1-, 2-, and 3-coordinated water molecules, respectively. As introduced in Fig. 3.2, disappearance of 1-coordinated water bands can be observed at $n \sim 10$. Drastic decrease of 2-coordinated water bands can also be seen at $n = 21$, showing reported
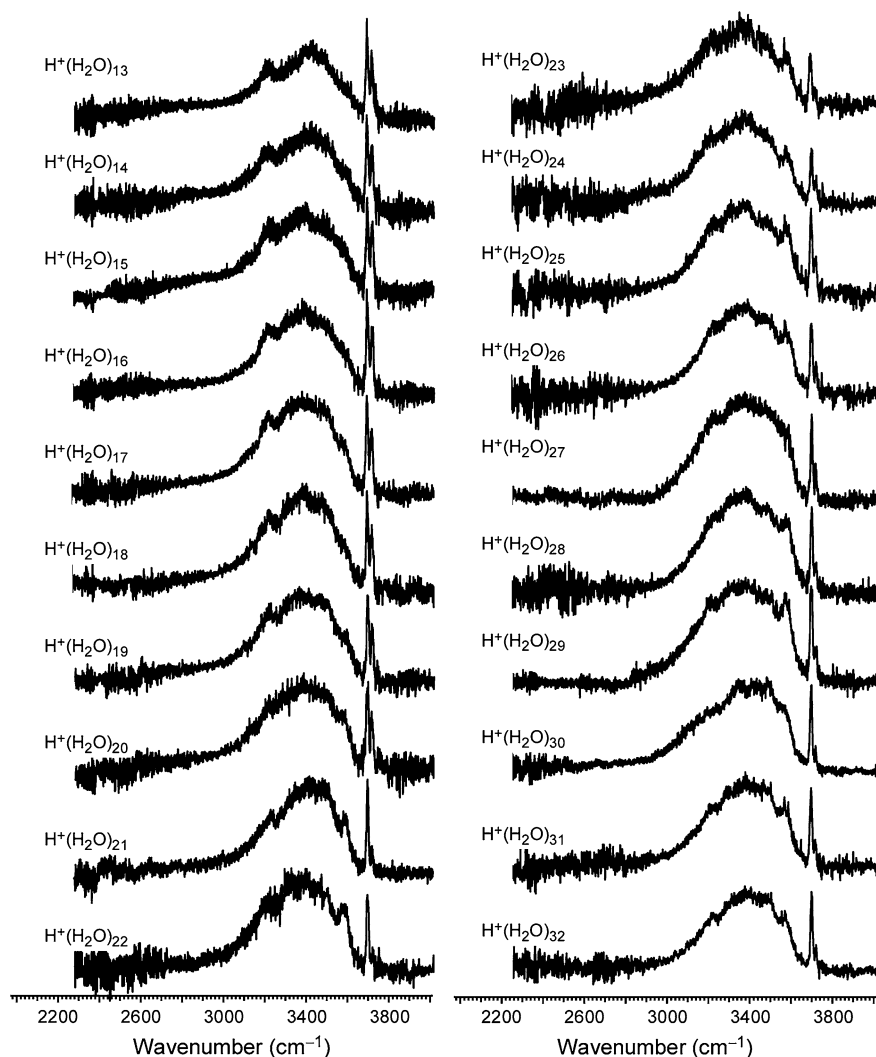
Fig. 3.13 IR spectra of
$H^+(H_2O)_n$ ($n = 3$–12) in the
OH stretching region
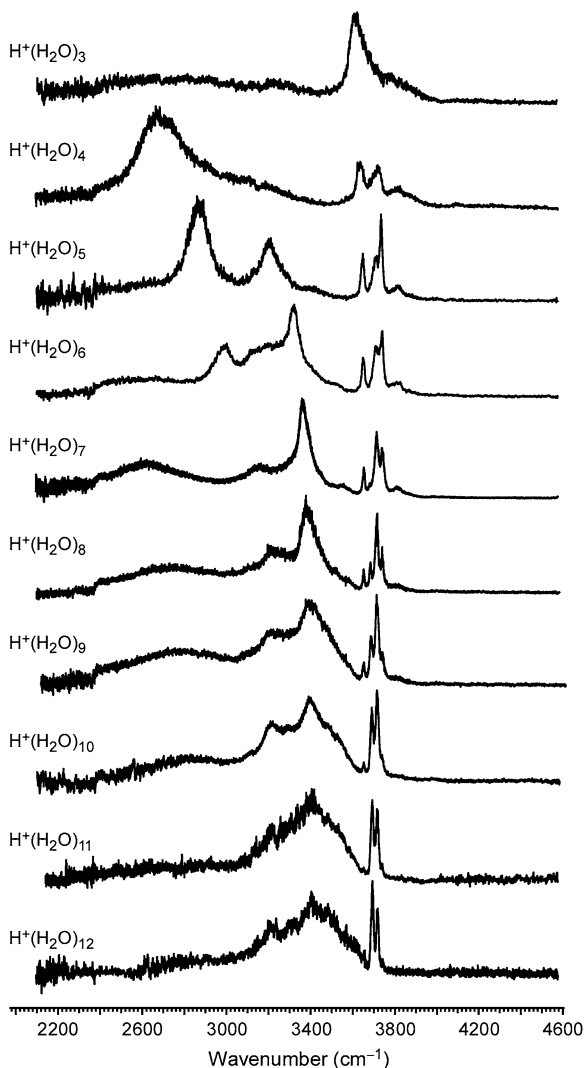
magic number behavior. Detailed discussions on structures and spectra of small
clusters ($n \leq 8$) and magic/antimagic number features on the basis of further
experiments will be given in Chap. 4.

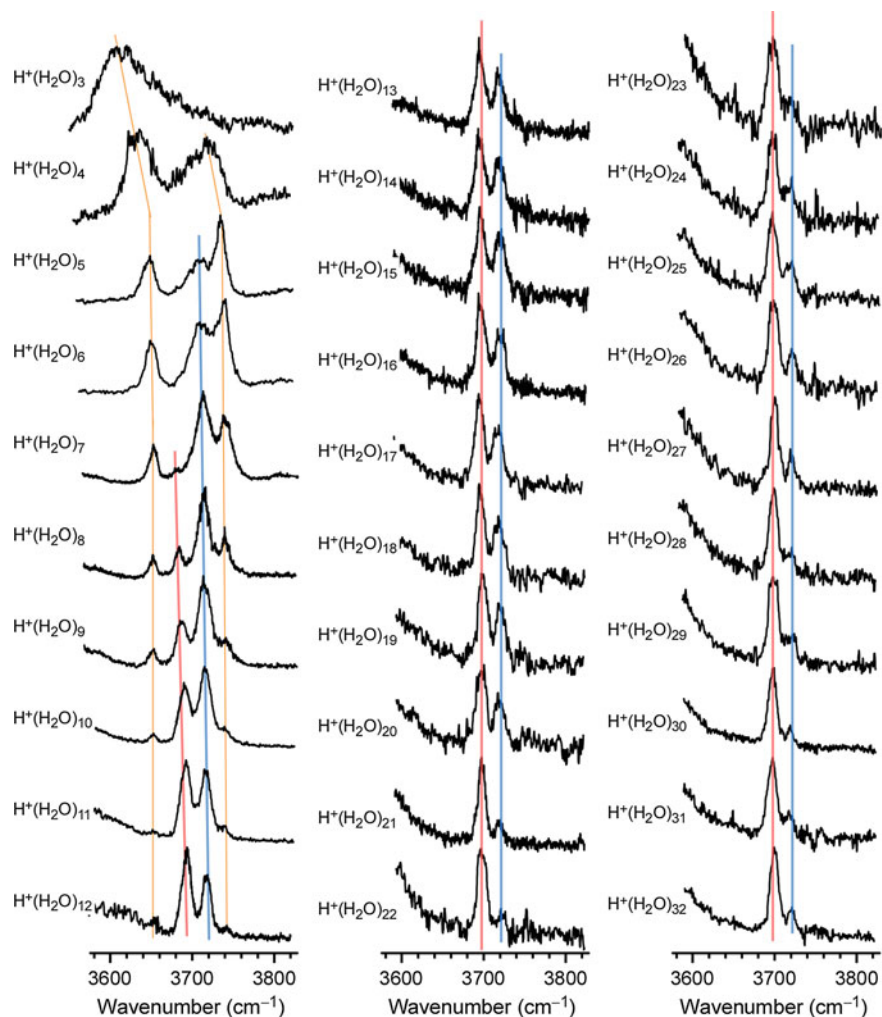## 3.3.2 IR Spectra of $H^+(H_2O)_n$ ($n = 20$–221)

Here we focus on the spectra and structural trends of larger clusters. We noted that
it is difficult to measure IR spectra of larger clusters by monitoring $H^+(H_2O)_{n-m}$
fragments, as shown in Sect. 3.2.3, and therefore, depletion of $H^+(H_2O)_n$ was

Fig. 3.14 IR spectra of $H^+(H_2O)_n$ ($n = 13$–32) in the OH stretching region

probed. Figure 3.16 compares spectra obtained with $H^+(H_2O)_n$ and $H^+(H_2O)_{n-1}$ intensities. Both series show similar spectral features. Depletion measurements led to a better signal to noise ratio, due to the high stability of our cluster ion source while the larger time-fluctuation of metastable backgrounds affects spectra in the $H^+(H_2O)_{n-1}$ channel.

Figure 3.17 shows precisely measured size-selective IR spectra of $H^+(H_2O)_n$ ($n = 20$–221) in the OH stretch region. Depths of cluster ion depletion, caused by the vibrational predissociation, have been plotted as a function of the IR

Fig. 3.15 Expanded IR spectra of $H^+(H_2O)_n$ ($n = 3$–32) in the free OH stretching region. Visual guides in orange, blue, and red indicate bands of 1-, 2-, and 3-coordinated water molecules, respectively

wavenumber. Better signal to noise ratio even though cluster yields of these sizes are less than those of smaller clusters. The spectra of $H^+(H_2O)_{20,\,21}$ are similar to those of reported previously. Bands at around 3,700 and 3,720 cm^{-1} are assigned to the free OH stretches of 3-coordinated and 2-coordinated water molecules, respectively. Broad bands below 3,600 cm^{-1} were hydrogen-bonded OH stretches. As is in the previous studies, the 2-coordinated water band was much weaker than the 3-coordinated band in $n \geq 21$ clusters. By comparison with the previous IR

(a) Depletion of H$^+$(H$_2$O)$_n$ **(b)** Enhancement of H$^+$(H$_2$O)$_{n-1}$ Fragment
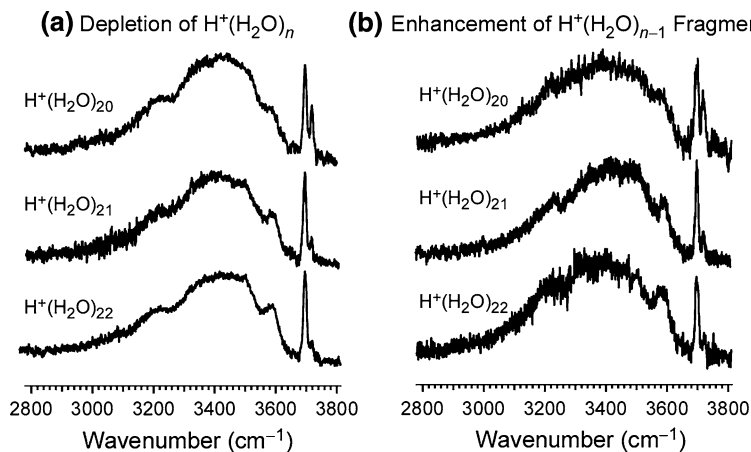
Fig. 3.16 Comparison between (**a**) IR photodissociation spectra measured by monitoring target H$^+$(H$_2$O)$_n$ ion intensity and (**b**) those measured by monitoring H$^+$(H$_2$O)$_{n-1}$ fragment intensity. In the spectra in (**a**), depletion depths are plotted

study on H$^+$(H$_2$O)$_{21}$ formed under various conditions and theoretical studies, we estimate that clusters observed here have finite vibrational temperatures of 150–200 K. The temperature (internal energy) effect will be addressed in Chap. 4.

3.4 Discussion

3.4.1 On the 4-Coordinated Water Band

The observed free OH band behavior (almost a singlet feature due to the 3-coordinated water) shows that closed cage (neither chain nor net) networks are maintained at least up to $n = 221$ and that the clusters of $n \geq 21$ consist mainly of 3- or 4-coordinated waters. In large-sized clusters, the free OH band is attributed only to 3-coordinated waters, while the hydrogen-bonded OH band can be attributed to 3- and 4-coordinated waters. As clearly seen in Fig. 3.17, the relative intensity of the free OH band decreases with increasing cluster size. This means that 4-coordinated water becomes dominant in larger clusters.

For detailed investigation of the band position of 4-coordinated waters, we carried out density functional theory calculations at the B3LYP/6-31+G(d) level. We calculated structures and their IR spectra for H$^+$(H$_2$O)$_{60}$ as a typical example of large-sized clusters. First, we constructed clusters consisting only of 3-coordinated waters. In this case, a buckyball-like hollow cage structure (Fig. 3.18b) is a possible structure, as Ludwig and Appelhagen have introduced for (H$_2$O)$_{60}$ [105]. Its simulated spectrum shows almost flat intensity distribution in the 2,950–3,550 cm^{-1} region and it clearly disagrees with the experimental data. Such
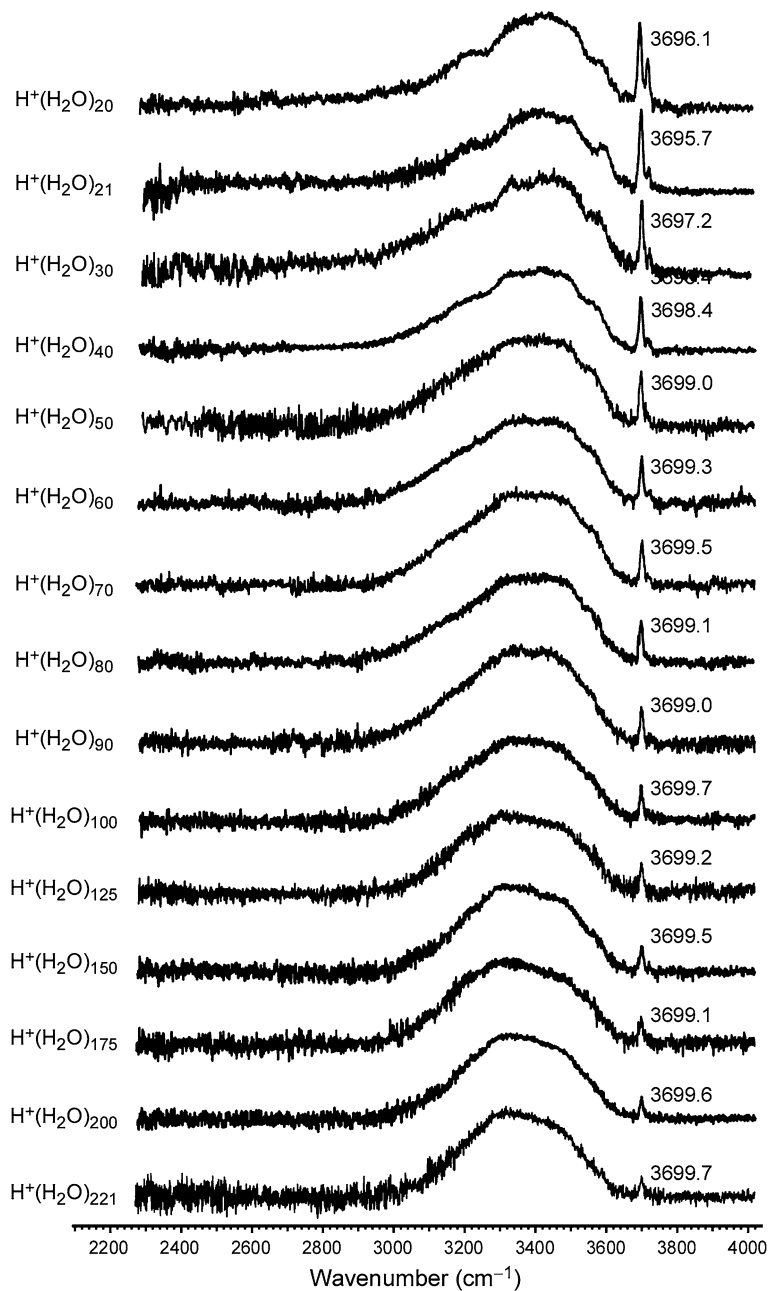
Fig. 3.17 IR photodissociation spectra of $H^+(H_2O)_n$ ($n = 20$–221) in the OH stretch region [67]. These spectra were measured by monitoring the depletion of the size-selected cluster ions of interest due to the vibrational predissociation. Depletion depths are plotted. Peak positions of free OH bands are indicated in cm^{-1}

disagreement implies that the contribution of 4-coordinated waters is necessary to reproduce the observed spectrum.

Then, we calculated two model structures having 18 and 32 waters in 4-coordinated sites, respectively (Fig. 3.18c, d). The corresponding spectra (black curves in Fig. 3.18c, d) are in better agreement with the experimental one. In these spectra, we decomposed bands into the contributions of the 3- and 4-coordinated waters according to the method shown in Sect. 2.2.4.2. In Fig. 3.18c, d, the curves in blue and red indicate the spectral contribution of the 3- and 4-coordinated water molecules, respectively. The 3-coordinated bands are similar to those in Fig. 3.2b, which is the "pure" 3-coordinated water spectrum. On the other hand, the 4-coordinated bands have a narrower intensity distribution, which has a maximum in the 3,300–3,400 cm^{-1} region. These analyses agree with our expectation that 4-coordinated water contributes to experimental spectra, which also have a maximum in the 3,300–3,400 cm^{-1} region. Of course, the observed spectrum is attributed to an ensemble of many structural isomers. In addition, the calculated structures are not necessarily spectral carriers. As a
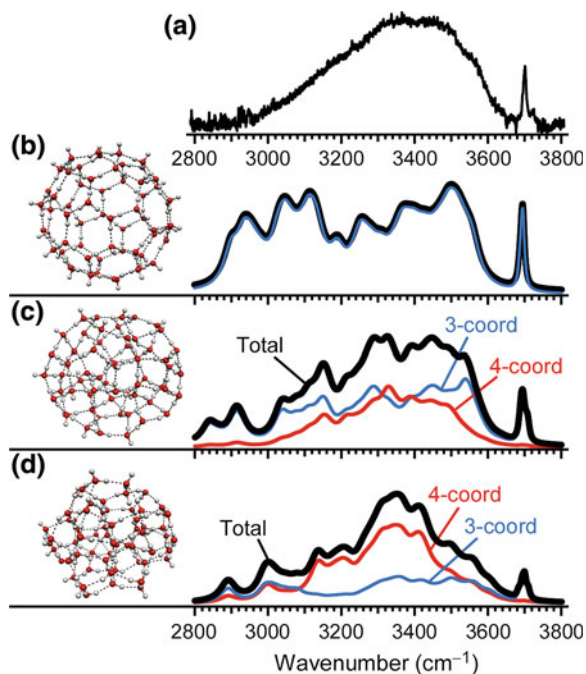
Fig. 3.18 a Experimental spectra of $H^+(H_2O)_{60}$. **b–d** Calculated model cluster structures of $H^+(H_2O)_{60}$ and their IR spectra obtained at B3LYP/6-31+G(d) with the scale factor of 0.9736. Curves in *blue* and *red* indicate decomposition of the spectra to 3- and 4-coordinated water molecules, respectively. Curves in black indicate the simulated spectra due to the sum of each component. To simulate spectra, Lorentzian functions of 10 and 50 cm^{-1} full widths at half maxima were used for free and hydrogen-bonded OH stretches, respectively. Reproduced from Ref. [67] after minor changes (Copyright 2010 John Wiley and Sons)

qualitative trend, however, the good agreement between the observed and calculated spectra can be seen, and it demonstrates that the contribution of 4-coordinated water is essential to reproduce the band shape in the observed spectrum.

Here, it should be noted that IR spectra of $H^+(H_2O)_{20,21}$, in which the 4-coordinated band has not been discussed, also show similar band shapes to that of $H^+(H_2O)_{60}$. This fact suggests that even with these smaller-sized clusters, at least $H^+(H_2O)_{n \geq 21}$ also contains 4-coordinated waters. (For $H^+(H_2O)_{n \leq 20}$, situations are complicated because quite a few 2-coordinated waters exist and their contribution to the IR band is expected to be overlapped by the 4-coordinated band.) As for $H^+(H_2O)_{21}$, reported structure is a dodecahedral cage enclosing one water molecule (Fig. 3.19). In such a structure, one interior and four surrounding water molecules are 4-coordinated. The band shape analysis for $H^+(H_2O)_{21}$ (Fig. 3.19) agrees with this structure.
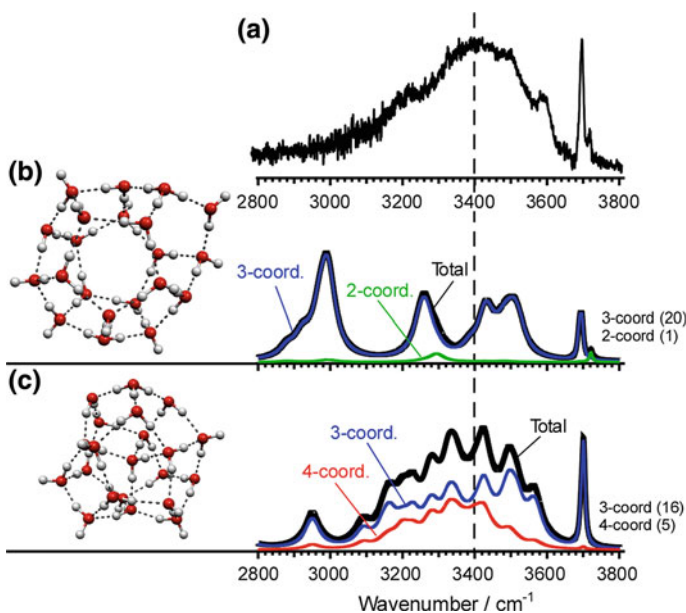
Fig. 3.19 a Experimental spectra of $H^+(H_2O)_{21}$. **b, c** Calculated model cluster structures of $H^+(H_2O)_{21}$ and their IR spectra obtained at B3LYP/6-31+G(d) with the scale factor of 0.9736. Structure (**b**) is a hollow cage (all-surface type). Structure (**c**) contains an interior water molecule. Curves in *green*, *blue*, and *red* indicate decomposition of the spectra to 2-, 3-, and 4-coordinated water molecules, respectively. Curves in *black* indicate the simulated spectra due to the sum of each component. The *dashed line* is a visual guide. Reproduced from Ref. [67] (Copyright 2010 John Wiley and Sons)
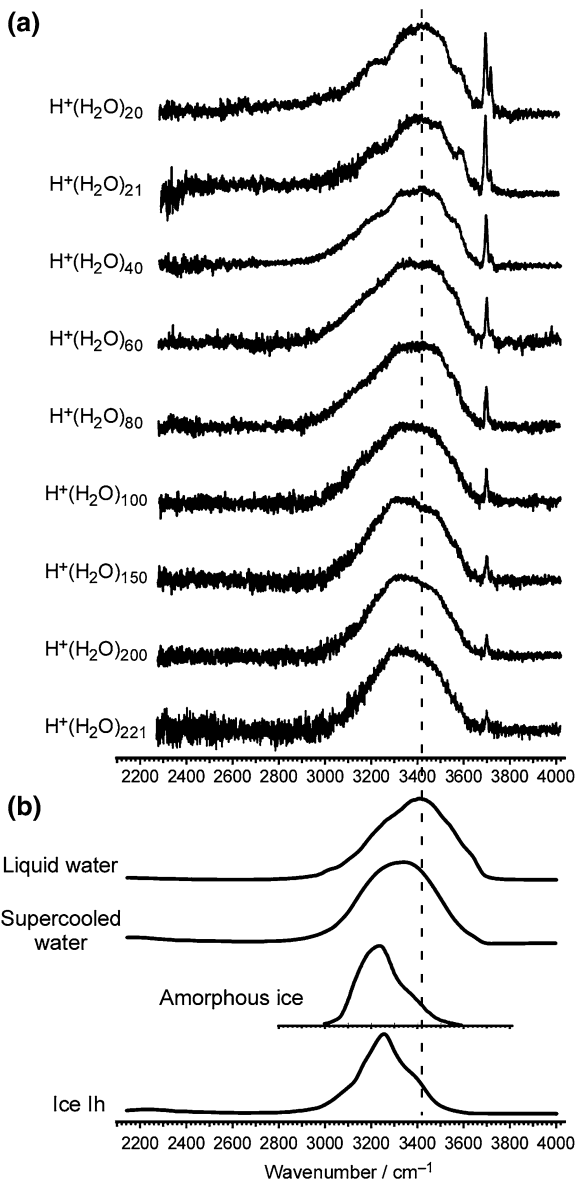
3.4.2 Structural Trends of Large Clusters

In addition to the consideration of coordination numbers, hydrogen-bonded network structures should also be discussed. In the experimental IR spectra (Fig. 3.17), the low-frequency shift of the hydrogen-bonded band can be observed with increasing cluster size. To interpret these results, we compared the spectra with those of bulk water and water surface.

Figure 3.20 compares experimental IR spectra of $H^+(H_2O)_n$ and previously reported IR spectra of liquid water, supercooled water, amorphous ice, and hexagonal ice [1, 106, 107]. Although free OH bands are absent in the bulk spectra, hydrogen-bonded bands of the $n \leq \sim 60$ clusters are similar to that of liquid water in their absorption maxima and band centers. On the other hand, in larger clusters, the maximum and center of the band have been shifted to $\sim 3,300$ cm^{-1}, thereby getting closer to supercooled water, amorphous ice, and hexagonal ice. Hexagonal ice has a crystal structure consisting only of 4-coordinated water, and it is supposed that supercooled water has partially ordered (crystalline) networks [108]. Amorphous ice does lack for such a long-range hydrogen bond order as ice Ih but it contains shorter-range order. These results, then, suggest that $H^+(H_2O)_n$ forms liquid-like, disordered structures in smaller-sized ($n \leq$ tens), while they form at least partially crystalline (ordered) structures in larger-sized clusters ($n \geq \sim 100$). Because the number of hydrogen bonds is not maximized in hexagonal crystalline structures, tens or smaller-sized clusters favor 4- or 5-membered ring motifs. Hexagonal networks (6-membered ring motifs) have an advantage in constructing larger, more ordered networks. Note that the development of 4-membered ring motifs is inherently limited to one direction (fused-cubic structures only) [109], and it is difficult to avoid defects in constructing the large-scaled networks consisting only of 5-menbered rings. Based on these discussions, we suggest that formation of ordered (crystalline) structures occurs in large-sized $H^+(H_2O)_n$ clusters of hundreds of water molecules. Such formation of a crystalline core in large-sized clusters has been predicted by theoretical research for low-energy structures and IR spectroscopy of average size-controlled clusters [2], and the present results are consistent with these previous studies.

For further support of the correlation of the ordering (crystallization) and low-frequency shift of the OH stretch band, we carried out semi-empirical calculations for two isomers of $H^+(H_2O)_{200}$ (Fig. 3.21). One of the isomers (Fig. 3.21b) has crystalline network moieties while the other one (Fig. 3.21a) does not. In their simulated IR spectra, the lowest frequency absorption maximum is expected for the isomer possessing crystalline networks. Although our calculations were preliminary ones, this is in agreement with the above discussion.

(a)

H$^+$(H$_2$O)$_{20}$

H$^+$(H$_2$O)$_{21}$

H$^+$(H$_2$O)$_{40}$

H$^+$(H$_2$O)$_{60}$

H$^+$(H$_2$O)$_{80}$

H$^+$(H$_2$O)$_{100}$

H$^+$(H$_2$O)$_{150}$

H$^+$(H$_2$O)$_{200}$

H$^+$(H$_2$O)$_{221}$

2200 2400 2600 2800 3000 3200 3400 3600 3800 4000

(b)

Liquid water

Supercooled water

Amorphous ice

Ice Ih

2200 2400 2600 2800 3000 3200 3400 3600 3800 4000

Wavenumber / cm^{-1}

3.4.3 Further Discussions

In Chap. 2, we showed that free OH stretching frequency is a good way to conduct a probe of hydrogen-bond network structures. Here we comment on the observed free OH frequencies. Figure 3.22 shows the plot of the free OH stretch frequencies as a function of the cluster size. In the region of $n \leq \sim 60$, free OH frequencies
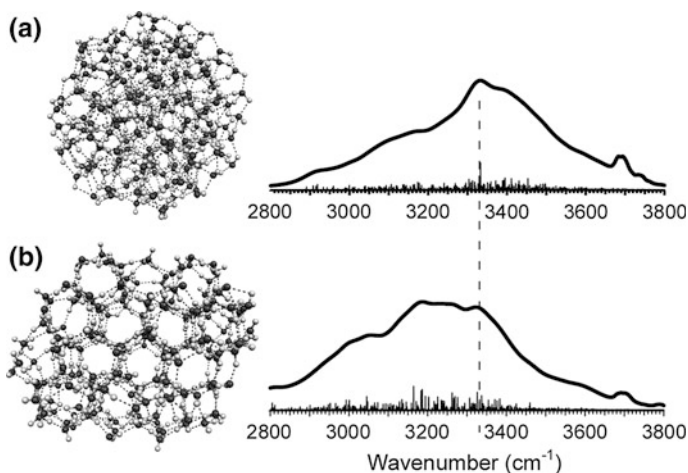
Fig. 3.21 Calculated cluster structures of $H^+(H_2O)_{200}$ and their IR spectra obtained at PM6 with the scale factor of 1.44. Structure (**b**), which has crystalline network moieties shows lower frequency absorption maximum. The *dashed line* is a visual guide

Fig. 3.22 The size-dependent free OH frequencies of $H^+(H_2O)_n$ (*filled circles*) compared with those of phenol-$(H_2O)_{n-1}$ (*open squares*), benzene-$(H_2O)_8$ (*filled square*) [112], $(H_2O)_{<n>}$ (*open triangles*) [111], and condensed phase liquid water and water ice (*open circle*). Reproduced from Ref. [67] (Copyright 2010 John Wiley and Sons)
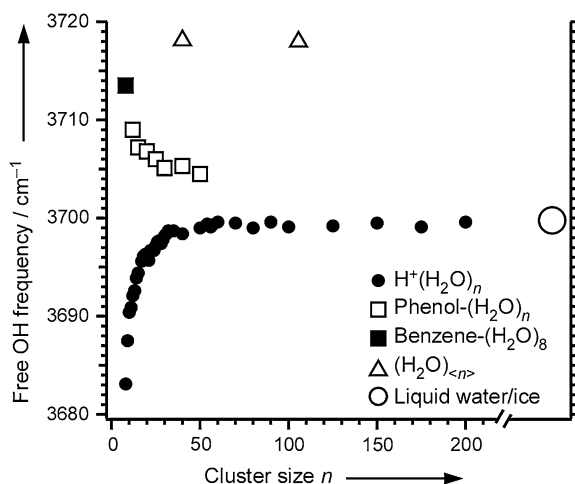
show a clear high-frequency shift, while the frequency becomes constant in the larger-sized region. Because the lower free OH frequency is generally expected when surrounding hydrogen bonds are stronger [109, 110], the high-frequency shift in Fig. 3.22 shows the weakening of hydrogen bonds in the networks. The strength of hydrogen bonds in $H^+(H_2O)_n$ clusters is enhanced by the charge of the excess proton. This shift, then, is accounted for by the dilution process of the effect of the excess proton. The frequency seems to have converged on 3,699–3,700 cm^{-1}. In the previous study on $H^+(H_2O)_n$, due to the fact that the OH frequency of

$3{,}699$–$3{,}700$ cm^{-1} is much lower than the previously reported value of $(H_2O)_{<n>=40,111}$ ($<n>$: average size, Fig. 3.22), $\sim 3{,}718$ cm^{-1} [111], it has been suggested that an excess proton affects hydrogen bonded network structures even in large-sized clusters [99]. For more accurate data on the free OH frequency of large-sized neutral water clusters, we can use free OH frequencies of phenol-$(H_2O)_n$ clusters, in which the perturbation from the phenol is negligible (Chap. 2) [109]. Figure 3.22 shows free OH frequency of phenol-$(H_2O)_{n-1}$ (and benzene-$(H_2O)_8$ [112]) approaches that of $H^+(H_2O)_n$ at least in $n \leq \sim 50$ region, meaning that structures of $H^+(H_2O)_n$ are more similar to $(H_2O)_n$ than expected previously. As support for this argument, Fig. 3.23 compares IR spectra of phenol-$(H_2O)_{49}$ and $H^+(H_2O)_{50}$. Both spectra show similar spectral features implying similar structures.

The free OH band is also detectable in condensed-phase liquid water and ice surfaces by using sum-frequency generation (SFG) spectroscopy and IR reflection–absorption spectroscopy (IRRAS) [113–116]. The reported value for liquid water and ice is at $\sim 3{,}700$ cm^{-1} (Fig. 3.22). From the fact that this value is essentially the same as that of large-sized $H^+(H_2O)_n$, it is suggested that the surface structure of the large-sized clusters is comparable to those of condensed-phase water and ice. This is in contrast to the average size-controlled study on large-sized $(H_2O)_{<n>}$ clusters ($<n> < 10^6$), in which free OH frequencies are converged to $\sim 3{,}692$ cm^{-1} [2]. One possible cause of this difference is the lower temperature of neutral $(H_2O)_{<n>}$, cooled in the cell of 4.2–140 K [2]. $H^+(H_2O)_n$ are estimated to have higher temperatures (~ 150–200 K) [38, 117, 118], and this temperature range is much closer to that used in condensed phase experiments.

Some very recent studies reported after our publications require a response from us. Pradzynski et al. [119] have reported IR spectra of size-selected Na-doped water clusters $Na(H_2O)_n$ ($n = 85$–475) by using UV single photon ionization-based detection. According to the frequency shift as analyzed in this study, they concluded the onset of crystallization is about $n = 275$ [119]. O'Brien and Williams [120] have reported ensemble size-selected M-$(H_2O)_{n \sim 250}$ (M = SO_4^{2-}, I$^-$, Na$^+$, Ca^{2+}, and La^{3+}). They analyzed free OH frequencies and concluded that singly charged ions do not strongly affect the water networks. These conclusions are basically in agreement with our findings. For a more detailed comparison,

Fig. 3.23 Comparison of IR spectra of (**a**) phenol-$(H_2O)_{49}$ and (**b**) $H^+(H_2O)_{50}$
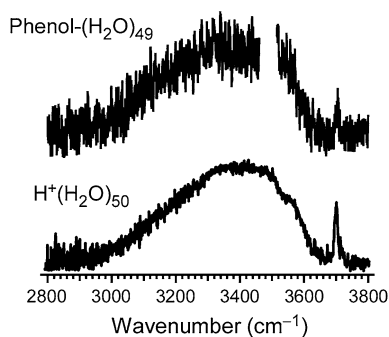
Fig. 3.24 Comparison between the previously reported IR spectra of other cluster ions and the present $H^+(H_2O)_{221}$. The top spectrum is reproduced from Ref. [119] (Copyright 2012 American Association for the Advancement of Science). The middle spectrum is reproduced from Ref. [120] (Copyright 2012 American Chemical Society)
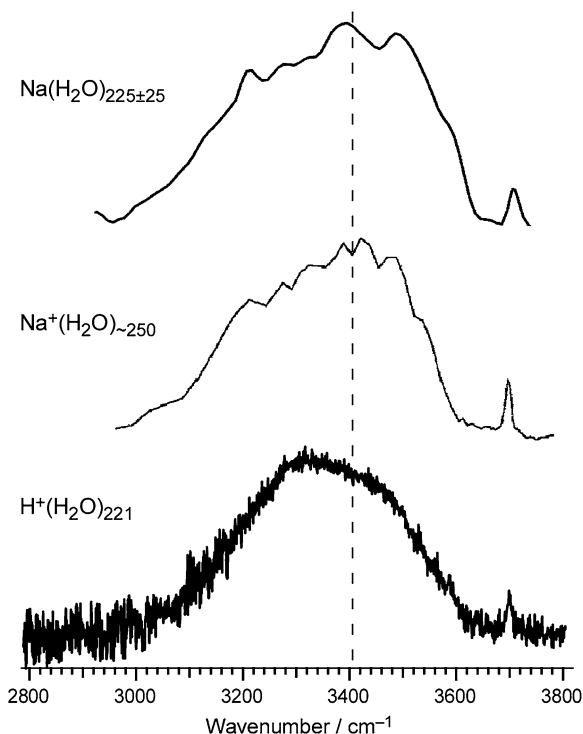
Fig. 3.24 compares these reported spectra and the present results. In Fig. 3.24, the absorption maxima of $Na(H_2O)_n$ and $Na^+(H_2O)_n$ are quite similar ($\sim 3,400$ cm^{-1}). On the other hand, the spectrum of $H^+(H_2O)_{221}$ shows a maximum at $\sim 3,300$ cm^{-1}. If this result is simply interpreted, crystallization of $H^+(H_2O)_n$ occurs from a smaller size than $Na(H_2O)_n$ and $Na^+(H_2O)_n$. Of course, it is possible that dopant (ion) effects on the water network ordering are different from each other. Furthermore, cluster condition (temperature) should be an important factor to discuss in the crystallization process. Further studies are necessary, with the present study and following studies opening the door to more systematic studies in such complicated, large-scale water networks.

3.5 Conclusion

In studying large-scale hydrogen-bonded water network structures, we have succeeded in measuring the IR spectra of the precisely size-selected protonated water clusters $H^+(H_2O)_n$ up to the hitherto uncovered size of $n = 221$. In IR spectra, we identified the 4-coordinated and 3-coordinated water bands. We also showed that the abundance of 4-coordinated waters gradually increases with increasing cluster

size. In the interior of the clusters, as has been seen in the size-averaged $(H_2O)_{<n>}$ studies [2, 121], the implication of network ordering (crystallization) was observed. The free OH frequency suggests that the surface structures of the large-sized clusters are similar to those of liquid water and ice. The observed spectra, in addition to recently reported spectra for large water clusters, are expected to be a benchmark for studies concerning large-scale hydrogen-bonded networks involving hundreds of water molecules.

References

1. M.S. Bergren, D. Schuh, M.G. Sceats, S.A. Rice, J. Chem. Phys. **69**, 3477 (1978)
2. V. Buch, S. Bauerecker, J.P. Devlin, U. Buck, J.K. Kazimirski, Int. Rev. Phys. Chem. **23**, 375–433 (2004)
3. M. Okumura, L.I. Yeh, Y.T. Lee, J. Chem. Phys. **83**, 3705–3706 (1985)
4. M. Okumura, L.I. Yeh, J.D. Myers, Y.T. Lee, J. Chem. Phys. **85**, 2328–2329 (1986)
5. J.M. Price, M.W. Crofton, Y.T. Lee, J. Chem. Phys. **91**, 2749–2751 (1989)
6. L.I. Yeh, M. Okumura, J.D. Myers, J.M. Price, Y.T. Lee, J. Chem. Phys. **91**, 7319–7330 (1989)
7. J.M. Lisy, J. Chem. Phys. **125**, 132302 (2006)
8. J.J. Valle, J.R. Eyler, J. Oomens, D.T. Moore, A.F.G. van der Meer, G. von Helden, G. Meijer, C.L. Hendrickson, A.G. Marshall, G.T. Blakney, Rev. Sci. Instrum. **76**, 023103 (2005)
9. L. MacAleese, P. Maître, Mass Spectrom. Rev. **26**, 583–605 (2007)
10. J. Oomens, B.G. Sartakov, G. Meijer, G. von Helden, Int. J. Mass Spectrom. **254**, 1–19 (2006)
11. P. Ayotte, M.A. Johnson, J. Chem. Phys. **106**, 811–814 (1997)
12. D.S. Cornett, M. Peschke, K. LaiHing, P.Y. Cheng, K.F. Willey, M.A. Duncan, Rev. Sci. Instrum. **63**, 2177 (1992)
13. O.V. Boyarkin, S.R. Mercier, A. Kamariotis, T.R. Rizzo, J. Am. Chem. Soc. **128**, 2816–2817 (2006)
14. T. Maeyama, T. Tsumura, A. Fujii, N. Mikami, Chem. Phys. Lett. **264**, 292–296 (1997)
15. C.E.H. Dessent, J. Kim, M.A. Johnson, Acc. Chem. Res. **31**, 527–534 (1998)
16. M. Okumura, L.I. Yeh, J.D. Myers, Y.T. Lee, J. Phys. Chem. **94**, 3416–3427 (1990)
17. M. Okumura, L.I. Yeh, Y.T. Lee, J. Chem. Phys. **88**, 79–91 (1988)
18. J.M. Price, M.W. Crofton, Y.T. Lee, J. Phys. Chem. **95**, 2182–2195 (1991)
19. W.H. Robertson, M.A. Johnson, Annu. Rev. Phys. Chem. **54**, 173–213 (2003)
20. M.A. Duncan, Int. Rev. Phys. Chem. **22**, 407–435 (2003)
21. E.J. Bieske, O. Dopfer, Chem. Rev. **100**, 3963–3998 (2000)
22. O. Dopfer, Z. Phys. Chem. **219**, 125–168 (2005)
23. N.C. Polfer, J. Oomens, Mass Spectrom. Rev. **28**, 468–494 (2009)
24. T. Rizzo, J. Stearns, O. Boyarkin, Int. Rev. Phys. Chem. **28**, 481–515 (2009)
25. K.R. Asmis, D.M. Neumark, Acc. Chem. Res. **45**, 43–52 (2011)
26. H.C. Chang, J.C. Jiang, Y.S. Wang, S.H. Lin, Y.T. Lee, J. Chin. Chem. Soc. **46**, 427–434 (1999)
27. J.C. Jiang, Y.S. Wang, H.C. Chang, S.H. Lin, Y.T. Lee, G. Niedner-Schatteburg, J. Am. Chem. Soc. **122**, 1398–1410 (2000)
28. Y.S. Wang, C.H. Tsai, Y.T. Lee, H.C. Chang, J.C. Jiang, O. Asvany, S. Schlemmer, D. Gerlich, J. Phys. Chem. A **107**, 4217–4225 (2003)
29. L.I. Yeh, Y.T. Lee, J.T. Hougen, J. Mol. Spectrosc. **164**, 473–488 (1994)

30. J.W. Shin, N.I. Hammer, E.G. Diken, M.A. Johnson, R.S. Walters, T.D. Jaeger, M.A. Duncan, R.A. Christie, K.D. Jordan, Science **304**, 1137–1140 (2004)
31. N.I. Hammer, E.G. Diken, J.R. Roscioli, M.A. Johnson, E.M. Myshakin, K.D. Jordan, A.B. McCoy, X. Huang, J.M. Bowman, S. Carter, J. Chem. Phys. **122**, 244301 (2005)
32. J.M. Headrick, E.G. Diken, R.S. Walters, N.I. Hammer, R.A. Christie, J. Cui, E.M. Myshakin, M.A. Duncan, M.A. Johnson, K.D. Jordan, Science **308**, 1765–1769 (2005)
33. G.E. Douberly, A.M. Ricks, M.A. Duncan, J. Phys. Chem. A **113**, 8449–8453 (2009)
34. G.E. Douberly, R.S. Walters, J. Cui, K.D. Jordan, M.A. Duncan, J. Phys. Chem. A **114**, 4570–4579 (2010)
35. M. Miyazaki, A. Fujii, T. Ebata, N. Mikami, Science **304**, 1134–1137 (2004)
36. K.R. Asmis, N.L. Pivonka, G. Santambrogio, B. Brümmer, C. Kaposta, D.M. Neumark, L. Wöste, Science **299**, 1375–1377 (2003)
37. H.C. Chang, C.C. Wu, J.L. Kuo, Int. Rev. Phys. Chem. **24**, 553–578 (2005)
38. C.-C. Wu, C.-K. Lin, H.-C. Chang, J.-C. Jiang, J.-L. Kuo, M.L. Klein, J. Chem. Phys. **122**, 074315 (2005)
39. H.C. Chang, Y.S. Wang, Y.T. Lee, Int. J. Mass Spectrom. **180**, 91–102 (1998)
40. Y.S. Wang, H.C. Chang, J.C. Jiang, S.H. Lin, Y.T. Lee, J. Am. Chem. Soc. **120**, 8777–8788 (1998)
41. E.G. Diken, N.I. Hammer, M.A. Johnson, R.A. Christie, K.D. Jordan, J. Chem. Phys. **123**, 164309 (2005)
42. J.A. Kelley, G.H. Weddle, W.H. Robertson, M.A. Johnson, J. Chem. Phys. **116**, 1201–1203 (2002)
43. N.I. Hammer, J.W. Shin, J.M. Headrick, E.G. Diken, J.R. Roscioli, G.H. Weddle, M.A. Johnson, Science **306**, 675–679 (2004)
44. E.G. Diken, J.M. Headrick, J.R. Roscioli, J.C. Bopp, M.A. Johnson, A.B. McCoy, J. Phys. Chem. A **109**, 1487–1490 (2005)
45. N.I. Hammer, J.R. Roscioli, J.C. Bopp, J.M. Headrick, M.A. Johnson, J. Chem. Phys. **123**, 244311 (2005)
46. N.I. Hammer, J.R. Roscioli, M.A. Johnson, J. Phys. Chem. A **109**, 7896–7901 (2005)
47. N.I. Hammer, J.R. Roscioli, M.A. Johnson, E.M. Myshakin, K.D. Jordan, J. Phys. Chem. A **109**, 11526–11530 (2005)
48. J.R. Roscioli, N.I. Hammer, M.A. Johnson, J. Phys. Chem. A **110**, 7517–7520 (2006)
49. K.R. Asmis, G. Santambrogio, J. Zhou, E. Garand, J. Headrick, D. Goebbert, M.A. Johnson, D.M. Neumark, J. Chem. Phys. **126**, 191105 (2007)
50. J.R. Roscioli, M.A. Johnson, J. Chem. Phys. **126**, 024307 (2007)
51. L.R. McCunn, G.H. Gardenier, T.L. Guasco, B.M. Elliott, J.C. Bopp, R.A. Relph, M.A. Johnson, J. Chem. Phys. **128**, 234311 (2008)
52. J.R. Roscioli, N.I. Hammer, M.A. Johnson, K. Diri, K.D. Jordan, J. Chem. Phys. **128**, 104314 (2008)
53. R.S. Walters, M.A. Duncan, Aust. J. Chem. **57**, 1145–1148 (2004)
54. R.S. Walters, E.D. Pillai, M.A. Duncan, J. Am. Chem. Soc. **127**, 16599–16610 (2005)
55. T.D. Vaden, J.M. Lisy, P.D. Carnegie, E. Dinesh Pillai, M.A. Duncan, Phys. Chem. Chem. Phys. **8**, 3078 (2006)
56. S.E. Rodriguez-Cruz, R.A. Jockusch, E.R. Williams, J. Am. Chem. Soc. **120**, 5842–5843 (1998)
57. M.F. Bush, R.J. Saykally, E.R. Williams, J. Am. Chem. Soc. **130**, 15482–15489 (2008)
58. J.S. Prell, T.G. Flick, J. Oomens, G. Berden, E.R. Williams, J. Phys. Chem. A **114**, 854–860 (2009)
59. J.S. Prell, E.R. Williams, J. Am. Chem. Soc. **131**, 4110–4119 (2009)
60. M. Eigen, L. de Maeyer, Proc. R. Soc. London, Ser. A **247**, 505–533 (1958)
61. M. Eigen, Angew. Chem. Int. Ed. **3**, 1–19 (1964)
62. R. Janoschek, E.G. Weidemann, H. Pfeiffer, G. Zundel, J. Am. Chem. Soc. **94**, 2387–2396 (1972)
63. N. Agmon, Chem. Phys. Lett. **244**, 456–462 (1995)

64. D. Marx, M.E. Tuckerman, J. Hutter, M. Parrinello, Nature **397**, 601–604 (1999)
65. C.J.T. de Grotthuss, Biochim. Biophys. Acta **1757**, 871–875 (2006)
66. D. Marx, Chem. Phys. Chem. **7**, 1848–1870 (2006)
67. K. Mizuse, N. Mikami, A. Fujii, Angew. Chem. Int. Ed. **49**, 10119–10122 (2010)
68. S–.S. Lin, Rev. Sci. Instrum. **44**, 516–517 (1973)
69. J.Q. Searcy, J.B. Fenn, J. Chem. Phys. **61**, 5282–5288 (1974)
70. H.R. Carlon, C.S. Harden, Appl. Opt. **19**, 1776–1786 (1980)
71. O. Echt, D. Kreisle, M. Knapp, E. Recknagel, Chem. Phys. Lett. **108**, 401–407 (1984)
72. H. Shinohara, U. Nagashima, N. Nishi, Chem. Phys. Lett. **111**, 511–513 (1984)
73. U. Nagashima, H. Shinohara, N. Nishi, H. Tanaka, J. Chem. Phys. **84**, 209–214 (1986)
74. X. Yang, A.W. Castleman, J. Am. Chem. Soc. **111**, 6845–6846 (1989)
75. T.F. Magnera, D.E. David, J. Michl, Chem. Phys. Lett. **182**, 363–370 (1991)
76. S. Wei, Z. Shi, J.A.W. Castleman, J. Chem. Phys. **94**, 3268–3270 (1991)
77. N.F. Dalleska, K. Honma, P.B. Armentrout, J. Am. Chem. Soc. **115**, 12125–12131 (1993)
78. Z. Shi, J.V. Ford, S. Wei, J.A.W. Castleman, J. Chem. Phys. **99**, 8009–8015 (1993)
79. T. Schindler, C. Berg, G. NiednerSchatteburg, V.E. Bondybey, Chem. Phys. Lett. **250**, 301–308 (1996)
80. K. Hansen, P.U. Andersson, E. Uggerud, J. Chem. Phys. **131**, 124303 (2009)
81. A.W. Castleman, K.H. Bowen, J. Phys. Chem. **100**, 12911–12944 (1996)
82. G. Niedner-Schatteburg, V.E. Bondybey, Chem. Rev. **100**, 4059–4086 (2000)
83. V.E. Bondybey, M.K. Beyer, Int. Rev. Phys. Chem. **21**, 277–306 (2002)
84. S.-W. Lee, P. Freivogel, T. Schindler, J.L. Beauchamp, J. Am. Chem. Soc. **120**, 11758–11765 (1998)
85. G. Hulthe, G. Stenhagen, O. Wennerström, C.-H. Ottosson, J. Chromatogr. A **777**, 155–165 (1997)
86. O. Echt, K. Sattler, E. Recknagel, Phys. Rev. Lett. **47**, 1121 (1981)
87. H.W. Kroto, J.R. Heath, S.C. O'Brien, R.F. Curl, R.E. Smalley, Nature **318**, 162–163 (1985)
88. W.D. Knight, K. Clemenger, W.A. de Heer, W.A. Saunders, M.Y. Chou, M.L. Cohen, Phys. Rev. Lett. **52**, 2141 (1984)
89. H. Haberland, C. Ludewigt, H.-G. Schindler, D.R. Worsnop, J. Chem. Phys. **81**, 3742–3744 (1984)
90. J. James, L. Kassner, D.E. Hagen, J. Chem. Phys. **64**, 1860–1861 (1976)
91. Z. Shi, S. Wei, J.V. Ford, A.W. Castleman Jr, Chem. Phys. Lett. **200**, 142–146 (1992)
92. Y. Kawai, S. Yamaguchi, Y. Okada, K. Takeuchi, Int. J. Mass Spectrom. **220**, 375–383 (2002)
93. C.K. Lin, C.C. Wu, Y.S. Wang, Y.T. Lee, H.C. Chang, J.L. Kuo, M.L. Klein, Phys. Chem. Chem. Phys. **7**, 938–944 (2005)
94. H.A. Schwarz, J. Chem. Phys. **67**, 5525 (1977)
95. O.F. Mohammed, D. Pines, J. Dreyer, E. Pines, E.T.J. Nibbering, Science **310**, 83–86 (2005)
96. K. Mizuse, A. Fujii, Phys. Chem. Chem. Phys. **13**, 7129–7135 (2011)
97. M.A. Duncan, Rev. Sci. Instrum. **83**, 041101 (2012)
98. G. Dieter, Phys. Scr. **1995**, 256 (1995)
99. K. Mizuse, A. Fujii, N. Mikami, J. Chem. Phys. **126**, 231101 (2007)
100. U. Even, J. Jortner, D. Noy, N. Lavie, C. Cossart-Magos, J. Chem. Phys. **112**, 8068–8071 (2000)
101. K. Luria, W. Christen, U. Even, J. Phys. Chem. A **115**, 7362–7367 (2011)
102. M. Mitsui, A. Nakajima, K. Kaya, U. Even, J. Chem. Phys. **115**, 5707 (2001)
103. M. Mitsui, A. Nakajima, Bull. Chem. Soc. Jpn. **80**, 1058–1074 (2007)
104. M.G. Liverman, S.M. Beck, D.L. Monts, R.E. Smalley, in *Rarefied Gas Dynamics Eleventh symposium*, ed. R. Campargue, vol. 2 (CEA, Paris, 1979), pp. 1037–1048
105. R. Ludwig, A. Appelhagen, Angew. Chem. Int. Ed. **44**, 811–815 (2005)
106. A.Y. Zasetsky, A.F. Khalizov, M.E. Earle, J.J. Sloan, J. Phys. Chem. A **109**, 2760–2764 (2005)
107. D.M. Wieliczka, S. Weng, M.R. Querry, Appl. Opt. **28**, 1714–1719 (1989)

108. A.Y. Zasetsky, A.F. Khalizov, J.J. Sloan, J. Chem. Phys. **121**, 6941–6947 (2004)
109. K. Mizuse, T. Hamashima, A. Fujii, J. Phys. Chem. A **113**, 12134–12141 (2009)
110. J.C. Jiang, J.C. Chang, B.C. Wang, S.H. Lin, Y.T. Lee, H.C. Chang, Chem. Phys. Lett. **289**, 373–382 (1998)
111. C. Steinbach, P. Andersson, J.K. Kazimirski, U. Buck, V. Buch, T.A. Beu, J. Phys. Chem. A **108**, 6165–6174 (2004)
112. C.J. Gruenloh, J.R. Carney, C.A. Arrington, T.S. Zwier, S.Y. Fredericks, K.D. Jordan, Science **276**, 1678–1681 (1997)
113. Q. Du, R. Superfine, E. Freysz, Y.R. Shen, Phys. Rev. Lett. **70**, 2313–2316 (1993)
114. L. Schriver-Mazzuoli, A. Schriver, A. Hallou, J. Mol. Struct. **554**, 289–300 (2000)
115. X. Wei, P.B. Miranda, Y.R. Shen, Phys. Rev. Lett. **86**, 1554–1557 (2001)
116. T.L. Tarbuck, S.T. Ota, G.L. Richmond, J. Am. Chem. Soc. **128**, 14519–14527 (2006)
117. J.-L. Kuo, M.L. Klein, J. Chem. Phys. **122**, 024516 (2005)
118. N.J. Singh, M. Park, S.K. Min, S.B. Suh, K.S. Kim, Angew. Chem. Int. Ed. **45**, 3795–3800 (2006)
119. C.C. Pradzynski, R.M. Forck, T. Zeuch, P. Slavíček, U. Buck, Science **337**, 1529–1532 (2012)
120. J.T. O'Brien, E.R. Williams, J. Am. Chem. Soc. **134**, 10228–10236 (2012)
121. G. Torchet, P. Schwartz, J. Farges, M.F. de Feraudy, B. Raoult, J. Chem. Phys. **79**, 6196–6202 (1983)

Chapter 4
Tuning of the Internal Energy and Isomer Distribution in Protonated Water Clusters $H^+(H_2O)_n$ ($n \leq 50$): Towards a More Detailed Understanding of Structures and Dynamics

Abstract We simplified the IR spectra of hydrated clusters by using an inert gas-mediated cooling technique. Internal energy-dependent spectra were measured and used to investigate dynamics as well as structures. This method also enabled isomer-specific analyses. On the basis of the present approach, molecular-level understanding of large water networks, consisting of more than 20 molecules, was achieved. For example, in the H_2-tagged antimagic clusters $H^+(H_2O)_{22}$, we observed the hitherto missing water molecule, which is at the outside of the magic-numbered ($n = 21$) water cage and should fluctuate in higher temperatures. The present study showed the tagging or messenger technique is a powerful tool to probe even such relatively large water networks, which fluctuate with thermal effects.

Keywords Messenger-mediated IR spectroscopy · Temperature effect · Hydrogen bond dynamics · Isomer distribution control · Cooling technique for cluster ions

4.1 Introduction

As mentioned previously in this thesis, there has already been extensive infrared (IR) spectroscopic studies of various hydrated clusters $X \cdot (H_2O)_n$ (X: solute molecule) in the gas phase, for the molecular-level understanding of hydrogen-bonded water networks [1–3]. These studies, especially of size-selective IR spectroscopy, began with small clusters and have successfully identified important water network motifs, hydration structures, and dynamics [3–7]. As Chap. 3 showed, recent experimental development has opened the way to measure spectra of large hydrated clusters consisting of tens to more than 100 water molecules [2, 8–17]. Generally, the observed spectra of large clusters show gradual development toward

bulky water networks with increasing cluster size. The success of spectroscopy implies the possibility of characterizing large-scale water networks at the molecular level. However, the observed spectra of the large clusters show broadened features due to the homogeneous and inhomogeneous bandwidths. This broadening makes it difficult to analyze the spectra. "Molecular-level" understanding, therefore, has not necessarily been achieved. Further simplification of the spectra has been needed. In this chapter, we develop an approach to addressing such a problem [10, 18–20].

One of the major sources of complexity is finite internal energy (vibrational temperature). Because typical ionic clusters formed in the gas phase have internal energy corresponding to ~ 100 K or higher temperatures [21–25], low-frequency modes of the cluster are excited, affecting the spectral structure (i.e., the bandwidths and hot band structures). Furthermore, the excitation of low-frequency modes (i.e., large-amplitude motions) sometimes stimulates large anharmonic couplings, which would cause the disappearance of the vibrational band [10, 26]. Another source of complexity is the coexistence of structural isomers, which makes it difficult to identify cluster structures on the basis of spectral patterns even when precisely size-selective spectra are measured [21]. Such complexity is seen even in small clusters, in which the number of isomers is not so large [21]. Conversely, these results suggest that if the internal energy and isomer distribution are variable, more information on the cluster structure and hydrogen-bonded networks should be available. Recently, IR–IR hole-burning spectroscopy has been introduced as a powerful tool to obtain isomer-specific spectra [27–29]. However, tuning of internal energy and isomer distribution should also be helpful in hole-burning and related spectroscopy. We note that, in IR spectra of large clusters, inhomogeneous broadening due to the large number of molecules is part of their intrinsic nature, and we may have no means of removing it. However, some parts of the inhomogeneous and homogeneous (lifetime) broadening can be suppressed if the internal energy (temperature) is lowered. Examining this in terms of clusters as a model for a complicated molecular system, many previously reported studies lack an investigation of internal energy dependence, which is necessary to analyze the dynamics of water networks. This means that tuning of internal energy should open the door to studies in this direction.

For the control of the internal energy and isomer distribution of ionic hydrated clusters, several approaches have been reported. The most direct and active approach is the use of a temperature-variable ion trap, because temperature is the controlling factor of both the internal energy and isomer distribution under thermal equilibrium [15, 30–33]. In this method, cluster temperature is controlled by collision with cold buffer gas or equilibrium with the blackbody radiation from a surrounding jacket [14, 15, 30]. For example, Wang et al. have reported IR spectroscopy of $H^+(H_2O)_6$ at temperatures of 77– ~ 200 K [30]. The observed spectra show a decrease of the bandwidth as temperatures decrease, thereby validating the cooling effect. However, no drastic change of the isomer distribution was observed in this temperature range. Further cooling should simplify the spectrum by suppressing hot bands and dynamic effects, and it might lead to

isomer distribution change. At low temperatures ($< \sim 77$ K), however, the photodissociation yield is quite low and therefore the IR action spectra cannot be measured, at least via single IR photon excitation [30]. This approach has been applied to large hydrated clusters such as $Ca^{2+}(H_2O)_n$ and $(H_2O)_n^-$ [14, 15]. While this technique may be the most powerful and active approach, the above-mentioned approach limits the temperature range that can be investigated [15, 30].

Another control method for internal energy and isomer distribution is the condition tuning of the cluster source [21, 22, 34, 35]. For example, in supersonic jet expansion, which has been a generally used technique for cluster production, several variables, such as carrier gases, carrier gas pressures, nozzle hole diameters, nozzle shapes, and so on, are controlling factors of cooling and clustering efficiency. Furthermore, the ionization method (e.g., discharge) and its conditions (e.g., voltage) are also important factors. By changing the source conditions, internal energy and isomer-distribution can sometimes be varied [21, 22, 34, 35]. However, such an approach is somewhat empirical, and wide-range tuning is generally difficult.

A different approach is the use of inert gas tagging (the so-called messenger technique), in which an inert gas atom/molecule such as an argon atom is weakly attached to a cluster of interest (without remarkable perturbation to a cluster) [10, 18, 25, 36–66]. Low binding energy to the inert gas restricts the total internal energy (typically several hundreds of wavenumbers or a few kJ/mol) of the system, because higher energy components should spontaneously dissociate before observation and will not be detected [67]. In other words, the vibrational temperature of surviving clusters with an inert gas should be lower (typically a few tens of Kelvins). Figure 4.1 shows a conceptual diagram for inert gas attachment-induced cooling taking $H^+(H_2O)_n$ as a case example—with and without Ar. In a bare system (left), maximum internal energy corresponds to hydrogen bond energy ($\sim 3,000$ cm^{-1}). On the other hand, in an Ar-tagged system (right), maximum internal energy corresponds to van der Waals interaction energy (typically ~ 500 cm^{-1}), because higher energy components lead to dissociation. As a result, surviving Ar-tagged clusters should have only low internal energy. This indirect "cooling" method also has the advantage of an enhanced IR photodissociation yield due to the lower energy dissociation (detachment of the inert gas) path. This means that such an inert gas has been called a "messenger" in dissociation spectroscopy. Such an advantage has made it possible to apply IR photodissociation spectroscopy in a low temperature ion trap [54, 66, 68, 69]. This method has also opened a way to probe relatively low-frequency vibrations [39, 40, 70]. It should be noted that the internal energy of a cluster would be varied by changing the messenger because each inert gas has a different interaction energy. Furthermore, several groups have reported that isomer distribution is sometimes strongly affected upon inert gas attachment [18, 51, 56, 58]. For example, Lisy et al. have reported Ar-tagging results in higher-energy isomer trapping in various systems such as $Li^+(H_2O)_4 \cdot Ar$ [25, 55, 56, 58, 71, 72]. These results imply that use of various messengers leads to the variation of internal energy and isomer distribution.
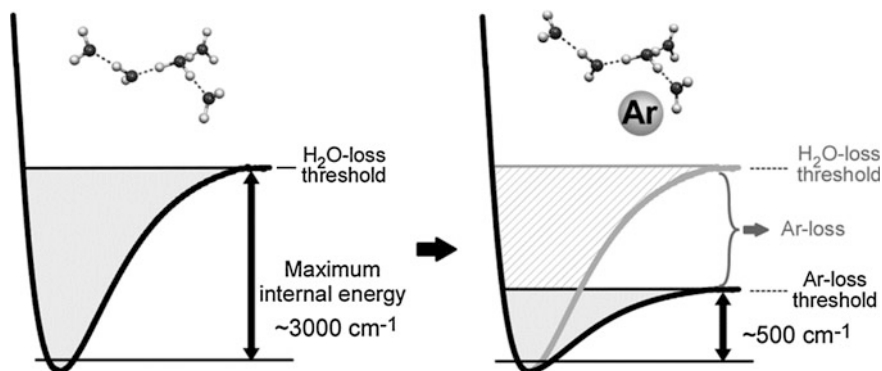
Fig. 4.1 Conceptual diagram for inert gas attachment-induced cooling. Curves are a potential energy curve along the dissociation channel. Populated energy regions are displayed in *grey*. In the bare system (*left*), maximum internal energy corresponds to hydrogen bond energy ($\sim 3,000$ cm^{-1}). In the Ar-tagged system (*right*), maximum internal energy corresponds to van der Waals interaction energy (typically ~ 500 cm^{-1}) and higher energy components lead to dissociation, resulting in the low internal energy of surviving Ar-tagged clusters

Although the messenger technique is a widely-used and powerful tool to probe ionic systems, systematic messenger-mediated spectroscopy concerning both the aspects of internal energy and isomer selectivity by changing the messenger has never been reported. Systematic IR spectroscopy has been reported for various clusters such as phenol$^+$·M$_m$ [48], H$_2$O$^+$·M$_m$ [43, 44, 47, 73], H$_3$O$^+$·M$_m$ [37, 38, 61, 74], and H$_5$O$_2$$^+$·M$_m$ [37, 39, 40] (M = rare gas, H$_2$, N$_2$, CH$_4$). However, isomerization in the moieties of interest cannot be expected in these relatively rigid systems. Here, we report on the messenger effect in protonated water clusters, which have been one of the most frequently-studied clusters with IR spectroscopy as discussed in Chap. 3.

In previous studies on protonated water clusters with messengers, H$_2$, Ne, and Ar have been mainly used. Okumura et al. have reported pioneering messenger spectroscopy for H$^+$(H$_2$O)$_n$·(H$_2$)$_m$ ($n \leq 4$) and H$^+$(H$_2$O)$_n$·Ne ($n \leq 3$) and have shown both the cooling effect and some perturbations of messengers [36–38]. Headrick et al. have reported IR spectra of H$^+$(H$_2$O)$_n$·Ar ($n = 2$–11) to cover the region of $1,000 \sim 3,800$ cm^{-1} [40]. Douberly et al. have carried out a systematic spectroscopic study of H$^+$(H$_2$O)$_{2-5}$ and D$^+$(H$_2$O)$_{2-5}$ with and without Ar attachment [41].

Here, to fill the gaps in messenger experiments of H$^+$(H$_2$O)$_n$ and to extract more information from experimental spectra, we report systematic IR photodissociation spectroscopy of H$^+$(H$_2$O)$_n$·M$_m$ ($n \leq 50$; M = Ne, Ar, Kr, Xe, H$_2$, N$_2$, and CH$_4$). We show the present approach is quite a powerful method of obtaining internal energy- and isomer distribution-dependent spectra of hydrated clusters and of analyzing these spectra in greater detail. Because internal energy and coexistence of multiple isomers are also problems in these small clusters (and analyses of messenger effect should be easier than for large clusters), we first focused on
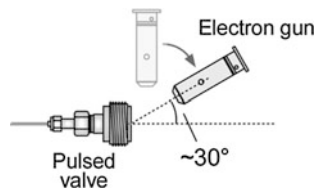
investigation of the messenger effect on internal energy and isomer distributions of small protonated water clusters by systematically measuring $H^+(H_2O)_n \cdot M$ ($n \leq 8$, M = rare gas, H_2, N_2, CH_4). After that, we extended our approach to larger clusters for the purpose of extracting more detailed information on large-scale hydrogen-bonded water networks. As shown in Chap. 3, protonated water clusters are of great interest because of their hydrated proton motifs and magic number behavior. More detailed motivations are shown in corresponding sections.

4.2 Experimental

4.2.1 Overview of Experiment

Most parts of the experimental set-up (the vacuum chamber, IR light source, and measurement systems) were the same as described in Chap. 3, and therefore only brief descriptions are given here. Inert gas attached $H^+(H_2O)_n$ was produced in a supersonic jet expansion. The gaseous mixture of H_2O (trace; $^{17,18}O$-depleted $H_2{}^{16}O$, 99.99 % ^{16}O, ISOTEC) and carrier gas was expanded into an ion source chamber through a high-pressure pulsed valve (Even-Lavie valve [75]), equipped with a conical nozzle. Carrier gases used for each tagging were Ne (10 MPa), Ar (5 MPa), Kr (2 MPa), Xe (1.5 MPa), H_2 (9 MPa), CH_4 (5 MPa), and N_2 (5 MPa), respectively. Stagnation pressures were chosen according to availabilities of gases or yields of tagged species (we also tried to produce He-tagged species; however, we were unable to observe any signal from them). For comparison, bare clusters formed in Ar (5 MPa) were probed. We tentatively investigated pressure dependence of the spectra by changing gas pressures (0.3–10 MPa for Ar and 3–10 MPa for Ne); however, we found that the pressure of carrier gas does not influence the spectra (i.e., internal energy and isomer distribution) very much. This is in agreement with the fact that the reported spectra of $H^+(H_2O)_6 \cdot Ar$ show similar spectral features both in high and low pressure experiments [40]. Therefore, we did not pay attention to pressure dependence in this study. A gas pulse was crossed by an electron beam of 200 eV from an electron gun (Omegatron). In Chap. 3, we employed a perpendicular crossing of an electron beam and a gas pulse, however, such configuration did not lead to production of sufficient very weakly-bound species such as $H^+(H_2O)_n \cdot Ne$. The incident angle of the electron beam relative to a molecular beam was then tuned to $\sim 30°$. Figure 4.2 presents the setup used. This angle allows electrons to penetrate into the cone of the nozzle in which many collisions occur. We found that such angle tuning increased the ion yield of weakly-bound clusters such as $H^+(H_2O)_6 \cdot Ne$ threefold compared to the perpendicular crossing. Ions of interest were selected by the first mass spectrometer and were irradiated by a counter-propagating coherent IR light pulse (from IR-OPO/OPA, LaserVision) in the ion guide. IR absorption was followed by vibrational predissociation of clusters. IR spectra of tagged clusters were then measured by

monitoring the photo fragment $H^+(H_2O)_n$ ion (loss of all messengers) intensity as a
function of the IR wavelength. No other fragments were observed upon the IR
irradiation in the present wavelength region. All the presented IR spectra were
normalized by the IR power. Because no remarkable background signals were
observed, background fluctuation corrections, as in Chaps. 2 and 3, were not
carried out. The wavelength of the IR light was calibrated in vacuum wavenum-
bers (± 2 cm^{-1}) by recording an ambient H_2O/CO_2 vapor spectrum. Although we
scanned the range of 2,200–4,500 cm^{-1} for $H^+(H_2O)_n\cdot(H_2)_m$, no apparent band
was observed in the 4,000–4,500 cm^{-1} (forbidden H_2 stretch) region. Therefore,
we show only the spectra in the 2,200–4,000 cm^{-1} region in the following dis-
cussion. In the H_2-tagging experiment, we mainly used two or three H_2 molecules
as messengers. Multiple messengers increase dissociation paths and the resulting
tagged species are expected to be more or less colder than $H^+(H_2O)_n\cdot(H_2)_1$.
Furthermore, in tagging experiments, we have to distinguish the masses of the bare
and tagged species. Because the H_2-tagged ions were two orders of magnitude less
than bare $H^+(H_2O)_n$, the signals of $H^+(H_2O)_n\cdot(H_2)_1$ and $H^+(H_2O)_n\cdot(H_2)_2$ over-
lapped with the tail of the very strong $H^+(H_2O)_n$ signal even though the mass
resolution was tuned to $\Delta m = 1$–1.5. We also note that we did not distinguish
nuclear spin isomers of H_2 (ortho- and para-H_2), because we could not evaluate the
rotational-level distribution of H_2 (e.g., by observation of the rotationally resolved
H_2 stretch band). In general, para-H_2 is more inert and therefore para-H_2 tagged
clusters can only observed when highly concentrated para-H_2 gas is used [76, 77].
In this study, because we used typical room temperature H_2 gas (ortho/para ~ 3),
we postulated ortho-H_2 tagged clusters were the major species in our ion source.

4.2.2 Quantum Chemical Calculations

4.2.2.1 Calculation Levels

For analyses of the spectra and estimation of the cooling effect upon the messenger
attachment, we carried out density functional theory (DFT) calculations similar to
the methods as described in Chap. 2. The simulated IR spectra of bare $H^+(H_2O)_n$
were obtained with harmonic frequency calculations at the B3LYP/6-31+G(d)
level [78, 79], which has been used in the pioneering IR spectroscopic work on
$H^+(H_2O)_n$ [21]. In the simulations, harmonic frequencies were scaled by 0.9736. The
stick spectrum was transformed into a continuous spectrum by using Lorentzian

functions of 10 and 50 cm^{-1} full widths at half-maximum for the free and hydrogen-bonded OH stretches, respectively. Here, two bandwidths were used to take into account the lifetime broadening induced by hydrogen bonding [80]. We note that this convolution was used only for convenience in comparison with the simulated spectra and the values of the bandwidth have no rigorous physical meanings.

It has been pointed out that the B3LYP functional is unable to treat systems in which the dispersion interaction plays vital roles [81]. Therefore, to treat the weak interaction between a messenger and H$^+$(H$_2$O)$_n$ moiety, we basically used the M06-2X functional [82, 83], which has shown reasonable agreements in calculations of various weakly-bounded systems [82–84]. In some cases, especially for larger systems, we also used the ωB97X-D functional [85], which shows comparable performance to the M06-2X [84], to reduce CPU time. In our cases, the M06-2X was more time-consuming than the ωB97X-D.

4.2.2.2 Estimation of the Cooling Effect

To estimate the cooling effect upon the messenger attachment, we evaluated the upper limit of the vibrational temperature (T_{max}) of the cluster on the basis of the relationship between the temperature and the internal energy. Here we assumed a condition for survival of clusters; the vibrational internal energy (E_{vib}) of a cluster is limited by the binding energy (D_e) of a messenger to the H$^+$(H$_2$O)$_n$ moiety ($E_{vib} < D_e$). To calculate the E_{vib} and D_e, we searched for the most stable structure of H$^+$(H$_2$O)$_n$·M by using a systematic procedure, described in the next section [10, 18, 64]. On the basis of the structures found in this search (at the ωB97X-D/6-311+G(d,p) level), optimized structure, harmonic vibrational frequencies and binding energy (D_e) to a messenger were finally calculated at the ωB97X-D/6-311++G(3df,2p). In statistical thermodynamics (under the harmonic oscillator approximation), E_{vib} is given as

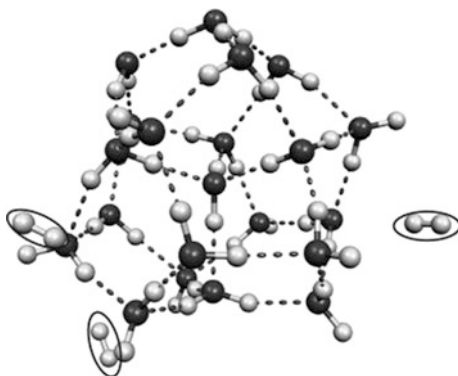$$E_{vib} = \sum_{j}^{3N-6} \frac{h\nu_j}{\exp(-h\nu_j/kT) - 1} \tag{4.1}$$

where $h\nu_j$ is the vibrational energy of the j-th vibrational mode, 3N–6 is the total number of vibrational modes, k is the Boltzmann constant, and T is temperature. According to these analyses, T_{max} was given as the maximum T in which E_{vib} does not exceed D_e.
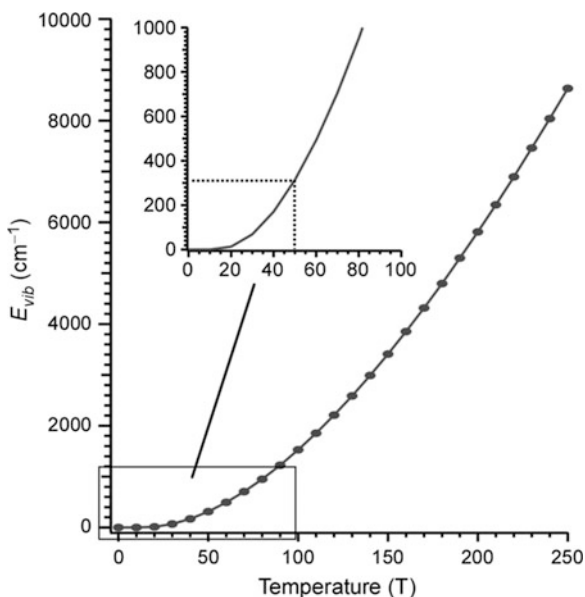
For example for H$^+$(H$_2$O)$_{21}$·(H$_2$)$_3$, Fig. 4.3 presents plausible structures. For this structure, the harmonic frequency calculation was carried out. By using $h\nu_j$, we evaluated E_{vib} (see Eq. 4.1). Figure 4.4 shows a plot of E_{vib} as a function of temperature (T). D_e calculated was $\sim$300 cm^{-1} both in the ωB97X-D/6-31+G(d) and ωB97X-D/6-311+G(3df,2p) levels. According to the condition for survival of clusters ($E_{vib} < D_e$), we obtained the maximum effective temperature of $\sim$50 K.

We note the calculated value of T_{max} strongly depends on the accuracy of calculations for low frequency vibrational modes. Because both experimental and theoretical benchmarks are still limited for such low frequency modes of hydrated

Fig. 4.3 The plausible
structure of $H^+(H_2O)_{21}\cdot(H_2)_3$

Fig. 4.4 The plot of E_{vib} of
$H^+(H_2O)_{21}\cdot(H_2)_3$ vs. T

clusters, the evaluation of the present calculations is difficult at the present stage. However, we found that the present T_{max} qualitatively agrees with our experimental cooling effect (as discussed below). It should be noted that we could not measure the temperature of clusters, and therefore, reported values are a rough estimation of the cooling effect.

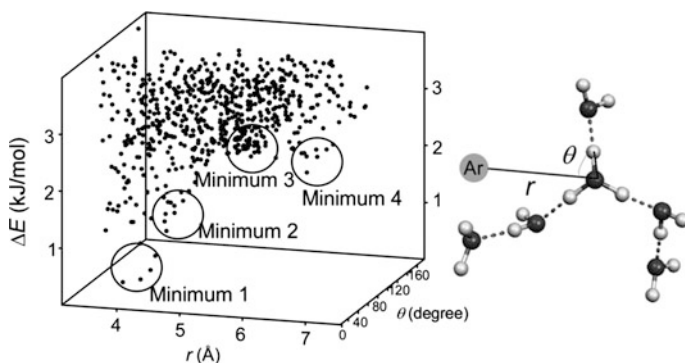### 4.2.2.3 Finding the Most Stable Inert Gas Locations

To find the most stable location of a messenger, we carried out a three-dimensional scan of the (center of mass) position of a messenger atom/molecule around the $H^+(H_2O)_n$ and found the lowest energy geometry. For example, for $H^+(H_2O)_6\cdot Ar$,

we first constructed a $(30 \text{ Å})^3$ cubic grid, which had a 0.6 Å grid length, around the optimized $H^+(H_2O)_6$ structures (Fig. 4.5). Ar was located at each grid point and we obtained $51^3 = 132{,}651$ initial structures. Some structures were excluded after the filtering, which requires that the shortest interatomic distance between Ar and one of the atoms in $H^+(H_2O)_6$ must be longer than 1.5 Å and shorter than 3.7 Å. All the structures remaining after this filtering were tested with the single point energy calculation at the ωB97X-D/6-31G(d) level. For the Eigen type isomer, one of the stable isomers of $H^+(H_2O)_6$ (see the following sections), energy calculations were carried out for 6,228 structures. The results were plotted as functions of geometric parameters (Fig. 4.6). In Fig. 4.6, four apparent minima were found. From these minimum structures, we carried out geometry optimizations at the M06-2X/6-311++G(3df,2p) level. Optimized structures and their relative energies are shown in Fig. 4.7. Geometry optimizations were also carried out for the corresponding structures of $H^+(H_2O)_6\cdot$Ne and quite similar structures were obtained. Figure 4.7 also shows the relative energies of the optimized $H^+(H_2O)_6\cdot$Ne structures. Similar analyses were carried out for the Zundel type, another isomer, and we found three minima in the energy plot (Fig. 4.8). Figure 4.9 shows the optimized structures of $H^+(H_2O)_6\cdot$Ar and the relative energies of both $H^+(H_2O)_6\cdot$Ne and $H^+(H_2O)_6\cdot$Ar.

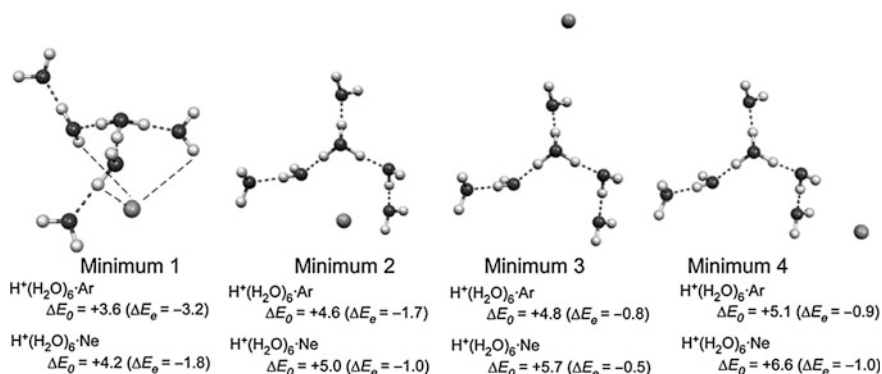Essentially the same procedures were carried out for the reported clusters. For the H_2-tagged clusters, an additional two dimensions for the orientation of the H_2 moiety were also taken into account (in total, a five-dimensional search). Thus,

Fig. 4.5 *Cubic grid* used for the low-lying Ar-location searches around $H^+(H_2O)_6$

Fig. 4.6 (*Left*) Relative energies plotted as a function of the Ar-location. (*Right*) Definitions of r and θ

Fig. 4.7 Optimized structures of the Eigen type $H^+(H_2O)_6 \cdot Ne$. Their energies and those of the corresponding $H^+(H_2O)_6 \cdot Ne$ relative to the most stable Zundel form (minimum 1 in Fig. 4.9) are also shown in kJ/mol
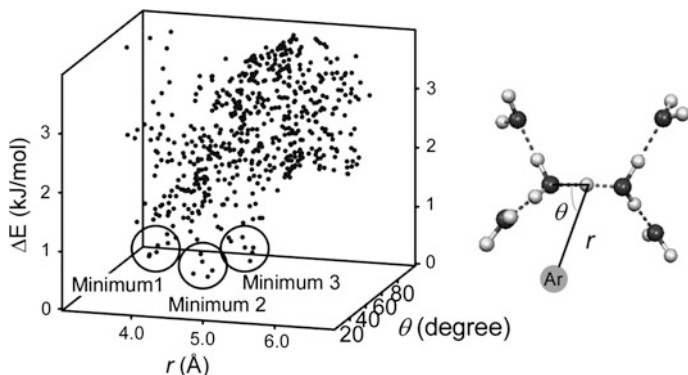
found structures and their trends of tagged clusters are in agreement with recent theoretical calculations of small $H^+(H_2O)_n \cdot M$ [41, 57, 62].
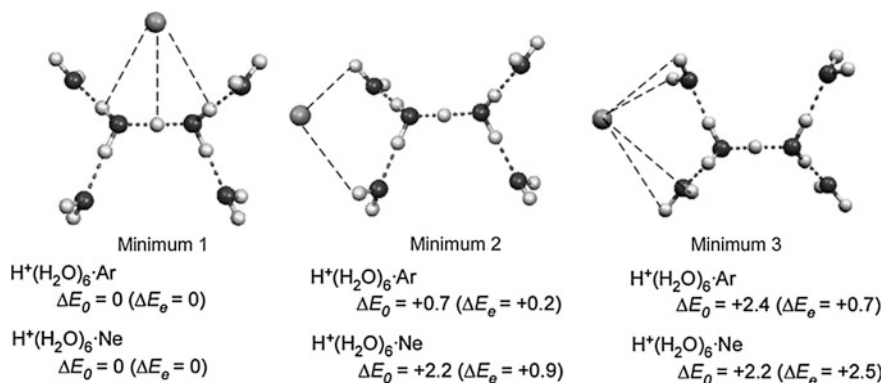
4.3 Results and Discussions

4.3.1 Small Clusters $H^+(H_2O)_n$ ($n \leq 8$)

4.3.1.1 $H^+(H_2O)_{2,3}$ Systems

Although the inert gas attachment technique has been systematically applied to $H^+(H_2O)_{2,3}$ in the previous studies, we measured IR spectra of Ar- and Ne-tagged $H^+(H_2O)_{2,3}$ for validation of current measurements and comparison with following

Fig. 4.8 (*Left*) Relative energies plotted as a function of the Ar-location. (*Right*) Definitions of r and θ

Fig. 4.9 Optimized structures of the Zundel type $H^+(H_2O)_6 \cdot Ar$. Their energies and those of the corresponding $H^+(H_2O)_6 \cdot Ne$ relative to minimum 1 are also shown in kJ/mol

larger clusters later. Detailed analyses have been already reported; therefore, only a brief discussion mainly concerning the effects of inert gas is given here. $H^+(H_2O)_2$ ($H_5O_2^+$) is called the Zundel ion, in which the excess proton is shared between two H_2O molecules. It has been of great interest because of its fundamental importance in aqueous proton transfer. Figure 4.10 shows the IR spectra of Ar-, Ne-, and $(Ne)_2$-tagged $H^+(H_2O)_2$ ($H_5O_2^+$). IR dissociation spectrum of bare $H_5O_2^+$ could not be observed because of its high dissociation energy. Simulated spectrum for bare $H_5O_2^+$ is also shown. Observed features are essentially the same as those reported previously. In spectra, only two main peaks can be seen in Ne- and $(Ne)_2$-mediated spectra, while Ar-mediated spectrum shows more bands. The observed two peaks are assigned to the symmetric and antisymmetric stretching of H_2O moiety. The complicated features in Ar-mediated spectrum are accounted for by the relatively large perturbation of Ar because of its larger polarization

Fig. 4.10 a–c IR spectra of
bare, Ar-, Ne-, and (Ne)$_2$-
tagged H$^+$(H$_2$O)$_2$,
respectively. **d** DFT-
simulated IR spectrum for the
bare cluster obtained with the
B3LYP/6-31+G(d) level.
Inset shows the structure of
bare H$^+$(H$_2$O)$_2$ (H$_5$O$_2$$^+$,
Zundel ion)
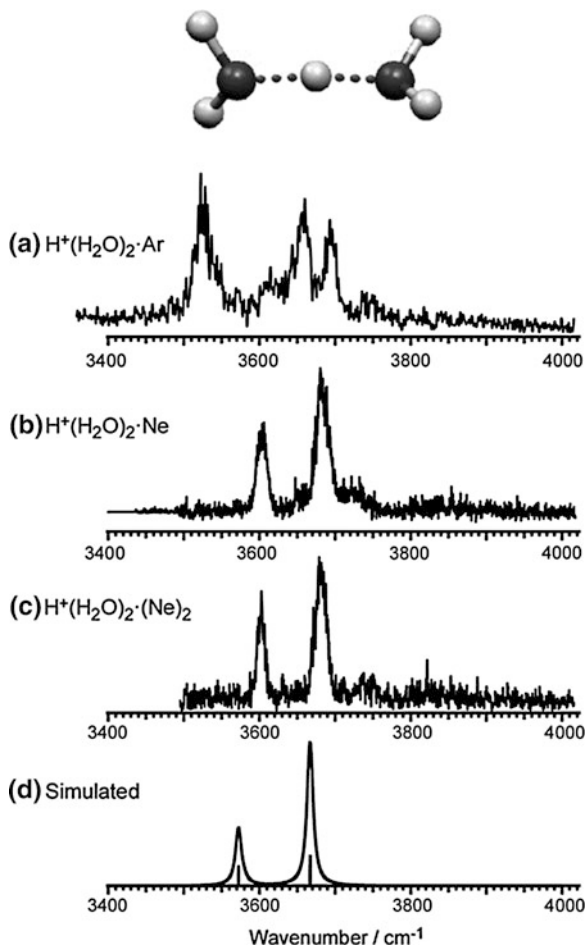
(interaction energy to H$_5$O$_2$$^+$) than Ne. This argument is in agreement with the fact
that simulated spectrum for the bare system also shows the doublet feature.

Figure 4.11 shows IR spectra of bare, Ar- and Ne-tagged H$^+$(H$_2$O)$_3$, respec-
tively. Calculations were also done for the bare cluster. Observed spectra of tagged
clusters show sharper bandwidths than in the bare cluster spectrum. Both rare gas-
mediated spectra show a triplet feature. Three bands can be attributed to the
symmetric and antisymmetric stretching of H$_2$O moiety, and OH stretching of
H$_3$O$^+$ moiety, which would directly interact with a rare gas atom. Because the
interaction energy of Ar is larger than that of Ne, the shift from the intact free OH
frequency of H$_3$O$^+$ moiety is larger in the Ar-mediated spectrum. The difference
between the simulated spectrum and observed spectra of the bare cluster is due to
the effects of internal rotation and hot bands, neither of which are taken into
account in the present calculations.
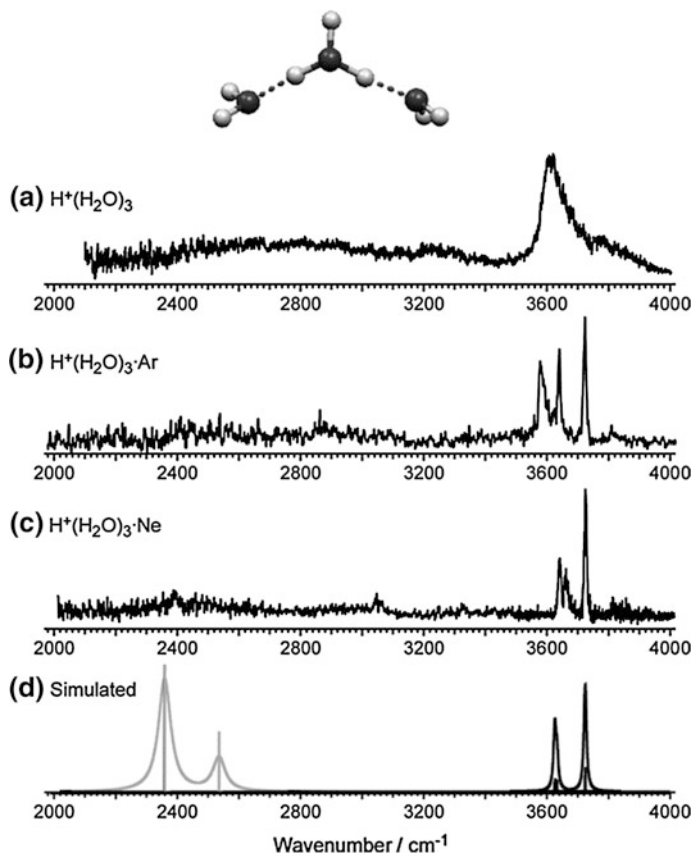
Fig. 4.11 a–c IR spectra of bare, Ar- and Ne-tagged H$^+$(H$_2$O)$_3$, respectively. **d** DFT-simulated IR spectrum of the bare cluster obtained with the B3LYP/6-31+G(d) level. *Inset* shows the structure of bare H$^+$(H$_2$O)$_3$

4.3.1.2 H$^+$(H$_2$O)$_4$

It has been known that H$^+$(H$_2$O)$_4$ has the form of the symmetrically hydrated H$_3$O$^+$ core and is called Eigen cation (Fig. 4.12) [37, 86, 87]. No other isomers have been observed [37, 38, 41] and therefore, only the internal energy would be a variable as a function of the messenger used in this system. In this system, in contrast to the cases of H$^+$(H$_2$O)$_{2,3}$, inert gas cannot be accommodated in the first solvation shell of the ion core, and therefore, weaker perturbation on the spectrum is expected. Figure 4.12a–c shows IR spectra of bare, Ar-tagged, and Ne-tagged H$^+$(H$_2$O)$_4$, respectively. Table 4.1 shows the collected frequencies and assignments of selected bands. The spectra of the bare and Ar-tagged clusters shows essentially the same spectral features as reported previously [37, 38, 40, 41]. The spectral similarity and agreement with the simulated spectrum (Fig. 4.12d) based
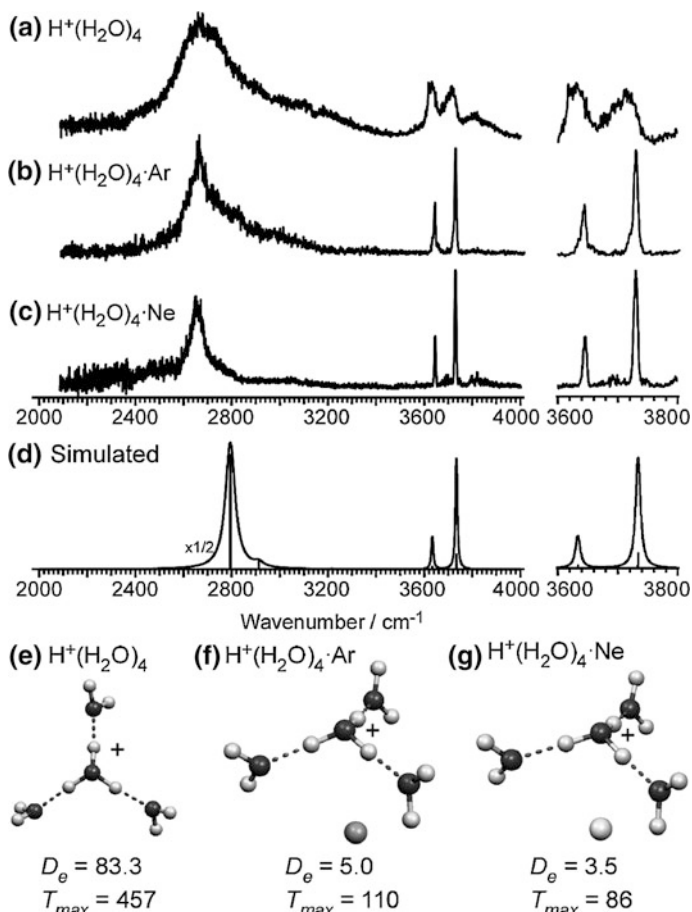
Fig. 4.12 **a–c** IR spectra of bare, Ar- and Ne-tagged $H^+(H_2O)_4$, respectively. **d** DFT-simulated IR spectrum of the structure in **e** obtained with the B3LYP/6-31+G(d) level. **e–g** The results of DFT (ωB97X-D/6-311++G(3df,2p)) calculations for $H^+(H_2O)_4$, $H^+(H_2O)_4 \cdot Ar$, and $H^+(H_2O)_4 \cdot Ne$, respectively. The most stable structures, calculated binding energies D_e (in kJ/mol), and maximum temperatures T_{max} (in K) are shown. Adopted from Ref. [19] (Copyright 2012 American Chemical Society)

on the Eigen cation shows all three observed spectra can be attributed to this structure [88]. The minor band at $\sim 3,800$ cm^{-1} has been accounted for by a combination band [37].

In Fig. 4.12a–c, the messenger-dependent bandwidth can be seen. The spectrum of the bare cluster shows the broadest bandwidths and the Ne-mediated spectrum shows the sharpest ones. This difference should be due to the different internal energy of the systems. If the internal energy becomes higher, it enhances hot bands, and anharmonic couplings reduce the lifetime of the vibrationally excited state of OH stretches. These lead to broader bandwidths.

Table 4.1 Vibrational frequencies (in cm^{-1}) and assignments of selected bands in IR spectra of H$^+$(H$_2$O)$_n$·M

H$^+$(H$_2$O)$_4$	H$^+$(H$_2$O)$_4$·(H$_2$)$_2$	H$^+$(H$_2$O)$_\mathbf{4}$ H$^+$(H$_2$O)$_4$·Ar	H$^+$(H$_2$O)$_4$·Ne	Assignment
2,686		2,665	2,657	H$_3$O$^+$ str.
3,634		3,644	3,647	1-coord. (v_sym)
3,714		3,730	3,732	1-coord. (v_antisym)

H$^+$(H$_2$O)$_5$	H$^+$(H$_2$O)$_5$·(H$_2$)$_2$	H$^+$(H$_2$O)$_\mathbf{5}$ H$^+$(H$_2$O)$_5$·Ar	H$^+$(H$_2$O)$_5$·Ne	Assignment
2,865	2,842/2,897	2,868	2,870	H$_3$O$^+$ str. to 1-coord.
3,201	3,202	3,201	3,191	2-coord.
3,646	3,642/3,650	3,649	3,650	1-coord. (v_sym)
3,709	3,697/3,713	3,711	3,713	2-coord.
3,734	3,728/3,736	3,735	3,736	1-coord. (v_antisym)

H$^+$(H$_2$O)$_6$	H$^+$(H$_2$O)$_6$·(H$_2$)$_2$	H$^+$(H$_2$O)$_\mathbf{6}$ H$^+$(H$_2$O)$_6$·Ar	H$^+$(H$_2$O)$_6$·Ne	Assignment
2,987	2,960		2,991	(Eigen) H$_3$O$^+$ str. to 1-coord.
	3,157	3,165	3,160	(Zundel) OH (H$_5$O$_2^+$) str. to 1-coord.
3,314	3,310		3,304/3,325	(Eigen) 2-coord.
3,648	3,650	3,652	3,652	1-coord. (v_sym)
3,710	3,705/3,715	3,712	3,716	(Eigen) 2-coord.
3,737	3,738	3,738	3,739	1-coord. (v_antisym)

H$^+$(H$_2$O)$_7$	H$^+$(H$_2$O)$_7$·(H$_2$)$_2$	H$^+$(H$_2$O)$_\mathbf{7}$ H$^+$(H$_2$O)$_7$·Ar	H$^+$(H$_2$O)$_7$·Ne	Assignment
3,160	3,182	3,174	3,194	("Ring") OH (H$_5$O$_2^+$) str. to 1-coord.
	3,308/3,334	3307.4/ 3327.8	3,310/3,325	("Ring") OH (H$_5$O$_2^+$) str. to 1-coord.
3,363	3,351/3,367	3,347	3,351/3,370	("Chain") 2-coord.
3,553	3,541	3,541/3,551	3,555	("Ring") 2-coord.
3,651	3,652	3,652	3,654	1-coord. (v_sym)
3,679	3,677	3,677	3,679	3-coord.
3,712	3,715	3,707/3,715	3,716	2-coord.
3,738	3,740	3,740	3,741	1-coord. (v_antisym)

H$^+$(H$_2$O)$_8$	H$^+$(H$_2$O)$_8$·(H$_2$)$_2$	H$^+$(H$_2$O)$_\mathbf{8}$ H$^+$(H$_2$O)$_8$·Ar	H$^+$(H$_2$O)$_8$·Ne	Assignment
	2,975	2,977		
	3,196	3,205		
	3,352	3,352		
3,385	3,366	3,367		
	3,394	3,391		

(continued)

Table 4.1 (continued)

| H$^+$(H$_2$O)$_8$	H$^+$(H$_2$O)$_8$·(H$_2$)$_2$	H$^+$(H$_2$O)$_8$ H$^+$(H$_2$O)$_8$·Ar	H$^+$(H$_2$O)$_8$·Ne	Assignment
	3,435	3,438		
	3,462	3,465		
	3,503	3,508		
	3,562	3,563		
3,651	3,653	3,653		1-coord. (ν_{sym})
3,683	3,672/3,677/3,680	3,681		3-coord.
3,714	3,715	3,715		2-coord.
3,739	3,742	3,741		1-coord. ($\nu_{antisym}$)

n-coord. means a *n*-coordinated water molecule. *str.* = stretch. ν_{sym} and $\nu_{antisym}$ are the symmetric and antisymmetric stretches, respectively. All the bands in 3,600–3,800 cm^{-1} are assigned to free OH stretch while all below 3,600 cm^{-1} are hydrogen-bonded OH stretch. Band frequencies were estimated by fitting each band with a single Lorentzian function. We note that all the bands are far from a single Gaussian or Lorentzian function. Errors of the frequencies are estimated to be 10 cm^{-1} or less for the hydrogen-bonded OH bands and 2 cm^{-1} for the free OH stretch bands. The errors for the hydrogen-bonded OH bands can mainly be attributed to the fitting error for the asymmetric-shaped, overlapped band

In the bare system, three strong H-bonds allow the cluster to accommodate the high internal energy (ca. <83.3 kJ/mol), and the cluster spectrum is highly broadened. On the other hand, in the Ar- and Ne- mediated spectra, each band is sharper, reflecting the reduced internal energy. By comparing Ne with Ar, the smaller interaction energy is expected for Ne because of its smaller polarizability. As a result, the Ne-tagged cluster would be lower in its internal energy; that is, colder in vibrational temperature. These considerations are qualitatively consistent with the calculated binding energies D_e, i.e., maximum internal energies, and maximum vibrational temperatures T_{max}, which are shown in Fig. 4.12e–g with the corresponding optimized structures. The present observation clearly shows that the change of the messenger enables us to vary the internal energy of the system.

Unfortunately, the band shape of each band, especially that of the hydrogen-bonded OH stretch band, is far from a single Gaussian or Lorentzian function. There should be contribution of hot bands. As for the hydrogen-bonded OH band, the overlap of the symmetric and asymmetric stretches of the H$_3$O$^+$ moiety and the contribution of the overtone of the bending mode are plausible factors for further complication of the band shape. These make it difficult to simply determine the values of the bandwidths and discuss detailed dynamics at the present stage.

4.3.1.3 H$^+$(H$_2$O)$_5$

In the previous studies on H$^+$(H$_2$O)$_5$ (and H$^+$(H$_2$O)$_5$·Ar), only one type of isomer (Fig. 4.13f) has been identified [21, 40, 41]. Other isomers, such as the branched-ring type, have never been identified though their relative energies are estimated to be sufficiently low [41, 89]. Figure 4.13a–d shows IR spectra of bare, H$_2$-tagged,
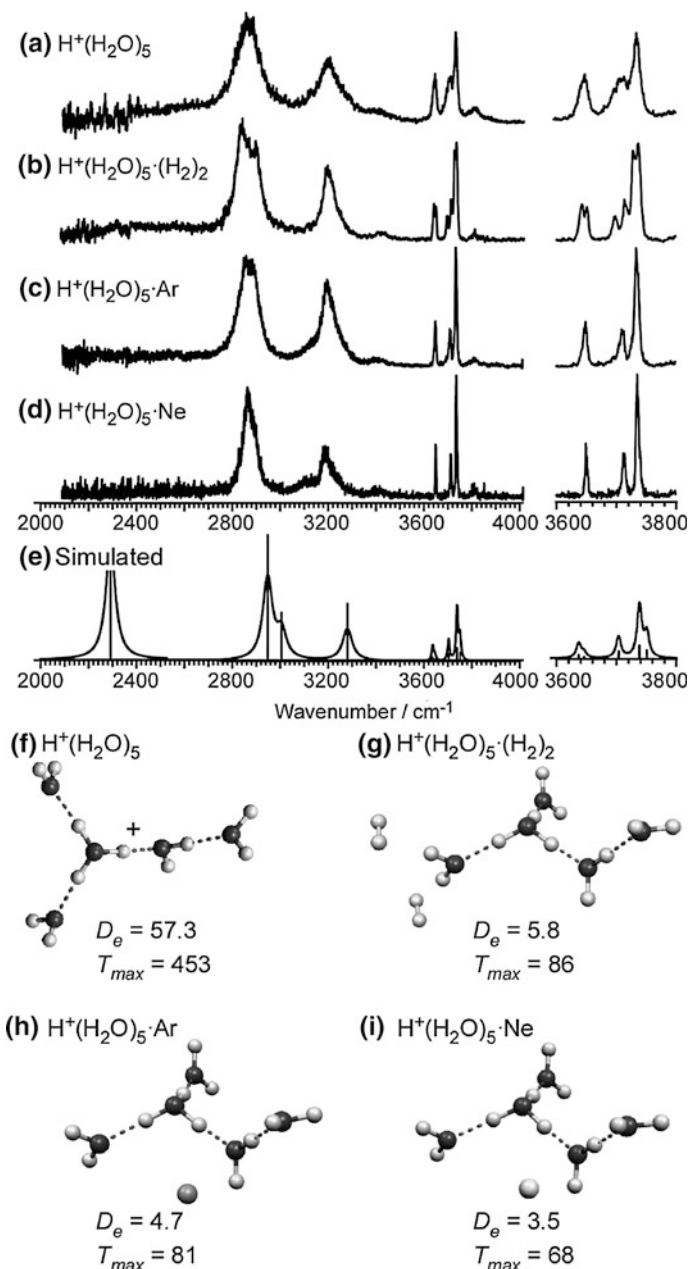
Fig. 4.13 a–d IR spectra of bare, H_2-, Ar- and Ne-tagged $H^+(H_2O)_5$, respectively. **e** DFT-simulated IR spectrum of the structure in **f** obtained with the B3LYP/6-31+G(d) level. **f–i** The results of DFT (ωB97X-D/6-311++G(3df,2p)) calculations for $H^+(H_2O)_5$, $H^+(H_2O)_5 \cdot (H_2)_2$, $H^+(H_2O)_5 \cdot Ar$, and $H^+(H_2O)_5 \cdot Ne$, respectively. The most stable structures, calculated binding energies D_e (in kJ/mol), and maximum temperatures T_{max} (in K) are shown. Adopted from Ref. [19] (Copyright 2012 American Chemical Society)

Ar-tagged, and Ne-tagged $H^+(H_2O)_5$, respectively. Frequencies of selected bands are shown in Table 4.1. Good agreement between the observed and the calculated spectra shows that only the single isomer shown in Fig. 4.13f is the spectral carrier. The tiny splitting of the bands in $H^+(H_2O)_5 \cdot (H_2)_2$ is due to the perturbation on H_2-attachments as seen in the previously reported spectrum of $H^+(H_2O)_4 \cdot (H_2)_1$ [36, 38]. Observed bands are assigned as in the previous studies (Table 4.1) [21, 40, 41]. The band at 2,400 cm^{-1} in the simulation is attributed to the H^+ motion partially shared by the H_3O^+ and the 2-coord H_2O, and its absence in the observed spectra is due to its large anharmonicity. Previous IR spectroscopy of $H^+(H_2O)_5 \cdot Ar$ has observed this band at around 1,900 cm^{-1} [40].

Here, again, the bandwidth depends on the messenger. The internal energy follows the order: bare $H^+(H_2O)_5 > H^+(H_2O)_5 \cdot (H_2)_2 > H^+(H_2O)_5 \cdot Ar > H^+(H_2O)_5 \cdot Ne$, as indicated in their bandwidths. This order implies that the interaction between H_2 and $H^+(H_2O)_5$ is stronger and the magnitude of the perturbation is larger. Figure 4.13f–i shows the calculated interaction (binding) energy and maximum temperature with each optimized lowest-energy structure. In the present calculation, we found that the most favorable position of H_2 is front of a free OH bond while those of Ar and Ne are under the H_3O^+ umbrella. It might be possible that the tiny splitting of the bands in $H^+(H_2O)_5 \cdot (H_2)_2$ is a signature of such positions of the messenger. An alternative interpretation is that this splitting is due to the larger perturbation of H_2 relative to Ar and Ne.

4.3.1.4 $H^+(H_2O)_6$

In Sects. 4.3.1.2 and 4.3.1.3 ($H^+(H_2O)_{4,5}$), it was shown that we can tune the internal energy by changing the messenger used. The control of another factor, isomer distribution, can be tested in a system in which multiple isomers can coexist. $H^+(H_2O)_6$ is the smallest system in which two types of isomers coexist [18, 21]. Figure 4.14 shows the identified structures of the two isomers in $H^+(H_2O)_6$. Here, the Eigen type isomer has a H_3O^+ type ion core, while the Zundel type has a $H_5O_2^+$ core. An energy diagram for the Eigen/Zundel interconversion

Fig. 4.14 Energy diagram for the Eigen/Zundel interconversion in the $H^+(H_2O)_6$ system calculated at the M06-2X/6-311++ G(3df,2p) level. Zero-point vibrational energies were corrected. Adopted from Ref. [18] (Copyright 2011 PCCP Owner Societies)
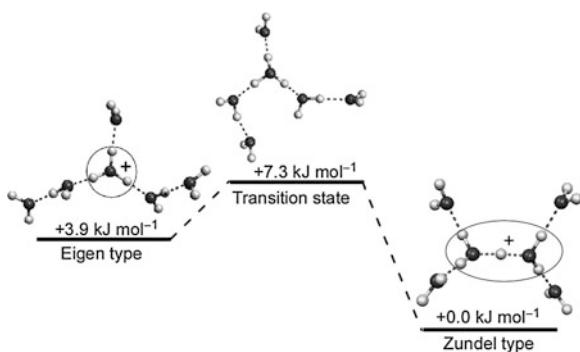
(isomerization) calculated at the M06-2X/6-311++G(3df,2p) level is also shown in Fig. 4.14. It has been thought that the elementary step of aqueous proton transfer, which is one of the most fundamental and important reactions in aqueous chemistry and biological systems, can be nominally regarded as an interconversion of the two limiting motifs, "Eigen" (H_3O^+ or $H_3O^+(H_2O)_3$) and "Zundel" ($H_5O_2^+$ or $H_2O\cdots H^+\cdots OH_2$) [86, 87, 90–94]. This system is, therefore, a prototype to study the Eigen/Zundel balance in water networks in addition to isomer distribution change upon inert gas attachment.

For the $H^+(H_2O)_6$ system, Headrick et al. have reported on Ar-mediated IR spectroscopy, and have shown that $H^+(H_2O)_6\cdot Ar$ is attributable only to the Zundel type [40]. Because Ar-tagged ions have internal energy lower than the binding energy with Ar (~ 500 cm^{-1}), low energy isomers are expected to be selectively observed. The result of $H^+(H_2O)_6\cdot Ar$ has therefore been accounted for by the higher stabilization energy of the Zundel type isomer [40, 95]. On the other hand, Wang et al. have reported IR spectra of temperature-controlled $H^+(H_2O)_6$ using a 22-pole ion trap in the temperature range of 77–200 K [30]. Although 77 K is close to the estimated temperature of Ar-tagged clusters, both the Eigen and Zundel type isomers coexist at all the temperatures. These studies on $H^+(H_2O)_6$ suggest that the balance between the Eigen and Zundel motifs is quite delicate, and further investigation is of importance.

Figure 4.15a–d shows the IR spectra of bare, H_2-tagged, Ar-tagged, and Ne-tagged $H^+(H_2O)_6$, respectively. Table 4.1 summarizes the frequencies. Bandwidths follow the order: $H^+(H_2O)_6 > H^+(H_2O)_6\cdot(H_2)_2 > H^+(H_2O)_6\cdot Ar \sim H^+(H_2O)_6\cdot Ne$, reflecting internal energy as in the case of $H^+(H_2O)_{4,5}$. Based on the simulated spectra (Fig. 4.15e, f) and previously reported assignments (Table 4.1) [10, 24], the bands in blue at around 2,980, 3,320, and 3,710 cm^{-1} can be regarded as markers of the "Eigen" type isomer (Fig. 4.15h). On the other hand, the somewhat broad band in red at around 3,160 cm^{-1} is the signature of the "Zundel" type (Fig. 4.15g). We note that expected bands in the 2,400–2,600 cm^{-1} region of the "Eigen" type were not observed. This can be due to the large anharmonicity of those H_3O^+ bands, as in the case of $H^+(H_2O)_5$. According to the spectral assignments (see also Table 4.1), the spectra of the bare, H_2-tagged, and Ne-tagged clusters can be attributed to the coexistence of the Eigen and Zundel isomers. On the other hand, as Headrick et al. have reported, the spectrum of $H^+(H_2O)_6\cdot Ar$ is clearly attributed almost exclusively to the Zundel type, and bands due to the Eigen type are negligible [40]. Here, the excellent agreement between the observed spectrum of $H^+(H_2O)_6\cdot Ar$ and the calculated one of the Zundel type $H^+(H_2O)_6$ suggests that perturbations of Ar on the vibrational structures are small in this region.

These results are (at least partial) achievement of control of the isomer-distribution. We also emphasize that the present control method enables us to deduce isomer specific spectral features. A typical example is found in the 2,800–3,400 cm^{-1} region. In the bare $H^+(H_2O)_6$ spectrum, the red band is not clear while the spectra of H_2 and Ne-tagged clusters shows three clear bands by virtue of the cooling effect. Because of the single band feature of the Ar-mediated spectrum and agreement of the band position, the central band in H_2- and Ne- mediated spectra can be immediately assigned
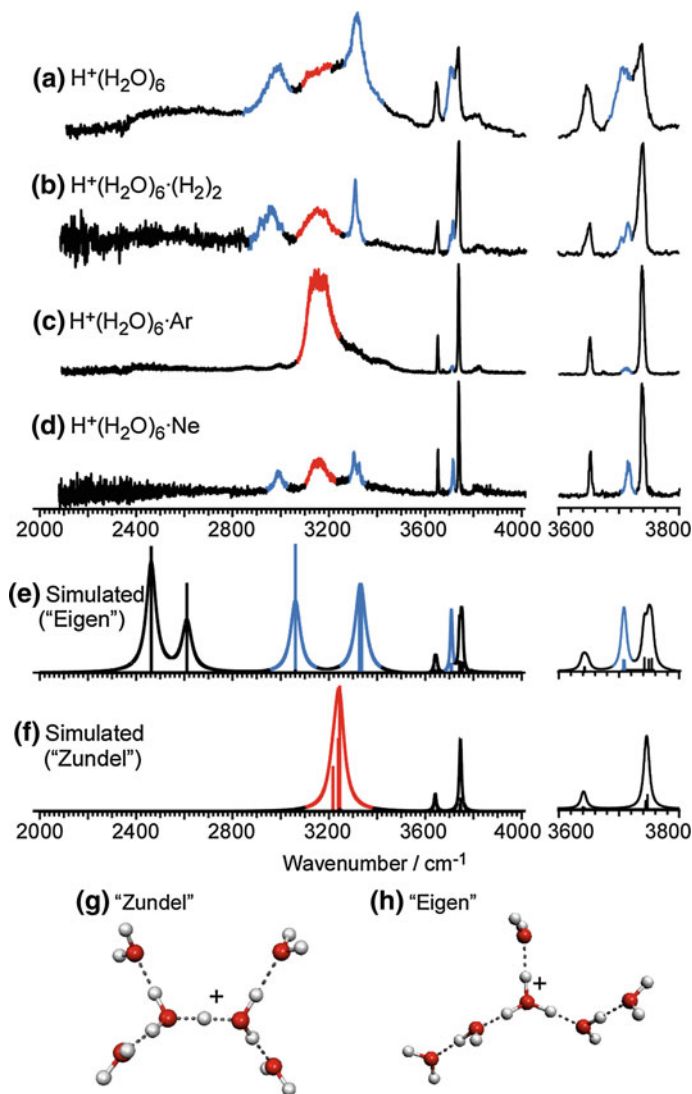
Fig. 4.15 a–d IR spectra of bare, H$_2$-, Ar- and Ne-tagged H$^+$(H$_2$O)$_6$, respectively. The bands in *red* show those of the "Zundel" isomer. The bands in *blue* show those of the "Eigen" isomer. **e**, **f** DFT-simulated IR spectra of the structure in (**g**, **h**) obtained with the B3LYP/6-31+G(d) level. **g**, **h** Optimized cluster structures of H$^+$(H$_2$O)$_6$. Adopted from Ref. [19] (Copyright 2012 American Chemical Society)

to the same isomer as that found in H$^+$(H$_2$O)$_6$·Ar (even without calculations). Such an analysis procedure is similar to that used in hole-burning spectroscopy, in which isomer-specific bands can be deduced. We will show this approach is useful in dealing with more complicated spectra in the next section.
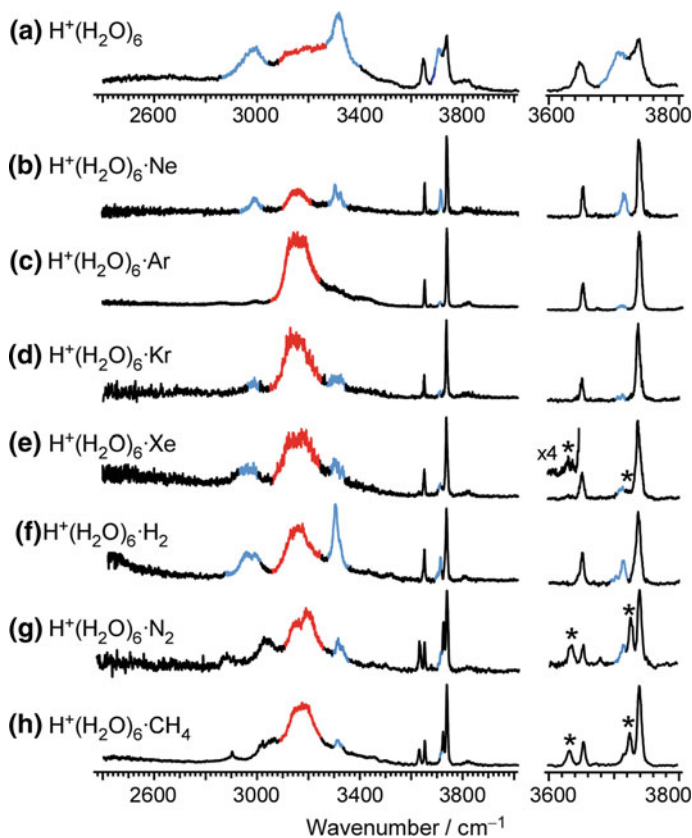
Fig. 4.16 Messenger-mediated IR spectra of $H^+(H_2O)_6$. **a** IR spectra of bare $H^+(H_2O)_6$ formed in a jet expansion of 5 MPa argon. **b–h** IR photodissociation spectra of $H^+(H_2O)_6 \cdot M_1$ (M = Ne, Ar, Kr, Xe, H_2, N_2, and CH_4) in the OH stretch region. The bands in *blue* and *red* are markers of the Eigen and Zundel type isomers, respectively. See text on the bands indicated by an *asterisk*. Adopted from Ref. [18] (Copyright 2011 PCCP Owner Societies)

For a more detailed understanding of messenger effects, we also used other inert gases. Figure 4.16 shows IR photodissociation spectra of $H^+(H_2O)_6 \cdot M_1$ (M = Ne, Ar, Kr, Xe, H_2, N_2, and CH_4) in the OH stretch region. All the messenger-mediated spectra show narrower bandwidths than the spectrum of bare $H^+(H_2O)_6$, reflecting their low internal energies (low vibrational/rotational temperatures). Cluster temperatures of bare $H^+(H_2O)_6$ and $H^+(H_2O)_6 \cdot M$ are estimated to be ∼200 K and several tens of Kelvins, respectively, by comparing the free OH stretch bandwidths with those in the IR spectra of temperature controlled $H^+(H_2O)_6$ reported by Wang et al. [30]. As mentioned above, the observed band patterns in Ne- and H_2-mediated spectra are accounted for by a comparable amount of the Eigen and the Zundel types, because both the red and blue bands are seen. On the other hand, Kr-, Xe-, N_2-, and CH_4-mediated spectra can mainly be attributed to the Zundel type isomer. In

particular, the Kr-mediated spectrum is exclusively for the Zundel type as that of Ar. Detailed descriptions on each spectrum are given below.

In the spectrum of $H^+(H_2O)_6 \cdot Ne$, a band splitting of $\sim 3,300$ cm^{-1} band is accounted for by the smaller bandwidth, which makes it possible to distinguish the two quasi-degenerated hydrogen-bonded OH stretches. An alternative explanation is the contributions made by internal rotation isomers of the Eigen type. In $H^+(H_2O)_6 \cdot Ar$ and $H^+(H_2O)_6 \cdot Kr$, the majority is clearly the Zundel type and only tiny contributions of the Eigen type can be seen. In the spectrum of $H^+(H_2O)_6 \cdot Xe$, the main component is also the Zundel type. However the Eigen marker bands can be observed more strongly than in the Ar- and Kr- mediated spectra. In this spectrum, weak bands (indicated by an asterisk) at the lower frequency side of both the v_1 (3,652 cm^{-1}) and v_3 (3,738 cm^{-1}) bands imply that Xe is bound to a free OH via the OH···Xe interaction. In the spectrum of $H^+(H_2O)_6 \cdot H_2$, the free OH bands are similar to those in $H^+(H_2O)_6 \cdot Ne$, showing coexistence of the Eigen and Zundel types. This is consistent with the triplet features in the hydrogen-bonded OH stretch region. The N_2 and CH_4- mediated spectra also show extra bands (indicated by an asterisk) in the free OH stretch region. These bands are due to the relatively strong OH···N_2/CH_4 type interactions. In these spectra, one of the Eigen bands ($\sim 3,000$ cm^{-1}) looks to be shifted to $\sim 3,050$ cm^{-1}. This shift would be due to the perturbations of the messenger. For the H_2, N_2, CH_4-mediated spectra, IR bands of the messengers themselves are expected. We extended the measurement range to between 2,200 and 4,500 cm^{-1}. However, only the CH stretch of CH_4 ($\sim 2,900$ cm^{-1} in Fig. 4.16) was observed.

The effect of the number of messengers should be also investigated. Figure 4.17 shows IR spectra of $H^+(H_2O)_6 \cdot (H_2/Ar/Ne)_m$ obtained by monitoring the $H^+(H_2O)_6$ signal. No signals were detected in other fragment channels. The observed spectra of $m \geq 2$ clusters show similar features to those of the $m = 1$ clusters. For $H^+(H_2O)_6 \cdot Ar_{m \geq 2}$, the weak features of the Eigen type can be seen, however, the Zundel type still remains in the majority. These results show that dependence on the number of messengers is not significant. The IR spectra of $H^+(H_2O)_6 \cdot M_m$ show that the Zundel type can be observed in all the systems, while the comparable contribution of the Eigen type appears only in the Ne- and H_2-mediated spectra. In the following section, we discuss the origins of this isomer-selectivity.

First, we examine the internal energy effect, because attachment of messengers lowers the upper limit of the internal energy (vibrational temperature) of systems to their binding energies with messengers. This lowering of the internal energy may reduce the number of accessible isomers. The observed messenger-dependent isomer-selectivity, however, is inconsistent with such simple expectation. The binding energy of each messenger would follow the order: Ne < Ar < Kr < Xe for rare gas series, and H_2 < N_2 < ($\sim$) CH_4 for molecular messengers. These orders are estimated by the orders of polarizabilities (for rare gases) [96] and proton affinities (for molecules) [97], respectively. In addition, the previously reported spectra of $H_5O_2^+ \cdot H_2$ and $H_5O_2^+ \cdot Ar$ show similar band patterns, and they suggest H_2 and Ar have similar binding energies [37–40]. These orders of the binding energies would be the same as that of the maximum internal energy (vibrational temperature) of the

Fig. 4.17 Infrared photodissociation spectra of $H^+(H_2O)_6 \cdot (H2/Ar/Ne)_m$ in the OH stretch region. The bands in *blue* and *red* are markers of the Eigen and Zundel type isomers, respectively
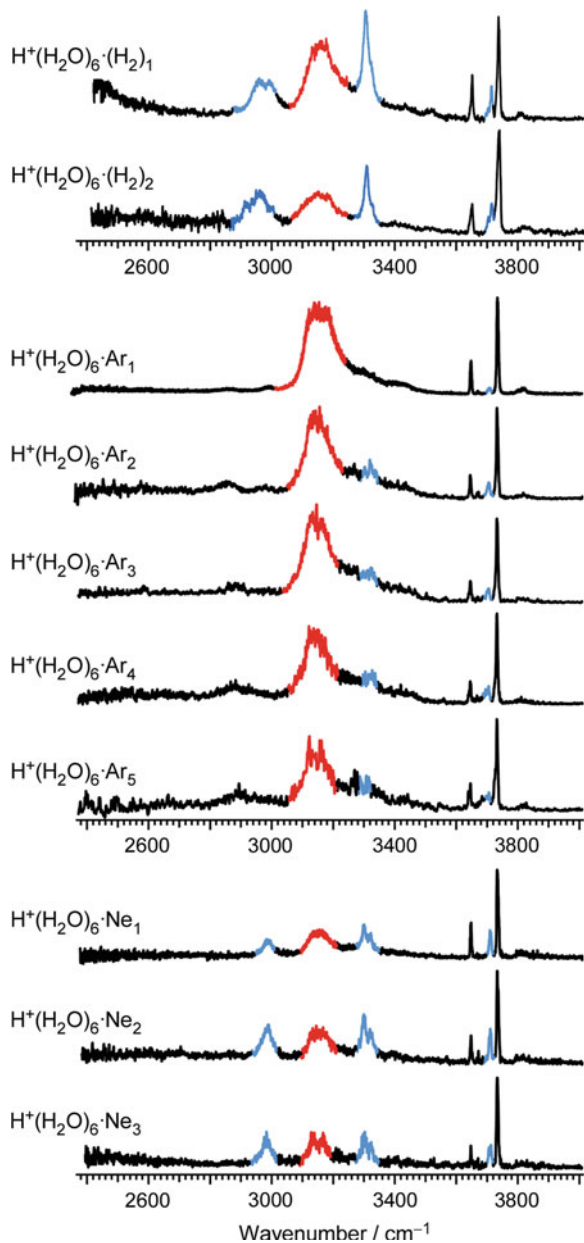
tagged clusters. If the lower energy isomer is preferred in lower internal energy, the minimum number of isomers can be seen in the "coldest" (the lowest internal energy) system (i.e., $H^+(H_2O)_6 \cdot Ne$). However, two types of isomers clearly coexist in $H^+(H_2O)_6 \cdot Ne$ while only one isomer can be found in "warmer" systems such as $H^+(H_2O)_6 \cdot Ar$ and $H^+(H_2O)_6 \cdot Kr$. Furthermore, although $H^+(H_2O)_6 \cdot H_2$ and

H$^+$(H$_2$O)$_6$·Ar should have similar internal energies, isomer distributions in these systems quite different from each other. These results mean that the internal energy does not necessarily correlate with the isomer distribution. That is, the isomer distribution does not necessarily follow the Boltzmann distribution expected by the vibrational temperature.

As for the relative stability of the Eigen and Zundel isomers, we also need to examine the relative energies including messengers. Recently, theoretical studies have suggested non-negligible effects of messengers themselves in the energetics of other systems [57, 62, 95, 98, 99]. These results suggest that inert gas attachment would affect potential energy surfaces (relative energies of isomers and barrier heights of interconversion). For example, the Ar-tagging of the V$_3$O$_{6-8}$ clusters causes clear reordering of the relative energies of isomers [99]. We carried out density functional theory calculations for H$^+$(H$_2$O)$_6$, H$^+$(H$_2$O)$_6$·Ar, and H$^+$(H$_2$O)$_6$·Ne. In the present calculations for the bare system, the Zundel type is more stable than the Eigen type by 3.9 kJ mol^{-1} (Fig. 4.14). This is consistent with previously reported calculations [21, 95]. The most stable locations of Ar with the Eigen and Zundel isomers were searched for by testing many messenger locations systematically, as described in Sect. 4.2. Figure 4.18 shows the most stable structures of the Eigen and Zundel isomers of H$^+$(H$_2$O)$_6$·M found in the present search. As in Fig. 4.18, the most favorable positions of the messengers are similar to those in H$^+$(H$_2$O)$_{4,\ 5}$·M: H$_2$ favors the front of an OH bond of H$_2$O; Ar/Ne lies near the H$_3$O$^+$ or shared proton. As for Ne and Ar, in the Eigen isomer, Ar/Ne is located below the H$_3$O$^+$ umbrella, while Ar/Ne is located near the shared H$^+$ in the Zundel isomer. Recent theoretical calculations have suggested that the
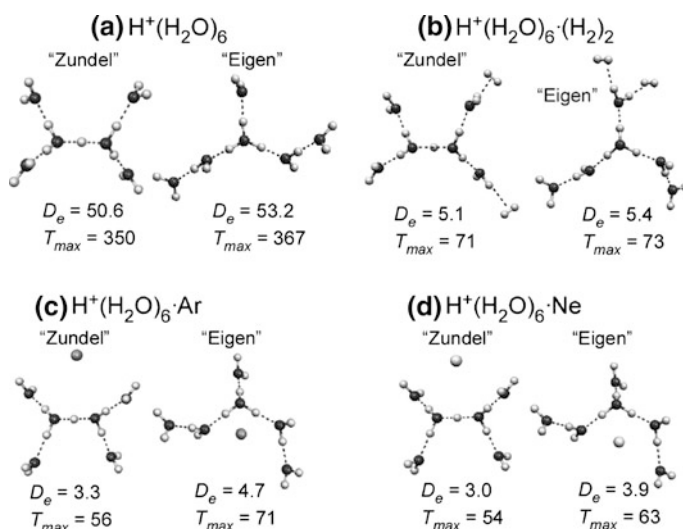
Fig. 4.18 The results of DFT (ωB97X-D/6-311++G(3df,2p)) calculations for (**a**) H$^+$(H$_2$O)$_6$, (**b**) H$^+$(H$_2$O)$_6$·(H$_2$)$_2$, (**c**) H$^+$(H$_2$O)$_6$·Ar, and (**d**) H$^+$(H$_2$O)$_6$·Ne, respectively. The most stable structures, calculated binding energies D_e (in kJ/mol), and maximum temperatures T_{max} (in K) are shown

messenger locations in $H^+(H_2O)_4 \cdot Ar$ (Eigen type) and $H^+(H_2O)_2 \cdot H_2$ (Zundel type) are quite similar to those in Fig. 4.18 [41, 57]. Figure 4.18 also shows the relative stability of each optimized structure of $H^+(H_2O)_6 \cdot M$. These results imply that the relative stability of the Eigen and Zundel isomers is not affected significantly upon inert gas attachment. These calculations are consistent with the Zundel selections of Ar; however, they are inconsistent with the coexistence of two types in the Ne-mediated spectrum as well as the bare $H^+(H_2O)_6$ spectrum. For further discussion, to estimate the entropic effect, we also calculated temperature-dependent abundance of Eigen and Zundel types with Ne/Ar (Fig. 4.19). However, we could not see any messenger dependence. According to these results, energetics is a less plausible reason for the observed messenger-dependent isomer-selectivity. However, we note that energetics reasons are not completely excluded because relative energies depend on calculation methods, especially the (anharmonic) zero-point vibration correction, as Kuo has reported (see also ΔE_0 and ΔE_e in Fig. 4.20) [95]. Further calculations are, however, beyond the scope of this study.
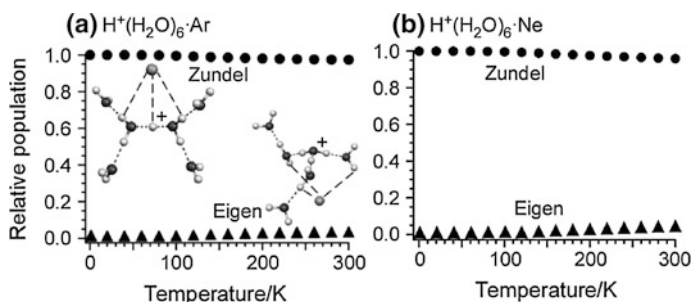
Fig. 4.19 Calculated temperature-dependent abundance of two isomers in $H^+(H_2O)_n \cdot M$ (**a**) $H^+(H_2O)_6 \cdot Ar$, (**b**) $H^+(H_2O)_6 \cdot Ne$
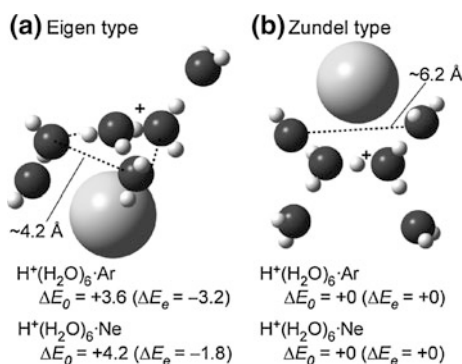
Fig. 4.20 The most stable structures of the (**a**) Eigen and (**b**) Zundel type $H^+(H_2O)_6 \cdot Ar$ (see text and the supporting information). Their relative energies and these of corresponding $H^+(H_2O)_6 \cdot Ne$ calculated at the M06-2X/6-311++G(3df,2p) level were also shown in kJ mol^{-1}. ΔE_0 includes zero-point energy corrections while ΔE_e does not. Adopted from Ref. [18] (Copyright 2011 PCCP Owner Societies)

If the energetics based on the present calculation is correct, the Zundel type is more stable than the Eigen type and it is expected to be the major spectral carrier in all the spectra. In Ne- and H_2-mediated spectra, however, a clear contribution of the Eigen type can be observed. This observation implies that the unexpected high-energy isomer trapping occurs in Ne- and H_2-tagging. Because of the finite height of the isomerization barrier in $H^+(H_2O)_6$ (see Fig. 4.14), once the Eigen is formed and vibrationally cooled, conversion to the Zundel type would not occur even though the Zundel type is more stable. Figure 4.21a shows a conceptual diagram of this situation. In this context, observation of the higher-energy isomer (Eigen type) would be attributed to the carrier gas-dependent jet-cooling efficiency. It has been shown that more efficient cooling in a supersonic jet expansion can be achieved by using a heavier carrier gas [100]. Because the clusters considered here were formed in an expansion of the pure messenger carrier gas, the observed isomer-selectivity is consistent with the assumption that a heavy carrier gas will lead to the most stable isomer (Fig. 4.21b). The Ne- and H_2-mediated spectra show similar free OH bandwidths to those in Ar- and Kr- mediated spectra, indicating their vibrational/rotational temperatures are similar. However, some population of the systems would be trapped at the Eigen type (high-energy) minimum (Fig. 4.21a). In other words, Ne- and H_2-tagged clusters would be "warmer" in the isomer distribution while they are cold in vibrational/rotational temperature. It should be also noted that the bare $H^+(H_2O)_6$ cluster contains both the isomers even though they formed in an Ar expansion (5 MPa). This would be because the relatively high vibrational temperature ($\sim$200 K), i.e., the high internal energy, of the bare cluster makes the isomerization between the Zundel and the Eigen types possible (Fig. 4.21c).

An alternative interpretation of the observed isomer-selectivity is a selective cluster formation process in a supersonic jet expansion. If we assume that the trapping of the higher energy isomer works in all the carrier gases, the Ne- and H_2-mediated spectra reflect the "unperturbed" Eigen/Zundel balance in the jet expansion. This is essentially the same as that in bare $H^+(H_2O)_6$. The spectra of Ar, Kr, and others are considered to show an unexpected selectivity toward the Zundel type. Here, we examine the possibility of a selective formation of tagged
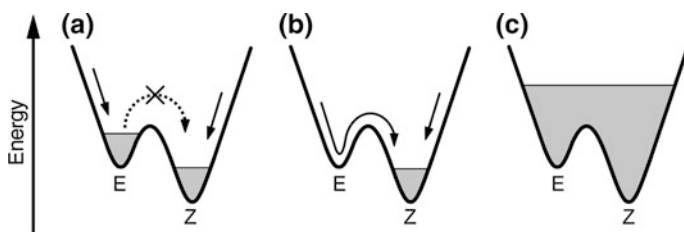
Fig. 4.21 Conceptual diagrams of carrier gas (messenger)-dependent cooling processes assumed in this study. *Curves* represent the potential energy surface along the Eigen (E)-Zundel (Z) isomerization. *Arrows* show the suggested cooling processes in a jet expansion. Populated energy regions of the systems are displayed in *gray*. **a** Case for light gases such as Ne and H_2. **b** Case for heavier gases such as Ar and Kr. **c** Situation for bare $H^+(H_2O)_6$, which has high internal energy. Adopted from Ref. [18] (Copyright 2011 PCCP Owner Societies)
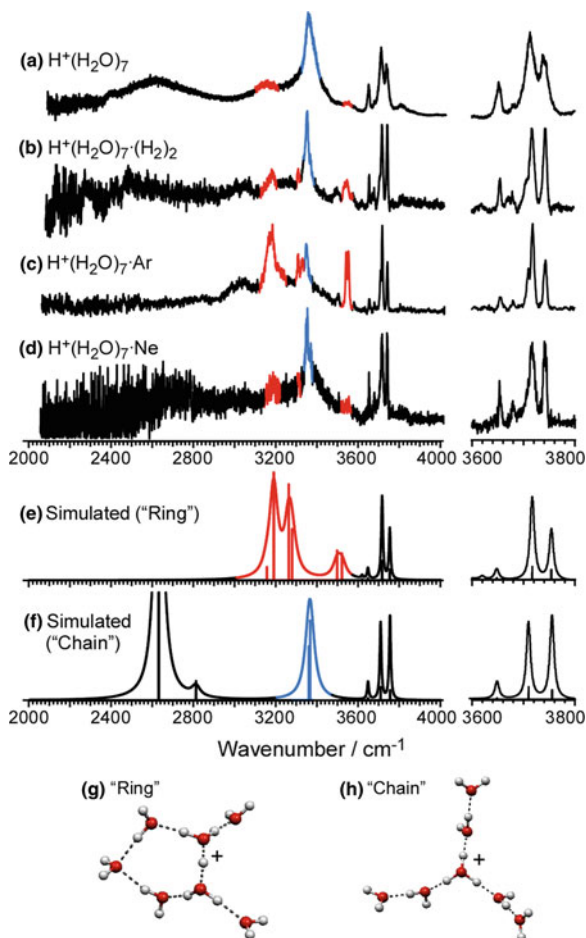
clusters by focusing on the estimated structures of $H^+(H_2O)_6 \cdot Ar$. In Fig. 4.20, Ar prefers locations near the charged site (shared proton or H_3O^+). We found that a larger space is available for a messenger in the Zundel type relative to the Eigen type. In the Eigen type, three water molecules in the first solvation shell of H_3O^+ inhibit an Ar-attachment towards H_3O^+ by forming a triangle just below the H_3O^+ umbrella (O–O distances ~ 4.2 Å, see Fig. 4.20). On the other hand, in the Zundel type, the O–O distance between the two terminal H_2O molecules (see Fig. 4.20) is ~ 6.2 Å and it seems to be easier for Ar to approach the charge. It is expected that these different spatial environments could affect a yield of each isomer in the supersonic jet. On the basis of this assumption, larger messengers may favor the Zundel type, in which a larger space is available. Sizes of the messengers considered here would follow the order; Ne $(2.75) < H_2$ $(2.93) < Ar$ $(3.41) < N_2$ $(3.70) < CH_4$ $(3.78) < Kr$ $(3.83) < Xe$ (4.06), where the reported Lennard-Jones (12–6) parameters (in Å) [101] are given in parentheses. In this order, we can see the trend that larger messengers are Zundel-selectors. The minor contribution of the Eigen type in the N_2-, CH_4-, and Xe-mediated spectra would be attributed to the contribution of the different messenger sites. The free OH band splitting in these spectra implies that the messenger locates itself in front of a free OH. In this position, the spatial effect or the steric repulsion would be less important than in the structures displayed in Fig. 4.20. These positions are rationalized by relatively larger proton affinities of N_2 and CH_4, and by the larger size of Xe, which would avoid the small space around the charge. Although we have not determined the messenger site experimentally and the formation processes of tagged-clusters remain unknown, such a selective formation is one of the plausible origins of the messenger-dependent isomer-selectivity.

In the above discussions, we discussed some plausible explanations for the observed isomer-selectivity. At the present stage, however, we cannot determine the exact mechanism. Furthermore, isomer-selectivity upon tagging should depend on the shape of the potential energy surface, especially isomerization barriers. In spite of such ambiguity, this study implies the suitable choice of the messenger in photodissociation spectroscopy of similar systems, such as various hydrated clusters. Xe, CH_4, and N_2 can cause some complex band patterns due to the relatively large perturbations. In this regard, Ne, Ar, Kr, and H_2 are better for spectroscopic purposes. Ne and H_2 are expected to be useful to survey isomers observed in the bare system, with lowering vibrational temperature. On the other hand, Ar and Kr would reduce the variety/number of isomers observed.

4.3.1.5 $H^+(H_2O)_7$

In the case of $H^+(H_2O)_6$, only the balance between the chain type, simplest hydrogen-bonded network motif, isomers have been probed. In the next stage, isomer distribution, including higher-order networks such as ring motifs, should be probed in order to study much more complicated network systems. The $H^+(H_2O)_7$ system is known as the smallest size in which the ring network arises (Fig. 4.22g)

(a) H$^+$(H$_2$O)$_7$

(b) H$^+$(H$_2$O)$_7$·(H$_2$)$_2$

(c) H$^+$(H$_2$O)$_7$·Ar

(d) H$^+$(H$_2$O)$_7$·Ne

(e) Simulated ("Ring")

(f) Simulated ("Chain")

Wavenumber / cm^{-1}

(g) "Ring"   (h) "Chain"

in addition to chain type isomers [21]. We can, therefore, probe the balance
between chain and ring network motifs.

Figure 4.22a–d shows IR spectra of bare, H$_2$-tagged, Ar-tagged, and Ne-tagged
H$^+$(H$_2$O)$_7$, respectively. H$^+$(H$_2$O)$_7$ is also a system in which mainly two isomers
coexist, as demonstrated by Jiang et al. [21]. Figure 4.22g, h shows structures of
the major isomers and Fig. 4.22e, f presents simulated spectra of these isomers,
respectively. Figure 4.23 shows calculated structures and energies of tagged
H$^+$(H$_2$O)$_7$ for comparison. Table 4.1 collects frequencies and assignments of
selected bands. The clear signature of the ring isomer is the bands at around
3,550 cm^{-1} (Fig. 4.22e) [21]. In the case of bare H$^+$(H$_2$O)$_7$, these marker bands
are quite weak, indicating the main part of the spectrum can be accounted for by
the chain type isomer (Fig. 4.22a). Other isomers can also populate as indicated in
the band at ~3,680 cm^{-1}, because this band is assigned to 3-coord H$_2$O and both of
the two major isomers do not include such a H$_2$O molecule [21]. However, as their

Fig. 4.23 The results of DFT (ωB97X-D/6-311++G(3df,2p)) calculations for **a** $H^+(H_2O)_7 \cdot (H_2)_2$, **b** $H^+(H_2O)_7 \cdot Ar$, and **c** $H^+(H_2O)_7 \cdot Ne$, respectively. The most stable structures, calculated binding energies D_e (in kJ/mol), and maximum temperatures T_{max} (in K) are shown

(a) $H^+(H_2O)_7 \cdot (H_2)_2$

"Ring"   "Chain"

$D_e = 5.6$ $D_e = 4.0$
$T_{max} = 71$ $T_{max} = 55$

(b) $H^+(H_2O)_6 \cdot Ar$

"Ring"   "Chain"

$D_e = 4.9$ $D_e = 3.3$
$T_{max} = 68$ $T_{max} = 50$

(c) $H^+(H_2O)_6 \cdot Ne$

"Ring"   "Chain"

$D_e = 4.2$ $D_e = 2.6$
$T_{max} = 63$ $T_{max} = 43$
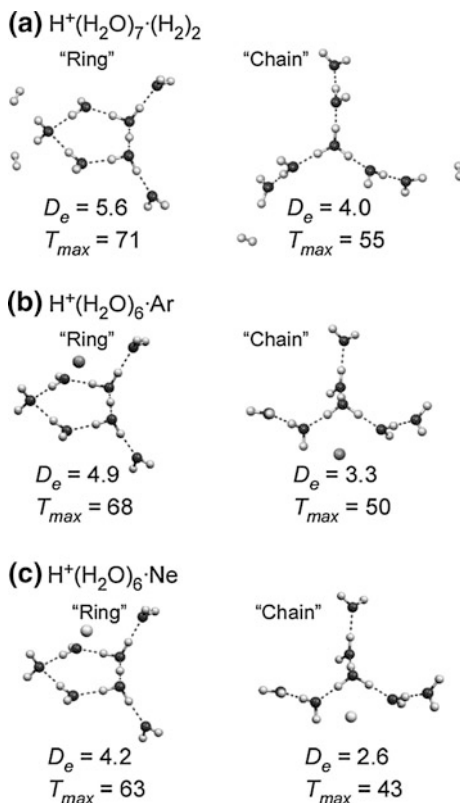
contribution is likely to be small, we focus the discussion only on the ring isomer (with the Zundel core) and chain isomer (Eigen core).

As shown in the previous Ar-tagging experiment by Headrick et al., the features of the ring isomer become dominant also in the present spectrum of $H^+(H_2O)_7 \cdot Ar$ and their bandwidth becomes narrower than the bare cluster [40]. These results show the isomer-selectivity and lowering of the internal energy upon the Ar-tagging. On the other hand, the $H^+(H_2O)_7 \cdot Ne$ spectrum shows similar spectral signatures to those of the bare cluster except for the narrower bandwidths. As for the isomer distribution, the spectrum of $H^+(H_2O)_7 \cdot (H_2)_2$ seems to be an intermediate case between the bare/Ne-tagged and Ar-tagged clusters because the marker bands of the ring isomer are substantially weaker than in the Ar-tagged cluster but stronger than in the bare/Ne-tagged clusters. In this system we achieved broader and finer tuning of the isomer distribution in hydrated clusters than in the case of $H^+(H_2O)_6$. These results also suggest that the surprising isomer-selectivity of Ar is the strongest and H_2 comes second. Ne is the weakest perturber to the isomer-distribution of the bare clusters. These results are quite similar to those in the $H^+(H_2O)_6$ system.

Here we comment on the entropic effect, which would be important in the balance between the ring and chain isomers. The ring isomer has more (seven)

H-bonds than chain (six) and therefore it is enthalpically favored while its relatively rigid ring framework lowers entropy relative to the flexible chain [21, 89, 102]. These considerations suggest that the ring isomer is dominant in lower temperature while the chain becomes more preferred at higher temperatures. A recent theoretical study indicates that the transition temperature of this switch is ~ 120 K [89]. Such an entropic effect was considered to explain the difference between the previously reported spectra of $H^+(H_2O)_7$ and its Ar-tagged cluster, because the Ar-tagged cluster was "colder" than the bare cluster and then the ring isomer was expected to be dominant [40, 89]. However, the present findings on the Ne- and $(H_2)_2$-tagged clusters conflict with such a simple interpretation due to the entropic effect on the isomer distribution. In the "coldest" system, $H^+(H_2O)_7 \cdot Ne$, the signature of the ring is very weak, meaning vibrational cooling upon the inert gas tagging is not necessarily accompanied by dominant population of enthalpically favored isomers. This conclusion is essentially the same as in $H^+(H_2O)_6$ although the entropic effect in this system is expected to be much more remarkable.

For spectroscopic purposes, as in the case of $H^+(H_2O)_6$, we found that the use of various messengers is a quite powerful tool to assign isomer (hydrogen-bonded network)-specific spectral features. Figure 4.24 shows the expanded spectra of Fig. 4.22. We assigned the red and blue bands in Figs. 4.22 and 4.24 to those of the ring and chain isomers, respectively. These spectral assignments can be done according to the following simple analyses. In the $H^+(H_2O)_7 \cdot Ne$ spectrum, the 3,550 cm^{-1} band is weaker, indicating the main component is the chain isomer. The main band in this spectrum (3,350 cm^{-1}) is, therefore, assigned to that of the chain isomer (blue). In the H_2- and Ar-mediated spectra, the bands at essentially the same frequency are also attributed to the chain isomer (blue bands). In the Ar-mediated spectrum, the bands which are weak in the Ne-mediated spectrum have larger intensities. These bands can be assigned to the ring isomer (red bands).

Fig. 4.24 a–d Expanded IR spectra of bare, H_2-, Ar- and Ne-tagged $H^+(H_2O)_7$, respectively. The bands in *red* show those of the ring isomer. The bands in *blue* show those of the chain isomer. *Dashed lines* are eye-guides. Adopted from Ref [19] (Copyright 2012 American Chemical Society)
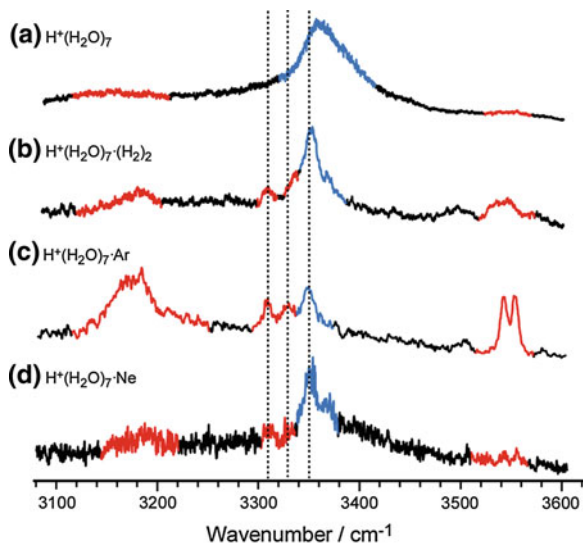
This is because they are accompanied by the emergence of the $3,550 \text{ cm}^{-1}$ bands, which are the marker of the ring isomer. Following a similar consideration of categories, the bands in the H_2-mediated spectrum can be classified as shown in Figs. 4.22b and 4.24b. Such experimental efforts make it easier to compare the experimental and simulated spectra and assign each band. In the $3,300–3,400 \text{ cm}^{-1}$ region, several bands of both the isomers can be seen and the previously reported assignments were not isomer-resolved [21]. By virtue of the isomer distribution control, each band can be assigned as follows. The bands at $\sim 3,180$, $\sim 3,310$, and $\sim 3,330 \text{ cm}^{-1}$ can be attributed to the hydrogen-bonded OH stretches of the $H_5O_2^+$ moiety of the ring; $\sim 3,350 \text{ cm}^{-1}$ band is due to the hydrogen-bonded OH stretch of the 2-coord H_2O moiety in the chain. We emphasize that these spectroscopic assignments are very difficult without the isomer separation by using multiple messengers, even if simulated spectra are available. We note we did not distinguish isomer types beyond the chain and ring type. Similar but different minor structures would arise as in previous studies. Further discussion on this aspect needs more experimental efforts such as IR–IR hole-burning spectroscopy, which enables us to measure isomer specific IR spectra using isomer-specific IR transition [27].

4.3.1.6 $H^+(H_2O)_8$

Figure 4.25a–c shows IR spectra of bare, H_2- and Ar-tagged $H^+(H_2O)_8$, respectively. Figure 4.26 presents calculated results from the corresponding systems. Table 4.1 collects frequencies and assignments of selected bands. Unfortunately,

Fig. 4.25 a–d IR spectra of bare, H_2-, and Ar-tagged $H^+(H_2O)_8$, respectively. The *red band* is a marker band of the structure in **e** (3-coordinated H_2O). **d** DFT-simulated IR spectrum of the structure in **e** obtained with the B3LYP/6-31+G(d) level. *Dashed lines* show a plausible correspondence between the experiment and theory. **e** Optimized cluster structure of $H^+(H_2O)_8$. The OH bond of 3-coordinated H_2O is highlighted in *red*. Adopted from Ref. [19] (Copyright 2012 American Chemical Society)
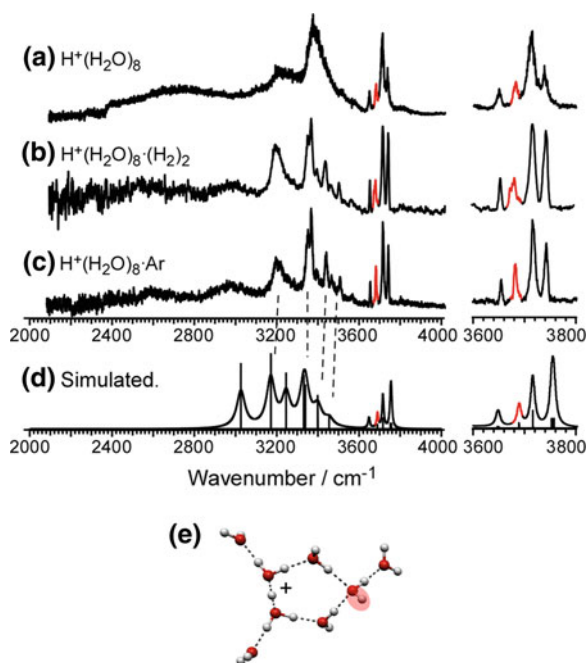
Fig. 4.26 The results of DFT (ωB97X-D/6-311++G(3df,2p)) calculations for **a** $H^+(H_2O)_8 \cdot (H_2)_2$, **b** $H^+(H_2O)_8 \cdot Ar$, and **c** $H^+(H_2O)_8 \cdot Ne$, respectively. The most stable structures, calculated binding energies D_e (in kJ/mol), and maximum temperatures T_{max} (in K) are shown

(a) $H^+(H_2O)_8 \cdot (H_2)_2$

$D_e = 4.7$
$T_{max} = 58$

(b) $H^+(H_2O)_8 \cdot Ar$

$D_e = 5.0$
$T_{max} = 63$

(c) $H^+(H_2O)_8 \cdot Ne$

$D_e = 4.3$
$T_{max} = 57$
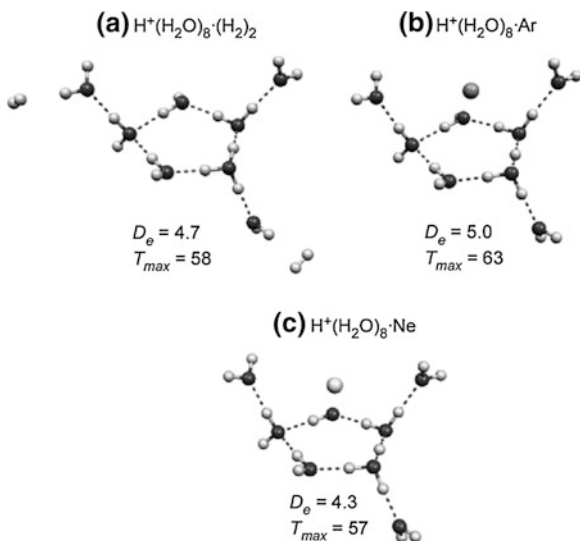
significant spontaneous dissociation of $H^+(H_2O)_8 \cdot Ne$ made the measurement of its spectrum difficult. In the previous studies of $H^+(H_2O)_8$, it has been suggested that the branched ring structure (Fig. 4.25e) reproduces the experimental spectrum of the bare cluster well (Fig. 4.25d) [21, 103]. This structure is evidenced with the band of the 3-coordinated water molecule at around 3,680 cm^{-1} as highlighted in red in Fig. 4.25. Coexistence of many isomers has been also implied, though further discussion has been difficult due to a large number of possible isomers and limited information from the broadened spectrum [21, 103, 104]. In Fig. 4.25, the Ar-mediated spectrum is reproduced well by the ring isomer as reported previously. Interestingly, the H_2-mediated spectrum shows a very similar trend to that of the Ar-tagged cluster even though Ar and H_2 show different isomer-selectivities in $H^+(H_2O)_{6,7}$. These results imply the isomer in Fig. 4.25e is dominant in the $H^+(H_2O)_8$ system and therefore it is always dominant even when the cluster is tagged by Ar/H_2. An alternative interpretation is that the effect of the Ar and H_2 attachment becomes similar at this size. Although the messenger technique successfully eliminates the broadening of the spectra, further investigation will also require the use of isomer-specific spectroscopy such as IR–IR hole-burning spectroscopy [27].

4.3.1.7 Summary for the Small Size Cluster Range

We probed the messenger effect on both the internal (vibrational) energy and isomer distribution in the IR spectroscopy of $H^+(H_2O)_n \cdot M$ ($n \leq 8$; M = Ne, Ar, $(H_2)_2$). All messengers can lower the internal energy, which generally causes, for example, spectral broadening. It was shown that the internal energy follows the

order: $H^+(H_2O)_n \gg H^+(H_2O)_n \cdot (H_2)_2 > H^+(H_2O)_n \cdot Ar > H^+(H_2O)_n \cdot Ne$, reflecting the interaction energy of each messenger. The magnitude of the perturbation to the isomer distribution in the bare system follows the order: $H^+(H_2O)_n \cdot Ar \gg H^+(H_2O)_n \cdot (H_2)_2 > H^+(H_2O)_n \cdot Ne \sim (H^+(H_2O)_n)$. While the origin of the isomer-selectivity is not necessarily clear, the present study, at least partly, achieves the control of both the internal energy and isomer distribution. By using such information, we next focus on large cluster systems to simplify and analyze spectra and network structures in detail.

4.3.2 Large Clusters $H^+(H_2O)_n$ $(n \leq 50)$

4.3.2.1 First Magic Number Region $H^+(H_2O)_{20–23}$

As first targets in large clusters, we focus on $H^+(H_2O)_{20–23}$ systems, which are in the so-called first magic number region. One of the most important areas of study on the properties of $H^+(H_2O)_n$ has been the origin of magic and antimagic numbers, in which the clusters show exceptionally higher or lower stability than in sizes immediately above or below the clusters or in larger sizes, respectively [8, 22, 23, 35, 41, 105–108]. In a typical mass spectrum of $H^+(H_2O)_n$ (as in Fig. 4.27), intensity anomalies can be seen at the $n = 21$ and 22 clusters [109–117]. After $n = 21$, intensity anomalies drop precipitously, with intensities of $n \geq 22$ showing a sharp decrease. The dissociation energy measurements show the high stability of $n = 21$ and the lower stability of $n = 22$ compared with neighboring sizes [113, 117]. In this meaning, $n = 21$ is a magic number while $n = 22$ is called an antimagic number cluster. Such magic number behaviors have been reported in various cluster systems, e.g., Xe_n, C_n, Na_n, and $(H_2O)_n^-$ [114, 118–121].
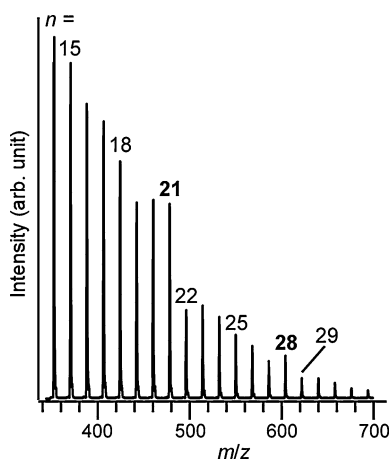
Fig. 4.27 Typical mass spectrum of $H^+(H_2O)_n$ formed in a supersonic jet expansion

The origin of these magic numbers is sometimes attributed to completion of a shell structure and/or a highly symmetric structure, as in C_{60} [118–120]. For $H^+(H_2O)_{21}$, similarly, a dodecahedral cage structure enclosing one H_2O or H_3O^+ (Fig. 4.28b) has been proposed [122], and several mass spectrometric studies support such a structure [123, 124]. As shown in Chap. 3, IR photodissociation spectroscopy of size-selected $H^+(H_2O)_n$ has succeeded in identifying the completion of such a closed cage (or a hydration shell) structure formation at $n = 21$ (Fig. 4.28a, b) [8, 22, 23, 35, 105, 106, 125]. This observation has stimulated many theoretical studies mainly on the cage type structures of $n = 21$ [22, 26, 107, 126, 127].

Despite the success of this magic number ($n = 21$) cluster, the structure of the antimagic $n = 22$ cluster has been ambiguous. The structure of the antimagic number cluster should provide an important insight on the hydrogen bond network evolution following the completion of the hydration shell or cage structure. Five groups have reported the IR spectrum of $n = 22$ using various cluster sources (Fig. 4.29). However, a very similar trend to that of $n = 21$ has always been observed [8, 22, 23, 35, 105, 106, 125]. These results apparently imply that structures of both the magic and antimagic number clusters are quite similar closed cages in spite of their very different stabilities. On the other hand, Singh et al. have carried out large-scale computations for $n = 21$ and 22, and reported that one of the most stable structures of $n = 22$ is the $H^+(H_2O)_{21}$-like dodecahedral cage with a water molecule bound to a dangling OH (Fig. 4.28c) [26]. In this structure, the free OH bands, which come from the loosely bound 1-coordinated (dangling) water molecule, were expected. Although five groups have reported IR spectra of $H^+(H_2O)_{22}$, no spectra show symmetric/antisymmetric stretching of dangling water (Fig. 4.29) [22, 23, 105, 106, 125]. Singh et al. have also reported that a thermal dynamic effect (i.e., fluctuation or large amplitude motion of the 22nd water) would suppress band intensities due to enhanced anharmonic couplings in the temperature range above several tens of Kelvins [26]. Because $H^+(H_2O)_n$ formed in a supersonic jet should have a finite temperature, estimated to be 100–200 K [22, 26, 30, 35, 105–107, 126, 127], experiments with much colder clusters are keenly awaited.
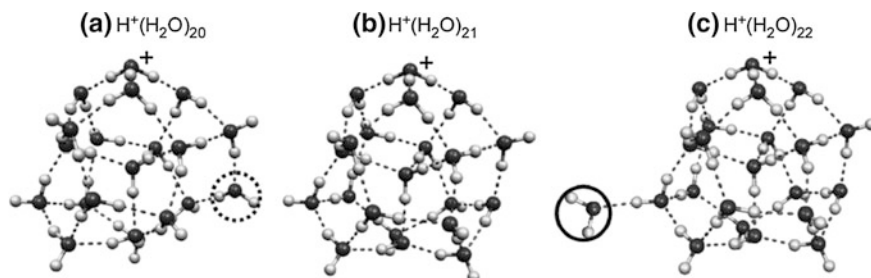
Fig. 4.28 Suggested structural evolution of $H^+(H_2O)_n$ in the $n = 20$–22 region. The 1- and 2-coordinated water molecules are indicated by the *solid* and *dotted circles*, respectively. All the other molecules are in 3- or 4-coordinated sites. **a** $H^+(H_2O)_{20}$, **b** $H^+(H_2O)_{21}$, **c** $H^+(H_2O)_{22}$. Adopted from Ref. [10] (Copyright 2011 American Chemical Society)
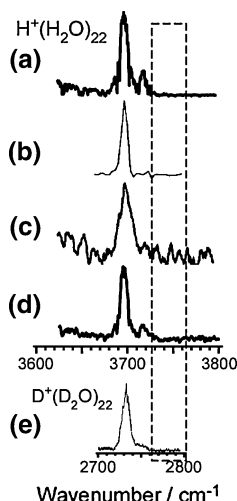
Fig. 4.29 Previously reported IR spectra of antimagic number cluster $H^+(H_2O)22$. *Open box in dashed line* shows region of antisymmetric stretching of dangling (1-coordinated) water. **a** Taken from Ref. [105] (Copyright 2004 American Association for the Advancement of Science). **b** Taken from Ref. [106] (Copyright 2004 American Association for the Advancement of Science). **c** Taken from Ref. [22] (Copyright 2005 American Institute of Physics). **d** Taken from Ref. [125] (Copyright 2007 American Institute of Physics). **e** Taken from Ref. [23] (Copyright 2009 American Chemical Society)

Fig. 4.30 Typical mass spectrum of $H^+(H_2O)_n \cdot (H_2)_m$ formed in the present cluster ion source
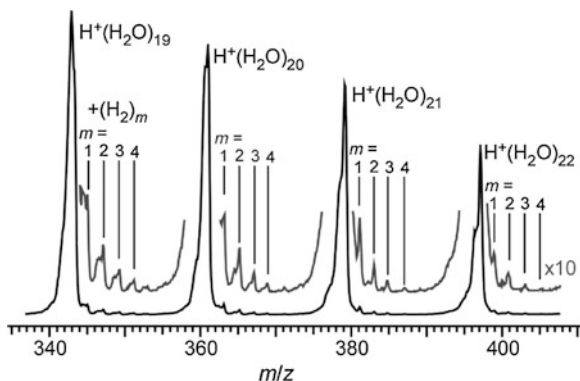
To eliminate the dynamic perturbations and investigate the origin of the magic/antimagic number clusters, we report here IR photodissociation spectra of cold $H^+(H_2O)_n \cdot (H_2)_3$ ($n = 20-23$). Before we focus on IR spectra, we present a typical mass spectrum of $H^+(H_2O)_n \cdot (H_2)_m$ (Fig. 4.30). The mass spectrum indicates the production of large, tagged clusters. In this spectrum, however, there are no remarkable magic/antimagic features. This is because rapid cooling of clusters leads to the absence of magic numbers, because once antimagic number clusters are stabilized, further dissociation of magic clusters does not occur. In our cluster source,

many collisions may induce rapid cooling because we used high-pressure (~ 10 MPa) carrier gas. Douberly et al. also reported a mass spectrum of $H^+(H_2O)_n$ without magic number features [23]. As the observed mass spectrum also imply, IR spectroscopic analyses is necessary for the investigation of magic/antimagic clusters.

Figure 4.31 shows IR photodissociation spectra of $H^+(H_2O)_{20-23}$ and $H^+(H_2O)_{20-23}\cdot(H_2)_3$ in the free OH stretch region. The estimated (vibrational) temperatures of $H^+(H_2O)_{20-23}$ and $H^+(H_2O)_{20-23}\cdot(H_2)_3$ are ~ 200 and ~ 50 K, respectively (see Sect. 4.2). In all the spectra, the strongest band at $\sim 3,700$ cm^{-1} is associated with the 3-coordinated water molecules and the band at $\sim 3,720$ cm^{-1} is due to the 2-coordinated waters [21, 105, 106]. The drastic decrease of the relative intensity of the 2-coordianted water band at $n = 21$ is the signature of the completion of the closed cage, as shown in Fig. 4.28a, b [22, 105, 106] (the minor contribution of the 2-coordinated waters is due to minor isomers having partially open cages. This aspect will be discussed later) [22]. This decrease can be observed in both the bare and tagged systems, suggesting that the H_2-tagging does not seriously perturb the hydrogen bond network evolution of $H^+(H_2O)_n$. That is, the hydrogen-bonded network structures of $H^+(H_2O)_n$ and $H^+(H_2O)_n\cdot(H_2)_3$ resemble each other. This is consistent with our findings on H_2-tagged $H^+(H_2O)_6$ (Sect. 4.3.1.4) [18]. However, only in the spectrum of $H^+(H_2O)_{22}\cdot(H_2)_3$, a unique band can be observed at $\sim 3,740$ cm^{-1}. This band has never been observed in the previously reported spectra of bare $H^+(H_2O)_{22}$ [22, 23, 35, 105, 106, 125]. This band, however, has been observed in small sized clusters $n < \sim 10$, and has been attributed to 1-coordinated (single acceptor) water molecules, because the frequency of this band is close to that of the anti-symmetric stretch vibration of a H_2O monomer
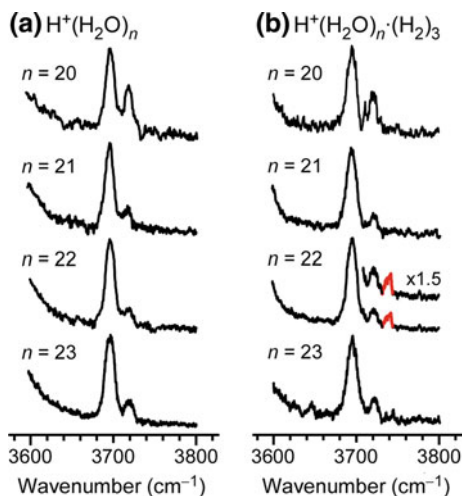
**Fig. 4.31** IR spectra of (**a**) $H^+(H_2O)_n$ (warmer) and (**b**) $H^+(H_2O)_n\cdot(H_2)_3$ (colder) in the free OH stretch region. The band in *red* is attributed to the 1-coordinated water molecule. Adopted from Ref. [10] (Copyright 2011 American Chemical Society)

$(3,756 \text{ cm}^{-1})$ [21, 40, 108]. Therefore, this band is uniquely assigned to the 1-coordinated water molecule as in Fig. 4.28c, which has two free OH bonds. We note that the symmetric stretch vibration of H_2O has a weaker IR intensity and would be overlapped by the broadened and intense hydrogen-bonded OH stretch band.

This observation of the 1-coordinated water molecule is the first experimental evidence for the structure having a dangling water molecule outside a large water cage, which was theoretically predicted by Singh et al. (Fig. 4.28c) [26]. In this structure, the 22nd water molecule is more loosely bound than the other water molecules in the closed cage, which are bound via three or four hydrogen bonds. This experimental identification supports the theory that the basis for the antimagic nature of $H^+(H_2O)_{22}$ is the existence of this dangling water molecule. A similar structural explanation for the origin of an antimagic number has been reported for $Al^+(H_2O)_n$ [128]. The re-disappearance of the $\sim 3,740 \text{ cm}^{-1}$ band at $n = 23$ also indicates the exceptionality of the antimagic cluster of $n = 22$. Of course, the observed spectra should reflect the ensemble of various isomers; however, the drastic and clear size-dependent spectral patterns suggest that the present observation gets the essential origin of the antimagic number.

We also considered the implications of the spectral difference between $H^+(H_2O)_{22}$ and $H^+(H_2O)_{22} \cdot (H_2)_3$. The H_2-tagging clearly cools down clusters and this cooling should be the origin of the present observations. However, there are two different interpretations of the "cooling". One of them is vibrational cooling. This effect is validated in principle as mentioned above and in the experimental section. If this vibrational cooling is a major factor, it could be suggested that the dangling water molecule in the outermost hydration shell exists in a bare $H^+(H_2O)_{22}$ system. However, this is not observable due to thermal and dynamic fluctuations at high temperatures ($> \sim 100$ K), as Singh et al. have predicted using Car-Parrinello MD simulations [26]. The H_2-tagging stitches the dangling water by cooling down the cluster. Figure 4.32a, b shows some conceptual schemes of this temperature (internal energy) dependence. The idea that one molecule moves while the closed shell moiety keeps the cage structure would be in agreement with the concept of the "premelting" reported, for example, with Na_n at the neighboring sizes (above and below) of the closed shells [129].

The other interpretation of the present "cooling" is the cooling of the isomer distribution, which increases the population of enthalpically favored isomers.
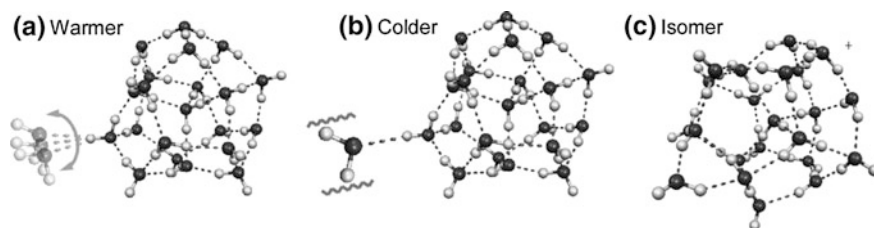
Fig. 4.32 Conceptual schemes of fluctuations of the dangling water molecule in (**a**) warmer and (**b**) colder $H^+(H_2O)22$. (**c**) Another isomer structure with no dangling H_2O

Although the lowering of internal energy (vibrational/rotational temperature) with tagging is not necessarily accompanied by cooling of the isomer distribution [18], a change of the isomer distribution is also a potential interpretation of the experimental observations. In this case, the structures with the 1-coordinated water are enthalpically favored and their population is lower in the bare and warmer systems than in the cold system, although this type of isomer would act as the culprit for the anti-magic behavior in the warmer system. Furthermore, in terms of a change in isomer distribution, messenger-induced isomer-selectivity [18] is an alternative possibility. We note that in our study on H_2-tagged $H^+(H_2O)_6$, no remarkable change in isomer distribution has been observed, while Ar- and Kr-tagged clusters show such a change [18]. We, however, cannot exclude this possibility at the present stage.

Next we will comment on the appearance of the 2-coordinated water band. As seen in Fig. 4.31, all the spectra of $n \geq 21$ have a minor band at ~3,720 cm^{-1}, which is attributed to 2-coordinated waters. This band is a signature of partially open cage isomers that are considered entropically favored and will become more dominant over completely closed cages at higher temperatures [22, 35, 106]. Several groups have reported the spectra of bare $H^+(H_2O)_{21,22}$ with no 3,720 cm^{-1} band, though their (vibrational) temperature is estimated to be higher than that of $H^+(H_2O)_{21,22}(H_2)_3$ [22, 23, 35, 106]. The present observation of the 3,720 cm^{-1} band in "cold" $H^+(H_2O)_{21,22}(H_2)_3$ indicates that the "cooling" upon the H_2-tagging is restricted to the lowering of internal energy (vibrational temperature) but it is not necessarily accompanied by the cooling of isomer distribution. In other words, some clusters are trapped in local minima and their vibrational and rotational motions are cooled down (such incompleteness of the thermal equilibrium should be noted in comparison with theoretical simulations). However, we emphasize that the structure with the 1-coordinated water is a calculated low-lying minimum [26] and the 1-coordinated water band has been missing in all the previously reported spectra of $H^+(H_2O)_{22}$ even though cold isomer distribution was achieved [8, 22, 23, 35, 105, 106, 125]. We think the discussion above supports the notion that the main effect of the H_2-tagging is vibrational cooling rather than isomer distribution change. The origin of the H_2-mediated spectral change would therefore be the vibrational cooling. Calculations by Singh et al. suggest the importance of several low-lying isomers of $H^+(H_2O)_{22}$ having a 2-coordinated water molecule [26].

For further examination of spectra, cluster structures, and messenger effects, we also used Ar as a messenger. The frequency region was also extended to the whole OH stretching region. Figure 4.33 shows IR spectra of $H^+(H_2O)_n$, $H^+(H_2O)_n \cdot (H_2)_3$, and $H^+(H_2O)_n \cdot Ar$ ($n = 20$–22) in the 2,200–4,000 cm^{-1} region. The broad band below $\sim 3,600$ cm^{-1} is due to the hydrogen-bonded OH stretches, while relatively sharp bands in the 3,600–3,800 cm^{-1} are assigned to the free OH stretches. All the spectra show similar spectral features, however, features are clearer and more easily seen in the spectra of colder $H^+(H_2O)_n \cdot (Ar/(H_2)_3)$. The most prominent difference between the colder and warmer clusters is the 3,550 cm^{-1} band, which has been assigned to the hydrogen-bonded OH stretches of the 3-coordinated (single H-bond acceptor-double H-bond donor: ADD type) water molecules [21, 22, 105, 106]. In the bare clusters, the 3,550 cm^{-1} band arises as a shoulder rather than a band, while

Fig. 4.33 IR spectra of (**a**) $H^+(H_2O)_{20-22}$, (**b**) $H^+(H_2O)_{20-22}\cdot(H_2)_3$, and (**c**) $H^+(H_2O)_{20-22}\cdot$Ar in the OH stretch region
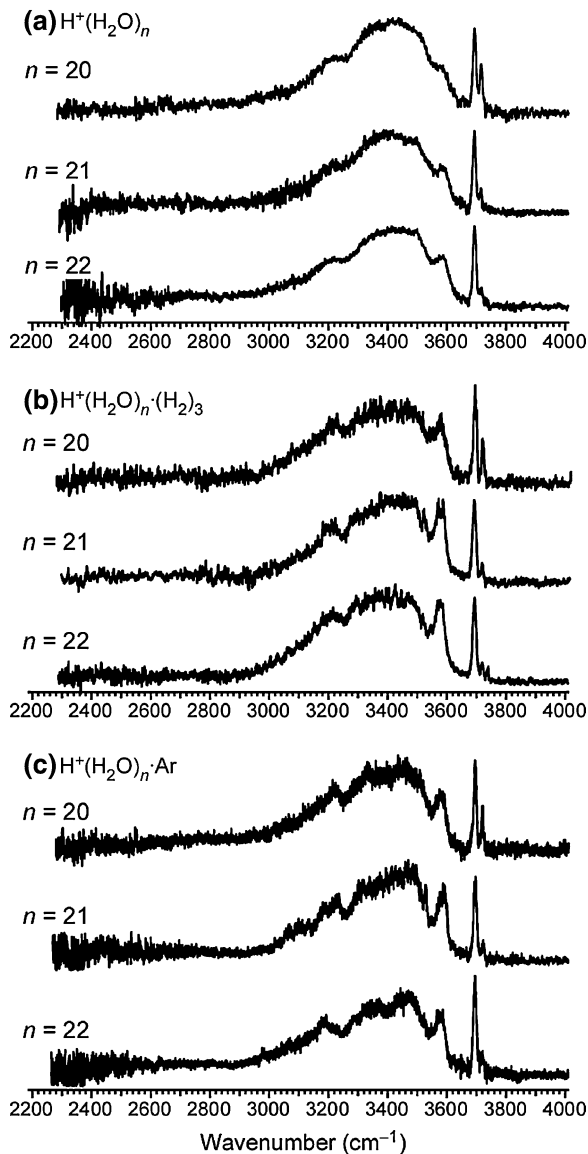
it becomes a clear band in the Ar/H_2-tagged clusters. In the previous study on bare $n = 18$–24 clusters, Douberly et al. have also reported the bandwidth of this $3,550$ cm^{-1} band becomes narrower as the cluster becomes colder [23]. Our present observations agree with their results. In addition to the $3,550$ cm^{-1} band, we can see similar narrowing of the $3,200$ cm^{-1} band, although the rigorous assignment of this band is difficult at the present stage (Suggested assignments are the 3- or 4-coordinated water band, the overtone of the bending of H_2O, and the signature of the $H_5O_2^+$ ion core [8, 21, 40]).

We also remark on vibration bands associated with the excess proton (H_3O^+). Recent theoretical calculations have predicted that bands of H_3O^+ stretches are expected to arise below 2,800 cm^{-1} and their absence in the observed spectra is also attributed to thermal or dynamic effects [22, 23, 26, 35, 106, 127]. Even in the present spectra with the H_2-tagging, no remarkable bands have been observed below 2,800 cm^{-1}. This implies that the band frequency of the H_3O^+ stretch is lower than $\sim 2,300$ cm^{-1}. This is consistent with recent theoretical calculations, including anharmonic corrections [130]. Another possibility is that much lower internal energy would be required to stop the proton motion.

As in small clusters, free OH behaviors are more sensitive to hydrogen bonding structures and dynamics. Figure 4.34 compares the expanded IR spectra of Fig. 4.33 in the free OH stretch region. All the series of the spectra show a drastic drop of the 2-coordinated water band ($\sim 3,720$ cm^{-1}) intensity from $n = 20$ to $n = 21$. This has been attributed to the formation of a closed cage structure at $n = 21$, the 1st magic number [22, 105, 106]. As for the antimagic number $n = 22$, only the spectrum of $H^+(H_2O)_{22} \cdot (H_2)_3$ shows the signature of the 1-coordinated water molecule, which attaches to the surface of the $H^+(H_2O)_{21}$ moiety at $\sim 3,740$ cm^{-1}. This band is missing in bare and Ar-tagged $H^+(H_2O)_{22}$. On the basis of these theoretical simulations, Singh et al. has proposed that the thermal fluctuation of the loosely-bound water on the cage surface induces anharmonic coupling which causes the absence of the band [26]. In this explanation, the marker band at $\sim 3,740$ cm^{-1} can be seen when the $n = 22$ cluster is cooled and thermal motion is suppressed. Although the Ar-tagging also shows the vibrational cooling effect as indicated by the bandwidth in the spectrum of $H^+(H_2O)_{22} \cdot Ar$, we could not observe the 3,740 cm^{-1} band. This result implies that the isomer distribution of the $H^+(H_2O)_{22}$ moiety in $H^+(H_2O)_{22} \cdot Ar$ is different from that in $H^+(H_2O)_{22} \cdot (H_2)_3$ and $H^+(H_2O)_{22}$. According to the spectral features, observed $H^+(H_2O)_{22} \cdot Ar$ may have cage structures consisting of all 22 water
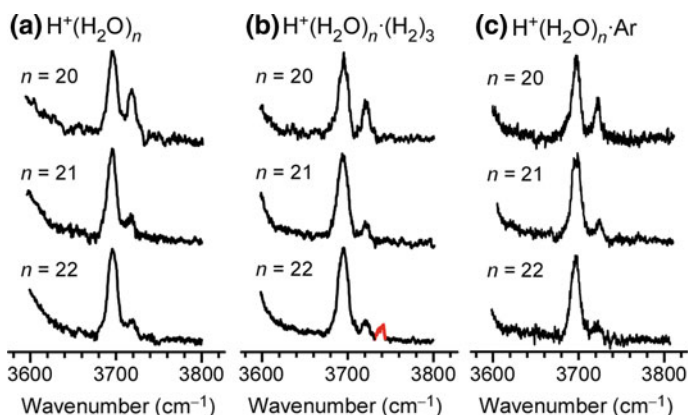
Fig. 4.34 IR spectra of (**a**) $H^+(H_2O)_{20-22}$, (**b**) $H^+(H_2O)_{20-22} \cdot (H_2)_3$, and (**c**) $H^+(H_2O)_{20-22} \cdot Ar$ in the free OH stretch region. The band in *red* is attributed to the one-coordinated (dangling) water molecule. Adopted from Ref. [20] (Copyright 2012 Elsevier)

molecules without any dangling water molecules (Fig. 4.32c). Such structures seem not to account for the origin of the antimagic number. However, a previous theoretical study has predicted such a cage structure also exists [26]. We have already demonstrated that the Ar attachment shows a large perturbation to isomer distribution [18]. The present suggestion that Ar changes the observable isomer type is in agreement with our findings. We note that there are numerous plausible isomers in the present size [26, 131]. For example, the presence of the 2-coordinated water band, which is the signature for partially open cage structures, indicates the coexistence of many other isomers. In conclusion, although the situation is very complicated, we characterized at least two types of the $n = 22$ system: One is a cage consisting of 21 water molecules with one dangling water (Fig. 4.32a, b) molecule and the other is a cage consisting of 22 water molecules (Fig. 4.32c).

4.3.2.2   The Second Magic Number Region $H^+(H_2O)_{27-29}$

As seen in the mass spectrum in Fig. 4.30, $n = 28$ and 29 are called the 2nd magic and antimagic numbers, respectively. However, there have been only a few spectroscopic studies on the 2nd magic number cluster $H^+(H_2O)_{28}$ [22, 35], and no spectroscopic studies have been reported for the antimagic cluster $H^+(H_2O)_{29}$, to the best of our knowledge. Wu et al. have reported IR spectra of $H^+(H_2O)_{28}$ and proposed a closed cage structure including two interior water molecules on the basis of theoretical calculations [22]. This study is the first report on the spectroscopic behavior of $H^+(H_2O)_n$ in the vicinity of the 2nd magic/antimagic number clusters. Figure 4.35 shows IR spectra of $H^+(H_2O)_{27-29}$ and $H^+(H_2O)_{27-29}\cdot(H_2)_3$. In all the sizes, the H_2 tagged clusters show clearer band separation than the bare clusters. However, we were unable to observe any other remarkable differences, such as relative band intensity or appearance of a new band. This result is in sharp contrast with the case of the 1st magic/antimagic number clusters. The present result implies the origin of the 2nd magic/antimagic number is not accessible with the present approach. At least, no signature of a dangling water molecule was observed, even in the cooled, antimagic number cluster. Another interpretation is

Fig. 4.35 IR spectra of (**a**) $H^+(H_2O)_{27-29}$ and (**b**) $H^+(H_2O)_{27-29}\cdot(H_2)_3$ in the free OH stretch region. Adopted from Ref. [20] (Copyright 2012 Elsevier)
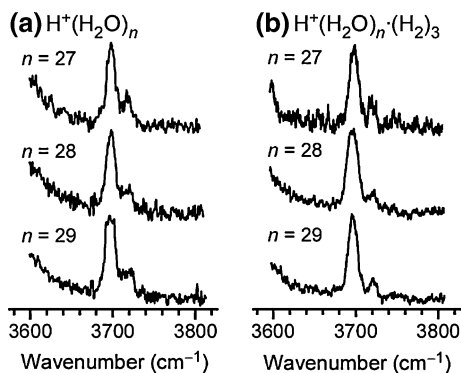
that the character of the 2nd magic/antimagic numbers is so weak that we could not observe it. This is reasonable because some mass spectrometric studies have shown the smaller intensity and greater stability changes in the $n = 28$–29 step than in the $n = 20$–21 step [112, 113, 115]. Unfortunately, further discussion is difficult at the present stage. Further experiments, such as systematic messenger experiments, cooling by other techniques, measurements of other vibrational bands are necessary to examine this complicated, large-scale hydrogen-bonded system.
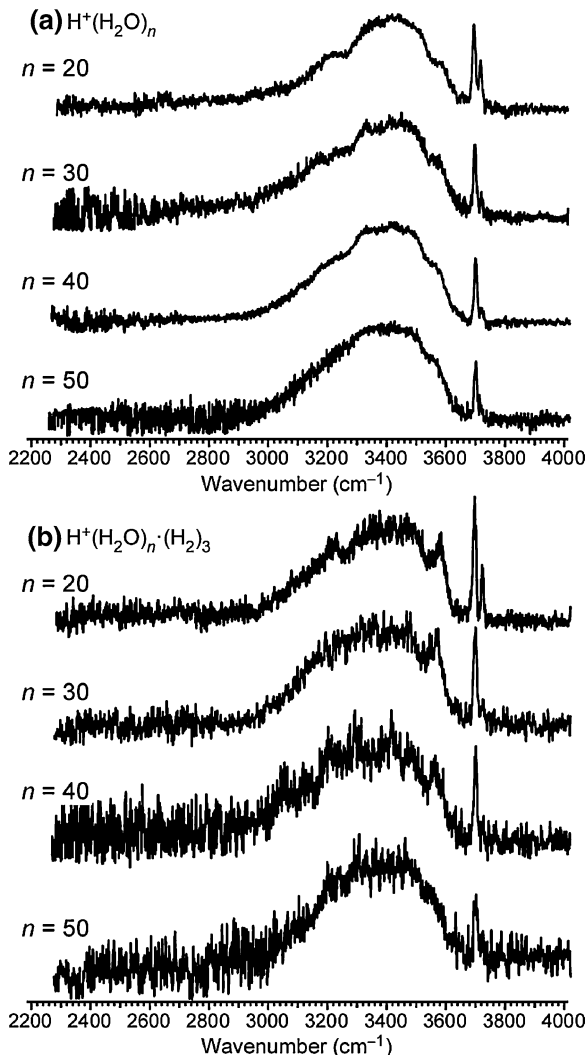
4.3.2.3 Much Larger Systems of $H^+(H_2O)_{20-50}$

As shown above, messenger-mediated cooling is a powerful tool to suppress the internal energy and dynamic motions of water molecules even in large clusters consisting of 10 or more molecules. Here, we applied this technique to clusters that were as large as possible. We optimized the cluster ion source (Sect. 4.2) and finally succeeded in measuring the inert gas-mediated spectra of large protonated water clusters up to $n = 50$ clusters. Messenger technique[18, 36–38, 40, 41, 57] has hitherto been applied mainly to smaller-sized clusters. IR spectra of $(H_2O)_{3-24}{}^-{\cdot}Ar$ reported by Roscioli et al. was a unique example which covered $n > 20$ systems [132]. To the best of our knowledge, $n = 50$ is the largest size that has ever been investigated with inert gas-mediated spectroscopy.

Figure 4.36b shows IR spectra of cold $H^+(H_2O)_{20-50}{\cdot}(H_2)_3$ in the OH stretch region. Figure 4.36a shows IR spectra of warmer, bare $H^+(H_2O)_{20-50}$ for comparison [8]. The broad band below $\sim 3{,}600$ cm^{-1} is due to the hydrogen-bonded OH stretches, while relatively sharp bands in the $3{,}600$–$3{,}800$ cm^{-1} are assigned to the free OH stretches. Both the spectra show similar spectral features. However, features are clearer and more easily seen in the spectra of colder $H^+(H_2O)_n{\cdot}(H_2)_3$. As can also be seen in Fig. 4.33, the inert gas attachment (cooling) induces narrowing of the $3{,}200$ and $3{,}550$ cm^{-1} bands. We note that the $H^+(H_2O)_{50}{\cdot}(H_2)_3$ spectrum looks similar to that of the bare, warmer cluster. In other word, the cooling effect on the spectrum can hardly be seen in this largest size. This might be because spectral bandwidths in such a large cluster are mainly based on inhomogeneity, which cannot be excluded by the cooling. For example, $H^+(H_2O)_{50}$ includes 101 OH stretches and each of them may have different vibrational frequencies. Another plausible explanation is that, due to the intrinsic difficulty in cooling large clusters because of the presence of a great number of low frequency modes, the clusters are not easily cooled down.

Figure 4.37 shows the expansion of the spectra of Fig. 4.36 in the free OH stretch region. In Fig. 4.37, two bands are seen at $\sim 3{,}700$ and $\sim 3{,}720$ cm^{-1}. In the spectra of cold, H_2-tagged clusters, the separation between these bands is better than that of bare clusters. This is due to the suppression of the tail of each band, and it reflects the cooling effect of the H_2 attachment. We note that the whole bandwidths are similar because these bands actually consist of many overlapping OH bonds. Such inhomogeneous broadening is the major factor of the bandwidths at the present sizes. The band at $\sim 3{,}700$ cm^{-1} can be attributed to the 3-coordinated

(double acceptor–single donor, AAD type) water molecules while the band at ∼3,720 cm^{-1} is due to the 2-coordinated (single acceptor–single donor, AD type) molecules. As reported previously, the depletion of the AD band upon increasing cluster size is a signature of the closed cage formation, in which most of the molecules are 3- or 4-coordinated [22, 105, 106]. The appearance of the AD band is due to the partially open cage structures, which might be higher in energy than completely closed cages because of the smaller number of H-bonds [22]. The intensity ratio between the AAD and AD bands is a good probe of structural trends. Figure 4.37 does not show remarkable difference in ratio between the cold,

Fig. 4.37 IR spectra of
a $H^+(H_2O)_{20-50}$ and
b $H^+(H_2O)_{20-50} \cdot (H_2)_3$ in the
free OH stretch region.
Adopted from Ref. [20]
(Copyright 2012 Elsevier)
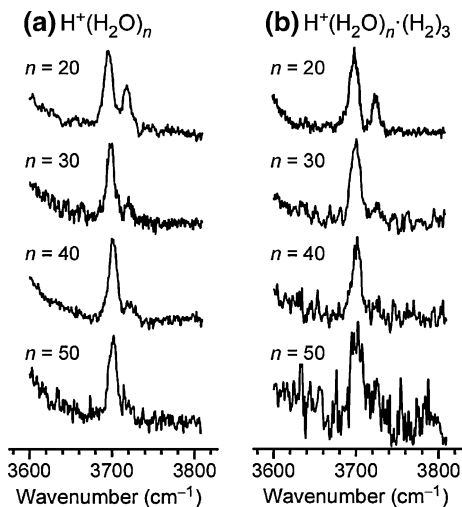
H_2-tagged clusters and the warmer, bare clusters. This means that the isomer distribution of the clusters is not largely affected upon the H_2 attachment while a vibrational cooling effect is achieved.

In the study of large, bare $H^+(H_2O)_n$ (Chap. 3), the relative intensity between the hydrogen-bonded and free OH stretch bands was used to probe the relative ratio of the 4-coordinated and 3-coordinated water molecules [8]. In the bare clusters, the relative intensity of the free OH band decreases with increasing cluster size, indicating the network development toward structures including a greater number of 4-coordinated water molecules. Here, if the cluster temperature is sufficiently low, structures containing more H-bonds become dominant due to the advantage in enthalpy over entropy. As a result, we would expect that the H_2-tagging should induce a more rapid decrease of the free OH band intensity as a function of cluster size. However, the observed spectra of $H^+(H_2O)_n \cdot (H_2)_3$ do not show a remarkable difference of the intensity ratio from that of bare $H^+(H_2O)_n$. This result also indicates that the H_2-mediated vibrational cooling is inert to the isomer distribution.

Although messenger-mediated spectroscopy did not lead to the molecular-level structural information of $H^+(H_2O)_{30-50}$, at least at the present stage, we should emphasize that detailed spectral information became accessible by virtue of this technique. Further experiments, such as broader wavelength scan, which covers, for example, bending and libration modes, is likely to provide new insights. In such new experiments, the present approach should be helpful in generating more detailed information.

4.4 Conclusions

We reported systematic IR spectroscopy for $H^+(H_2O)_n \cdot M_m$ in the broad size range and with various inert gas messengers. For small clusters, all messengers can lower the internal energy, which generally causes, for example, spectral broadening. It was shown that internal energy follows the order: $H^+(H_2O)_n \gg H^+(H_2O)_n \cdot (H_2)_2 > H^+(H_2O)_n \cdot Ar > H^+(H_2O)_n \cdot Ne$, reflecting the interaction energy of each messenger. The magnitude of the perturbation to the isomer distribution in the bare system follows the order: $H^+(H_2O)_n \cdot Ar \gg H^+(H_2O)_n \cdot (H_2)_2 > H^+(H_2O)_n \cdot Ne \sim (H^+(H_2O)_n)$. We, at least partly, achieved control of both the internal energy and isomer distribution by changing the inert gas used, although the origin of the isomer-selectivity was not necessarily clear. Such control enables us to gather much more detailed spectral and structural information on clusters of interest. For large clusters, all the inert gas-mediated spectra also showed clearer spectral features due to reduced bandwidths than spectra of bare clusters, validating the cooling effect of the inert gas attachment even in the large size region. In the present size region, the origin of magic and antimagic number clusters is of interest. In the H_2-tagged antimagic number ($n = 22$) cluster, we observed the hitherto missing water molecule, which is at the outside of the magic-numbered ($n = 21$) water cage and should fluctuate in higher temperatures. This result provided evidence for the structural origin of the antimagic number cluster. The present observations may provide insights into the other magic/antimagic number clusters and hydrogen-bonded network evolution after the completion of a closed cage (hydration shell) formation. The present IR spectroscopy for cold clusters also shows the tagging or messenger technique is a powerful tool to probe even such relatively large water networks, which fluctuate with thermal effects. It is hoped that the present approach may become helpful in detailed analyses of hydrogen-bonded network structures and the dynamics of small to large, complicated systems.

References and Notes

1. S.S. Xantheas, *Recent Theoretical and Experimental Advances in Hydrogen Bonded Clusters* (Kluwer Acadenlic Publishers, Dordrecht, 2000)
2. V. Buch, S. Bauerecker, J.P. Devlin, U. Buck, J.K. Kazimirski, Int. Rev. Phys. Chem. **23**, 375–433 (2004)
3. U. Buck, F. Huisken, Chem. Rev. **100**, 3863–3890 (2000)
4. K. Liu, J.D. Cruzan, R.J. Saykally, Science **271**, 929–933 (1996)
5. F.N. Keutsch, R.J. Saykally, Proc. Natl. Acad. Sci. U.S.A. **98**, 10533–10540 (2001)
6. T.S. Zwier, Annu. Rev. Phys. Chem. **47**, 205–241 (1996)
7. U. Buck, I. Ettischer, M. Melzer, V. Buch, J. Sadlej, Phys. Rev. Lett. **80**, 2578 (1998)
8. K. Mizuse, N. Mikami, A. Fujii, Angew. Chem. Int. Ed. **49**, 10119–10122 (2010)
9. K. Mizuse, T. Hamashima, A. Fujii, J. Phys. Chem. A **113**, 12134–12141 (2009)
10. K. Mizuse, A. Fujii, J. Phys. Chem. Lett. **2**, 2130–2134 (2011)
11. J.P. Devlin, C. Joyce, V. Buch, J. Phys. Chem. A **104**, 1974–1977 (2000)

12. C. Steinbach, P. Andersson, J.K. Kazimirski, U. Buck, V. Buch, T.A. Beu, J. Phys. Chem. A **108**, 6165–6174 (2004)
13. C. Steinbach, U. Buck, J. Phys. Chem. A **110**, 3128–3131 (2005)
14. K.R. Asmis, G. Santambrogio, J. Zhou, E. Garand, J. Headrick, D. Goebbert, M.A. Johnson, D.M. Neumark, J. Chem. Phys. **126**, 191105 (2007)
15. M.F. Bush, R.J. Saykally, E.R. Williams, J. Am. Chem. Soc. **130**, 15482–15489 (2008)
16. J.T. O'Brien, J.S. Prell, M.F. Bush, E.R. Williams, J. Am. Chem. Soc. **132**, 8248–8249 (2010)
17. J.T. O'Brien, E.R. Williams, J. Am. Chem. Soc. **134**, 10228–10236 (2012)
18. K. Mizuse, A. Fujii, Phys. Chem. Chem. Phys. **13**, 7129–7135 (2011)
19. K. Mizuse, A. Fujii, J. Phys. Chem. A **116**, 4868–4877 (2012)
20. K. Mizuse, A. Fujii in *Chem. Phys*. (2013, in press)
21. J.C. Jiang, Y.S. Wang, H.C. Chang, S.H. Lin, Y.T. Lee, G. Niedner-Schatteburg, J. Am. Chem. Soc. **122**, 1398–1410 (2000)
22. C–.C. Wu, C.-K. Lin, H.-C. Chang, J.-C. Jiang, J.-L. Kuo, M.L. Klein, J. Chem. Phys. **122**, 074315 (2005)
23. G.E. Douberly, A.M. Ricks, M.A. Duncan, J. Phys. Chem. A **113**, 8449–8453 (2009)
24. D.J. Miller, J.M. Lisy, J. Am. Chem. Soc. **130**, 15393–15404 (2008)
25. D.J. Miller, J.M. Lisy, J. Am. Chem. Soc. **130**, 15381–15392 (2008)
26. N.J. Singh, M. Park, S.K. Min, S.B. Suh, K.S. Kim, Angew. Chem. Int. Ed. **45**, 3795–3800 (2006)
27. B.M. Elliott, R.A. Relph, J.R. Roscioli, J.C. Bopp, G.H. Gardenier, T.L. Guasco, M.A. Johnson, J. Chem. Phys. **129**, 094303 (2008)
28. R.A. Relph, T.L. Guasco, B.M. Elliott, M.Z. Kamrath, A.B. McCoy, R.P. Steele, D.P. Schofield, K.D. Jordan, A.A. Viggiano, E.E. Ferguson, M.A. Johnson, Science **327**, 308–312 (2010)
29. T.L. Guasco, M.A. Johnson, A.B. McCoy, J. Phys. Chem. A **115**, 5847–5858 (2011)
30. Y.S. Wang, C.H. Tsai, Y.T. Lee, H.C. Chang, J.C. Jiang, O. Asvany, S. Schlemmer, D. Gerlich, J. Phys. Chem. A **107**, 4217–4225 (2003)
31. S.R. Mercier, O.V. Boyarkin, A. Kamariotis, M. Guglielmi, I. Tavernelli, M. Cascella, U. Rothlisberger, T.R. Rizzo, J. Am. Chem. Soc. **128**, 16938–16943 (2006)
32. H. Ishikawa, T. Nakano, T. Eguchi, T. Shibukawa, K. Fuke, Chem. Phys. Lett. **514**, 234–238 (2011)
33. L. Jiang, T. Wende, R. Bergmann, G. Meijer, K.R. Asmis, J. Am. Chem. Soc. **132**, 7398–7404 (2010)
34. Y.S. Wang, H.C. Chang, J.C. Jiang, S.H. Lin, Y.T. Lee, J. Am. Chem. Soc. **120**, 8777–8788 (1998)
35. H.C. Chang, C.C. Wu, J.L. Kuo, Int. Rev. Phys. Chem. **24**, 553–578 (2005)
36. M. Okumura, L.I. Yeh, J.D. Myers, Y.T. Lee, J. Chem. Phys. **85**, 2328–2329 (1986)
37. L.I. Yeh, M. Okumura, J.D. Myers, J.M. Price, Y.T. Lee, J. Chem. Phys. **91**, 7319–7330 (1989)
38. M. Okumura, L.I. Yeh, J.D. Myers, Y.T. Lee, J. Phys. Chem. **94**, 3416–3427 (1990)
39. N.I. Hammer, E.G. Diken, J.R. Roscioli, M.A. Johnson, E.M. Myshakin, K.D. Jordan, A.B. McCoy, X. Huang, J.M. Bowman, S. Carter, J. Chem. Phys. **122**, 244301 (2005)
40. J.M. Headrick, E.G. Diken, R.S. Walters, N.I. Hammer, R.A. Christie, J. Cui, E.M. Myshakin, M.A. Duncan, M.A. Johnson, K.D. Jordan, Science **308**, 1765–1769 (2005)
41. G.E. Douberly, R.S. Walters, J. Cui, K.D. Jordan, M.A. Duncan, J. Phys. Chem. A **114**, 4570–4579 (2010)
42. E.J. Bieske, O. Dopfer, Chem. Rev. **100**, 3963–3998 (2000)
43. O. Dopfer, J. Phys. Chem. A **104**, 11693–11701 (2000)
44. O. Dopfer, D. Roth, J.P. Maier, J. Phys. Chem. A **104**, 11702–11713 (2000)
45. W.H. Robertson, J.A. Kelley, M.A. Johnson, Rev. Sci. Instrum. **71**, 4431–4434 (2000)
46. N.M. Lakin, R.V. Olkhov, O. Dopfer, Faraday Discuss. **118**, 455–476 (2001)
47. D. Roth, O. Dopfer, J.P. Maier, Phys. Chem. Chem. Phys. **3**, 2400–2410 (2001)

48. N. Solcà, O. Dopfer, J. Phys. Chem. A **105**, 5637–5645 (2001)
49. M.A. Duncan, Int. Rev. Phys. Chem. **22**, 407–435 (2003)
50. W.H. Robertson, M.A. Johnson, Annu. Rev. Phys. Chem. **54**, 173–213 (2003)
51. N.I. Hammer, J.R. Roscioli, M.A. Johnson, J. Phys. Chem. A **109**, 7896–7901 (2005)
52. L.R. McCunn, J.R. Roscioli, B.M. Elliott, M.A. Johnson, A.B. McCoy, J. Phys. Chem. A **112**, 6074–6078 (2008)
53. G. Niedner-Schatteburg, Angew. Chem. Int. Ed. **47**, 1008–1011 (2008)
54. D.J. Goebbert, T. Wende, R. Bergmann, G. Meijer, K.R. Asmis, J. Phys. Chem. A **113**, 5874–5880 (2009)
55. A.L. Nicely, D.J. Miller, J.M. Lisy, J. Am. Chem. Soc. **131**, 6314–6315 (2009)
56. J.D. Rodriguez, J.M. Lisy, Int. J. Mass Spectrom. **283**, 135–139 (2009)
57. M. Baer, D. Marx, G. Mathias, Angew. Chem. Int. Ed. **49**, 7346–7349 (2010)
58. J.P. Beck, J.M. Lisy, J. Phys. Chem. A **114**, 10011–10015 (2010)
59. T. Imamura, K. Ohashi, J. Sasaki, K. Inoue, K. Furukawa, K. Judai, N. Nishi, H. Sekiya, Phys. Chem. Chem. Phys. **12**, 11647–11656 (2010)
60. L. Lin, P. Claes, T. Holtzl, E. Janssens, T. Wende, R. Bergmann, G. Santambrogio, G. Meijer, K.R. Asmis, M.T. Nguyen, P. Lievens, Phys. Chem. Chem. Phys. **12**, 13907–13913 (2010)
61. S.G. Olesen, T.L. Gausco, G.H. Weddle, S. Hammerum, M.A. Johnson, Mol. Phys. **108**, 1191–1197 (2010)
62. M. Baer, D. Marx, G. Mathias, ChemPhysChem **12**, 1906–1915 (2011)
63. K. Mizuse, J.-L. Kuo, A. Fujii, Chem. Sci. **2**, 868–876 (2011)
64. K. Mizuse, Y. Suzuki, N. Mikami, A. Fujii, J. Phys. Chem. A **115**, 11156–11161 (2011)
65. K. Mizuse, A. Fujii, N. Mikami, J. Phys. Chem. A **110**, 6387–6390 (2006)
66. M. Brümmer, C. Kaposta, G. Santambrogio, K.R. Asmis, J. Chem. Phys. **119**, 12700 (2003)
67. This condition depends on timescale of measurements. In our present measurement, tagged clusters arrive at the interaction region with the IR light a few hundreds ms after their production. Spontaneous dissociation of the tagged clusters is almost negligible after the interaction region (the ion guide) and it indicates that high energy components have already dissociated before the detection
68. M.Z. Kamrath, E. Garand, P.A. Jordan, C.M. Leavitt, A.B. Wolk, M.J. Van Stipdonk, S.J. Miller, M.A. Johnson, J. Am. Chem. Soc. **133**, 6440–6448 (2011)
69. M.Z. Kamrath, R.A. Relph, T.L. Guasco, C.M. Leavitt, M.A. Johnson, Int. J. Mass Spectrom. **300**, 91–98 (2011)
70. E.G. Diken, J.M. Headrick, J.R. Roscioli, J.C. Bopp, M.A. Johnson, A.B. McCoy, J. Phys. Chem. A **109**, 1487–1490 (2005)
71. O. Rodriguez, J.M. Lisy, J. Phys. Chem. Lett. **2**, 1444–1448 (2011)
72. F. Grandinetti, Eur. J. Mass Spectrom. **17**, 423 (2011)
73. O. Dopfer, D. Roth, J.P. Maier, J. Chem. Phys. **114**, 7081 (2001)
74. B. Bandyopadhyay, T.C. Cheng, M.A. Duncan, Int. J. Mass Spectrom. **297**, 124–130 (2010)
75. U. Even, J. Jortner, D. Noy, N. Lavie, C. Cossart-Magos, J. Chem. Phys. **112**, 8068–8071 (2000)
76. J. Tang, A.R.W. McKellar, J. Chem. Phys. **116**, 646 (2002)
77. M. Hayashi, Y. Ohshima, J. Phys. Chem. A (submitted)
78. C. Lee, W. Yang, R.G. Parr, Phys. Rev. B **37**, 785 (1988)
79. A.D. Becke, J. Chem. Phys. **98**, 5648–5652 (1993)
80. Y. Maréchal, *The Hydrogen Bond and the Water Molecule* (ELSEVIER, Amsterdam, 2007)
81. P. Hobza, J. Sponer, T. Reschel, J. Comput. Chem. **16**, 1315–1325 (1995)
82. Y. Zhao, D. Truhlar, Theor. Chem. Acc. **120**, 215–241 (2008)
83. Y. Zhao, D.G. Truhlar, Acc. Chem. Res. **41**, 157–167 (2008)
84. K.E. Riley, M. Pitoňák, P. Jurečka and P. Hobza. Chem. Rev. **110**, 5023–5063 (2010)
85. J.-D. Chai, M. Head-Gordon, Phys. Chem. Chem. Phys. **10**, 6615–6620 (2008)
86. M. Eigen, L. de Maeyer, Proc. R. Soc. London, Ser. A **247**, 505–533 (1958)
87. M. Eigen, Angew. Chem. Int. Ed. **3**, 1–19 (1964)

88. Here we note that the contribution of hot bands in the bare cluster also causes the difficulty in the precise evaluation of the vibrational frequency shifts by the rare gas tagging. The simple comparison between the observed spectra shows the effective frequency shifts of 12–18 and 20–30 cm^{-1} for the free and H-bonded OH bands, respectively. These magnitudes of the shifts are overestimated since the peak positions of the bands of the bare cluster should be affected by hot bands. In Table 4.1, it is seen that the effective shifts by the tagging are actually smaller in larger clusters (for example, a few cm^{-1} for the free OH stretches). Suppression of hot bands in bare clusters (because of the lowering the dissociation energy) would be a reason though lowering the interaction strength is an alternative interpretation

89. Y. Luo, S. Maeda, K. Ohno, J. Comput. Chem. **30**, 952–961 (2009)

90. R. Janoschek, E.G. Weidemann, H. Pfeiffer, G. Zundel, J. Am. Chem. Soc. **94**, 2387–2396 (1972)

91. N. Agmon, Chem. Phys. Lett. **244**, 456–462 (1995)

92. D. Marx, M.E. Tuckerman, J. Hutter, M. Parrinello, Nature **397**, 601–604 (1999)

93. C.J.T. de Grotthuss, Biochim. Biophys. Acta **1757**, 871–875 (2006)

94. D. Marx, ChemPhysChem **7**, 1848–1870 (2006)

95. J.-L. Kuo, J. Phys, Conf. Ser. **28**, 87–90 (2006)

96. *NIST Chemistry WebBook*, National Institute of Standards and Technology (2008)

97. E.P.L. Hunter, S.G. Lias, J. Phys. Chem. Ref. Data **27**, 413–656 (1998)

98. M. Morita, K. Takahashi, Phys. Chem. Chem. Phys. **14**, 2797–2808 (2012)

99. K.R. Asmis, T. Wende, M. Brummer, O. Gause, G. Santambrogio, E.C. Stanca-Kaposta, J. Dobler, A. Niedziela, J. Sauer, Phys. Chem. Chem. Phys. **14**, 9377–9388 (2012)

100. A. Amirav, U. Even, J. Jortner, Chem. Phys. **51**, 31–42 (1980)

101. F. Cuadros, I. Cachadiña, W. Ahumada, Mol. Eng. **6**, 319–325 (1996)

102. I. Shin, M. Park, S.K. Min, E.C. Lee, S.B. Suh, K.S. Kim, J. Chem. Phys. **125**, 234305 (2006)

103. S. Karthikeyan, M. Park, I. Shin, K.S. Kim, J. Phys. Chem. A **112**, 10120–10124 (2008)

104. Y. Luo, S. Maeda, K. Ohno, J. Phys. Chem. A **111**, 10732–10737 (2007)

105. M. Miyazaki, A. Fujii, T. Ebata, N. Mikami, Science **304**, 1134–1137 (2004)

106. J.W. Shin, N.I. Hammer, E.G. Diken, M.A. Johnson, R.S. Walters, T.D. Jaeger, M.A. Duncan, R.A. Christie, K.D. Jordan, Science **304**, 1137–1140 (2004)

107. J.-L. Kuo, M.L. Klein, J. Chem. Phys. **122**, 024516 (2005)

108. C.K. Lin, C.C. Wu, Y.S. Wang, Y.T. Lee, H.C. Chang, J.L. Kuo, M.L. Klein, Phys. Chem. Chem. Phys. **7**, 938–944 (2005)

109. S–.S. Lin, Rev. Sci. Instrum. **44**, 516–517 (1973)

110. J.Q. Searcy, J.B. Fenn, J. Chem. Phys. **61**, 5282–5288 (1974)

111. O. Echt, D. Kreisle, M. Knapp, E. Recknagel, Chem. Phys. Lett. **108**, 401–407 (1984)

112. U. Nagashima, H. Shinohara, N. Nishi, H. Tanaka, J. Chem. Phys. **84**, 209–214 (1986)

113. Z. Shi, J.V. Ford, S. Wei, J.A.W. Castleman, J. Chem. Phys. **99**, 8009–8015 (1993)

114. A.W. Castleman, K.H. Bowen, J. Phys. Chem. **100**, 12911–12944 (1996)

115. T. Schindler, C. Berg, G. NiednerSchatteburg, V.E. Bondybey, Chem. Phys. Lett. **250**, 301–308 (1996)

116. G. Niedner-Schatteburg, V.E. Bondybey, Chem. Rev. **100**, 4059–4086 (2000)

117. K. Hansen, P.U. Andersson, E. Uggerud, J. Chem. Phys. **131**, 124303 (2009)

118. O. Echt, K. Sattler, E. Recknagel, Phys. Rev. Lett. **47**, 1121 (1981)

119. H.W. Kroto, J.R. Heath, S.C. O'Brien, R.F. Curl, R.E. Smalley, Nature **318**, 162–163 (1985)

120. W.D. Knight, K. Clemenger, W.A. de Heer, W.A. Saunders, M.Y. Chou, M.L. Cohen, Phys. Rev. Lett. **52**, 2141 (1984)

121. H. Haberland, C. Ludewigt, H.-G. Schindler, D.R. Worsnop, J. Chem. Phys. **81**, 3742–3744 (1984)

122. J. James, L. Kassner, D.E. Hagen, J. Chem. Phys. **64**, 1860–1861 (1976)

123. S. Wei, Z. Shi, J.A.W. Castleman, J. Chem. Phys. **94**, 3268–3270 (1991)

124. Z. Shi, S. Wei, J.V. Ford, A.W. Castleman Jr, Chem. Phys. Lett. **200**, 142–146 (1992)

125. K. Mizuse, A. Fujii, N. Mikami, J. Chem. Phys. **126**, 231101 (2007)

126. S.S. Iyengar, M.K. Petersen, T.J.F. Day, C.J. Burnham, V.E. Teige, G.A. Voth, J. Chem. Phys. **123**, 084309 (2005)
127. S.S. Iyengar, J. Chem. Phys. **126**, 216101 (2007)
128. M. Beyer, U. Achatz, C. Berg, S. Joos, G. Niedner-Schatteburg, V.E. Bondybey, J. Phys. Chem. A **103**, 671–678 (1999)
129. H. Haberland, T. Hippler, J. Donges, O. Kostko, M. Schmidt, B. von Issendorff, Phys. Rev. Lett. **94**, 035701 (2005)
130. M. Torrent-Sucarrat, J.M. Anglada, J. Chem. Theor. Comp. **7**, 467–472 (2011)
131. T.H. Choi, K.D. Jordan, J. Phys. Chem. B **114**, 6932–6936 (2010)
132. J.R. Roscioli, N.I. Hammer, M.A. Johnson, J. Phys. Chem. A **110**, 7517–7520 (2006)

Chapter 5
Infrared Spectroscopy of Water Cluster Radical Cations $(H_2O)_n^+$ ($n \leq 11$)

Abstract Studies on reactive water networks provide us with substantive information on the radiation chemistry of water. Water cluster radical cations $(H_2O)_n^+$ have been probed with IR spectroscopy. Observed spectra were systematically analyzed and characteristic structural trends were established: Nominal water cluster cations $(H_2O)_n^+$ form proton-transferred type clusters $H^+(H_2O)_{n-1}(OH)$. Shapes of the hydrogen bond network are quite similar to those of $H^+(H_2O)_n$. Structures of $(H_2O)_n^+$ can be constructed from the structures of $H^+(H_2O)_n$ by substituting one of the next neighbor molecules from the protonated site with an OH radical. Reactivity of water exposed to ionizing radiation should depend on hydrogen bond network structures around the created radicals. We therefore hope the findings in this study may be helpful in understanding the detailed processes of ionizing radiation-initiated reactions in liquid water and aqueous solutions.

Keywords Water cluster radical cations · Radiation chemistry of water · Ionizing radiations · Reaction mechanisms

5.1 Introduction

5.1.1 Towards Insights into Chemical Reactions in Hydrogen Bond Networks

In Chaps. 2–4 we demonstrated that infrared (IR) spectroscopic studies of clusters can provide detailed insights into structural trends and dynamics of hydrogen-bonded water networks. Another advance in studying hydrated clusters in the gas phase is to understand chemical reactions in aqueous solutions from microscopic observations. Reactions in the liquid phase include not only reactant and products

but also solvent water molecules. Furthermore, numerous surrounding solvents are sometimes directly included in reaction mechanisms. Therefore, there are circumstances in which condensed phase studies may be unable to adequately investigate such detailed reaction mechanisms. A Reduced number of molecules in a cluster system can provide deeper insights into such a complicated system.

In this chapter, we show that structural studies of hydrated clusters leads to the characterization of a new reaction mechanism of an important chemical reaction: ionizing radiation-induced reactions of water. Our motivations for the investigation and the importance of such systems will be provided in the following section. We will focus on water cluster radical cations $(H_2O)_n^+$ as models of ionized, reactive hydrogen bond networks. Structural trends and the nature of cationized water networks have been systematically investigated with IR spectroscopy. By virtue of well-controlled numbers of water molecules included in clusters, we can take into account not only solutes but also solvents.

5.1.2 Radiation Chemistry of Water

In this section, we provide a summary of the current research on the chemical importance of radiation-induced processes of water. Interaction between water and ionizing radiations (e.g., X-rays and fast electrons) creates two important radicals, hydroxyl (OH) radicals and hydrated electrons (e_{aq}^-) [1–3]. Because of their high reactivity, the ionization of water and subsequent processes play central roles in radiation-related chemistry and biology in aqueous environments [1–7]. One of the most important examples is radiotherapy, in which water in a cancer cell is ionized by radiations, resulting in hydrated electrons and/or OH radicals thought to break the DNA strand, leading to cell death (Fig. 5.1) [2, 3, 7]. Hydrogen bond network structures, including ionization-induced rearrangements, are expected to be closely related to chemistry in irradiated water [2]. Despite its importance, there are many open questions concerning the detailed mechanisms of ionization processes as well as hydrogen bond network structures around product ions/radicals [2].

In the condensed phase, especially in aqueous solutions, chemical reactions following the ionization of water have been extensively studied using various techniques such as ultrafast spectroscopy, and primary processes have been described as Eqs. (5.1) and (5.2a, b) [1–3, 8–11]:

Fig. 5.1 Schematic of DNA strand break induced by an attack of the hydrated electron or OH radical

$$H_2O \rightarrow H_2O^+ + e^- \tag{5.1}$$

$$e^- \rightarrow e^-_{aq} \tag{5.2a}$$

$$H_2O^+ + H_2O \rightarrow H_3O^+ + OH \tag{5.2b}$$
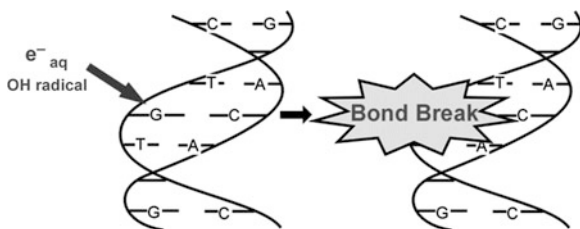
Equation (5.1) is ionization of a water molecule; Eqs. (5.2a) and (5.2b) are the hydration of the ejected electron, and the production of the OH radical via the H_2O^+-H_2O ion-molecule reaction, respectively. These reactions actually occur with surrounding water molecules, and therefore it is important to understand the mechanisms involved, including the roles played by the surrounding water molecules. The microscopic information (especially about hydrogen bond network structures), however, tends to be veiled by the complexity of a great number of solvent molecules and competing processes. As a result, molecular-level analyses in the condensed phase are still difficult.

5.1.3 Cluster Studies for Radiation Chemistry of Water

For molecular level understanding of structures and dynamics of hydrogen-bonded water networks, a hydrated cluster study in the gas phase is a powerful approach [12–85]. For example, water cluster anions $(H_2O)_n^-$ have been extensively studied as microscopic models for hydrated electrons in Eq. 5.2a. Photoelectron and optical [infrared (IR) and visible] spectroscopies as well as mass spectrometry have been applied to a broad size range ($n \leq \sim 200$) of $(H_2O)_n^-$ [15–28, 83]. In these studies, network structures, electron-binding motifs, and reactivities have been discussed in detail. On the other hand, for the microscopic models of the cationic moiety (Eq. 5.2b), namely water cluster radical cations $(H_2O)_n^+$, structural information is still limited, as mentioned below. This study focuses on this problem.

Ionization of water clusters can be regarded as microscopic views of ionization of bulk water and they have been studied using mass spectrometry, photoionization/photoelectron spectroscopy, and theoretical calculations [29–60, 84, 85]. In general, in the cluster sources for cationic water clusters, protonated water clusters are the main products and only limited cases lead to the production of water cluster radical cations $(H_2O)_n^+$. This aspect seemed to limit the number of previous studies on this clusters. We note that this aspect also implies the inherent instability (high reactivity) of this species. Although $(H_2O)_n^+$ has been produced in several experimental studies, no direct structural information about $(H_2O)_n^+$ has as yet been reported. Furthermore, it has been pointed out that theoretical calculations often suffer from symmetry-breaking, spin contamination, and/or self-interaction error in such open-shell doublet systems [57, 60]. Unique consensus for cluster structures has therefore not been achieved. Even for the simplest case $(H_2O)_2^+$, two structural motifs have been suggested [30–32, 35–37]. One of them is the dimer

cation $[H_2O \cdots OH_2]^+$ type and the other is the proton-transferred $[H_3O^+-OH]$ type. It should be noted that the latter one has OH radical moiety and corresponds to the exit channel of the reaction in Eq. 5.2b. Very recently, Gardenier et al. presented IR spectra of argon-tagged $(H_2O)_2^+$ and they have shown that only the proton-transferred $[H_3O^+-OH]$ type was observable [61]. Recent fine theoretical studies, one of which was combined with photoelectron spectroscopy, agree with this result [40, 45, 46, 50–52, 57, 60]. Spectroscopic investigation of $(H_2O)_n^+$ structures, however, has been limited to the dimer case so far. Though confirmation of the OH radical creation in the dimer cation is an indication of important progress, the ion-core structure in larger clusters is still ambiguous because the ion-core structure often changes with solvation.

Further experimental studies are also required to elucidate the general trends of network structures and the interplay between the protonated site and the OH radical under the hydration environment. For larger systems ($n \geq 3$), three groups have reported structural motifs from their mass spectrometric analyses, however, these three motifs are different from each other [30–32]. Figure 5.2 shows the structural motifs constructed based on their results. In Fig. 5.2, the structure (a) is a solvated "dimer cation core" type, as suggested by Yamaguchi et al. No OH radical exists in this type [32]. Both structures (b) and (c) are the proton-transferred type, however, these two differ in the position of the OH radical. In structure (b), suggested by Angel and Stace, the H_3O^+-OH ion-radical contact pair is fully hydrated via three hydrogen bonds [31]. However, in structure (c) suggested by Jongma et al., the contact pair dissociates and the OH radical locates at the terminal of the network [30]. Structure (a) is expected to show very different reactivity from structures (b) and (c) due to the absence of the OH radical. Furthermore, if the OH radical is formed as in structure (b) and (c), its relative location to the protonated site may be a crucial factor for the reactivity of ionized water networks because the mobility of the OH radical (reactor) may depend on whether the radical is tightly bound to the protonated (charged) site or not.
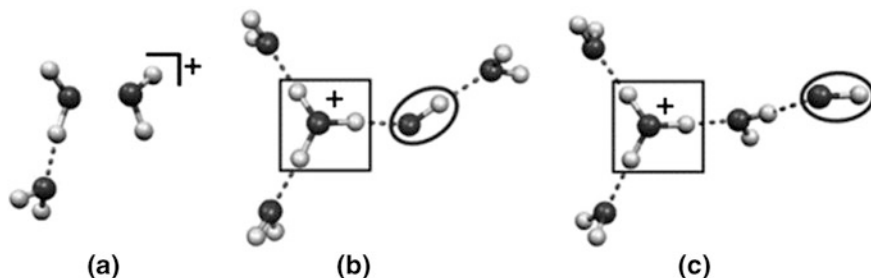
Fig. 5.2   Three different structural motifs of $(H_2O)_n^+$ ($n \geq 3$). These structures were constructed from previous results [30–32] (see text for details). The protonated site is indicated by a border. The OH radical moiety is circled. (**a**) "Dimer cation core" type. (**b**) H_3O^+-OH ion-radical contact pair type. (**c**) Solvent separated H_3O^+-OH ion-radical pair

5.1.4 Purposes of this Study

Structures of $(H_2O)_n^+$ should reflect the inherent instability of H_2O^+ and the reactivity of cationized water networks. Such knowledge is quite important in understanding ionizing radiation-induced chemistry in water. To reveal structures of $(H_2O)_n^+$ at the molecular level, we report here IR spectra of $(H_2O)_n^+$ ($n = 3$–11) in the OH stretch region. To simplify the spectral analyses and to obtain more detailed cluster structures, we also employed an inert gas attachment technique as described in Chap. 4. On the basis of the observed spectra, we show structural trends such as network shapes, ion core motifs ("dimer cation" or "proton transferred"), and the existence and location of the OH radical. We also demonstrate that the structural trends obtained this way lead to a new chemical model for the radiation chemistry of water, which cannot necessarily be achieved in condensed phase experiments.

5.2 Experimental

5.2.1 Overview of Experiment

Most parts of the experimental set up (the vacuum chamber, IR light source, and measurement systems) were the same as described in Chaps. 3 and 4, therefore, only brief descriptions are given here. IR spectra of water cluster cations $(H_2O)_n^+$ ($n = 3$–11) were measured as photodissociation spectra by using a tandem quadrupole mass spectrometer and a coherent IR source. IR spectra of $(H_2O)_n^+ \cdot Ar$ ($n = 3$–7) were also measured using essentially the same technique. Because intensities of $H^+(H_2O)_n$ and $H^+(H_2O)n Ar$ are much larger than those of $(H_2O)_n^+$ and $(H_2O)_n^+ \cdot Ar$ (see the following section and Fig. 5.3), mass spectrometric separation of protonated and radical cationic species is difficult, especially in large systems. This fact limited the size region investigated in this study. Water cluster cations $(H_2O)_n^+$ and $(H_2O)_n^+ \cdot Ar$ were generated in a supersonic jet expansion. The gaseous mixture of H_2O (trace; $^{17,18}O$-depleted $H_2^{16}O$, 99.99 % ^{16}O, ISOTEC) and Ar (5 MPa) was expanded into a vacuum chamber through a high-pressure pulsed valve (Even-Lavie valve) [86]. The gas pulse was crossed by the electron beam of 200 eV from an electron gun (Omegatron) in the collisional region of the jet. Cluster ions formed became larger and were cooled following the collisions. The cluster ion of interest was selected by the first mass spectrometer (the mass resolution (Δm) was ~ 1) and was irradiated by coherent IR light (Laser Vision OPO/OPA). IR spectra were measured by monitoring the photofragment intensity as functions of the IR wavelength. The second mass spectrometer was tuned to select the fragments of both the H_2O-loss and the OH-loss channels ($\Delta m \sim 3$) for spectroscopy of bare $(H_2O)_n^+$. For the measurements for $(H_2O)_n^+ Ar$, Ar-loss as well as $(Ar + H_2O)$-loss and the $(Ar + OH)$-loss channels were independently

Fig. 5.3 Mass spectrum of
ions produced by the present
ion source. For details of the
ion source, see text
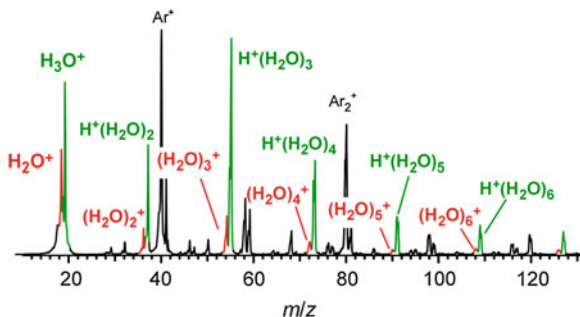
measured and summed up. Additional details on fragment dependence will be
given in the following section. The wavelength of the IR light was calibrated in
vacuum wavenumbers (± 2 cm^{-1}) by recording an ambient H_2O and CO_2 vapor
spectrum. All the presented IR spectra were normalized by the IR power.

5.2.2 Cluster Ion Production

As mentioned in Sect. 5.1.3, cluster production is the key to the study of reactive
$(H_2O)_n^+$. We optimized cluster source as in Chap. 4 and found that cooling effi-
ciency and the choice of the carrier gas are critical to the yields of $(H_2O)_n^+$.
Figure 5.3 shows a mass spectrum of the above mentioned ion source (5 MPa Ar
carrier, electron beam crossing). Here, the use of a high pressure pulsed valve
leads to efficient cooling of clusters ("colder" cluster source). Although $(H_2O)_n^+$
series is a minor relative to the $H^+(H_2O)_n$, the yields of $(H_2O)_n^+$ were sufficient for
spectroscopic experiments. In contrast to this ion source, we also tried a "warmer"
ion source, as described in Chap. 3: The gaseous mixture of H_2O (trace) and
Ar (0.3 MPa) was expanded into a vacuum chamber through a pulsed valve
(General Valve Series 9, ϕ 0.8 mm orifice) equipped with a channel nozzle (ϕ 2.0,
13.0 mm length) in front of the valve. In the channel nozzle, ionization was caused
by a pulsed discharge induced by an inserted pin electrode (-320 V). We note,
"warmer" in this sentence means that the lower stagnation pressure should reduce
the degree of collisional cooling. Final relative temperature reflects the degree of
evaporative cooling as well as collisional cooling and therefore it is not possible to
differentiate them in this study. Figure 5.4 compares typical mass distributions of
our "colder" and "warmer" ion sources. In the "warmer" ion source, we were
unable to observe $(H_2O)_n^+$—only $H^+(H_2O)_n$ was observed. This cooling condition
dependence of the $(H_2O)_n^+$ yield is consistent with the previous mass spectrometric
studies by Shinohara et al. and Jongma et al. in which they suggested rapid cooling
processes after ionization are necessary to produce $(H_2O)_n^+$ [29, 30]. As for the
"colder" ion source, we also checked carrier gas dependences. When we used Ne
as a carrier gas, relative yields of $(H_2O)_n^+$ became smaller. In the case of He, only

Fig. 5.4 Comparison of cluster ion distributions obtained with (**a**) "colder" (higher stagnation pressure, 5 MPa) cluster ion source and (**b**) "warmer" (lower stagnation pressure, 0.3 MPa). See text for details of each ion source. The bands indicated by the asterisk are attributed to $(H_2O)_n^+ \cdot Ar_m$ or $H^+(H_2O)_n \cdot Ar_m$
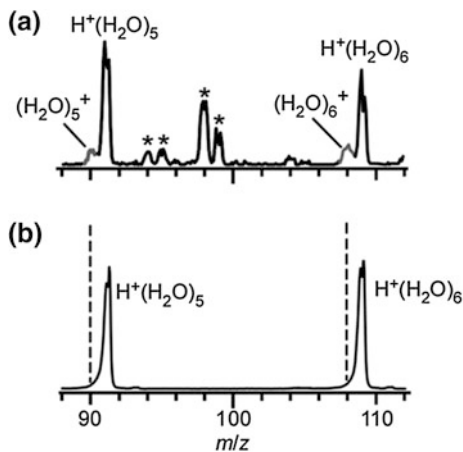

much a smaller amount of $(H_2O)_n^+$ was produced. Such carrier gas dependence was also in agreement with previous mass spectrometric studies [30]. According to these results, we used only Ar as a carrier gas. Therefore, inert gas attachment technique is also limited to Ar-tagging, though variations of inert gas should provide more spectral information, as in Chap. 4.

5.2.3 Monitored Fragments

In the IR photodissociation spectral measurements, we had to check fragment patterns. This is because if $H^+(H_2O)_{n-1}OH$ type structures are produced, OH radical loss may be observed while $(H_2O)_2^+ - (H_2O)_{n-2}$ cannot lead to such fragments. Figure 5.5 shows IR photodissociation mass spectrum of $(H_2O)_5^+$. Here, $(H_2O)_5^+$ was selected by the first mass filter and was irradiated by the IR light pulse of 3,734 cm^{-1}. The second mass filter then analyzed the m/z ratio of the resulting ions and this spectrum was obtained. The IR light of this photon energy was resonant with the antisymmetric stretch of the terminal water moiety. Note that all the structures of $(H_2O)_5^+$ (structure I–III, see Sect. 5.3) have terminal water molecules and should be excited if they exist. With this measurement, we found that only the OH-loss fragment actually contributes to the observed IR spectra, at least for $(H_2O)_{3-5}^+$. This result implies $H^+(H_2O)_{n-1}OH$ type structures. Of course IR spectroscopy is necessary for more detailed structural information.

In the spectroscopy of $(H_2O)_n^+ \cdot Ar$, we observed fragment dependence of the spectrum. In the case of small clusters ($n = 3, 4$), the Ar-loss channel was a unique path upon IR irradiation of the present wavelength range. In contrast, for $n \geq 5$, low-frequency ($< \sim 2,800$ cm^{-1}) excitation led to Ar-loss channel while high frequency ($> \sim 3,000$ cm^{-1}) excitation led to the (Ar + H$_2$O/OH) loss channel. We note we could not resolve the (Ar + H$_2$O)-loss and (Ar + OH)-loss channels in fragment
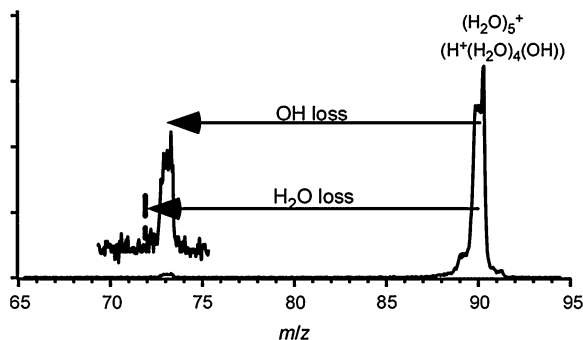
Fig. 5.5 Infrared photodissociation mass spectrum of $(H_2O)_5^+$ $(H^+(H_2O)_4(\cdot OH))$. $(H_2O)_5^+$ was selected by the first mass filter and was irradiated by the IR light pulse of 3,734 cm^{-1}. The second mass filter analyzed the m/z ratio of the resulting ions and generating this spectrum. The IR light of this photon energy was in resonant with the antisymmetric stretch of the terminal water moiety. Note that all the structures of $(H_2O)_5^+$ (structure I–III, see Sect. 5.3) have terminal water molecules and should be excited if they exist

mass spectrometry due to the weaker signal of Ar-tagged species. In the intermediate frequency (2,700–2,900 cm^{-1}), a branching of dissociation path was observed. Figure 5.6a, b shows the fragment dependence of the measured spectrum of $(H_2O)_5^+ \cdot Ar$. Because the IR spectrum should be summation of the all fragment channels, we took a weighted average of both channels. The resulting spectrum in Fig. 5.6c was used in the following analyses. Figure 5.7 shows similar spectra for the $n = 6$ system. We note that fragment dependence can be explained by simple energetics. As in Chap. 4, interaction energy of Ar is $\sim$500 cm^{-1}, and excitation energy of IR light is used for the evaporation of Ar. If residual energy (IR photon energy $\sim$500 cm^{-1}) is higher than evaporation energy OH or H$_2$O, OH/H$_2$O is removed as well as Ar. The present observation indicated the OH or H$_2$O evaporation energy is $\sim$2,400 cm^{-1} when we assume Ar evaporation energy. Furthermore, because H$_2$O evaporation energy in cationic clusters is higher than 3,000 cm^{-1}, the present observations might be attributed to the OH and Ar loss channel.

5.2.4 Quantum Chemical Calculations

5.2.4.1 Calculation Levels

For detailed analyses of IR spectra and cluster structures, we carried out density functional theory (DFT) calculations at the MPW1K/6-311++G(3df,2p) level [87]. Computational details and resources were also given in Chap. 2. For the $(H_2O)_2^+$ system, Lee and Kim have reported that this functional gives similar results to the high-level calculations at CCSD(T)/CBS [53]. Furthermore, it has been pointed out that the standard B3LYP functional overestimates the stabilization energy in
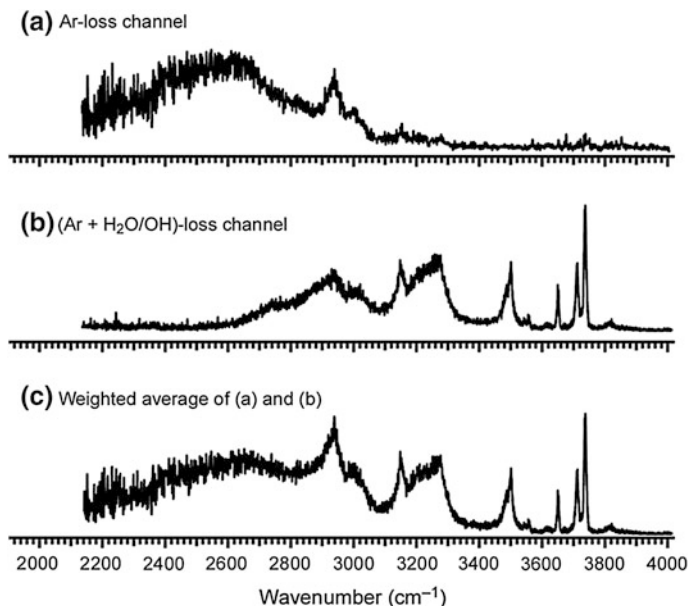
(a) Ar-loss channel

(b) (Ar + H$_2$O/OH)-loss channel

(c) Weighted average of (a) and (b)

Wavenumber (cm^{-1})
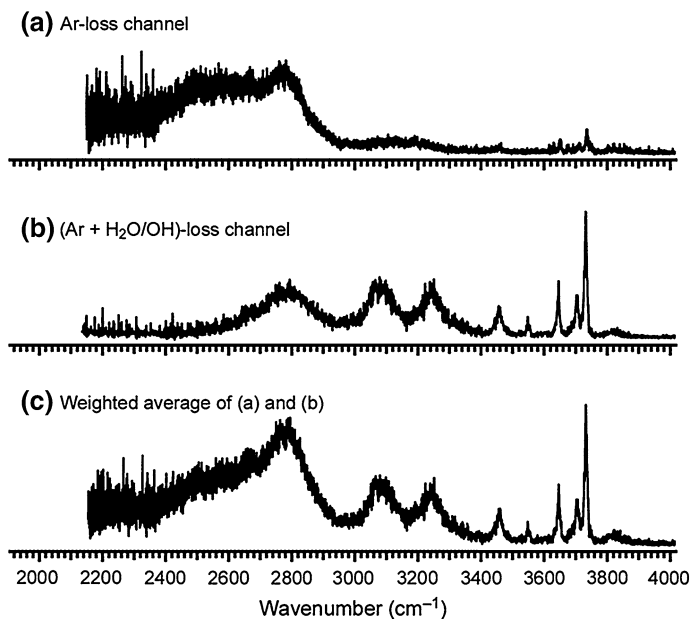
Fig. 5.6 IR photodissociation spectra of (H$_2$O)$_5^+$·Ar. Spectrum (**a**) and (**b**) were measured by monitoring Ar-loss and (Ar + H$_2$O/OH)-loss channel, respectively. Spectrum (**c**) is a weighted average of (**a**) and (**b**), and it is used in the following analyses

dimer cation core types. Initial geometries were systematically constructed as mentioned in the following sections. Geometries were fully optimized and harmonic frequency calculations were performed. Calculated frequencies were scaled by a factor of 0.9185. To simulate IR spectra, we used Lorentzian functions with 10 and 50 cm^{-1} full widths at half maximum for free OH and hydrogen-bonded OH stretch modes, respectively.

5.2.4.2 Global Reaction Route Mapping Calculations

In addition to the manual construction of isomer structures, we carried out systematic explorations of stable isomers of (H$_2$O)$_n^+$ on the DFT/ *ab initio* potential energy surfaces using the GRRM program developed by Ohno and Maeda [80–82, 88–90]. The structural exploration of stable isomers using the GRRM program bases on the anharmonic downward distortion (ADD) following algorithm [80–82, 88–90]. An automated search was begun at an optimized structure. To reduce the cost of calculations, we used some contraction methods as the developers recommend [80–82]. (1) Only L (typically, 5 or 6) largest ADDs among were followed. (2) AAD-following was applied only to N lowest free energy structures at each temperature ($T = 0 - T_{max}$). We used parameters of $L \geq 5$, $N \geq$ (the number of atoms), and $T_{max} = 298.15$ K. Levels of theory used for GRRM calculations

Fig. 5.7 IR photodissociation spectra of $(H_2O)_6^+ \cdot Ar$. Spectrum (**a**) and (**b**) were measured by monitoring Ar-loss and $(Ar + H_2O/OH)$-loss channel, respectively. Spectrum (**c**) is a weighted average of (**a**) and (**b**), and it is used in the following analyses

were HF/6-31G(d) and B3LYP/6-31+G(d). Because GRRM calculations are quite time-consuming, the choice of these relatively low-cost methods was necessary. For example, GRRM calculations for $(H_2O)_5^+$ at the HF/6-31G(d) took more than 3 months with our personal computer (Chap. 2). We note that HF/6-31G(d) failed to describe the dimer cation core type (as in Fig. 5.2a). However, such a limitation allowed us to conduct a limited (partial) search of a vast potential energy surface. At the B3LYP/6-31+G(d) level, both dimer cation core and proton-transferred types were found in spite of the reported overestimation of dimer cation core types. From the structures found in the GRRM calculations, we also carried out geometry re-optimization at MPW1K/6-311++G(3df,2p) for energetic discussions.

5.3 Results

Figure 5.8 IR photodissociation spectra of size-selected $(H_2O)_n^+$ ($n = 3$–11) in the OH stretch region. The band patterns in Fig. 5.8 depend sensitively on the cluster size. Figure 5.9 shows IR spectra of $(H_2O)_{3-7}^+ \cdot Ar$ in the same region. Spectra of bare and Ar-tagged clusters show similar spectral features in the $n = 4$–6 except for sharper bandwidths in Ar-mediated spectra while spectra of $n = 3$ and 7 show remarkable differences. Free OH band behavior is quite sensitive to cluster
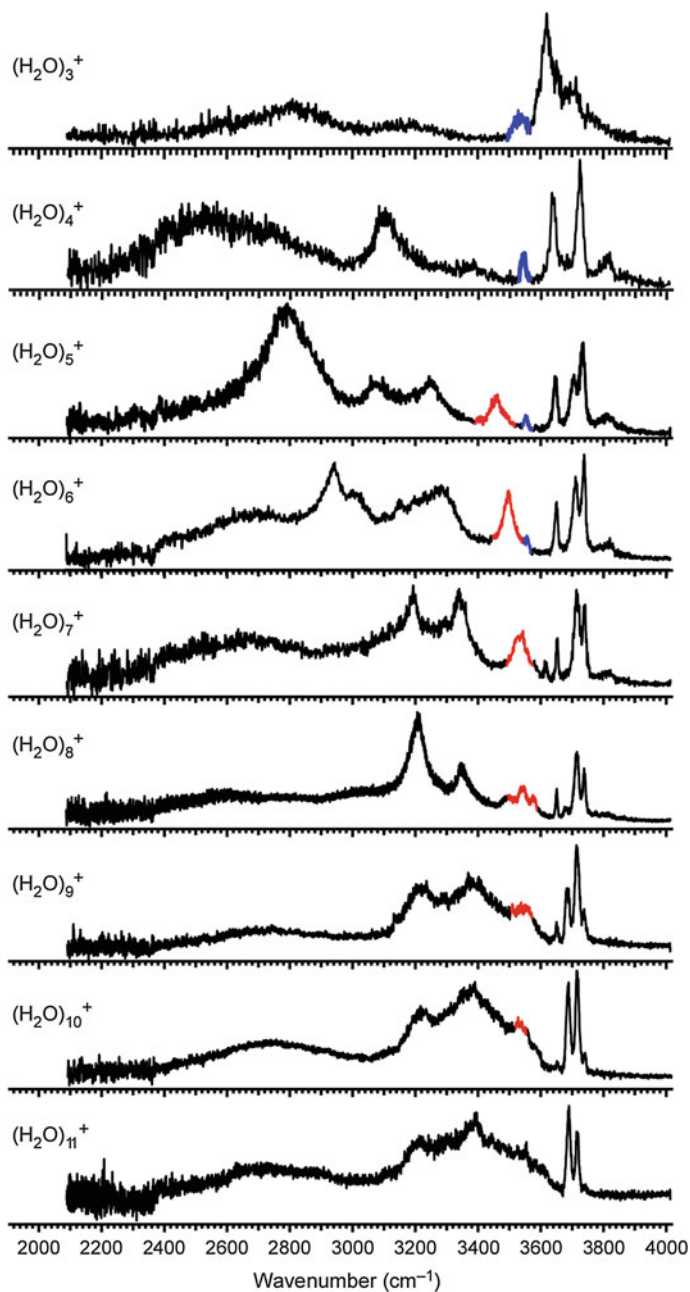
Fig. 5.8 IR spectra of $(H_2O)_{3-11}^+$ in the 2,100–4,000 cm^{-1} region. The *red* and *blue bands* are characteristic in this system and they are used in the structural analyses (see text)
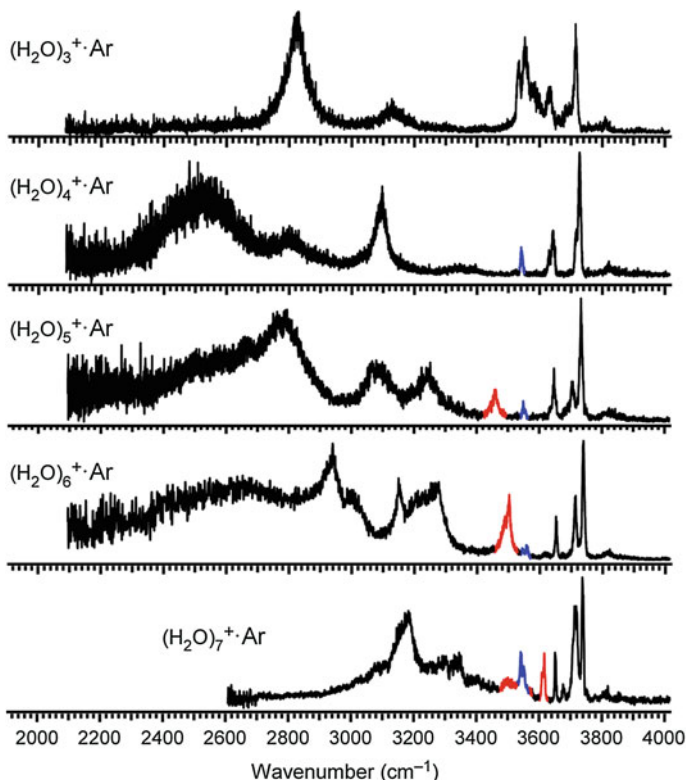
Fig. 5.9 IR spectra of $(H_2O)_{3-7}^+ \cdot Ar$ in the 2,100–4,000 cm^{-1} region. The *red* and *blue bands* are characteristic in this system and they are used in the structural analyses (see text)

structures as described in Chaps. 2, 3 and 4. Figure 5.10a shows expanded IR spectra of the free OH region and Table 5.1 collates frequencies of selected bands in this region. It was found that these band patterns of $(H_2O)_n^+$ are quite similar to those of protonated water clusters $H^+(H_2O)_n$ (shown in Fig. 5.10b) reported by several groups so far [64–71, 73, 78]. From these spectra, we discuss structures of such ionized water networks in the following sections.

5.4 Discussions

5.4.1 Analyses of Free OH Stretch Bands

In contrast to the $H^+(H_2O)_n$ system (Chaps. 3 and 4), red bands and blue bands are more characteristic in free OH stretch bands. In the case of ionic hydrated clusters such as $H^+(H_2O)_n$, free OH band behavior gives us much more structural information

Fig. 5.10 a IR spectra of $(H_2O)_n^+$ ($n = 3$–11) in the free OH stretch region. **b** IR spectra and representative structures of $H^+(H_2O)_n$. *Dotted curves* show each series of bands as assigned in Chap. 3. The bands indicated by *arrows* are the free stretch of the OH radical moiety
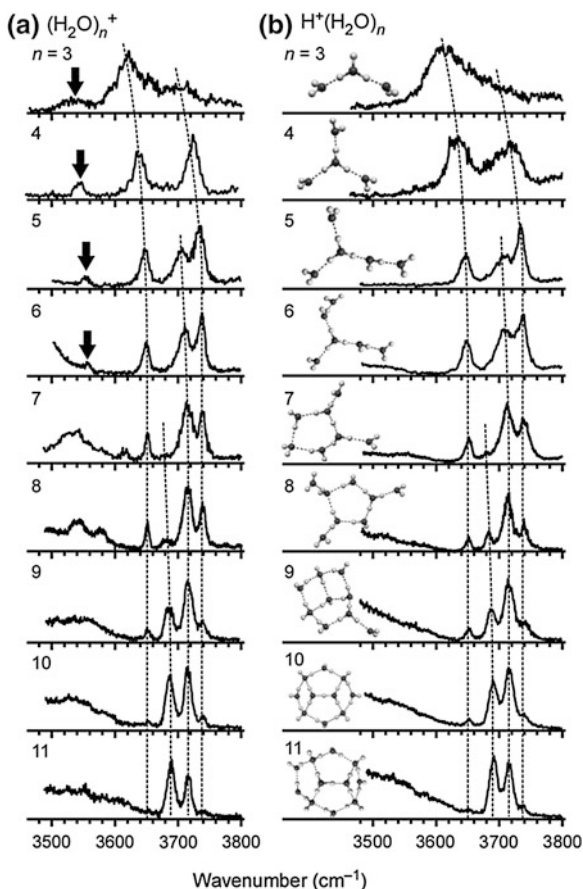
on hydrogen-bonded water networks [64–71, 73, 78]. It was found that these band patterns of $(H_2O)_n^+$ are quite similar to those of protonated water clusters $H^+(H_2O)_n$ (shown in Fig. 5.10b) reported by several groups so far [64–71, 73, 78]. For $H^+(H_2O)_n$, the correlation between hydrogen bond network shapes and IR spectra has been well understood (see Chaps. 3 and 4) [64–71, 73, 78]. A similar discussion may also be applicable to $(H_2O)_n^+$. Briefly, bands are categorized into four band series, shown as dotted lines in Fig. 5.10. From the low frequency side, there is a symmetric stretch of 1-coordinated water, a free OH stretch of 3-coordinated water, a free OH stretch of 2-coordinated water, and an antisymmetric stretch of 1-coordinated water, respectively. With increasing cluster size, bands of higher coordination numbers become stronger and 1-coordinated water bands fade out, corresponding to the structural development from chain ($n \leq 3$) to tree ($4 \leq n \leq \sim 7$), branched ring ($\sim 7 \leq n \leq \sim 10$), and closed net (multiple ring) structures ($n \geq \sim 10$). Some of the corresponding cluster structures of $H^+(H_2O)_n$ are shown as insets in Fig. 5.10b. The spectral similarity suggests that $(H_2O)_n^+$ clusters have similar network shapes (oxygen-framework) to that of $H^+(H_2O)_n$.

Table 5.1 Frequencies (in cm^{-1}) and assignments of selected bands in IR spectra of $(H_2O)_{3-8}^+$ and $(H_2O)_{3-7}^+ \cdot Ar$

Freq. (cm^{-1})	Assignment	Freq. (cm^{-1})	Assignment	Freq. (cm^{-1})	Assignment
$(H_2O)_3^+$		$(H_2O)_5^+$		$(H_2O)_7^+$	
3,536(4)	OH radical	3,458(1)	HB to ·OH	3,520(10)	HB to ·OH
				3,612(1)	
				3,618(1)	
3,624(1)	1-coordinated (v_{sym})/H_3O^+	3,553(1)	OH radical	3,543(3)	OH radical
3,697(3)	1-coordinated ($v_{antisym}$)	3,647(1)	1-coordinated (v_{sym})	3,651(1)	1-coordinated (v_{sym})
		3,707(1)	2-coordinated H_2O	3,714(1)	2-coordinated H_2O
		3,734(1)	1-coordinated ($v_{antisym}$)	3,739(1)	1-coordinated ($v_{antisym}$)
$(H_2O)_4^+$		$(H_2O)_6^+$		$(H_2O)_8^+$	
3,103(3)	HB to ·OH	3,496(1)	HB to ·OH	3,497(1)	HB to ·OH
				3,543(2)	
				3,576(1)	
3,543(1)	OH radical	3,557(1)	OH radical		
3,639(1)	1-coordinated (v_{sym})	3,649(1)	1-coordinated (v_{sym})	3,652(1)	1-coordinated (v_{sym})
3,725(1)	1-coordinated ($v_{antisym}$)	3,711(1)	2-coordinated H_2O	3,684(1)	3-coordinated H_2O
		3,737(1)	1-coordinated ($v_{antisym}$)	3,715(1)	2-coordinated H_2O
				3,739(1)	1-coordinated ($v_{antisym}$)
$(H_2O)_3^+ \cdot Ar$		$(H_2O)_5^+ \cdot Ar$		$(H_2O)_7^+ \cdot Ar$	
3,533(4)	OH radical/H_3O^+ to Ar	3,458(1)	HB to ·OH	3,612(1)	HB to ·OH
3,553(2)				3,618(1)	
3630(1)	1-coordinated (v_{sym})	3549(1)	OH radical	3542(1)	OH radical
				3552(1)	
3,715(1)	1-coordinated ($v_{antisym}$)	3,646(1)	1-coordinated (v_{sym})	3,652(1)	1-coordinated (v_{sym})
		3,704(1)	2-coordinated H_2O	3,716(1)	2-coordinated H_2O
		3,737(1)	1-coordinated ($v_{antisym}$)	3,739(1)	1-coordinated ($v_{antisym}$)
$(H_2O)_4^+ \cdot Ar$		$(H_2O)_6^+ \cdot Ar$			
3,094(2)	HB to ·OH	3,487(2)	HB to ·OH		
		3,499(2)			
3,542(1)	OH radical	3,543(1)	OH radical		
		3,556(1)			

Table 5.1   (continued)

Freq. (cm^{-1})	Assignment	Freq. (cm^{-1})	Assignment	Freq. (cm^{-1})	Assignment
3,630(1) 3,642(1)	1-coordinated (v_{sym})	3,650(1)	1-coordinated (v_{sym})		
3,717(1) 3,727(1)	1-coordinated ($v_{antisym}$)	3,711(1)	2-coordinated H$_2$O		
		3,737(1)	1-coordinated ($v_{antisym}$)		

"HB to ·OH" means hydrogen-bonded OH stretch of water towards an OH radical. All the other bands shown here are attributed to free OH stretches of assigned moieties. v_{sym} and $v_{antisym}$ are the symmetric and antisymmetric stretches, respectively. Band frequencies were determined by fitting each bandwidth a single Lorentzian function. Errors in the fitting are shown in parentheses. Absolute accuracy is ± 2 cm^{-1} due to the bandwidth of our IR source ($< \sim 3$ cm^{-1}) and the calibration method

The spectra of (H$_2$O)$_n^+$ are not exactly identical to those of H$^+$(H$_2$O)$_n$. In the 3,500–3,600 cm^{-1} region, an additional band can be observed for (H$_2$O)$_{3-6}^+$ and it is indicated by the arrow in Fig. 5.10a (blue bands in Figs. 5.8 and 5.9). The frequency of this band is too low to be attributed to any free OH stretch of the H$_2$O moieties. Because the gas-phase frequency of the stretch vibration of OH radical is 3,570 cm^{-1} [91], we assign this band to the free stretch of an OH radical moiety in the clusters. This assignment is consistent with the OH radical stretch frequencies in (H$_2$O)$_2^+$ Ar$_{1, 2}$, 3,511 and 3,499 cm^{-1}, respectively [61]. The presence of the OH radical stretch band as well as the spectral similarity to H$^+$(H$_2$O)$_n$ indicates that nominal water cluster cations (H$_2$O)$_n^+$ ($n \geq 3$) should be regarded as "protonated water clusters with an OH radical", H$^+$(H$_2$O)$_{n-1}$(OH), as has been reported for (H$_2$O)$_2^+$ [61]. In this study, we use the notation, (H$_2$O)$_n^+$, for simplicity. These considerations also provide negative evidence for the "dimer ion core" type as in Fig. 5.2a. Evidence for the lack of plausibility of the "dimer cation core" type will also be confirmed in the following sections. For H$^+$(H$_2$O)$_{n-1}$(OH) type structures, mutual positions of the protonated core and the OH radical (i.e., the distinction between the two structures in Fig. 5.2b and c) are essential in characterizing cluster structures, implying the reactivity (mobility) of the produced OH radical. In the following sections, we will discuss more detailed structures for each cluster size on the basis of the spectra including the hydrogen-bonded OH stretch region.

5.4.2   (H$_2$O)$_3^+$

Figure 5.11a shows the IR spectrum of (H$_2$O)$_3^+$ in the 2,100–4,000 cm^{-1} region. For comparison, the structure and IR spectrum of H$^+$(H$_2$O)$_3$ are shown in Fig. 5.11d. As was described in the former section, these two spectra are similar to each other. However, the spectrum of (H$_2$O)$_3^+$ has additional bands at around 2,800
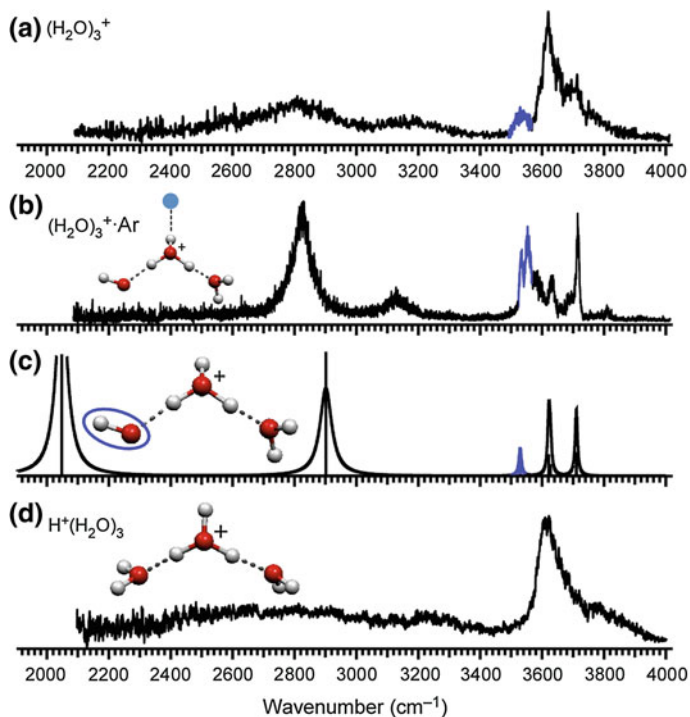
Fig. 5.11 **a** IR spectrum of $(H_2O)_3^+$. **b** IR spectrum of $(H_2O)_3^+ \cdot Ar$. The band highlighted in *blue* is the free stretch of the OH radical moiety. **c** Calculated cluster structure and corresponding IR spectrum at the MPW1K/6-311++G(3df,2p) level. The OH radical moiety is *circled*. **d** IR spectrum and structure of $H^+(H_2O)_3$

and 3,536 cm^{-1}. The latter band, displayed in blue, is attributable to the OH radical stretch. The free OH bands suggest that the structure of $(H_2O)_3^+$ should resemble that of $H^+(H_2O)_3$ and have an OH radical moiety. From these requirements, the structural motif of $(H_2O)_3^+$ can be identified as shown in Fig. 5.11c. The structure in Fig. 5.11c was constructed by substituting one of the water molecules in $H^+(H_2O)_3$ with an OH radical [throughout this thesis, we did not distinguish position isomers, internal rotation isomers, and enantiomer (mirror image isomers)]. On the basis of this structure, we carried out DFT calculations at the MPW1K/6-311++G(3df,2p) level to obtain the energy-optimized structure and its simulated IR spectrum. The calculated IR spectrum shown in Fig. 5.11c reproduces the band pattern in the free OH stretch region and the band at around 2,800 cm^{-1}. This agreement supports the structure shown in Fig. 5.11c. The calculation indicates that the observed band at around 2,800 cm^{-1} should be assigned to the OH stretch of the H_3O^+ core, hydrogen-bonded to the OH radical moiety. This is reasonable because no clear corresponding peak was observed for $H^+(H_2O)_3$, which does not contain an OH radical (a broad absorption in the

$H^+(H_2O)_3$ spectrum ($< \sim 3400$ cm^{-1}) would be attributable to the long tail of the lower frequency H_3O^+ stretch band, which has been observed at $\sim 1,880$ cm^{-1} in the Ar-mediated spectrum [72]. An additional band can be seen at around 3,150 cm^{-1} in the $(H_2O)_3^+$ spectrum, while it is absent from the calculated spectrum. We tentatively assigned this band to the overtone of the H_3O^+ stretch.

For further discussion, the Ar-mediated spectrum is also shown (Fig. 5.11b). The observed features seem to be different from the spectrum of the bare cluster although the band at around 3,530 cm^{-1} implies the spectral carrier is the structure in Fig. 5.11c. The observed differences can be attributed to the different internal energy and perturbation of Ar. The former one accounts for the sharper bandwidths of all the bands. To estimate the effect of Ar attachment, we constructed $(H_2O)_3^+ \cdot Ar$ structures. The inset in Fig. 5.11b shows the most plausible structure of $(H_2O)_3^+ \cdot Ar$ obtained with the previously reported systematic calculations. Furthermore, this structure is reasonable because the polarizable Ar atom is directly bound to the charged site (H_3O^+). Such a position of Ar is in agreement with that reported for $H^+(H_2O)_3 \cdot Ar$. Because Ar attachment leads to a small low-frequency shift of OH stretching, free OH stretching of the H_3O^+ moiety at $\sim 3,620$ cm^{-1} in the bare $(H_2O)_n^+$ becomes one of the blue bands ($\sim 3,530$ cm^{-1}) in $(H_2O)_3^+ \cdot Ar$. According to these discussions, two adjacent bands in blue were assigned to the OH stretching of the H_3O^+ moiety toward Ar and the OH radical stretching, both of which may be coupled to each other.

5.4.3 $(H_2O)_4^+$

The same analysis as in $(H_2O)_3^+$ is applicable to $(H_2O)_4^+$. Figure 5.12a, b shows the experimental IR spectrum of $(H_2O)_4^+$ and $(H_2O)_4^+ \cdot Ar$, respectively. In this system, both spectra of the bare and Ar-tagged clusters show essentially the same spectral features except for the clearer structures and tiny split in Fig. 5.12b. Spectral similarity shows the spectral carrier of these spectra is the same. Here, reduced internal energy and perturbation of Ar account for tiny spectral differences. Figure 5.12d shows the structure and the spectrum of $H^+(H_2O)_4$ for comparison. $H^+(H_2O)_4$ has a symmetrically solvated H_3O^+ core (Eigen cation) [64, 65, 72, 79]. One of the solvating water molecules was replaced with a OH radical, and the plausible $(H_2O)_4^+$ structure (Fig. 5.12c) was obtained. By using DFT, we calculated the IR spectrum (Fig. 5.12c). The simulated IR spectrum is in good agreement with the observed spectrum, verifying the structure in Fig. 5.12c. The minor extra band at around 3,800 cm^{-1} in the observed spectrum can be assigned to the combination band of a free OH stretch and a low-frequency mode as in the previously reported IR spectroscopy of various hydrated clusters including $H^+(H_2O)_4$ (Fig. 5.12d) [64, 67, 79]. A weak shoulder at around 3,380 cm^{-1} is not expected by the calculation. The tentative assignment is an overtone/combination band or minor contribution from other isomers. The latter would be less plausible because the presence of other isomers affects band patterns in the free OH stretch region.
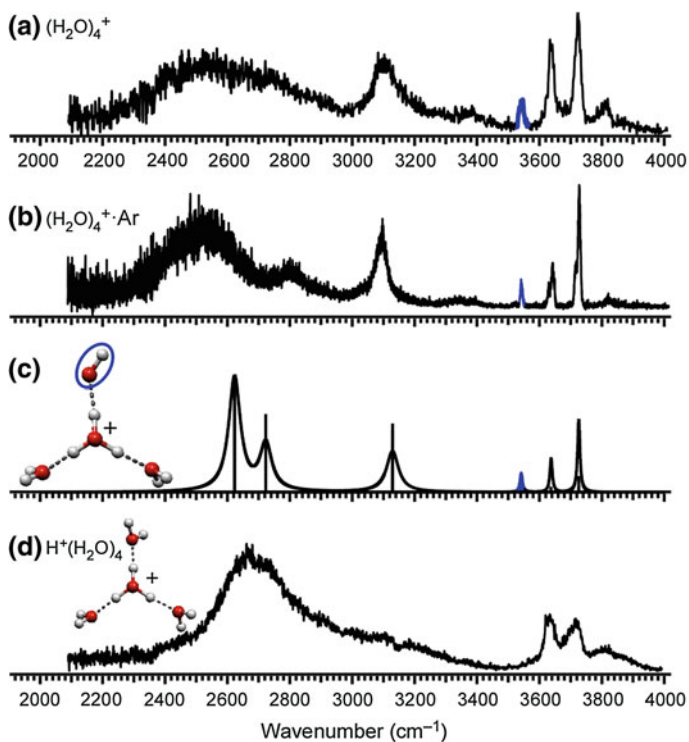
Fig. 5.12 a IR spectrum of $(H_2O)_4^+$. **b** IR spectrum of $(H_2O)_4^+ \cdot Ar$. The band highlighted in *blue* is the free stretch of the OH radical moiety. **c** Calculated cluster structure and corresponding IR spectrum at the MPW1K/6-311++G(3df,2p) level. The OH radical moiety is *circled*. **d** IR spectrum and structure of $H^+(H_2O)_4$

The IR spectrum of $(H_2O)_4^+$ also provides insight into hydrogen bond strength, which should be an important factor for further structure determination. In the observed spectrum, two hydrogen-bonded OH bands can be seen. The lower frequency band below 2,800 cm^{-1} corresponds to a similar band in $H^+(H_2O)_4$, and can be assigned to the hydrogen-bonded OH stretches toward the water molecules. On the other hand, the higher frequency band at around 3,100 cm^{-1} is characteristic in $(H_2O)_4^+$ and therefore attributable to the hydrogen-bonded OH stretch toward the OH radical. Because a stronger hydrogen bond generally results in a lower OH stretch frequency [72, 92, 93], the higher frequency of the band at 3,100 cm^{-1} shows that the OH radical is a weaker hydrogen bond acceptor than water. This is consistent with the smaller proton affinity of OH (593 kJ/mol) than H_2O (691 kJ/mol) [94]. In the following section, we show that this different hydrogen bond strength is a key to determining the structures of larger-sized clusters. It should be noted that a similar discussion can be applied to $(H_2O)_3^+$, however, the band of the hydrogen-bonded OH toward a water molecule is expected to be located outside of the measurement range ($\sim 2,050$ cm^{-1}, in Fig. 5.11c).
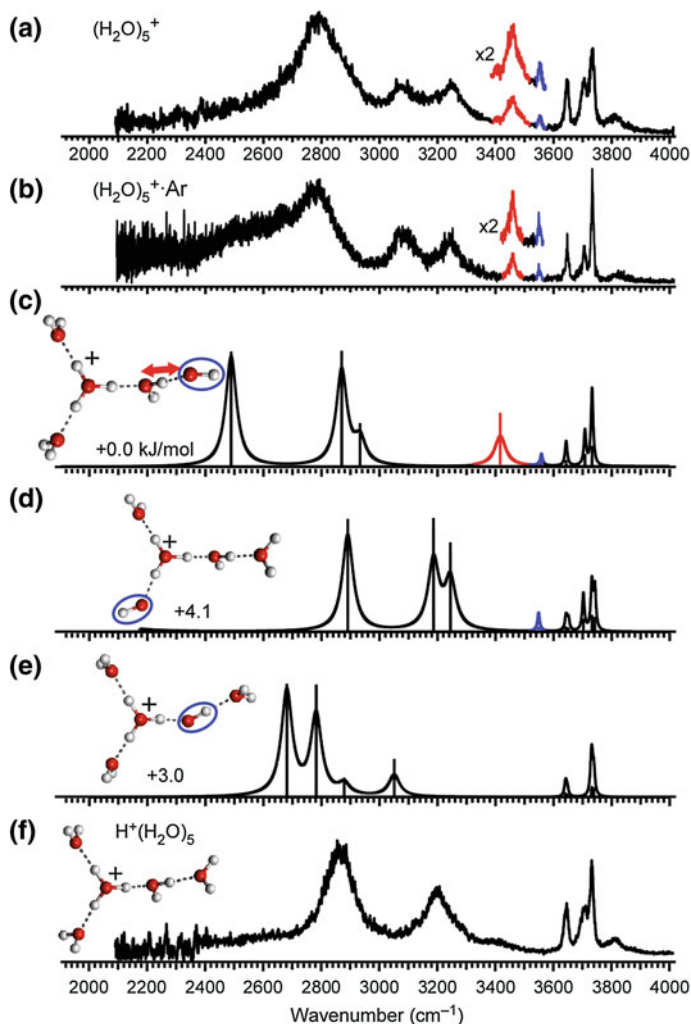
Fig. 5.13 a IR spectrum of $(H_2O)_5^+$. **b** IR spectrum of $(H_2O)_5^+ \cdot Ar$. The band highlighted in *blue* is the free stretch of the OH radical moiety. The *red band* is the marker of a hydrogen bond from H_2O to $\cdot OH$ (see text). **c–e** Calculated cluster structures and corresponding IR spectra at the MPW1K/6-311++G(3df,2p) level. Relative energies are also indicated in kJ/mol. The OH radical moiety is *circled*. **f** IR spectrum and structure of $H^+(H_2O)_5$

5.4.4 $(H_2O)_5^+$

Figure 5.13a shows the experimental IR spectrum of $(H_2O)_5^+$. As in the case of $(H_2O)_4^+ \cdot Ar$, the Ar-mediated spectrum in Fig. 5.13b exhibits essentially the same features as Fig. 5.13a. Figure 5.13f shows the structure and the spectrum of $H^+(H_2O)_5$. Here, two bands highlighted in blue $(3,553 \text{ cm}^{-1})$ and in red

(3,458 cm^{-1}) are characteristic in $(H_2O)_5^+$ and absent in $H^+(H_2O)_5$, implying they are related to the OH radical moiety. The band in blue is the stretch of the OH radical as in $(H_2O)_{3,4}^+$. The band in red (3,458 cm^{-1}) is absent in both $H^+(H_2O)_n$ and $(H_2O)_{3,4}^+$. The bandwidth is broader than the free OH bands, indicating this is a hydrogen-bonded OH stretch band. In addition, its band frequency is the highest among the hydrogen-bonded OH bands. This means the band in red is a signature of a weakly hydrogen-bonded site (note that lower-frequency is expected for stronger hydrogen bonds as mentioned in Sect. 1.3.2).

For the structural consideration, the same argument as in $(H_2O)_{3,4}^+$ can be applied; however, there is complexity in $(H_2O)_5^+$. Although only one type of structure has been identified experimentally for $H^+(H_2O)_5$ (Fig. 5.13f) [67, 72, 79], three possibilities arise for the corresponding $(H_2O)_5^+$ (Fig. 5.13c–e). Structures in Fig. 5.5b–d differ in the position of the OH radical. In structure I (Fig. 5.13c), the H_3O^+–OH ion-radical contact pair is dissociated by a water molecule, and the OH radical locates at the terminal (surface) of the hydrogen bond network. In structure II (Fig. 5.13d), the OH radical is also at the terminal, but is directly bound to the H_3O^+ core. In structure III (Fig. 5.13e), the H_3O^+–OH ion-radical contact pair is fully hydrated and the OH radical is inside the network. Here, Structure I and III are the same as those in Fig. 5.2b and c, respectively.

In the following section, we examine the plausible spectral carriers and band assignments on the basis of simulated spectra shown in Fig. 5.13c–e. The contribution of the most stable structure I is obvious because of the appearance of the characteristic red band, which can be seen only in structure I. According to the normal mode analysis, the characteristic red band (3,458 cm^{-1}) can be attributed to the hydrogen-bonded OH stretch of a water molecule toward the OH radical (denoted by the red arrow in Fig. 5.13c). Here this water molecule bridges the H_3O^+ core and the OH radical. This assignment is reasonable considering the weaker hydrogen bond accepting ability of the OH radical, as discussed with $(H_2O)_4^+$. The calculated spectrum of structure I reproduces the observed spectrum in the 3,500–3,800 cm^{-1} region well, but the calculated 2,500 cm^{-1} band is missing in the observed spectrum. This missing band is attributable to the OH stretch of H_3O^+ toward the 2-coordinated water. The proton toward the 2-coordinated water is partially delocalized to the neighboring water because of the cooperative hydrogen bond to the second solvation shell molecule (the OH radical). Its transition frequency is therefore expected to be much lower than the present harmonic frequency due to the large anharmonicity. The same argument has been reported for $H^+(H_2O)_5$ [72, 79].

The calculated spectrum of structure I does not also account for the observed features in the 3,000–3,200 cm^{-1} region, and it seems that the significant coexistence of structure II explains these bands. In this case, structure III may also coexist because of its similar relative energy, and its spectrum overlaps with the observed one well. Alternative assignments of the bands are overtones and/or combination bands of structure I. The unexpected band at 3,270 cm^{-1} in the spectrum of $(H_2O)_2^+$·Ar has been explained by the overtone of the bonded H_3O^+ stretch [61]. Here, we should note that the major contribution of structures II and III causes a

serious conflict with the high frequency region of the observed spectrum. The intensity of the red marker band relative to the free OH bands can be reproduced only by the major contribution of structure I. Moreover, we observed that the loss of the OH radical only occurs upon the IR vibrational excitation of the free OH stretch band at 3,734 cm^{-1} (Fig. 5.5), which is the vibration of a terminal water molecule and is commonly expected in all of the three isomers. The H_2O-loss is quite negligible in this excitation (Fig. 5.5). This suggests that the OH radical lies at the terminal of the network. A hydrogen bond to the OH radical moiety should be the weakest one in the cluster. Because the hydrogen bond with the ion-core is much stronger than those between neutral moieties, the OH moiety should be bound to a neutral moiety, as in structure I. If there is a greater contribution of structures II and III, then the fragmentation pattern should be largely different. These results support the view that the features at 3,000–3,200 cm^{-1} are assigned to overtone/combination bands and therefore structure I is dominant in $(H_2O)_5^+$. The coexistence of structures II and III cannot be excluded, but they should be minor.

For further confirmation of the dominance of structure I, we examined the energetics. Because clusters formed in the present ion source have finite temperatures, the energetics including entropy are worth mentioning. We calculated relative Gibbs free energies and relative populations (canonical probabilities) at the temperature range of 0–400 K (Figs. 5.14 and 5.15, respectively). We found that both structures II and III are less stable than structure I at this entire temperature range (Fig. 5.14). While the relative instability of structure III is constant, that of structure II increases with rising temperature (this would be due to the presence of the low frequency mode in structure I (~ 8 cm^{-1}) corresponding to the rearrangement motion of the weakly bound OH radical. In structure II, the OH radical is tightly bound to H_3O^+, and no low frequency modes below 10 cm^{-1} can be found). At 180 K, the relative populations (canonical probabilities) of structure I, II, and III are calculated to be 0.90, 0.04, and 0.06, respectively, under the harmonic vibrational approximation (Fig. 5.15). This evaluation also shows the quite minor contribution of these isomers.

In structure I, the red marker band is due to the hydrogen-bonded OH to the OH radical moiety, and its high frequency reflects the weak ability of the OH radical as

Fig. 5.14 Gibbs free energies relative to the most stable structure of $(H_2O)_5^+$. *Open squares*, *filled dots*, and *open dots* show relative energies of structures I, II, and III, respectively (see also Fig. 5.13). Structure I is the most stable of all the temperatures considered here
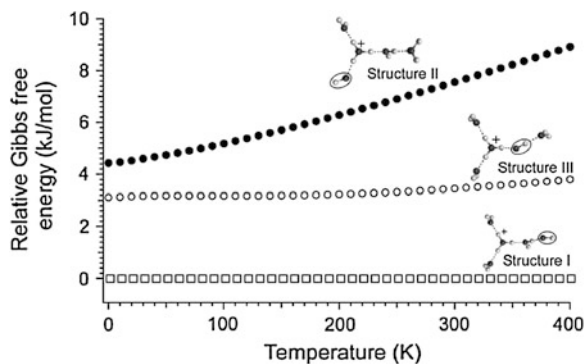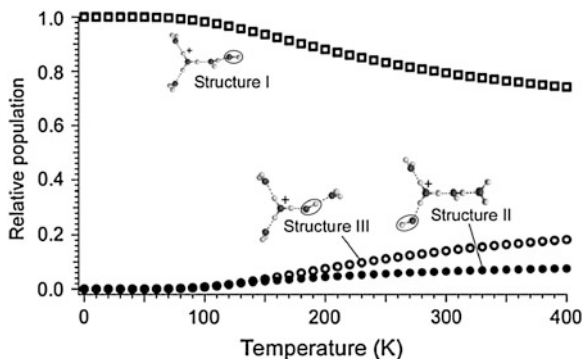
Fig. 5.15 Relative populations (canonical probabilities) of three isomers in $(H_2O)_5^+$. *Open squares*, *filled dots*, and *open dots* show populations of structure I, II, and III, respectively (see also Fig. 5.13). The population ratio of isomer A to isomer B is given by $\frac{P_A}{P_B} = \frac{Q_A}{Q_B} \exp(-\Delta E_{AB}/kT)$, where Q_A and Q_B are partition functions of isomer A and B, respectively, ΔE_{AB} is the energy difference of two isomers, k is the Boltzmann constant, and T is temperature. The partition functions were calculated using harmonic frequencies

a hydrogen bond acceptor. From the viewpoint of the hydrogen bond strength, structure I is rationalized because the first solvation shell of the H_3O^+ is filled with three water molecules, which can form a stronger hydrogen bond than the OH radical, and the OH radical, weaker hydrogen bond acceptor, is pushed out to the second solvation shell.

Such an ion-radical contact pair separation has also been indicated by the recent *ab initio* molecular dynamics calculations. Tachikawa has calculated vertical ionization dynamics of $(H_2O)_{n \leq 5}$ and reported that the second proton transfer occurs after the H_3O^+–OH pair formation resulting in separation of the contact pair [41]. Similar results have been reported by Novakovskaya [46, 47] and by Livshits et al. [85]. Though our cluster ion source does not utilize vertical ionization of neutral $(H_2O)_n$ and detailed processes in the cluster formation are unknown, the reported calculations are consistent with the present results in terms of the separation of the H_3O^+–OH contact pair.

According to the above discussion, we have shown that the band highlighted in red is due to the "bridging" water weakly hydrogen bonding to the OH radical, and this band is an important signature for the separation between the protonated ion core and the OH radical. On the basis of this knowledge, we analyzed the structures of larger clusters.

5.4.5 Overview of $(H_2O)_n^+$ (n ≥ 6) Structures

As clearly seen in the 3,500–3,570 cm^{-1} region in the spectra in Figs. 5.8 and 5.9, the marker band attributed to the "bridging" water moiety remains remarkable in the $n \geq 6$ region. This result indicates that the separation between the protonated

site and the OH radical is a general trend in larger-sized $(H_2O)_n^+$. It should be noted that spectra of larger-sized $(H_2O)_n^+$ become more similar to those of $H^+(H_2O)_n$ due to the decrease of the relative weight of the OH radical and the "bridging" water site. As a result, we could not find remarkable differences between the spectra of $(H_2O)_{11}^+$ and $H^+(H_2O)_{11}$ (Fig. 5.8). However, the clear appearance of the marker band and the smooth spectral changes in $n \leq 10$ strongly suggest the trends remain in clusters larger than $n = 10$.

We thus obtained three general trends in structures of $(H_2O)_n^+$: (1) Nominal water cluster cations $(H_2O)_n^+$ form proton-transferred type $H^+(H_2O)_{n-1}(OH)$. (2) Structures (oxygen-frameworks) of networks are quite similar to those of $H^+(H_2O)_n$. (3) After the first solvation shell of the protonated ion core is completed, the OH radical is separated from the ion core by at least one water molecule. We note that the third trend is in agreement with the absence of $(H_2O)_n^+$ in the "warmer" cluster source (Fig. 5.4). This is because the absence of $(H_2O)_n^+$ indicates that the OH radical is easily ejected by thermal evaporation, resulting in production of $H^+(H_2O)_{n-x}$. This weakly-bound nature of the OH radical is consistent with the present IR spectroscopic findings for $(H_2O)_n^+$ that the OH radical is separated from the protonated site and is bound by a weaker hydrogen bond than water–water hydrogen bonds.

On the basis of these insights, we can easily infer the preferential structures of larger-sized $(H_2O)_n^+$: Structures of $(H_2O)_n^+$ were constructed from well-known structures of $H^+(H_2O)_n$ [67, 72, 82] by substituting one of the water molecules away from the protonated site with an OH radical. For $n \geq 6$, the coexistence of multiple isomers is expected even for $H^+(H_2O)_n$ [67, 76, 81], however, we can deduce cluster structures by the same procedure. For confirmation of the present findings, systematic analyses of $(H_2O)_{6-8}^+$ will be given below.

5.4.6 $(H_2O)_6^+$

Figure 5.16 shows the experimental IR spectrum of $(H_2O)_6^+$ and $(H_2O)_6^+ \cdot Ar$, respectively. Both spectra again exhibit similar features except for well-resolved spectral structures of $(H_2O)_6^+ \cdot Ar$. As discussed in Chap. 4, two isomers ("Zundel" and "Eigen") coexist in bare $H^+(H_2O)_6$. According to the above-mentioned structural trends, two plausible isomers, "Zundel-like" and "Eigen-like", of $(H_2O)_6^+$ were constructed (Fig. 5.16c, d, respectively). Here, in contrast to Zundel type $H^+(H_2O)_6$, symmetry of the system is lifted due to the OH radical, a weaker proton (hydrogen bond) acceptor, and therefore the position of the excess proton in Zundel-like $(H_2O)_6^+$ is not the center so as to create a distance from the OH radical. We use the notation of "-like" for this reason. Spectral simulations for both isomers reproduce the characteristic red (hydrogen-bonded OH toward the OH radical) and blue (OH radical stretch) bands well.

Spectral comparison in the free OH stretch region shows that the Eigen-like structure in Fig. 5.16c should be a spectral carrier, because this structure has 2-coordinated water molecules and they account for the observed $\sim 3,710 \text{ cm}^{-1}$
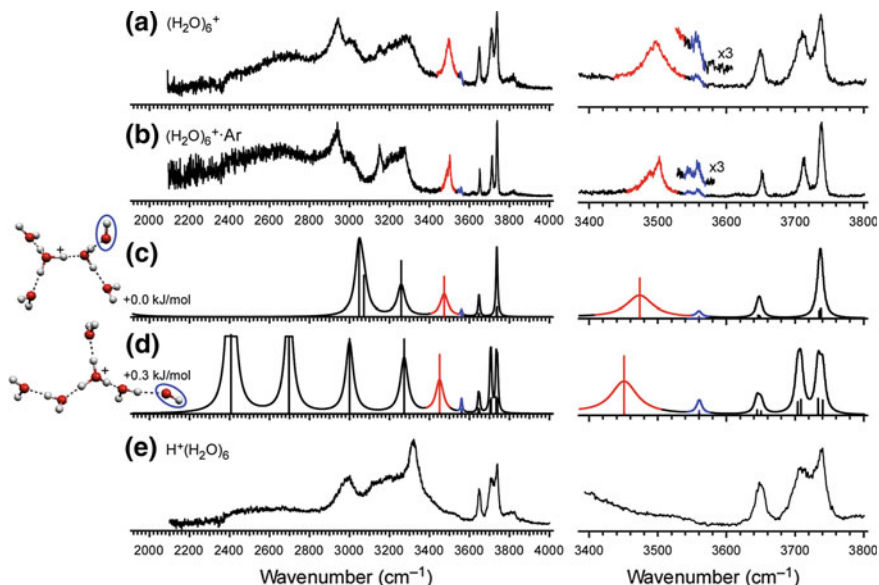
Fig. 5.16 a IR spectrum of $(H_2O)_6^+$. **b** IR spectrum of $(H_2O)_6^+ \cdot Ar$. The band highlighted in *blue* is the free stretch of the OH radical moiety. The *red band* is the marker of a hydrogen bond from H_2O to $\cdot OH$ (see text). **c, d** Calculated cluster structures and corresponding IR spectra at the MPW1K/6-311++G(3df,2p) level. The OH radical moiety is *circled*. Relative energies are also indicated in kJ/mol. **e** IR spectrum and structure of $H^+(H_2O)_6$. The *right* column shows expanded spectra of the *left* columns

band (Chaps. 3 and 4). However, the relative intensity of this band in the simulated spectrum is significantly larger than that of observed spectra. Furthermore, in the hydrogen-bonded OH stretch region, the simulated spectrum for the Eigen-like isomer accounts for only a part of observed features. For example, only two bands are expected for the Eigen-like isomer in the 2,800–3,300 cm^{-1} simulated spectrum, while observed spectra show four or more bands. These facts imply the coexistence of isomers. When we assume the mixture of the Eigen-like and Zundel-like isomers, spectral similarity to experimental spectra is much closer. Because the Zundel-like isomer does not include the 2-coordinated water, the 3,710 cm^{-1} band becomes weaker upon inclusion of the Zundel-like type. More bands can be expected in the 2,800–3,300 cm^{-1} regions. Furthermore, in the Ar-mediated spectrum (Fig. 5.16b), splitting of OH radical-related bands (both red and blue bands) can be observed. Because only one OH radical should be in each cluster, this observation indicates the coexistence of at least two isomers, both of which are in agreement with the above-mentioned structural trends of $(H_2O)_n^+$.

We emphasize that all the other type structures which satisfy all the conditions in $(H_2O)_6^+$ potential energy surface cannot reproduce spectra because these structures have an unsolvated charged site or a branched ring. The former type is energetically unfavorable. The latter should show characteristic bands, as in the

ring type isomers in $(H_2O)_{7,8}^+$ (see the following sections). According to these discussions, we conclude the coexistence of the Eigen-like and Zundel-like types, both of which can be constructed from the $H^+(H_2O)_n$ structures with the present structural trends. We note that more detailed analyses of spectra need spectral separation. IR–IR hole-burning spectroscopy, which enables isomer-specific spectroscopy, would be a great help in realizing such a purpose.

We also note that, in the case of $H^+(H_2O)_6$, only the Zundel type is found in Ar-tagged clusters. Coexistence in $(H_2O)_6^+$, even with Ar-tagging, would correlate with the OH radical induced displacement of the excess proton. This fact is in agreement with the assumption that Ar-tagging favors the Zundel-type ion core as in Chap. 4.

5.4.7 $(H_2O)_7^+$

Figure 5.17 shows the experimental IR spectrum of $(H_2O)_7^+$ and $(H_2O)_7^+ \cdot Ar$, respectively. In contrast to smaller clusters, Ar induced spectral changes in this system. Furthermore, a characteristic band was found at $\sim 3{,}615$ cm^{-1}, in which no band has been observed in $H^+(H_2O)_7$ or smaller $(H_2O)_n^+$. Later, we show this band is an indicator of an important isomeric structure.
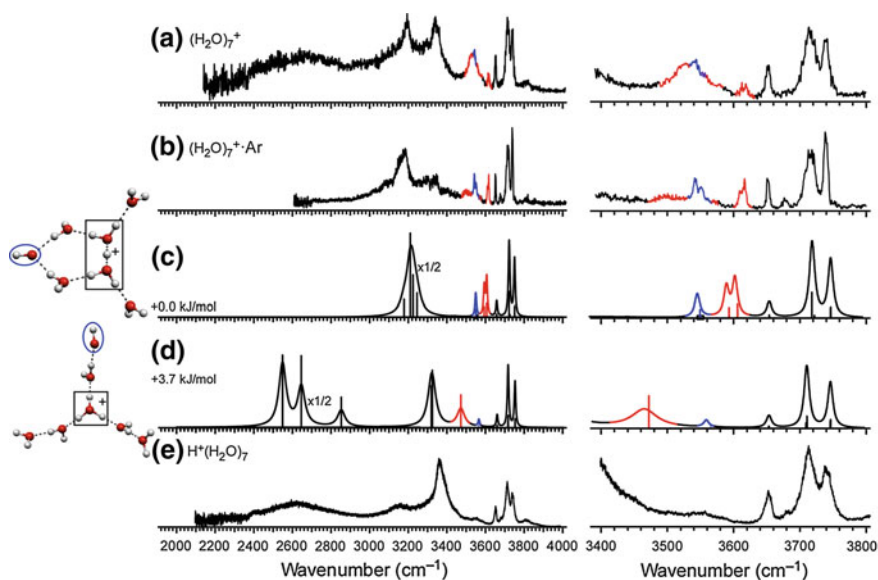
Fig. 5.17 a IR spectrum of $(H_2O)_7^+$. **b** IR spectrum of $(H_2O)_7^+ \cdot Ar$. The band highlighted in *blue* is the free stretch of the OH radical moiety. The *red band* is the marker of a hydrogen bond from H_2O to $\cdot OH$ (see text). **c, d** Calculated cluster structures and corresponding IR spectra at the MPW1K/6-311++G(3df,2p) level. The OH radical moiety is *circled*. Relative energies are also indicated in kJ/mol. **e** IR spectrum and structure of $H^+(H_2O)_7$. The right column shows expanded spectra of the left columns

From the structures of $H^+(H_2O)_7$, the chain type with Eigen core and the ring type with Zundel core, we constructed two plausible structures of $(H_2O)_7^+$ (Fig. 5.17c, d). By spectral comparison, the characteristic $\sim 3,615$ cm^{-1} bands are attributable to the ring type $(H_2O)_7^+$. According to our calculations, these bands are due to the hydrogen-bonded OH stretching of the bridging (2-coordinated) H_2O toward the OH radical. This frequency is higher than the free OH radical band because the weaker hydrogen bond acceptor accepts two hydrogen bonds, resulting in much weaker hydrogen bonding. This ring type isomer does not account for all of the spectral features. The observed 3,550 cm^{-1} band, which is a typical hydrogen-bonded OH toward the OH radical, can be assigned to the chain type isomer. The coexistence of these two isomers reproduced the experimental spectral features well. Furthermore, in the Ar-mediated spectrum, the contribution of the ring type, which has a Zundel core, is larger than in the bare cluster. This is consistent with the $H^+(H_2O)_7$ case, in which Ar-mediated isomer distribution change has been observed.

5.4.8 $(H_2O)_8^+$

Figure 5.18 shows the experimental IR spectrum of $(H_2O)_8^+$. The red band due to the $H_2O \cdots OH$ hydrogen bond can be seen; however, the presence of the OH radical stretching is not clear. In the case of $H^+(H_2O)_8$ (and its inert gas-attached
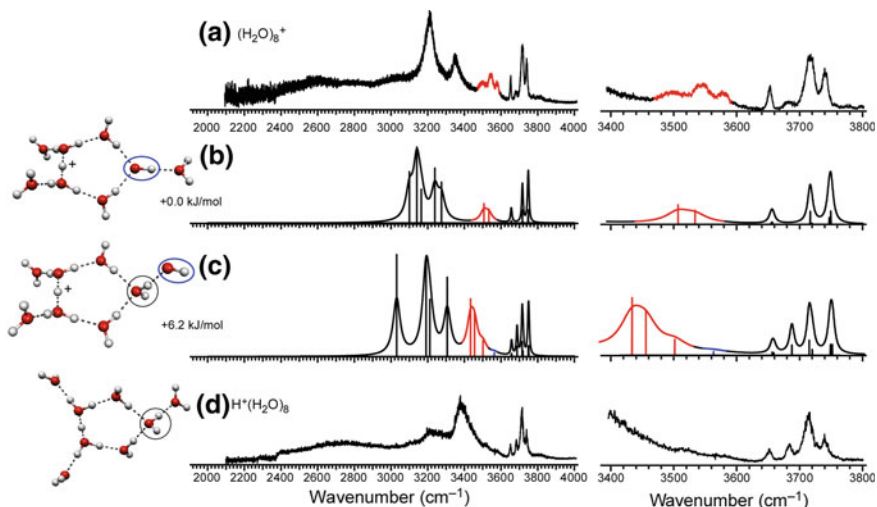
Fig. 5.18 **a** IR spectrum of $(H_2O)_8^+$. The *red band* is the marker of a hydrogen bond from H_2O to $\cdot OH$ (see text). **b, c** Calculated cluster structures and corresponding IR spectra at the MPW1K/6-311++G(3df,2p) level. The OH radical moiety is *circled in blue*. 3-coordinated water is *circled in black*. Relative energies are also indicated in kJ/mol. **d** IR spectrum and structure of $H^+(H_2O)_8$. The *right* column shows expanded spectra of the *left* columns

species), the branched ring type shown is a major (or unique) spectral carrier. According to the construction methods for $(H_2O)_8^+$, we obtained two candidates ("interior" and "terminal", in Fig. 5.18b, c). The interior type, OH radical replaces the 3-coordinated water in the $H^+(H_2O)_8$ structure while the terminal type does the terminal, dangling H_2O. When we compare the observed spectrum with that of $H^+(H_2O)_8$, we can clearly find that the band at ~ 3680 cm^{-1} is loose its intensity in $(H_2O)_8^+$. Because this band is due to the 3-coordinated water molecule, the observed decreased intensity of this band indicates that the OH radical takes the place of the 3-coordinated site.

On the basis of these discussions, we conclude that the observed spectrum is well accounted for by the interior type isomer. In the interior type, the OH radical is separated by only one H_2O molecule and it is also solvated by the terminal water. In other words, the OH radical in the interior type acts as a hydrogen bond donor as well as an acceptor. This fact provides a sharp contrast with the smaller clusters, in which the OH radical always acts just as a hydrogen bond acceptor. This is because a charged site should always be a hydrogen bond donor and it does not accept a hydrogen bond because the positive charge repels positively polarized hydrogen atoms. In the neutral OH-H_2O cluster, on the other hand, the OH radical acts as a hydrogen bond donor, indicating that the OH radical is a stronger hydrogen bond donor than H_2O. The present observation of the hydrogen bond donating OH radical suggests that dilution of the charge by adding many water molecules leads to structural motifs of the neutral networks. We note minor isomers that have a 3-coordinated site are also evidenced by the weak 3,680 cm^{-1}. The broad absorption below 3,000 cm^{-1} indicates the Eigen-like structural motifs. Further discussions need IR–IR hole-burning spectroscopy. We should emphasize that we characterized at least one isomer and obtained the important structural trends for radical cationic water networks.

5.4.9 Other Isomers in a Global Potential Energy Surface

We experimentally revealed structures of $(H_2O)_n^+$; however, in the present study, we did not observe some structures suggested so far, such as the dimer cation core type shown in Fig. 5.2a. It is also valuable to characterize both the observed and other stable structures on the potential energy surface. For this purpose, we carried out systematic explorations of stable isomers of $(H_2O)_{3-8}^+$ on the HF/6-31G(d) and B3LYP/6-31+G(d) potential energy surfaces by using the GRRM program [80–82, 88–90]. This approach has been applied to $H^+(H_2O)_{5-8}$ and has successfully found many local minima including the experimentally identified ones [81, 82]. We used this program with similar parameters to those reported for $H^+(H_2O)_n$ (Sect. 5.2) [81, 82]. In the B3LYP/6-31+G(d) calculations, we obtained 3, 15, and 82 stable isomers for $(H_2O)_3^+$, $(H_2O)_4^+$, and $(H_2O)_5^+$, respectively (see Figs. 5.19, 5.20 and 5.21). After the re-optimization at the MPW1K/6-311++G(3df,2p) level, we found that all the structures observed in this study are global minima in each size.
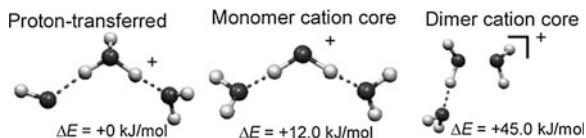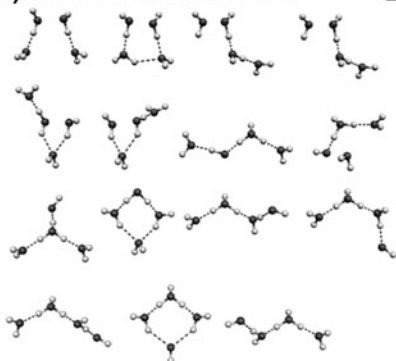
Fig. 5.19 Three isomer structures of $(H_2O)_3^+$ and their relative energies obtained with the present GRRM calculations. Relative energies of each structure were calculated at the MPW1K/6-311++G(3df,2p) level
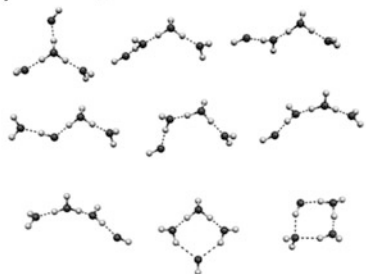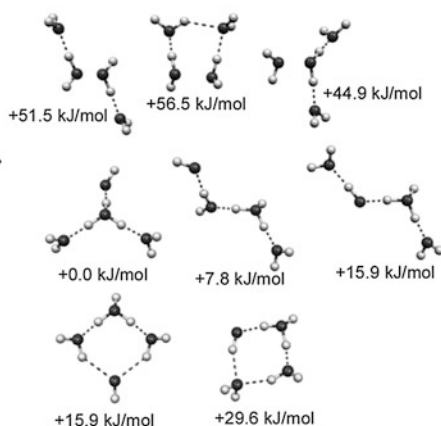
Fig. 5.20 Isomer structures of $(H_2O)_4^+$ and their relative energies obtained with the present calculations. **a** Results of GRRM calculation at the HF/6-31G(d) level. **b** Results of GRRM calculation at the B3LYP/6-31+G(d) level. **c** Re-optimization of structures in (**a**, **b**) at the MPW1K/6-311++G(3df,2p) level. Relative energies of each structure were calculated at the MPW1K/6-311++G(3df,2p) level

Figures 5.19, 5.20 and 5.21 also show relative energies of each structure calculated at the MPW1K/6-311++G(3df,2p) level. Dimer cation core type structures as in Fig. 5.2a are at least 40 kJ/mol higher in energy than the global minimum structures. For further confirmation, IR spectra based on the most stable "dimer cation core" type structures are simulated and given in Fig. 5.22. We found that observed spectral patterns, e.g., similarity to $H^+(H_2O)_n$, are not accounted for by these
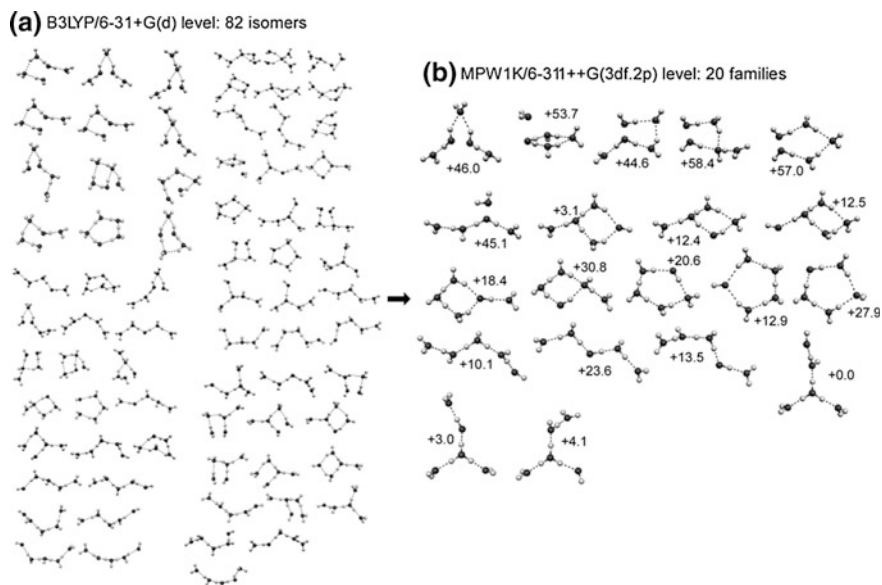
Fig. 5.21 Isomer structures of $(H_2O)_5^+$ and their relative energies obtained with the present calculations. **a** Results of GRRM calculation at the B3LYP/6-31+G(d) level. **b** Re-optimization of structures in (**a**, **b**) at the MPW1K/6-311++G(3df,2p) level. Relative energies of each structure were calculated at the MPW1K/6-311++G(3df,2p) level

simulated spectra. These results are consistent with our experimental findings and also with recent theoretical studies [85].

We also carried out calculations at the HF/6-31G(d) level. We found that this level does not describe dimer cation core type structures. However, we used this method for partial searches of stable isomers. This limitation had the advantage of reducing computation times. In the HF/6-31G(d) level, we found 2, 9, 40, 62, 170, and 224 isomers for $(H_2O)_{3-8}^+$, respectively. By checking their relative energies, we found isomers with a separated pair of H_3O^+ and OH are lower in energy by 3–10 kJ/mol than those with a H_3O^+-OH contact pair, even in the same network shapes (i.e. chain and ring). This suggests generality of the stabilization effect in the separation of the ion-radical contact pair.

5.4.10 Importance of the Characterized Structural Trends

Figure 5.23 presents experimentally-characterized structures of $(H_2O)_n^+$. These clusters are easily constructed from the $H^+(H_2O)_n$ structures by substituting one of the water molecules, which is the next neighbor of the charged site. The results obtained here seem to be very simple but may have important implications for the ionizing radiation-induced processes in bulk water. As seen in structures of $(H_2O)_n^+$,
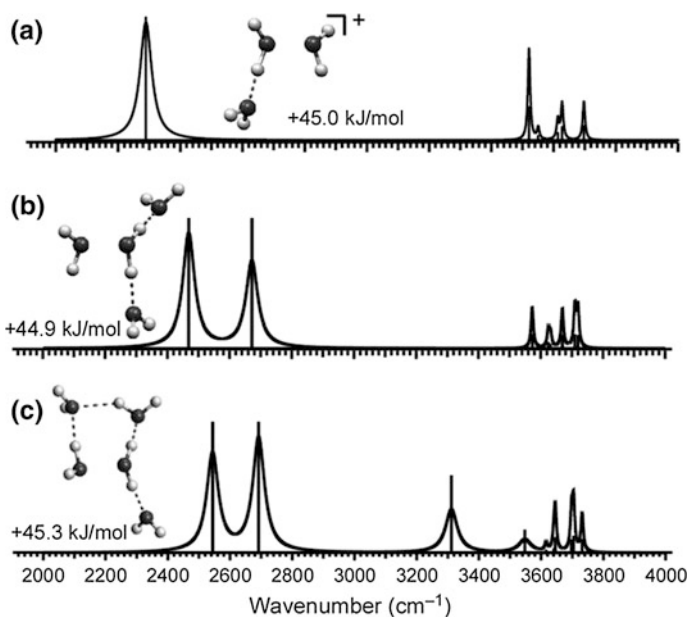
Fig. 5.22 IR spectral simulations for the most stable "dimer cation core" type isomers of $(H_2O)_{3-5}^+$. We note they are less plausible structures
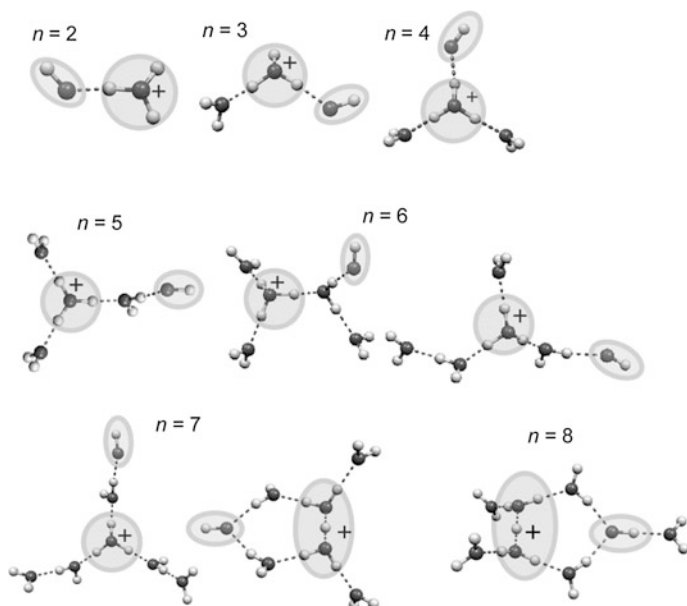
Fig. 5.23 Experimentally characterized cluster structures of $(H_2O)_n^+$
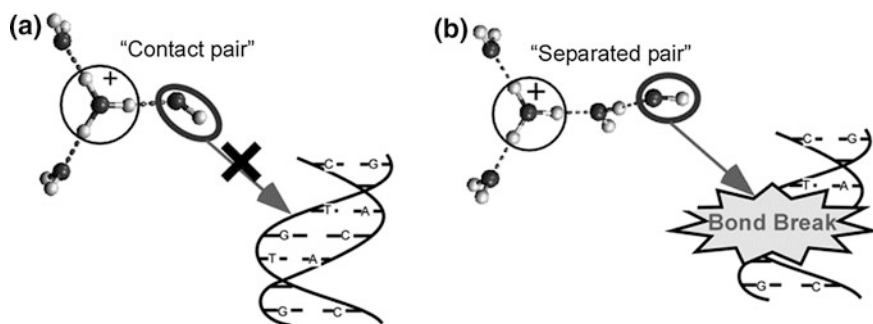
Fig. 5.24 Supposed reaction mechanisms in cationized water networks. **a** OH radical is tightly bound with the charged site and therefore, less reactive. **b** OH radical is free from the charged site and ready for reactions

the ionization of a water molecule should result in a H_3O^+–OH contact pair formation via a fast proton transfer. This study demonstrated that this H_3O^+–OH contact pair is not stable in water networks and the separation between the ion core and the OH radical occurs. In radical reactions, reaction barrier height is generally quite low and reaction rate should be determined by the mobility of radicals. It is expected that the OH radical separation from the protonated site would lead to higher reactivity compared with the case of the contact pair, in which the OH radical is tightly bound to the charged site. This motif is presented in Fig. 5.24. This study provides a new chemical model, which will be governed by hydrogen bond strength. We emphasize that the present findings are not accessible in the condensed phase studies due to the numerous surrounding molecules.

5.5 Conclusions

To investigate detailed structures of cationized water networks, we reported the IR photodissociation spectra of the water cluster radical cations $(H_2O)_n^+$ ($n = 3$–11) and $(H_2O)_n^+\cdot Ar$ ($n = 3$–7) in the OH stretch region. The spectral similarity to $H^+(H_2O)_n$ and the presence of the OH radical stretch band shows that nominal water cluster cations $(H_2O)_n^+$ form proton-transferred type clusters $H^+(H_2O)_{n-1}(OH)$ and also that shapes of the hydrogen bond network are quite similar to those of $H^+(H_2O)_n$. Because an OH radical is a weaker hydrogen bond acceptor than a water molecule, the first solvation shell of the protonated site is preferentially filled with water. As a result, the OH radical is separated from the protonated site by one water molecule in the $n \geq 5$ clusters. In the region away from the protonated site, we found the OH radical tends to act as a hydrogen bond donor. According to these findings, structures of $(H_2O)_n^+$ can be constructed from the structures of $H^+(H_2O)_n$ by substituting one of the next neighbor molecules from the protonated site with an OH radical. Reactivity of water exposed to ionizing radiation should depend on

hydrogen bond network structures around the created radicals. We therefore hope the findings in this study may be helpful in understanding the detailed processes of ionizing radiation-initiated reactions in liquid water and aqueous solutions.

References

1. I.G. Draganic, Z.D. Draganic, *The radiation chemistry of water* (Academic Press, New York, 1971)
2. B.C. Garrett, D.A. Dixon, D.M. Camaioni, D.M. Chipman, M.A. Johnson, C.D. Jonah, G.A. Kimmel, J.H. Miller, T.N. Rescigno, P.J. Rossky, S.S. Xantheas, S.D. Colson, A.H. Laufer, D. Ray, P.F. Barbara, D.M. Bartels, K.H. Becker, K.H. Bowen, S.E. Bradforth, I. Carmichael, J.V. Coe, L.R. Corrales, J.P. Cowin, M. Dupuis, K.B. Eisenthal, J.A. Franz, M.S. Gutowski, K.D. Jordan, B.D. Kay, J.A. LaVerne, S.V. Lymar, T.E. Madey, C.W. McCurdy, D. Meisel, S. Mukamel, A.R. Nilsson, T.M. Orlando, N.G. Petrik, S.M. Pimblott, J.R. Rustad, G.K. Schenter, S.J. Singer, A. Tokmakoff, L.-S. Wang, T.S. Zwier, Chem. Rev. **105**, 355–390 (2005)
3. S. Lehnert, *Biomolecular Action of Ionizing Radiation* (Taylor & Francis Group, New York, 2008)
4. J.F. Ward, Prog. Nucl. Acid Res. Mol. Biol. **35**, 95–125 (1988)
5. S.G. Swarts, M.D. Sevilla, D. Becker, C.J. Tokar, K.T. Wheeler, Radiat. Res. **129**, 333–344 (1992)
6. J. Cadet, T. Douki, D. Gasparutto, J.-L. Ravanat, Mutat. Res. **531**, 5–23 (2003)
7. C.-R. Wang, J. Nguyen, Q.-B. Lu, J. Am. Chem. Soc. **131**, 11320–11322 (2009)
8. C. Silva, P.K. Walhout, K. Yokoyama, P.F. Barbara, Phys. Rev. Lett. **1998**, 80 (1086)
9. Y. Gauduel, S. Pommeret, A. Migus, A. Antonetti, Chem. Phys. **149**, 1–10 (1990)
10. C.L. Thomsen, D. Madsen, S.R. Keiding, J. Thogersen, O. Christiansen, J. Chem. Phys. **110**, 3453–3462 (1999)
11. A. Migus, Y. Gauduel, J.L. Martin, A. Antonetti, Phys. Rev. Lett. **58**, 1559 (1987)
12. V. Buch, S. Bauerecker, J.P. Devlin, U. Buck, J.K. Kazimirski, Int. Rev. Phys. Chem. **23**, 375–433 (2004)
13. U. Buck, F. Huisken, Chem. Rev. **100**, 3863–3890 (2000)
14. K. Mizuse, T. Hamashima, A. Fujii, J. Phys. Chem. A. **113**, 12134–12141 (2009)
15. J.V. Coe, G.H. Lee, J.G. Eaton, S.T. Arnold, H.W. Sarkas, K.H. Bowen, C. Ludewigt, H. Haberland, D.R. Worsnop, J. Chem. Phys. **92**, 3980–3982 (1990)
16. J.V. Coe, Int. Rev. Phys. Chem. **20**, 33–58 (2001)
17. A.E. Bragg, J.R.R. Verlet, A. Kammrath, O. Cheshnovsky, D.M. Neumark, Science **306**, 669–671 (2004)
18. J.R.R. Verlet, A.E. Bragg, A. Kammrath, O. Cheshnovsky, D.M. Neumark, Science **307**, 93–96 (2005)
19. A.E. Bragg, J.R.R. Verlet, A. Kammrath, O. Cheshnovsky, D.M. Neumark, J. Am. Chem. Soc. **127**, 15283–15295 (2005)
20. D.M. Neumark, Mol. Phys. **106**, 2183–2197 (2008)
21. O.T. Ehrler, D.M. Neumark, Acc. Chem. Res. **42**, 769–777 (2009)
22. T. Maeyama, T. Tsumura, A. Fujii, N. Mikami, Chem. Phys. Lett. **264**, 292–296 (1997)
23. P. Ayotte, M.A. Johnson, J. Chem. Phys. **106**, 811–814 (1997)
24. N.I. Hammer, J.W. Shin, J.M. Headrick, E.G. Diken, J.R. Roscioli, G.H. Weddle, M.A. Johnson, Science **306**, 675–679 (2004)
25. N.I. Hammer, J.R. Roscioli, J.C. Bopp, J.M. Headrick, M.A. Johnson, J. Chem. Phys. **123**, 244311 (2005)

26. K.R. Asmis, G. Santambrogio, J. Zhou, E. Garand, J. Headrick, D. Goebbert, M.A. Johnson, D.M. Neumark, J. Chem. Phys. **126**, 191105 (2007)
27. L.A. Posey, M.J. DeLuca, P.J. Campagnola, M.A. Johnson, J. Phys. Chem. **93**, 1178–1181 (1989)
28. O.P. Balaj, C.-K. Siu, I. Balteanu, M.K. Beyer, V.E. Bondybey, Int. J. Mass Spectrom. **238**, 65–74 (2004)
29. H. Shinohara, N. Nishi, N. Washida, J. Chem. Phys. **84**, 5561–5567 (1986)
30. R.T. Jongma, Y. Huang, S. Shi, A.M. Wodtke, J. Phys. Chem. A **102**, 8847–8854 (1998)
31. L. Angel, A.J. Stace, Chem. Phys. Lett. **345**, 277–281 (2001)
32. S. Yamaguchi, S. Kudoh, Y. Kawai, Y. Okada, T. Orii, K. Takeuchi, Chem. Phys. Lett. **377**, 37–42 (2003)
33. S. Tomoda, K. Kimura, Chem. Phys. **82**, 215–227 (1983)
34. K. Norwood, A. Ali, C.Y. Ng, J. Chem. Phys. **95**, 8029–8037 (1991)
35. S.P. de Visser, L.J. de Koning, N.M.M. Nibbering, J. Phys. Chem. **99**, 15444–15447 (1995)
36. R.N. Barnett, U. Landman, J. Phys. Chem. **99**, 17305–17310 (1995)
37. R.N. Barnett, U. Landman, J. Phys. Chem. A **101**, 164–169 (1997)
38. Y.V. Novakovskaya, N.F. Stepanov, Int. J. Quant. Chem. **61**, 981–990 (1997)
39. Y.V. Novakovskaya, N.F. Stepanov, J. Phys. Chem. A **103**, 3285–3288 (1999)
40. H. Tachikawa, J. Phys. Chem. A **106**, 6915–6921 (2002)
41. H. Tachikawa, J. Phys. Chem. A **108**, 7853–7862 (2004)
42. A. Furuhama, M. Dupuis, K. Hirao, J. Chem. Phys. **124**, 164310 (2006)
43. I.B. Muller, L.S. Cederbaum, J. Chem. Phys. **125**, 204305 (2006)
44. L. Belau, K.R. Wilson, S.R. Leone, M. Ahmed, J. Phys. Chem. A **111**, 10075–10083 (2007)
45. Y. Novakovskaya, Russ. J. Phys. Chem. A **81**, 216–224 (2007)
46. Y. Novakovskaya, Russ. J. Phys. Chem. A **81**, 225–234 (2007)
47. Y.V. Novakovskaya, Int. J. Quant. Chem. **107**, 2763–2780 (2007)
48. S. Yang, S.M. Brereton, S. Nandhra, A.M. Ellis, B. Shang, L.-F. Yuan, J. Yang, J. Chem. Phys. **127**, 134303 (2007)
49. A. Furuhama, M. Dupuis, K. Hirao, Phys. Chem. Chem. Phys. **10**, 2033–2042 (2008)
50. A. Kumar, M. Kołaski, H.M. Lee, K.S. Kim, J. Phys. Chem. A **112**, 5502–5508 (2008)
51. P.A. Pieniazek, J. VandeVondele, P. Jungwirth, A.I. Krylov, S.E. Bradforth, J. Phys. Chem. A **112**, 6159–6170 (2008)
52. Q. Cheng, F.A. Evangelista, A.C. Simmonett, Y. Yamaguchi, H.F. Schaefer, J. Phys. Chem. A **113**, 13779–13789 (2009)
53. H.M. Lee, K.S. Kim, J. Chem. Theor. Comp. **5**, 976–981 (2009)
54. G. Periyasamy, R.D. Levine, F. Remacle, Chem. Phys. **366**, 129–138 (2009)
55. P.A. Pieniazek, E.J. Sundstrom, S.E. Bradforth, A.I. Krylov, J. Phys. Chem. A **113**, 8141 (2009)
56. T. Jahnke, H. Sann, T. Havermeier, K. Kreidi, C. Stuck, M. Meckel, M. Schoffler, N. Neumann, R. Wallauer, S. Voss, A. Czasch, O. Jagutzki, A. Malakzadeh, F. Afaneh, T. Weber, H. Schmidt-Bocking, R. Dorner, Nat. Phys. **6**, 139–142 (2010)
57. E. Kamarchik, O. Kostko, J.M. Bowman, M. Ahmed, A.I. Krylov, J. Chem. Phys. **132**, 194311 (2010)
58. M. Mucke, M. Braune, S. Barth, M. Forstel, T. Lischke, V. Ulrich, T. Arion, U. Becker, A. Bradshaw, U. Hergenhahn, Nat. Phys. **6**, 143–146 (2010)
59. S. Barth, M. Ončák, V. Ulrich, M. Mucke, T. Lischke, P. Slavíček, U. Hergenhahn, J. Phys. Chem. A **113**, 13519–13527 (2009)
60. M. Sodupe, J. Bertran, L. Rodriguez-Santiago, E.J. Baerends, J. Phys. Chem. A **103**, 166–170 (1998)
61. G.H. Gardenier, M.A. Johnson, A.B. McCoy, J. Phys. Chem. A **113**, 4772–4779 (2009)
62. Y. Matsuda, N. Mikami, A. Fujii, Phys. Chem. Chem. Phys. **11**, 1279–1290 (2009)
63. M. Hachiya, Y. Matsuda, K. Suhara, N. Mikami, A. Fujii, J. Chem. Phys **129**, 094306 (2008)
64. L.I. Yeh, M. Okumura, J.D. Myers, J.M. Price, Y.T. Lee, J. Chem. Phys. **91**, 7319–7330 (1989)

65. M. Okumura, L.I. Yeh, J.D. Myers, Y.T. Lee, J. Phys. Chem. **94**, 3416–3427 (1990)
66. Y.S. Wang, J.C. Jiang, C.L. Cheng, S.H. Lin, Y.T. Lee, H.C. Chang, J. Chem. Phys. **107**, 9695–9698 (1997)
67. J.C. Jiang, Y.S. Wang, H.C. Chang, S.H. Lin, Y.T. Lee, G. Niedner-Schatteburg, J. Am. Chem. Soc. **122**, 1398–1410 (2000)
68. Y.S. Wang, C.H. Tsai, Y.T. Lee, H.C. Chang, J.C. Jiang, O. Asvany, S. Schlemmer, D. Gerlich, J. Phys. Chem. A **107**, 4217–4225 (2003)
69. M. Miyazaki, A. Fujii, T. Ebata, N. Mikami, Science **304**, 1134–1137 (2004)
70. J.W. Shin, N.I. Hammer, E.G. Diken, M.A. Johnson, R.S. Walters, T.D. Jaeger, M.A. Duncan, R.A. Christie, K.D. Jordan, Science **304**, 1137–1140 (2004)
71. H.C. Chang, C.C. Wu, J.L. Kuo, Int. Rev. Phys. Chem. **24**, 553–578 (2005)
72. J.M. Headrick, E.G. Diken, R.S. Walters, N.I. Hammer, R.A. Christie, J. Cui, E.M. Myshakin, M.A. Duncan, M.A. Johnson, K.D. Jordan, Science **308**, 1765–1769 (2005)
73. C.K. Lin, C.C. Wu, Y.S. Wang, Y.T. Lee, H.C. Chang, J.L. Kuo, M.L. Klein, Phys. Chem. Chem. Phys. **7**, 938–944 (2005)
74. C.-C. Wu, C.-K. Lin, H.-C. Chang, J.-C. Jiang, J.-L. Kuo, M.L. Klein, J. Chem. Phys. **122**, 074315 (2005)
75. S. Karthikeyan, M. Park, I. Shin, K.S. Kim, J. Phys. Chem. A **112**, 10120–10124 (2008)
76. Q.C. Nguyen, Y.-S. Ong, J.-L. Kuo, J. Chem. Theor. Comp. **5**, 2629–2639 (2009)
77. K. Mizuse, A. Fujii, N. Mikami, J. Chem. Phys. **126**, 231101 (2007)
78. G.E. Douberly, A.M. Ricks, M.A. Duncan, J. Phys. Chem. A **113**, 8449–8453 (2009)
79. G.E. Douberly, R.S. Walters, J. Cui, K.D. Jordan, M.A. Duncan, J. Phys. Chem. A **114**, 4570–4579 (2010)
80. S. Maeda, K. Ohno, J. Phys. Chem. A **111**, 4527–4534 (2007)
81. Y. Luo, S. Maeda, K. Ohno, J. Phys. Chem. A **111**, 10732–10737 (2007)
82. Y. Luo, S. Maeda, K. Ohno, J. Comput. Chem. **30**, 952–961 (2009)
83. L. Ma, K. Majer, F. Chirot, B. von Issendorff, J. Chem. Phys. **131**, 144303 (2009)
84. C.Y. Ng, D.J. Trevor, P.W. Tiedemann, S.T. Ceyer, P.L. Kronebusch, B.H. Mahan, Y.T. Lee, J. Chem. Phys. **67**, 4235–4237 (1977)
85. E. Livshits, R.S. Granot, R. Baer, J. Phys. Chem. A **115**, 5735–5744 (2011)
86. U. Even, J. Jortner, D. Noy, N. Lavie, C. Cossart-Magos, J. Chem. Phys. **112**, 8068–8071 (2000)
87. B.J. Lynch, P.L. Fast, M. Harris, D.G. Truhlar, J. Phys. Chem. A **104**, 4811–4815 (2000)
88. K. Ohno, S. Maeda, Chem. Phys. Lett. **384**, 277–282 (2004)
89. S. Maeda, K. Ohno, J. Phys. Chem. A **109**, 5742–5753 (2005)
90. K. Ohno, S. Maeda, J. Phys. Chem. A **110**, 8933–8941 (2006)
91. R.C. Herman, G.A. Hornbeck, Astrophys. J. **118**, 214–227 (1953)
92. Y. Maréchal, *The Hydrogen Bond and the Water Molecule* (Elsevier, Amsterdam, 2007)
93. J.R. Roscioli, L.R. McCunn, M.A. Johnson, Science **316**, 249–254 (2007)
94. E.P.L. Hunter, S.G. Lias, J. Phys. Chem. Ref. Data **27**, 413–656 (1998)

Chapter 6
Conclusions and Future Work

Abstract In order to develop our understanding of the nature of hydrogen-bonded water networks, we extended the spectroscopic investigation of water clusters to previously inaccessible regions in cluster chemistry. We established a new experimental scheme and developed a new experimental setup, using it to successfully measure size-selective IR spectra of large clusters as well as highly reactive water clusters. Problems in cluster spectroscopy, internal energy and isomer distribution, were addressed with a systematic cooling method. The observed findings have provided us with hitherto unrecognized information on the nature of hydrogen-bonded water networks.

In this thesis, in order to develop our understanding of the nature of hydrogen-bonded water networks, we extended the spectroscopic investigation of water clusters to previously inaccessible regions in cluster chemistry. We established a new experimental scheme and developed a new experimental setup, using it to successfully measure size-selective IR spectra of large clusters as well as highly reactive water clusters. Problems in cluster spectroscopy, internal energy and isomer distribution, were addressed with a systematic cooling method. The observed findings have provided us with hitherto unrecognized information on the nature of hydrogen-bonded water networks.

In our study of large water clusters, we investigated two types of labeled water clusters, phenol-$(H_2O)_n$ ($n < \sim 50$) and $H^+(H_2O)_n$ ($n \leq 221$). For Phenol-$(H_2O)_n$, "chromophore-labeled" clusters, moderate size-selection was achieved by using resonant two-photon ionization mass spectrometry. $H^+(H_2O)_n$ are "charge-labeled" clusters, and precise size-selection was performed with mass spectrometry. The observed spectra were analyzed in terms of ring-size motifs of the network shapes, the coordination number of water molecules, and order in the network. In both phenol-$(H_2O)_n$ and $H^+(H_2O)_n$ systems, the appearance and increase of 4-coordinated water molecules was observed. The spectral pattern of phenol-$(H_2O)_n$ suggested a structural evolution from the strained 4-membered ring

motif to more relaxed 5- and 6-membered ring motifs. In the spectra of $H^+(H_2O)_n$, the ordered network formation or the crystallization was implied at $n \geq \sim 100$.

Simplification provides a way of doing more detailed analysis of the cluster structures and spectra. We simplified the IR spectra of hydrated clusters by using an inert gas-mediated cooling technique. Internal energy-dependent spectra were measured and used to investigate dynamics as well as structures. This method also enabled isomer-specific analyses. On the basis of the present approach, molecular-level understanding of large water networks, consisting of more than 20 molecules, was achieved. For example, in the H_2-tagged antimagic clusters $H^+(H_2O)_{22}$, we observed the hitherto missing water molecule, which is at the outside of the magic-numbered ($n = 21$) water cage and should fluctuate in higher temperatures. The present study showed the tagging or messenger technique is a powerful tool to probe even such relatively large water networks, which fluctuate with thermal effects.

Studies on reactive water networks provide us with substantive information on the radiation chemistry of water. Water cluster radical cations $(H_2O)_n^+$ have been probed with our spectroscopy. Observed spectra were systematically analyzed and characteristic structural trends were established: Nominal water cluster cations $(H_2O)_n^+$ form proton-transferred type clusters $H^+(H_2O)_{n-1}(OH)$. Shapes of the hydrogen bond network are quite similar to those of $H^+(H_2O)_n$. Structures of $(H_2O)_n^+$ can be constructed from the structures of $H^+(H_2O)_n$ by substituting one of the next neighbor molecules from the protonated site with an OH radical. Based on these characterized trends, a new chemical model for the radiation-induced aqueous reaction was built.

Although water plays essential roles in various chemical and biological systems, our knowledge of water is still limited due to its complicated, fluctuating nature. The present findings on hydrogen-bonded water networks from cluster chemistry add to our knowledge of water chemistry.

As a result of our studies reported here, several future studies are suggested. Direct application of this thesis is expected. Spectroscopy of much larger clusters in much broader frequency regions will result in detailed structural insights. While this study focused mainly on structural trends, finer spectroscopic methods, such as hole-burning techniques, will enable better isomer-based understanding. In this study, we tuned internal energy, not temperature. Direct control of temperature should lead to the qualitative understanding of temperature (entropic) effects. I hope this thesis stimulates studies in these directions and provides a useful guide for structural analyses of large or reactive water clusters.

From the viewpoint of structural analyses of hydrogen bond networks, the present and previous studies have mainly provided insights into static structures, which correspond to the minima on the potential energy surfaces. The dynamic aspect of hydrogen bond networks is also important because of the fluctuating nature of water. Such a dynamic region corresponds to high-energy states (vibrational excited states). Energy deposition or heating of clusters leads to these regions; however, the dissociation process limits the temperature (energy) region of typical heating methods. Mode-specific excitation techniques will help to address this problem. I hope the hydrogen bond dynamics of water will be characterized at the molecular level in the near future.

Curriculum Vitae

Kenta Mizuse, Ph.D.
Date of Birth: February 16, 1984
Place of Birth: Niigata, Japan
Nationality: Japan

Since April 2011
Department of Photo-Molecular Science (Prof. Yasuhiro Ohshima's Lab.), Institute for Molecular Science, Japan

 Assistant professor

April 2008–March 2011

 The Japan Society for the Promotion of Science (JSPS) Research fellow

April 2006–March 2011
Department of Chemistry, Graduate School of Science, Tohoku University, Japan

 Ph.D. student

   Supervisor: Professor Asuka Fujii
   Degree obtained: Ph.D. in Science

April 2002–March 2006
Department of Chemistry, Faculty of Science, Tohoku University, Japan

 Undergraduate student

   Supervisor: Professor Naohiko Mikami

Publications

1. Mizuse, K. & Fujii, A. Infrared Spectroscopy of Large Protonated Water Clusters $H^+(H_2O)_{20-50}$ Cooled by Inert Gas Attachment. *Chem. Phys.* **in press**, doi:10.1016/j.chemphys.2012.07.012 (2013).

2. Mizuse, K. & Fujii, A. Tuning of the Internal Energy and Isomer Distribution in Small Protonated Water Clusters $H^+(H_2O)_{4-8}$: An Application of the Inert Gas Messenger Technique. *J. Phys. Chem. A* **116**, 4868–4877 (2012).

3. Mizuse, K., Suzuki, Y., Mikami, N. & Fujii, A. Solvation-Induced σ-Complex Structure Formation in the Gas Phase: A Revisit to the Infrared Spectroscopy of $[C_6H_6–(CH_3OH)_2]^+$. *J. Phys. Chem. A* **115**, 11156–11161 (2011).

4. Mizuse, K., Kuo, J.-L. & Fujii, A. Structural trends of ionized water networks: Infrared spectroscopy of water cluster radical cations $(H_2O)_n^+$ (n = 3–11). *Chem. Sci.* **2**, 868–876 (2011).

5. Mizuse, K. & Fujii, A. Structural Origin of the Antimagic Number in Protonated Water Clusters $H^+(H_2O)_n$: Spectroscopic Observation of the "Missing" Water Molecule in the Outermost Hydration Shell. *J. Phys. Chem. Lett.* **2**, 2130–2134 (2011).

6. Mizuse, K. & Fujii, A. Infrared photodissociation spectroscopy of $H^+(H_2O)_6 \cdot M_m$ (M = Ne, Ar, Kr, Xe, H_2, N_2, and CH_4): messenger-dependent balance between H_3O^+ and $H_5O_2^+$ core isomers. *Phys. Chem. Chem. Phys.* **13**, 7129–7135 (2011).

7. Hamashima, T., Mizuse, K. & Fujii, A. Spectral Signatures of Four-Coordinated Sites in Water Clusters: Infrared Spectroscopy of Phenol−$(H_2O)_n$ ($\sim 20 \le n \le \sim 50$). *J. Phys. Chem. A* **115**, 620–625 (2011).

8. Mizuse, K., Mikami, N. & Fujii, A. Infrared Spectra and Hydrogen-Bonded Network Structures of Large Protonated Water Clusters $H^+(H_2O)_n$ (n = 20–200). *Angew. Chem. Int. Ed.* **49**, 10119–10122 (2010).

9. Mizuse, K., Hasegawa, H., Mikami, N. & Fujii, A. Infrared and Electronic Spectroscopy of Benzene−Ammonia Cluster Radical Cations $[C_6H_6(NH_3)_{1,2}]^+$: Observation of Isolated and Microsolvated σ-Complexes†. *J. Phys. Chem. A* **114**, 11060–11069 (2010).

10. Mizuse, K., Hamashima, T. & Fujii, A. Infrared Spectroscopy of Phenol−$(H_2O)_{n>10}$: Structural Strains in Hydrogen Bond Networks of Neutral Water Clusters. *J. Phys. Chem. A* **113**, 12134–12141 (2009).

11. Hasegawa, H. *et al.* Observation of an isolated intermediate of the nucleophilic aromatic substition reaction by infrared spectroscopy. *Angew. Chem. Int. Ed.* **47**, 6008–6010 (2008).

12. Suhara, K., Fujii, A., Mizuse, K., Mikami, N. & Kuo, J. L. Compatibility between methanol and water in the three-dimensional cage formation of large-sized protonated methanol-water mixed clusters. *J. Chem. Phys.* **126**, 194306 (2007).

13. Mizuse, K., Fujii, A. & Mikami, N. Long range influence of an excess proton on the architecture of the hydrogen bond network in large-sized water clusters. *J. Chem. Phys.* **126**, 231101 (2007).
14. Mizuse, K., Fujii, A. & Mikami, N. Infrared and electronic spectroscopy of a model system for the nucleophilic substitution intermediate in the gas phase: The C–N valence bond formation in the benzene-ammonia cluster cation. *J. Phys. Chem. A* **110**, 6387–6390 (2006).